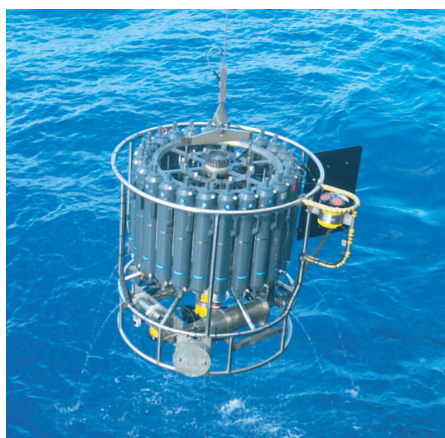# Development of a dynamical wetlands hydrology scheme and its application under different climate conditions

Tobias Stacke

Hinweis

Die Berichte zur Erdsystemforschung werden vom Max-Planck-Institut für Meteorologie in Hamburg in unregelmäßiger Abfolge herausgegeben.

Sie enthalten wissenschaftliche und technische Beiträge, inklusive Dissertationen.

Die Beiträge geben nicht notwendigerweise die Auffassung des Instituts wieder.

Die "Berichte zur Erdsystemforschung" führen die vorherigen Reihen "Reports" und "Examensarbeiten" weiter.

Notice

The Reports on Earth System Science are published by the Max Planck Institute for Meteorology in Hamburg. They appear in irregular intervals.

They contain scientific and technical contributions, including Ph. D. theses.

The Reports do not necessarily reflect the opinion of the Institute.

The "Reports on Earth System Science" continue the former "Reports" and "Examensarbeiten" of the Max Planck Institute.

Anschrift / Address

Max-Planck-Institut für Meteorologie
Bundesstrasse 53
20146 Hamburg
Deutschland

Tel.: +49-(0)40-4 11 73-0
Fax: +49-(0)40-4 11 73-298
Web: www.mpimet.mpg.de

Layout:

Bettina Diallo, PR & Grafik

Titelfotos:
vorne:
Christian Klepp - Jochem Marotzke - Christian Klepp
hinten:
Clotilde Dubois - Christian Klepp - Katsumasa Tanaka

Development of a dynamical wetlands hydrology scheme and its application under different climate conditions

Tobias Stacke

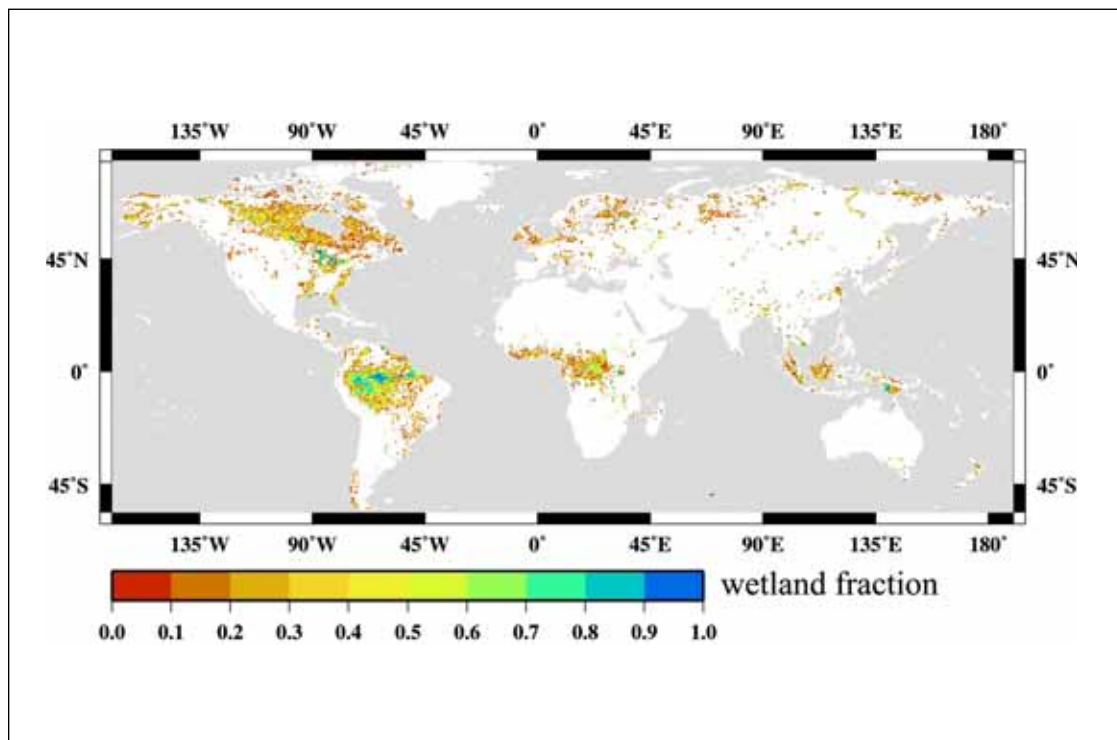aus Eisenach, Deutschland

Hamburg 2011

Tobias Stacke
Max-Planck-Institut für Meteorologie
Bundesstrasse 53
20146 Hamburg
Germany

Development of a dynamical wetlands hydrology scheme and its application under different climate conditions

Tobias Stacke

Hamburg 2011

A wetland emerged where there previously was a turnaround spot in the campground.

Randy Westmoreland

Contents

Contents

Acronyms

CRU Climatic Research Unit

DWES dynamical wetland extent scheme

GLWD Global Lake and Wetland Database

GRDC Global River Data Center

GRLM Global Reservoir and Lake Monitor

ET evapotranspiration

HD model Hydrological Discharge model

ITCZ Inter-Tropical Convergence Zone

LSP2 Land Surface Parameter Dataset 2

MATT Matthews and Fung wetland distribution dataset

MPI-HM Max Planck Institute – Hydrology Model

NRMSE normalized root mean squared error

PET potential evapotranspiration

SIND Satellite inundation dynamics dataset

SL scheme Simplified Land Surface scheme

WFD WATCH forcing data

wetland wetlands and lakes within the model

yBP years before present

Abstract

This PhD study concerns the development and validation of the dynamical wetland extent scheme (DWES) as well as its application under projected past and future climate conditions. The DWES is designed for global scale hydrological simulations. It solves the water balance of wetlands and derives their extent dynamically. Currently the scheme is embedded into the Max Planck Institute – Hydrology Model (MPI-HM), which was used as testbed for the scheme's development. The DWES might be applied to generate hydrological boundary data for the biogeochemical modeling of the wetland carbon cycle or to simulate the response of wetlands to changes in climatic conditions.

The core component of the DWES is the water flux equilibrium approach. The idea underlying this approach is that wetland water flows depend differently on water volume, depth and extent of the wetland. The wetland extent can then be adapted until the overall water inflows and outflows are balanced, resulting in a wetland which is stable under these hydrological conditions. The approach is further modified by the subgrid slope distribution of the respective model grid cell. This distribution determines how fast the wetland extent may adapt to changes in the water balance.

For present climate, the model validation reveals a good agreement between the occurrence of simulated and observed wetlands on the global scale. The best result is achieved for the northern hemisphere where not only the wetland distribution pattern but also their extent is simulated reasonably well by the DWES. However, the wetland fraction in the tropical parts of South America and Central Africa is strongly overestimated. The validation on monthly basis demonstrates a good correlation between observed and simulated wetland extent variations. Large scale processes like the influence of northern snow melt on wetland extent as well as its reaction to the rainy and dry seasons in the tropics are successfully reproduced by the DWES.

Simulations under past and future climate conditions yield plausible wetland distributions in respect to the forcing data. For the Mid-Holocene period, the DWES demonstrates its ability to represent realistic water level changes in accordance to Mid-Holocene lake level reconstructions for most regions. Discrepancies can mostly be attributed to the climate forcing data and to missing feedbacks between the DWES and the atmosphere. Likewise, the wetland simulations for the future time period are strongly influenced by the climate forcing. Their results reveal wetland growth in regions where precipitation exceeds evaporation while they desiccate in areas with reduced precipitation. Exceptions occur locally where processes like lateral water flow modify the direct climate forcing influence. Here, rivers efficiently drain the land surface in spite of a moisture surplus or transport water into an otherwise dry region.

In summary, the validation analysis and the model applications demonstrate the DWES' ability to simulate the global distribution of wetlands and their seasonal variations. Thus, it can provide hydrological boundary conditions for methane modeling as well as for paleoclimate studies. In future applications, the DWES should be implemented into an earth system model to study feedbacks between wetlands and climate.

1. Introduction

1.1. Motivation

Climate change is expected to have a significant impact on the earth's environment as well as on the human society. During the last decades climate science progressed considerably, and the IPCC reports (`http://ipcc.ch/index.htm`) regularly summarize the state of the art. The actual climate warming is strongly connected to anthropogenic greenhouse gas emissions. Next to CO_2, methane is recognized as an efficient greenhouse gas, and its current radiative forcing equals one third of the forcing of CO_2 (IPCC, 2007b). However, in the fourth IPCC assessment report the magnitude of methane emissions from different sources is still a key factor of uncertainty (IPCC, 2007a).

The largest single source of methane emissions are wetlands (IPCC, 2007b; O'Connor et al., 2010). While most of them are seen as net carbon sinks (Bohn et al., 2007; Friborg et al., 2003; Gorham, 1991), a number of studies concluded that some wetlands might turn into carbon sources in a warmer climate (Gorham, 1991; St-Hilaire et al., 2010). Next to the soil temperature, the water table depth plays an important role for the wetland's biogeochemistry leading to carbon sequestration or decomposition (e.g. O'Connor et al., 2010, and references therein). Additionally, the extent of wetlands needs to be computed for different climate conditions in order to estimate the accumulated amount of emitted methane. However, even for today the distribution and extent of wetlands are all but certain (e.g. Frey and Smith, 2007; O'Connor et al., 2010).

Furthermore, the wetland hydrology in itself is an important key player in the climate system. On the one hand, surface water has to be considered in climate models because of its feedbacks to the atmosphere (Coe and Bonan, 1997). The effect of open water surfaces on the energy and water balance was investigated by several studies, e.g. Bonan (1995) and Mishra et al. (2010), who reported a significant impact of wetlands on the local climate. On the other hand, wetlands interact in several ways with the hydrological cycle of their surrounding area (e.g. Bullock and Acreman, 2003, and Sect. 1.2). These processes are of high interest for impact studies that investigate how climate change might effect the water storage capacities in a region or the characteristics of river flooding.

The numerical modeling of wetland biogeochemistry relies on a correct representation of its hydrological cycle, especially its actual water table and extent. Furthermore, the knowledge about wetland hydrology and how it adapts to climate changes is the basis to project the wetland's influence on our environment for past and future epochs. For such reasons, O'Connor et al. (2010) stated the necessity to better represent the spatial extent and seasonality distribution of wetlands in climate models by improving the simulation of their hydrological cycle.

While a number of models exist which simulate wetland extent dynamics, only few of them are designed for the application on global scale (see Sect. 1.4). Instead, most simulation approaches are explicitly depending on detailed soil properties information (e.g. Bowling and Lettenmaier, 2010; Yu et al., 2006) or are calibrated to work in specific catchments (e.g. Bohn et al., 2007). Thus, the main objective of this PhD research is the development of a global hydrological scheme that represents a realistic water cycle for wetlands and computes their extent and distribution dynamically. Explicit requirements for this dynamical wetland extent scheme (DWES) are to use a simple approach for the wetland dynamics calculation and to be independent of fine scale boundary data such as soil conductivity distributions or porosity. Thus, the DWES might also be valid for paleoclimate simulations which lack detailed land surface boundary data. The DWES is not a hydrology model by itself. It is developed as part of the Max Planck Institute – Hydrology Model (MPI-HM) and will be structured in a way to ensure its easy transferability into other models.

It has to be noted that a pure hydrological model like the MPI-HM is not able to distinguish wetlands from lakes on grid cell scale. Albeit the motivation of the study is based on wetland hydrology, both, lakes and wetlands, are combined and referred to as wetlands whenever the model is concerned.

1.1.1. Research questions and structure of the PhD thesis

Following, a number of research questions are defined. These questions provide the leitmotif for this PhD thesis.

1. Is it possible to simulate the lake and wetland distribution and seasonal dynamics at global scale using a simple approach?
2. Is the DWES applicable for different states of climate or is it restricted to present-day climate conditions?
3. What changes can be expected for the future wetland development?
4. Does the DWES provide an added value compared to the existing suite of wetland models?

The first question is the main topic of the second and third chapter which are focused on the development and validation of the DWES, respectively. The second chapter investigates two approaches for wetland extent calculation and describes the implementation and parameter optimization of the superior method into the MPI-HM. The third chapter thoroughly validates the simulation results against global data of wetland observations as well as local station and satellite observations. Here, the emphasis lies on the correct representation of large scale wetland structures and their seasonality as well as the local water table depth variations.

The second and third questions will be answered in the fourth chapter in which the MPI-HM is applied for different climate projections. The plausibility of its results will be discussed. The projected changes of wetland extent in the future and its implications will receive special attention here.

The fourth question receives input from all three chapters. For easier reference, the advantages of the DWES will be summarized in the thesis' conclusion part (see Sect. 5.1).

1.2. Wetland hydrology and hydrological functions

Wetlands are characterized by very special hydrological conditions, which set them apart from other land cover types. They are perceived as being transitional between terrestrial and aquatic ecosystems (Mitsch and Gosselink, 1993). As wetlands are rather diverse as a ecosystem type themselves, it is difficult to phrase a definition which certainly includes all wetlands but excludes other ecosystem types (Cowardin and Golet, 1995; Reichhardt, 1995). The Ramsar Convention on wetlands (`www.ramsar.org`) states that wetlands are found in regions with a high water table and a therefore saturated soil, which might be temporarily or permanently covered by water (Ramsar, 2007). Hydrologically, they can be distinguished from lakes by a maximum water depth of 2 m because wetland plants are not able to survive in deeper water (Cowardin and Golet, 1995).

The hydrological cycle of wetlands shows strong inter-annual and year to year variations with wet and dry seasons (e.g. Gamble and Mitsch, 2009; Niemuth et al., 2010; Schedlbauer et al., 2010). Mitsch and Gosselink (1993) attributed such variations mainly to the balance of water inflow and outflow as well as to the topographical conditions of the surrounding land surface, the soil characteristics, geology and groundwater interactions. The latter parameters constrain the size of the wetland water storage while the water flow balance is determining its content. In order to compute the wetland water content, Mitsch and Gosselink (1993) described temporal variation of its volume V as

$$\frac{\Delta V}{\Delta t} = P_n + S_i + G_i - ET - S_O - G_0 \pm T \tag{1.1}$$

where P_n is the net precipitation, S_i and S_o are the surface inflows and outflow, G_i and G_o are groundwater inflow and outflow, ET is evapotranspiration and T is the balance of tidal flows. A simplified sketch of this water balance is displayed in figure 1.1. For a given time step, the authors formulated the mean wetland depth $\overline{d}$ as

$$\overline{d} = \frac{V}{A} \tag{1.2}$$

with A being the wetland's surface area. Depending on the type of wetland only a selection of the water fluxes of equation 1.1 exists. Mitsch and Gosselink (1993) distinguished several wetland ecosystems:

- Coastal wetlands are usually dominated by tides. They host a very specific plant community which is tolerant against regular inundations and sea water intrusion.
- Freshwater marshes experience strong seasonal variations in their water supply, which can be provided by different sources. These are mostly precipitation and surface inflow but also groundwater. Grasses, sedges and other emergent hydrophytes are the dominant plant type in this ecosystem.
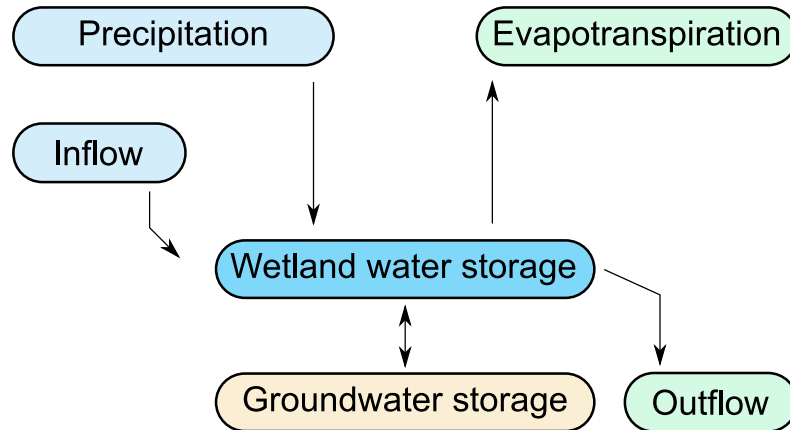
Figure 1.1.: Simplified water balance for wetlands. The inflow and outflow box contain all lateral water flows like streamflow and tidal water movements. Modified and redrawn from Mitsch and Gosselink (1993).

- Peatlands occur in the high northern latitudes and are subdivided in bogs and fens. Bogs are nutrient poor structures with high water table relying on precipitation as their only water source. In contrast, fens receive water from their surrounding land surface and from groundwater, too (Holden, 2005). Of all wetlands, bogs and fens attract most attention as they accumulate great amounts of peat and, thus, are a key factor in the generation of methane.
- Deepwater swamps are characterized by standing surface water for most of the year. Usually, this wetland type is forested.
- Riparian wetlands occur close to rivers and are periodically flooded. They support a wide range of plant species.

Another features which are very specific for wetlands are their soil characteristics. Here, soil properties and hydrology are strongly connected as the soil is the primary water storage. Wetland soils are referred to as hydric soils and defined by the Soil Conservation Service (1991) as being saturated during the growing season long enough to allow for the development of anaerobic conditions. The water depth in a wetland determines the partition of its soil into an aerobic and an anaerobic soil layer. From the perspective of climate science the position of the wetland water table and the soil temperature are most interesting as they control the biochemical reactions resulting in methane and CO_2 emissions. A sketch for methane production and transmission is displayed in figure 1.2. As illustrated by Lai (2009) the anaerobic soil layer is the origin of methane which is generated by microbes and diffuses to the surface. In the aerobic soil layer and in the water layer oxidic respiration by microbes and inorganic oxidation takes places and transforms organic carbon and parts of the rising methane into CO_2 (Mitsch and Gosselink, 1993). Whether a wetland acts as net carbon sink or as a source of methane and CO_2 depends on the ratio of sequestration versus decomposition of organic material.
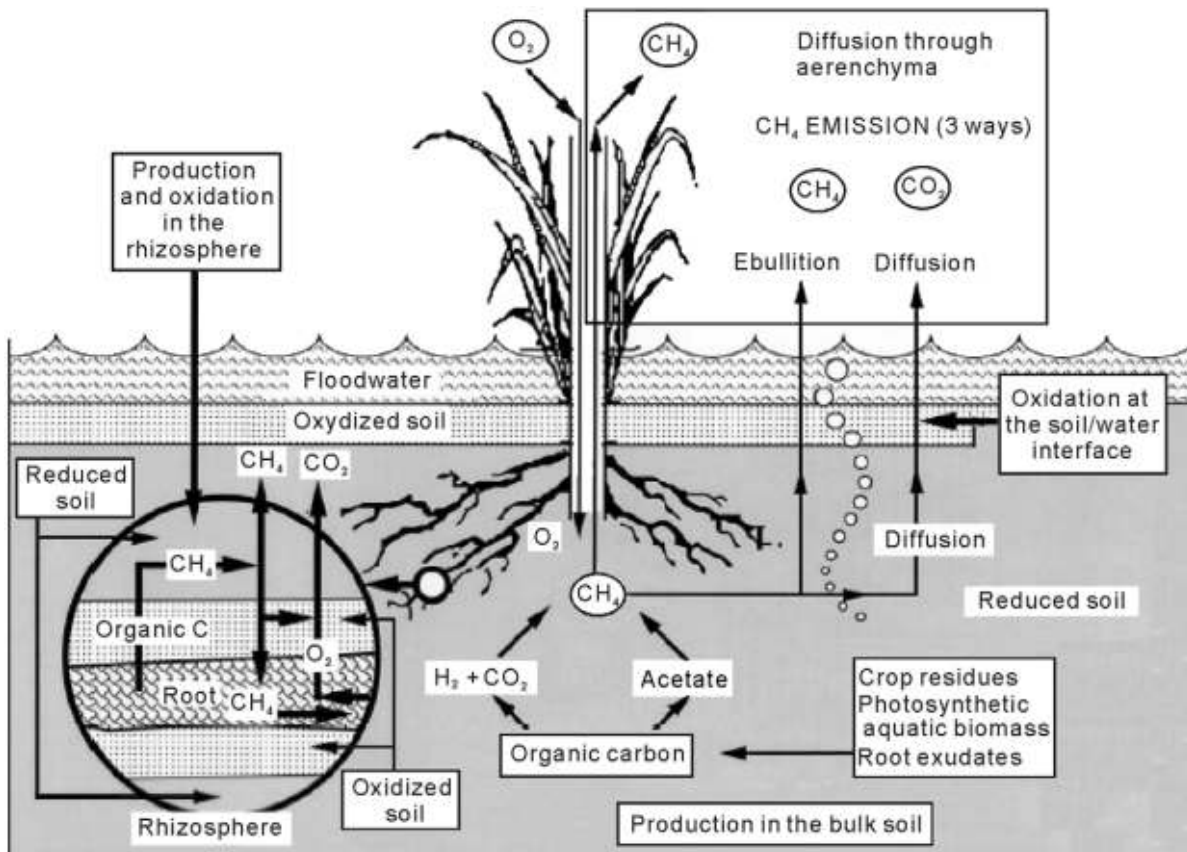
Figure 1.2.: Production, consumption and transport of methane in peatland. This figure is taken from Lai (2009).

Wetlands provide a number of ecosystem services such as water storage, groundwater recharge, flood control, shoreline stabilization, water quality control, stabilization of local climate as well as biodiversity and wildlife support (Mitra et al., 2005). As this thesis applies a pure hydrological model for the simulation of wetlands, only the hydrological functions will be discussed. An excellent review about the role of wetlands in the hydrological cycle is given by Bullock and Acreman (2003) and their main conclusions are summarized in the following paragraph.

Bullock and Acreman (2003) stated that the majority of published wetland hydrology studies found a significant influence of wetlands on the hydrological cycle. In the most widespread opinion, wetlands reduce floods, promote groundwater recharge and regulate river flows. While this seems to be true for most floodplain wetlands, several headwater wetlands appear to increase flood events by immediately transferring rainfall into the river network. Usually, wetlands are known to be the strongest evaporating land cover type and therefore reduce river flow. This effect is strongest in the dry season. Again, the authors noted several exceptions from this rule. However, these wetlands, which are causing no or even the opposite effect, do not show a noticeable bias in their geographical location or wetland type. Overall, the wetland interactions with groundwater are very

diverse. While most wetlands are found on impermeable soils or bedrock, there are a significant number who receive groundwater or recharge it. The latter are mostly found at temporary inundation areas, the former at springs. Some wetlands even change between groundwater recharge and discharge depending on the water budget.

The Bullock and Acreman (2003) study demonstrated that in most cases wetlands follow the traditional view and in fact are mitigating flood events, regulating river flow, recharging groundwater and increasing evaporation. However, their complex hydrology and their different types lead to several exceptions from this rule.

1.3. Global wetland observations

Global observations of wetland extent are necessary in order to parametrize and, finally, to validate the DWES. However, there is a large uncertainty in identifying wetlands, which is reflected by the available observation data sets. One reason for this uncertainty is the large variety in wetland definitions. Beside hydrological conditions (see Sect. 1.2), wetlands can alternatively be identified by certain soil types (Megonigal et al., 1993; Soil Conservation Service, 1991) or plant communities (Riefner Jr and Boyd, 2007; Tiner, 2006) in most cases. Still, there are special types of wetlands, like drained wetlands or artificial ones, which are not captured by these definitions (Wakeley, 1994). For this reason, the model development and validation are not based on a single dataset, which might be biased towards a certain wetland type, but use a selection of four global datasets (see Fig. 1.3). Thus, it is expected to balance the deviations of the respective datasets from reality to a certain degree. In this section, these four datasets will be presented.

The oldest wetland dataset which is used in this study is the Matthews and Fung wetland distribution dataset (MATT) by Matthews and Fung (1987). Its original resolution is 1°. It contains wetlands identified by their vegetation, soil properties and grid cell inundation fraction, all based on field data and aerial photography. Five wetland types are distinguished, namely forested bogs, non-forested bogs, forested swamps, non-forested swamps and alluvial wetlands. In total, they cover an area of about $5.3 \cdot 10^6$ km^2 which translates into 3.6% of the land surface excluding Antarctica. The authors found most wetlands in western Siberia, northeastern Europe as well as in the area between Alaska and the Hudson Bay. Also, they located tropical wetlands in Indonesia, Africa and South America. While the authors admitted a distinct uncertainty in their data sources, they were confident about their wetland compilation as all separate data sources result in similar zonal mean wetland distributions.

The Land Surface Parameter Dataset 2 (LSP2) was compiled by Hagemann et al. (1999) and revised by Hagemann (2002). It includes lakes as well as wetlands, and it is derived from the Global Land Cover Characteristics Data Base (U.S. Geological Survey, 2001), which was generated using satellite data with a resolution of 1 km. While lakes are easily identified, the authors stated an increased uncertainty in the distribution and extent of the wetland fraction. Hagemann (2002); Hagemann et al. (1999) explained this insufficiency by the fact that a number of wetlands were ignored in the data set compilation because they are not the primary land cover type for the respective grid

cell. The authors referred especially to the poor representation of the Pantanal swamps and the wetlands in the Parana catchments in Central South America as well as to the wetland distribution in the Congo catchments. In total, the LSP2 claims a land surface lake and wetland fraction of about 4.9%. It shows most wetlands for the high latitudes in North America and Siberia as well as in India and China. There are only few wetlands visible in the tropical parts of South America and Africa.

Lehner and Döll (2004) combined several existing maps and data bases into the Global Lake and Wetland Database (GLWD). It provides the maximum extent of lakes, reservoirs, rivers and wetlands at a resolution of 30" divided into 12 classes. The total wetland coverage amounts to 7.8% of the land surface. The wetlands cluster mainly in North America, Scandinavia and the western and eastern regions of Siberia. Again, tropical wetlands can be seen for central Africa, the Amazon catchment and major parts of Brazil. The authors validated the GLWD against other land cover data bases and find significant differences for some regions. Especially for Northern Europe and Northern Russia they expected the GLWD to underestimate the wetland area. However, when generating a gross wetlands map using the maximum extent of all validation datasets, Lehner and Döll (2004) achieved a good agreement between their GLWD and the gross wetlands map for the latitudinal and longitudinal wetland distribution for many regions.

Finally, a pure satellite product is taken into account which represents surface water covered areas on a monthly basis (Papa et al., 2010; Prigent et al., 2001, 2007). In this PhD thesis these data is referred to as Satellite inundation dynamics dataset (SIND). The SIND is based on a 12 years time series originating from several different satellites using active and passive microwaves measurements as well as visible and near-infrared imagery. From this data Prigent et al. (2001, 2007) and Papa et al. (2010) calculated inundated area fractions for 0.25° grid cells. While the authors claimed that their multisatellite approach accounts even for open water under dense canopy, snow covered areas were masked out to avoid any confusion between open water and snow pack. The monthly variability of the SIND is validated on catchment scale and its global extent is compared against other databases. From this, the authors concluded that the SIND represents a realistic distribution of inundation area in space and time. In agreement with the other three datasets, the SIND shows extensive wetlands for Northern America, Western Siberia and Northeastern Europe. Additionally, it finds an enhanced inundation fraction in India, China and the Amazon catchment. On average, the SIND shows a yearly maximum inundation of about 5.9% of the land surface.

The four observation databases are remapped to 0.5° resolution and displayed in figure 1.3. They mostly show a good agreement in large scale features like the wetland band between Alaska and the Hudson Bay, as well as the increased wetland fractions in western Siberia. The also concur in the existence of tropical wetlands although to a varying degree. However, in detail these maps are very different. Partly, this is suspected to be caused by the different methods by which they were generated. Also, the datasets apply different wetland definitions ranging from open water on the surface to wetland associated plant communities. Lehner and Döll (2004) already discovered a strong disagreement on local and even regional scales between different wetland datasets. This is confirmed by Frey and Smith (2007) who compared several satellite and mapping products in respect
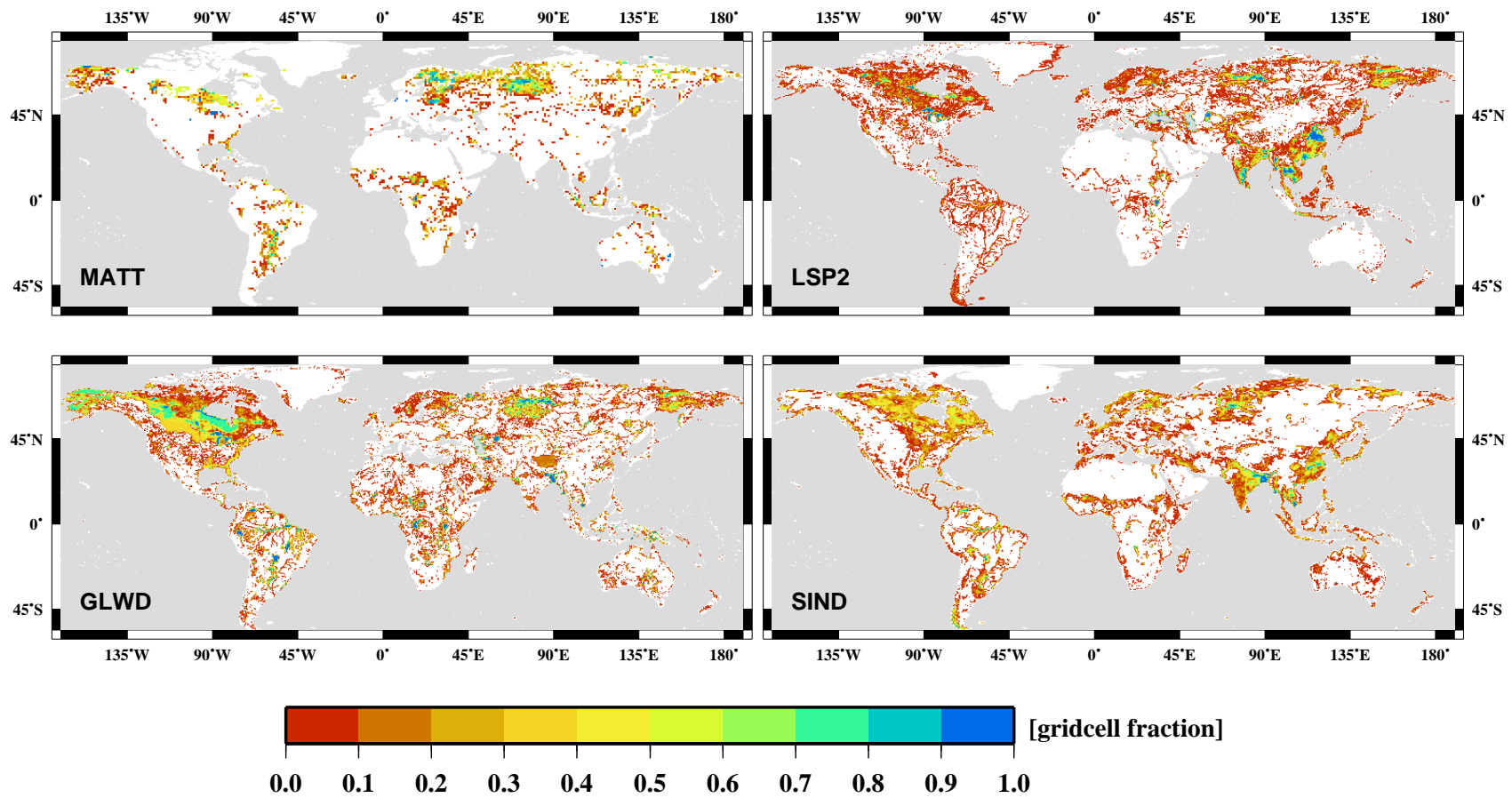
Figure 1.3.: Global observations of wetland or surface water area at 0.5° resolution. Wetlands covering a fraction less than 0.01 are masked out. The SIND shows the maximum inundation fraction of its monthly climatology for every grid cell.

to wetland extent in West Siberia. Not only did they find large differences between the datasets, but they also demonstrated a significant disagreement of these datasets with the ground-truth data they collected themselves during a field trip. Finally, Frey and Smith (2007) concluded that even databases using multiple resources, like the GLWD, do not compensate for the errors in their single sources but more likely compound them. For this reasons, the DWES will not aim to match any of the four observations perfectly but will rather work within the range of observations and try to agree in the large scale wetland clusters.

1.4. Review of wetland models

Due to the high interest in methane emission processes, several models already exist which try to simulate the hydrological cycle in wetlands. This section will present a short review about the different approaches for this task. The review will focus on models which simulate wetland extent dynamically.

For wetland simulation on the scale of river catchments a method is available based on the topographical wetness index. This index was developed by Beven and Kirkby (1979) for their hydrological runoff model *TOPMODEL*. They assumed that the topography dominates the distribution of soil moisture within a catchment. Their index is derived from the ratio of uphill area and slope for certain points within the catchment. It is low for steep areas and increases in lowlands. The average soil moisture of the catchment is then distributed such that flat areas with a high index get a higher soil water content than uphill areas with a low index. Thus, a high topographical wetness index can be used as a proxy for wetlands as it indicates the lowland fraction of a catchment, which is much more likely to become saturated. Later on, Barling et al. (1994) expanded this method by also considering the slope shape and the time to redistribute soil moisture throughout the catchment. Some other models used a similar reasoning but included more complex hydrological processes (e.g. O'Loughlin, 1986).

The *TOPMODEL* approach is widely used and inspired a number of wetland modeling studies. For example, Bohn et al. (2007) combined the topographical wetness index with a hydrological model, a vegetation model and a methane emission model to predict wetland methane emissions at regional scale for a bog in western Siberia. Merot et al. (2003) replaced the uphill area in the topographical wetness index with its effective rainfall water volume and tested the simulation of wetlands for some catchments in Europe.

A very complex model was presented by Bowling and Lettenmaier (2010). They simulated lakes and wetlands for several Arctic catchments applying a full water balance and energy cycle. Their wetlands are allowed to vary in depth as well as in space, determined by a fixed volume-area relationship which the authors derived from high resolution land cover and DEM data.

On continental scale wetlands were simulated by Coe (1998). The author computed wetland extent based on topographical data. In this method, depressions in the land surface are equated with potential wetland areas which are filled depending on the actual water balance. While the approach works well for lakes, the author stated that the

models ability to identify wetlands is poor caused by the insufficient vertical accuracy of the topographical data.

The hydrology model by Yu et al. (2006) explicitly simulates the groundwater table and allocates lakes and wetlands at its intersection with the land surface. It works on a highly resolved grid and uses detailed hydrological information for soils and bedrock. The authors applied this model for an interactive climate-hydrology simulation over the North American continent.

Finally, models on global scale are reviewed. A very simple approach was taken by Kaplan (2002). By comparison of model parameters with wetland observations he achieved a good agreement for all grid cells with a volumetric soil moisture above 65 % and mean slope less than 0.3 %. A similar method was used by Kaplan et al. (2006). Another study was presented by Gedney and Cox (2003) who investigated the sensitivity of global climate simulations to wetland representation. For this task, they implemented a simplified version of *TOPMODEL* into a land surface scheme and conducted coupled atmosphere – land surface simulations under different CO_2 concentrations.

Furthermore, there are a number of wetland models which do not vary the spatial extent of the wetlands. An early approach was the modeling of wetlands as a single hydrological unit (Bavina, 1970). Here, the focus was on the computation of the local water balance of a single swamp. This approach is based on observations of the distribution of the filtration coefficient in the active layer of the wetland and the subsequent discharge. Other studies used only one dimensional models or relied on static masks of wetland observations. They allowed for vertical dynamics in the wetlands water table calculation only. Examples for these are the studies by Petrescu et al. (2010); Walter et al. (2001); Wania et al. (2009) on global scale and Comer et al. (2000); Tamea et al. (2010); Van Huissteden et al. (2009) for separate sites.

2. Development of the dynamical extent scheme for wetlands

2.1. Introduction to the MPI-HM

The Max Planck Institute – Hydrology Model (MPI-HM) is a global hydrological model, designed to simulate the vertical and lateral water balance on the land surface. Its area of operation focuses on the simulation of river discharge for different large scale catchments. Additionally, a wide range of hydrological parameters like evapotranspiration (ET), soil moisture, surface runoff and drainage are also calculated. Similar to climate models the MPI-HM shows an internal variability which complicates the direct comparison of its results to observations. This variability is mainly due to the variability of the input data, but also caused by some empirical formulations used within the model itself. For this reason its results are usually averaged over at least 30 years on a monthly basis. Thus it is necessary to obtain equally extensive time series of observation for comparison. Technical details about the model are presented in table 2.1.

Scale	global
Time steps	daily
Resolution	$0.5° \approx 55 \times 55$ km at equator
Input data	2 m temperature, precipitation, optionally potential evapotranspiration
Boundary data	soil's field capacity, vegetation cover fraction, land fraction, glacier fraction, permafrost fraction, sub-grid slope and water holding capacity information, elevation, river routing direction, storage retention times
Simulation results	Snowmelt, Snowcover, ET, Soil moisture, Surface runoff, Drainage, wetland distribution, wetland water depth, Snowfall, River discharge

Table 2.1.: Technical details about the MPI-HM.

A new feature of the MPI-HM is the dynamical simulation of wetland area, which was developed during this study. Based on highly resolved topographical information together with an explicit simulation of the wetland water balance, it is now possible to estimate its variations in size and volume.

13

The MPI-HM consists of two submodels and the DWES which acts as an interface between them. The Simplified Land Surface scheme (SL scheme) (Hagemann and Dümenil Gates, 2003) calculates vertical water fluxes while the Hydrological Discharge model (HD model) (Hagemann and Dümenil, 1998a, 1999; Hagemann and Dümenil Gates, 2001) computes lateral water fluxes and river routing. Before this study started, both submodels were separate models of their own and usually applied in a serial mode. However, the implementation of dynamical wetlands in both submodels made it necessary to exchange information between the lateral and vertical water balance at model time step level. Thus, an interface was designed to combine the SL scheme and HD model. The coupled version of both is called the MPI-HM.

2.1.1. The Simplified Land Surface scheme

The SL scheme simulates the vertical water fluxes on the land surface. Its main purpose is the calculation of surface runoff and drainage, which are input variables for the HD model. The standard SL scheme input variables are global fields of 2m temperature and precipitation. Water storages and fluxes are computed from top to bottom as shown in figure 2.1.
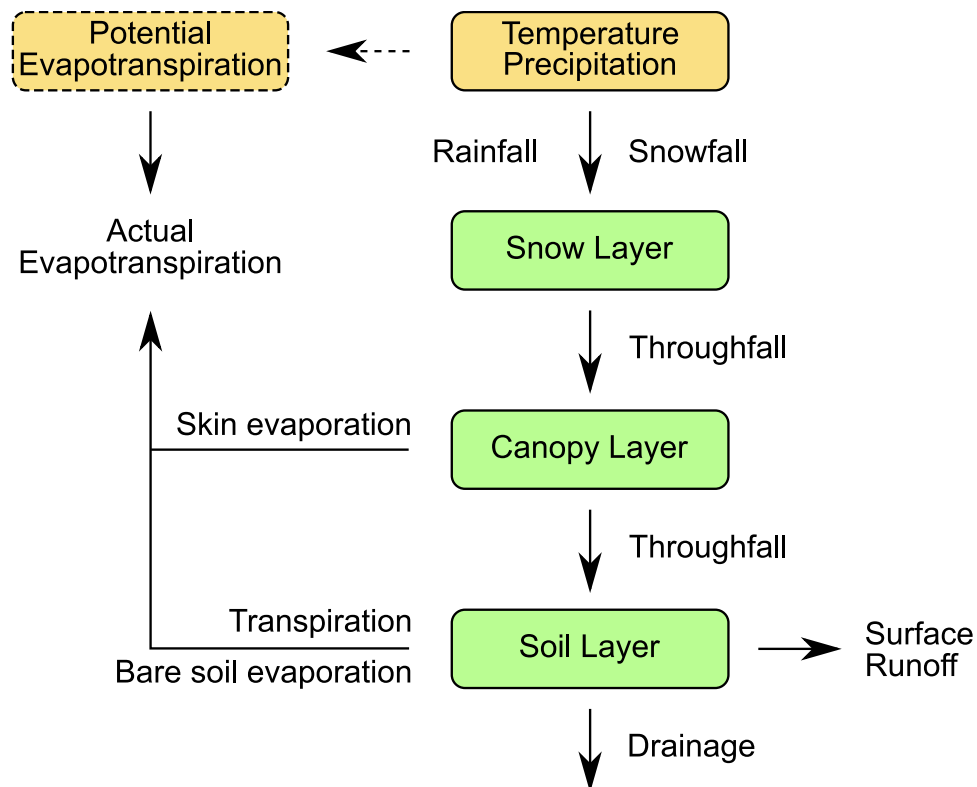

Figure 2.1.: Overview about the structure of the SL scheme. Orange boxes indicate input variables, green boxes indicate water storages, and black arrows indicate fluxes.

The following calculation steps are conducted for every model timestep and every land

surface grid cell:

An upper boundary for actual ET is provided by potential evapotranspiration (PET). PET can either be imported as an additional input variable or estimated internally. The latter is done using the approach after Thornthwaite (Thornthwaite, 1948; Thornthwaite and Mather, 1955). The Thornthwaite formula describes an empirical relation between PET and the daily mean temperature scaled by relative day-length. Thus, pure temperature data is already sufficient to get an estimate of PET. However, there are disadvantages, too. Federer et al. (1996) and Vörösmarty et al. (1998) conducted an intensive comparison of different PET estimation methods. They found a poor performance of the Thornthwaite formulation. Furthermore, they recommended to use surface cover dependent algorithms instead of reference surface schemes for climate change simulations. For this reason, an optional forcing with PET data is implemented into the SL scheme.

Depending on temperature, precipitation is divided into rainfall and snowfall. When appropriate, they are added to the snow layer. A daily degree snow scheme is applied to calculate the amount of snowmelt. This, together with rainfall, forms the throughfall which enters the canopy storage. This storage was not active in former SL scheme simulations. However, in combination with externally calculated PET the storage improves the scheme's performance. The canopy storage is allowed to evaporate as much water as it can hold or PET allows. Overflow from the canopy storage reaches the ground as interception and is divided into infiltration and surface runoff as computed by the improved Arno scheme (Hagemann and Dümenil Gates, 2003). The infiltration is added to a bucket type soil layer. The amount of soil moisture determines the water available for drainage and ET. Drainage is calculated using a scheme after Dümenil and Todini (1992). This scheme scales drainage linearly when soil moisture is below a certain moisture threshold, but it increases drainages exponentially when the threshold is exceeded. Bare soil evaporation and plant transpiration are calculated separately. The bare soil evaporation uses a scheme after Bauer et al. (1983) which assumes a linear relation of evaporation to the PET – soil moisture ratio. Transpiration is set to maximum for soil moisture above the critical soil moisture. It decreases linearly towards zero at the wilting point. Both fluxes are then scaled according to the bare soil and vegetated fractions of the grid cell.

In summary the SL scheme includes a sophisticated hydrological cycle which is similar to the water balance calculations done by the land surface schemes of climate models. However, since it lacks an energy balance, it is less complex and consumes less computational power.

2.1.2. The Hydrological Discharge model

The Hydrological Discharge model (HD model) is a state of the art river routing model. The purpose of this model is the calculation of river discharge as well as its lateral propagation over the land surface grid cells to the ocean.

Originally, the HD model employs three water storages for every model grid cell (Fig 2.2). These are an overland flow storage, a baseflow storage and a river flow storage. While the first two storages get water from the SL scheme surface runoff and drainage

fields, the river flow storage gains inflow from upstream grid cells. The storages act as reservoirs and have specific water retention times which control the release of water. These retention times are based on the slope within and between grid cells as wells as the distance between them. In case of the river flow storage, a linear flow cascade with 5 reservoirs is used. This leads to a more realistic representation of hydrographs (Singh, 1988). The outflow of all three storages is combined as river flow and routed to the next downstream grid cell.
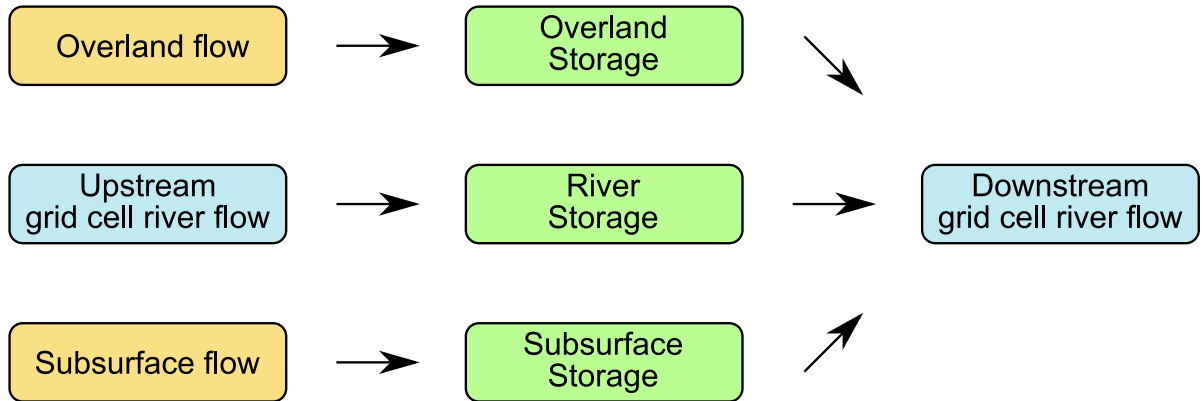

Figure 2.2.: Overview about the structure of the HD model. Orange boxes indicate input fields, green boxes indicate water storages, blue boxes indicate fields generated by the HD model, and black arrows indicate water fluxes.

The river routing is another crucial part of the HD model. River flow directions are based on the land surface topography. It is assumed that every grid cell drains into the neighboring grid cell with the lowest elevation. Thus a drainage network, similar to a real river network, is created. The quality of this routing network depends mostly on the resolution of the underlying topographical dataset. Details about this method can be found in Hagemann and Dümenil (1998a).

The routing network in combination with the linear flow cascade water storages simulates realistic hydrographs. Figure 2.3 show examples how peak flows are routed along the network.

Further information about the performance of the HD model as well as comparison with observations can be found in Graham et al. (2007); Hagemann and Dümenil (1998a, 1999); Hagemann and Dümenil Gates (2001).
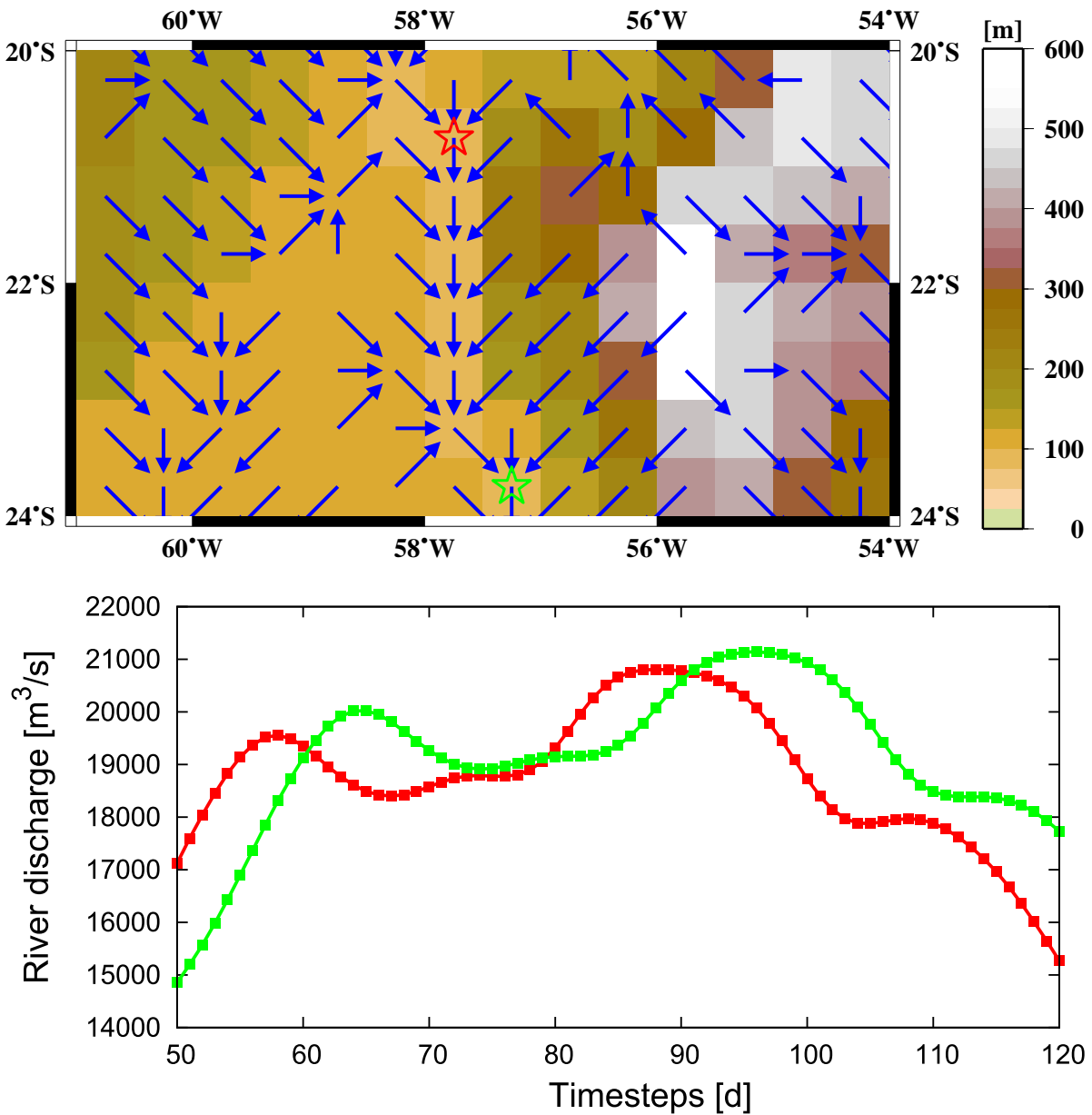
Figure 2.3.: Influence of the river network on peak times and overall flow of simulated river discharge. The top panel shows river flow directions (blue arrows) and topography of a part of the Paraguay river basin. The stars mark the positions of two simulated river gauging stations. The red star indicates a grid cell in the upstream area, the green one indicates a grid cell in the downstream area. The bottom panel displays the simulated river discharge at the positions of the similarly colored stars in the upper panel. Note that the green curve, originating from the downstream grid cell, shows a delayed peak flow due to the distance to the upstream grid cell (red curve) as well as an increased total river flow due to the greater number of inflow grid cells.

2.2. Water balance in wetlands

The hydrological conditions of a region play the major role in the formation and desiccation of wetlands. Water depth and spatial extent depend strongly on the balance of water inflow and outflow. The new version of the MPI-HM regards now three vertical and two horizontal water fluxes for wetlands. These are throughfall, ET, drainage, lateral inflow and lateral outflow. Additionally, the surface water storage interacts with the soil moisture storage. Connections to a groundwater storage are not implemented. Currently the MPI-HM does not include any groundwater interactions. This is mainly due to the lack of global groundwater data, which would be needed to parametrize and validate groundwater processes.

This section describes in detail the water fluxes of the wetland water balance. Further information about the interaction of storages and fluxes between them are found in section 2.5.

2.2.1. Vertical water fluxes in wetlands

Most processes of the vertical wetland water balance are similar to ones the land surface water balance. Thus, a number of already existing subroutines can be reused. This is done in order to keep the model as simple and fast as possible. However, some important changes are applied. These are the implicit snow layer, the surface water storage and the interaction with lateral water fluxes. The setup of the water balance is shown in figure 2.4. Below it will be discussed from top to bottom.

Snowfall, Rainfall and PET are achieved similar to the land surface water balance (see Sect. 2.1.1). Using rainfall and snowfall directly would require to simulate an explicit snow layer over wetlands. This snow layer could only exist if the surface of the wetland is frozen. However, freezing and melting of open water surfaces are very complex processes, which would demand an explicit energy balance and increase the model complexity significantly. As an alternative, the throughfall calculated by the land surface water balance is used as input for the respective grid cells in the wetland water balance. Thus realistic amounts of rainfall and snowmelt are feed into the wetlands, without the need to calculate any freezing or explicit snow layer.

Although wetlands usually have a vegetation cover, the canopy layer is neglected in the DWES. This is valid as the MPI-HM does not simulate any physical plant related processes or dynamics. The only purpose of canopy in the MPI-HM land surface water balance is the increase of evaporation. Since the surface water storage already provides the maximum ET, it implicitly includes the canopy layer.

As will be discussed in section 2.3.1 wetlands are supposed to form on flat terrain. Surface runoff can therefore be neglected, and all water that can not infiltrate into the soil is added to the surface water storage.

The surface water storage is only active, if it actually does contain some water. In this case the ET is set to PET to account for open water evaporation. Likewise drainage is set to maximum as the soil below the wetlands is saturated. In addition, the surface water storage interacts with the lateral water balance. Depending on upstream grid cells
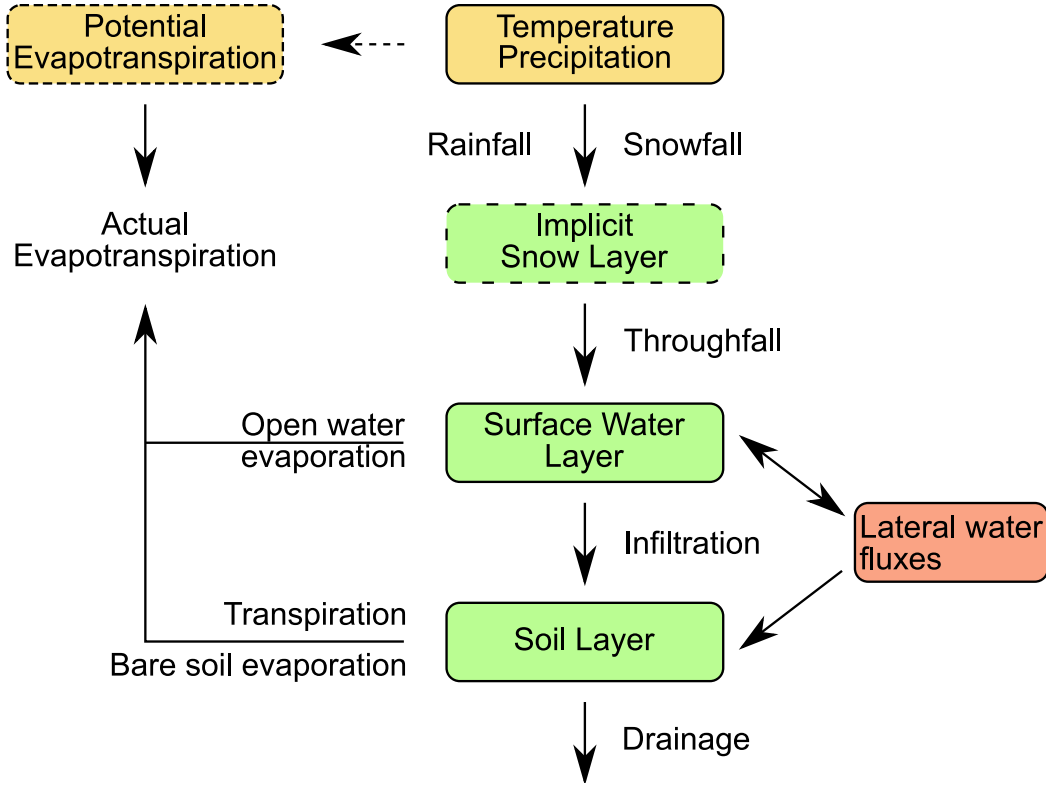
Figure 2.4.: Overview about the vertical wetland water balance setup of the MPI-HM. Orange boxes indicate input variables, green boxes indicate water storages, and black arrows indicate fluxes. The red box indicates interactions with the lateral water balance.

the storage may either have a net inflow or loose water to downstream grid cells.

If the surface water storage is empty, the generation of ET and drainage is taken over by the soil storage. These fluxes are provided by the same routines which are used in the land surface water balance (see Sect. 2.1.1) and are dependent on the soil moisture content of the storage. A distinctive feature of the soil water balance is that it accounts for permafrost. Permafrost areas are assumed to be favorable terrains for wetland formation since the soil is frozen and cannot absorb or release any water. Whenever a grid cell contains a fraction of permafrost, ET and drainage are scaled accordingly to exclude this fraction:

$$Flux = Flux \cdot \text{MAX}\left(\frac{f_{wetl} - f_{PF}}{f_{wetl}}, 0\right) \quad (2.1)$$

with $Flux$ being either ET or drainage and f being the area fractions of permafrost PF and wetland $wetl$, respectively. Thus, the precipitation directly fills the surface water storage and hence promote the generation of wetlands as long as their extent does not exceed the permafrost fraction.

Likewise to the surface water storage the soil storage is connected to the lateral water balance, but it can only gain water from lateral inflow.

The soil and surface water storages

The soil and surface water storages are closely linked together. Water accumulation in the surface storage is possible only when the soil storage is already saturated. Technically the storages replace each other depending on whether or not surface water exists. For this reason both possess separate water balances phrased as changes in the storages ΔS:

$$\Delta S_{soil} = \begin{cases} Thr + F_{lat} - ET - DR & \text{if } F_{lat} \geq 0 \\ Thr - ET - DR & \text{if } F_{lat} < 0 \end{cases} \tag{2.2}$$

$$\Delta S_{surf} = Thr + F_{lat} - PET - DR_{max} \tag{2.3}$$

with Thr as throughfall, DR as drainage and F_{lat} as lateral flow. When wetlands form or vanish both storages are active. In this cases ET and drainage are scaled accordingly.

In case of formation the scaling factors R for the timestep i are calculated as

$$R_{soil,i} = \text{MIN}\left(\frac{S_{soil,max} - S_{soil,i}}{\Delta S_{soil,i}}, 1\right) \tag{2.4}$$

$$R_{surf,i} = 1 - R_{soil,i} \tag{2.5}$$

with $S_{soil,max}$ being the maximum soil moisture capacity and $S_{soil,i}$ being the actual soil moisture storage. The state of the storages and size of the fluxes are then determined as:

$$S_{soil,i+1} = S_{soil,i} + \Delta S_{soil,i} \cdot R_{soil,i} \tag{2.6}$$

$$S_{surf,i+1} = S_{surf,i} + \Delta S_{surf,i} \cdot R_{surf,i} \tag{2.7}$$

$$ET_i = ET_{soil,i} \cdot R_{soil,i} + ET_{surf,i} \cdot R_{surf,i} \tag{2.8}$$

$$DR_i = DR_{soil,i} \cdot R_{soil,i} + DR_{surf,i} \cdot R_{surf,i} \tag{2.9}$$

The desiccation of wetlands works in a similar way but takes into account that the soil storage is finite and that it cannot produce any lateral outflow. Therefore, F_{lat} is directly subtracted from the wetland storage before the scaling of drainage and ET is calculated. In case the soil storage looses all water, a second scaling is applied to confine drainage and ET to the actual existing water amount.

Figure 2.5 displays the variations of water content in soil and wetland and their influence on ET and drainage. In this example grid cell the soil storage is mostly saturated. Although the wetland is temporarily desiccated, the soil moisture is still high enough to sustain almost potential ET. However, the drainage reacts very sensitive to soil moisture variations. It reaches its maximum flux during wet surface conditions.

2.2.2. Lateral water flow in wetlands

The lateral components of the wetland water balance are managed by the HD model part. However, some structural changes were necessary. In the old HD model some wetland processes were already implicitly simulated within the river flow storage (Hagemann and Dümenil, 1998b). In contrast, the new MPI-HM has an explicit wetland storage (see Fig. 2.6) while the wetland influence is removed from the river flow storage. Also the
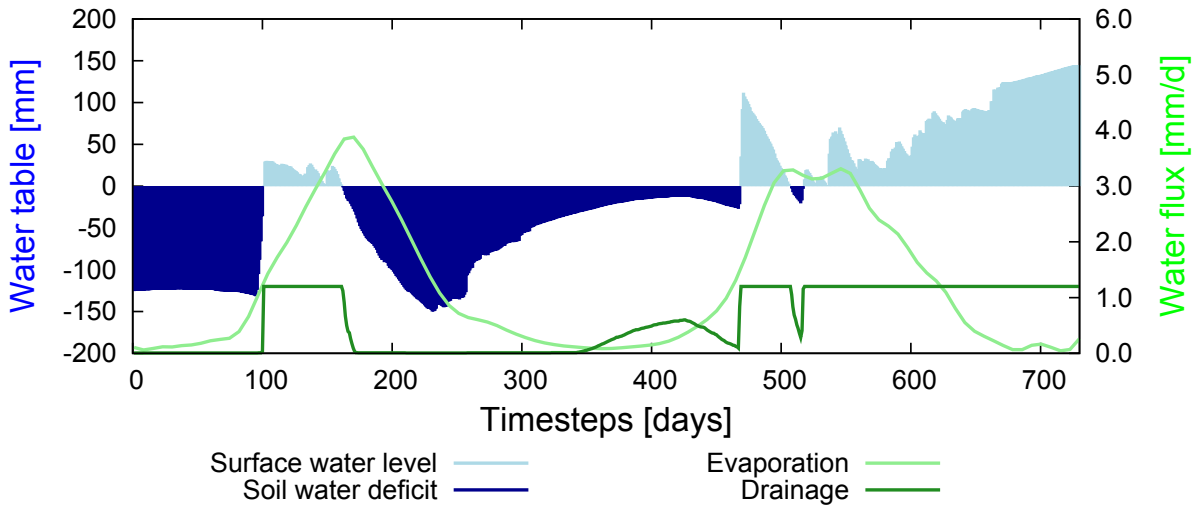
Figure 2.5.: Two years time series of water level variations (blue), ET (light green), and drainage (dark green) for a single grid cell. Drainage is increased by a factor of five to be clearly visible in this plot.

Figure 2.6.: Overview about the setup of the lateral water balance in the MPI-HM. Orange boxes indicate input fields, green boxes indicate water storages, blue boxes indicate fields generated by the HD model and black arrows indicate water fluxes. The red box indicates interactions with the vertical water balance.

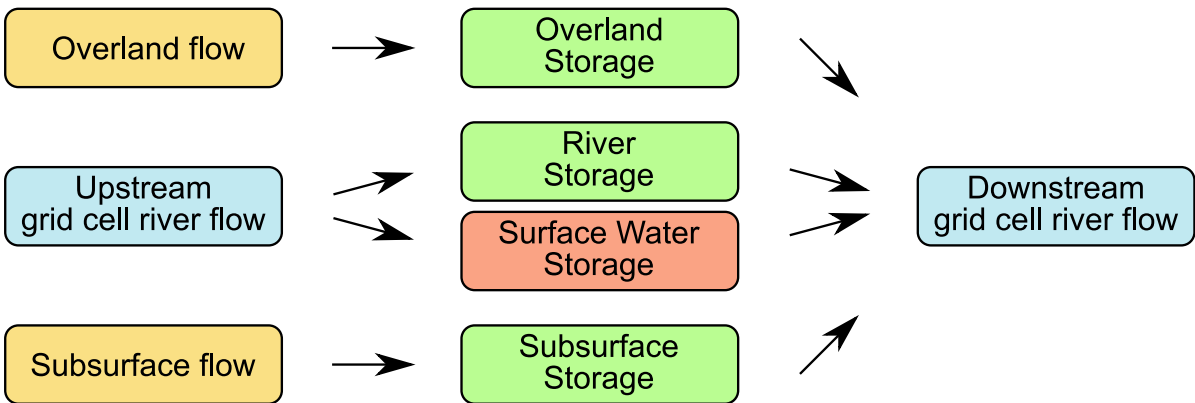parametrization is subject to considerable changes. The retention time of the wetland storage is not a static value anymore, but changes dynamically with the surface water volume.

Inflow

The introduction of the wetland storage demands a separation of inflow into itself and the river flow storage as both are fed by the upstream grid cells. Therefore, the lateral inflow has to be divided between them. Unfortunately, there are no measurements available to draw conclusions about this separation as there are no observations of water fluxes and storages for grid cell sized areas.

Basically, two options are possible. First, the ratio of inflow F_{in} could be a function of the respective area fraction f_{wetl} that the wetland is covering in the grid cell. Second, inflow F_{in} into wetlands could only occur if a certain threshold in river discharge is exceeded. Both schemes are shown in figure 2.7.
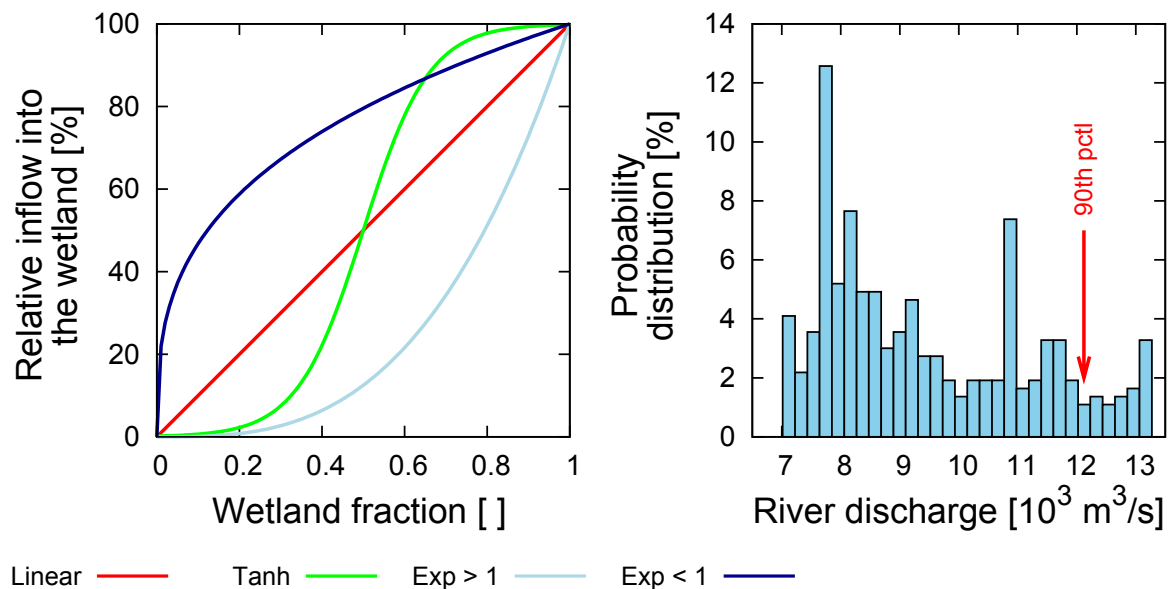
Figure 2.7.: Different approaches to divide inflow between the river flow and the wetland storage in a given grid cell. The left panel displays area dependent inflow schemes. Shown are linear, exponential and tanh like dependencies on area fraction. The right panel displays a scheme for discharge dependent inflow. There, only such amounts of inflow are routed into wetlands which exceeds a certain percentile (red line) of the discharge probability distribution.

The reasoning behind the area dependent approach is that more extensive wetlands would collect more inflow from their environment. Obviously, wetlands covering the whole grid cell would obtain one hundred percent of it. Small wetlands may obtain almost no inflow since most river would bypass them. The most simple case is to assume a linear

scaling of inflow with size. However, other scalings may be more realistic. Exponential scaling like

$$F_{in,wetl} = F_{in} \cdot f_{wetl}{}^{x} \tag{2.10}$$

would set an emphasis on larger or smaller wetlands. Both is justifiable. Using an exponent $x < 1$ results in small wetlands already getting a large portion of inflow. This might be reasonable because most wetland usually are close to rivers and are able to store considerable amounts of water. In contrast an exponent $x > 1$ restricts inflow collection to larger wetlands. This would be realistic if water transport is dominated by river channels. A third possibility is to assume a tipping point. Below a certain wetland coverage its ability to collect inflow would be low due to rivers bypassing it. Above this tipping point almost all water is going into the wetlands, because every river channel might already be confined with them. An appropriate formula for this behavior is:

$$F_{in,wetl} = F_{in} \cdot \text{MIN} \left[(\tanh \left(4 \cdot \pi \cdot (f_{wetl} - 0.5) \right) + 1) \cdot 0.5, 1 \right]. \tag{2.11}$$

which was already applied by Hagemann and Dümenil (1998b) for a related process. There, the authors used it to increase the lag time of river flow due to wetland influence.

Alternatively, the discharge dependent approach can be used. The shape of the river channels is generated by its mean discharge throughout the year. It can be assumed that during most of that time the channel is able to accommodate the river flow. However, extreme discharge is expected to exceed the river's capacity and flood the surroundings. Therefore, the discharge dependent approach defines a certain inflow percentile above which the exceeding inflow is directed into the wetland storage. The remaining inflow below the inflow percentile is still directed into the river flow storage. Thus, inflow into wetlands only occurs during peak flow events.

Section 2.4.1 present details about the optimization of the inflow scheme. It was found that the most appropriate approach is the area dependent inflow calculation using the exponential scaling with an exponent of two.

Outflow

The calculation of lateral outflow is based on the linear reservoir approach (see Sect. 2.1.2). Similar to the base flow and overland flow storages, the wetland storage uses only one reservoir. Thus its outflow Q_{wetl} is calculated as:

$$Q_{wetl} = \frac{S_{wetl}}{k}, \text{ with } k \geq 1 \text{ and} \tag{2.12}$$

$$k = \frac{\Delta x}{v} \tag{2.13}$$

The parameter k is the retention time of water in the reservoir and depends on the distance Δx between two neighboring grid cells and the water flow velocity v. Observations indicate much lower water flow velocities in wetlands compared to rivers. A study by Stern et al. (2001) stated velocities between 0.02 and 0.38 $^{m}/_{s}$ for shrub covered wetlands and 0.01 to 0.12 $^{m}/_{s}$ for emergent ones. The authors demonstrated that flow velocity in wetlands is

not constant, but it is dependent on vegetation cover, discharge amount and slope. For this reason no observational flow velocity constant is used, which would result in a fixed retention time k. Instead, an empirical relation is applied to estimate flow velocity in a dynamical way. For this task the Manning-Strickler formula was chosen, as it regards slope, water table depth and surface roughness (e.g. Jirka, 2007). Here the water flow velocity v is calculated as:

$$v = k_{st} \cdot R_h^{\frac{2}{3}} \cdot S^{\frac{1}{2}}, \tag{2.14}$$

with R_h being the hydraulic radius, S being the topographical gradient $\Delta h/\Delta x$ and k_{st} being the discharge coefficient after Strickler. The discharge coefficient k_{st} describes the roughness of the river bed. While k_{st} estimations exist for river flow on local scales (see table 2.2), they can not be directly used for wetland water flow on grid cell scale. Additionally, the respective wetland coefficient k_{wetl} is expected to vary for different vegetation covers in wetlands. However, during this study a global value for wetland's k_{wetl} was chosen (see Sect. 2.4). The hydraulic radius R_h is defined as

$$R_h = \frac{A}{P}. \tag{2.15}$$

A is the cross sectional area of flow and P is the length of the wetted perimeter. For very broad structures like wetlands, R_h converges against its average water depth h_{wetl}. Therefore, equation 2.14 becomes

$$v_{wetl}(h, s) = k_{wetl} \cdot h_{wetl}^{\frac{2}{3}} \cdot s_{mean,wetl}^{\frac{1}{2}}. \tag{2.16}$$

The calculation of the mean slope $s_{mean,wetl}$ of the respective wetland grid cell fraction f_{wetl} is based on subgrid slope calculation function (see Eqn. 2.36), which is explained in detail in section 2.3.2. This function is used to derived the actual slope of a certain grid cell fraction in dependence of the slope distribution parameter b, the range between minimal and maximal subgrid slope s_{range} and the minimal slope s_{minmod}. The value $s_{mean,wetl}$ is then calculated as the mean of equation 2.36 in the interval $[0, f_{wetl}]$. The mean of any continuous function for the interval $[a, b]$ is given as

$$\overline{f(x)} = \frac{1}{b-a} \int_a^b f(x)dx \ . \tag{2.17}$$

The primitive S of equation 2.36 for the area fraction f within this interval is calculated as:

$$S(f) = s_{range} \cdot \left(f + \frac{b}{b+1} \cdot (1-f)^{\left(\frac{1}{b}+1\right)} \right) \Big|_0^{f_{wetl}} + s_{minmod} \cdot f \Big|_0^{f_{wetl}} \quad , \text{ therefore} \tag{2.18}$$

$$s_{mean}(f) = \frac{s_{range} \cdot f + \frac{s_{range} \cdot b}{b+1} \cdot (1-f)^{\left(\frac{1}{b}+1\right)} - \frac{s_{range} \cdot b}{b+1}}{f} + \frac{s_{minmod} \cdot f}{f} \quad , \text{ simplified to} \tag{2.19}$$

$$= s_{max} + \frac{\frac{s_{range} \cdot b}{b+1} \left[(1-f)^{\left(\frac{1}{b}+1\right)} - 1 \right]}{f} \quad . \tag{2.20}$$

extremely smooth river channels (e.g. cemented surfaces)	$k_{st} \approx 100^{m^{-3}}/s$
natural river channels	$k_{st} \approx 30 - 40^{m^{-3}}/s$
very rough river channels (e.g. mountain torrents)	$k_{st} \approx 20^{m^{-3}}/s$

Table 2.2.: Example k_{st} values for river flow (Jirka, 2007).

Figure 2.8 (left) gives an example of the slope function and its respective mean slope function. At $f = 0$ both functions produce the same value, which is determined by the
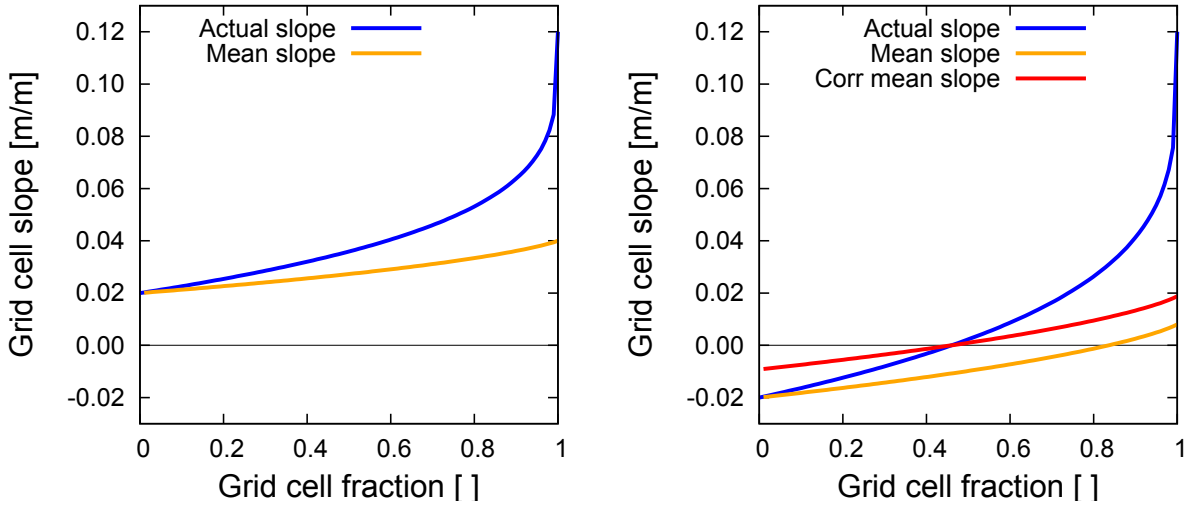

Figure 2.8.: Actual (blue) and mean slope (orange and red) function for two example grid cells. The left panel's grid cell has a minimum slope > 0. The right panel's grid cell includes a zero slope fraction.

minimum slope in this grid cell. However, in grid cells with a certain zero slope fraction a negative s_{minmod} value occurs for numerical reasons. As figure 2.8 (right) shows, this value causes an offset of the mean slope function and leads to a systematically underestimated mean slope for these grid cells. This effect has to be counteracted by subtracting the offset calculated as the mean slope at the function root $f_\circ$ of the subgrid slope calculation function 2.36:

$$f_\circ = 1. - \left(\frac{s_{minmod}}{s_{range}} + 1. \right)^b \qquad \text{, therefore} \qquad (2.21)$$

$$s_{off}(f_\circ) = s_{max} + \frac{\frac{s_{range} \cdot b}{b+1} \left[(1 - f_\circ)^{\left(\frac{1}{b} + 1 \right)} - 1 \right]}{f_\circ} \qquad \text{, leading to} \qquad (2.22)$$

$$s_{mean}(f) = s_{max} + \frac{\frac{s_{range} \cdot b}{b+1} \left[(1 - f)^{\left(\frac{1}{b} + 1 \right)} - 1 \right]}{f} - s_{off}(f_\circ) \qquad (2.23)$$

25

for grid cells with negative s_{minmod}. During the model runtime, all negative slope values are considered as zero slope.

This slope treatment is valid for the vast majority of grid cells. However, exceptions occur when the observed slope of grid cells is zero. Thus, also the flow velocity would decrease to zero and no outflow would be produced. In such grid cells i the calculation of the internal slope $s_{mean,i}$ has to fall back to a more simple algorithm:

$$s_{mean,i} = \frac{(E_i + h_{wetl,i}) - (E_{i+1} + h_{wetl,i+1})}{\Delta x},$$

(2.24)

where E is the topographical elevation and $i + 1$ indicates the downstream grid cell. While the topography related part of $s_{mean,i}$ remains constant during the simulation, the overall $s_{mean,i}$ varies with the water table differences between actual and downstream grid cell.

Another exception takes place in case the MPI-HM is run in the static wetlands mode (see Sect. 2.4.1). Since wetland fractions are fixed in this setup is it possible that wetlands cover only the zero slope fraction of a grid cell. Again, the s_{mean} calculation falls back to a simpler scheme:

$$s_{mean} = \frac{h_{wetl}}{\Delta x} \qquad \text{, with}$$

(2.25)

$$\Delta x = r_{wetl} + \frac{r_{GC} - r_{wetl}}{2},$$

(2.26)

where r_{wetl} and r_{GC} are the mean radii of the wetland and land surface grid cell fractions, respectively.

An example time series of lateral water flow is shown in figure 2.9 (top). Flow peaks in the lateral water inflow usually lead to an increase in the surface water storage. The surface storage then determines the lateral outflow, which is proportional to the surface water table and drops to zero in case the water table decreases below the soil surface.

In conclusion of this section figure 2.9 (bottom) displays a two years time series of the balances of the vertical and lateral water fluxes. As the red line illustrates, the overall grid cell water balance is perfectly closed within the range of numerical model accuracy. Figure 2.9 (bottom) shows all important interactions, which are described in the sections 2.2.1 and 2.2.2. The events in this time series can be described as follows:

Around timestep 100 a strong positive peak can be seen in both balances, which lead to the formation of a surface water storage. Although the net lateral flow remains positive during the next time steps, the pronounced decline of the vertical balance causes a drop in water level between timestep 150 to 250. This decline becomes diminished when the vertical balance passes its minima at time step 170. Later on, slightly positive balances enable the soil moisture storage to increase again until another positive peak finally induces the increase of the surface water storage at timestep 470. Here, vertical and lateral water fluxes oscillate strongly. Their balance is positive and causes a net water inflow into the grid cell.
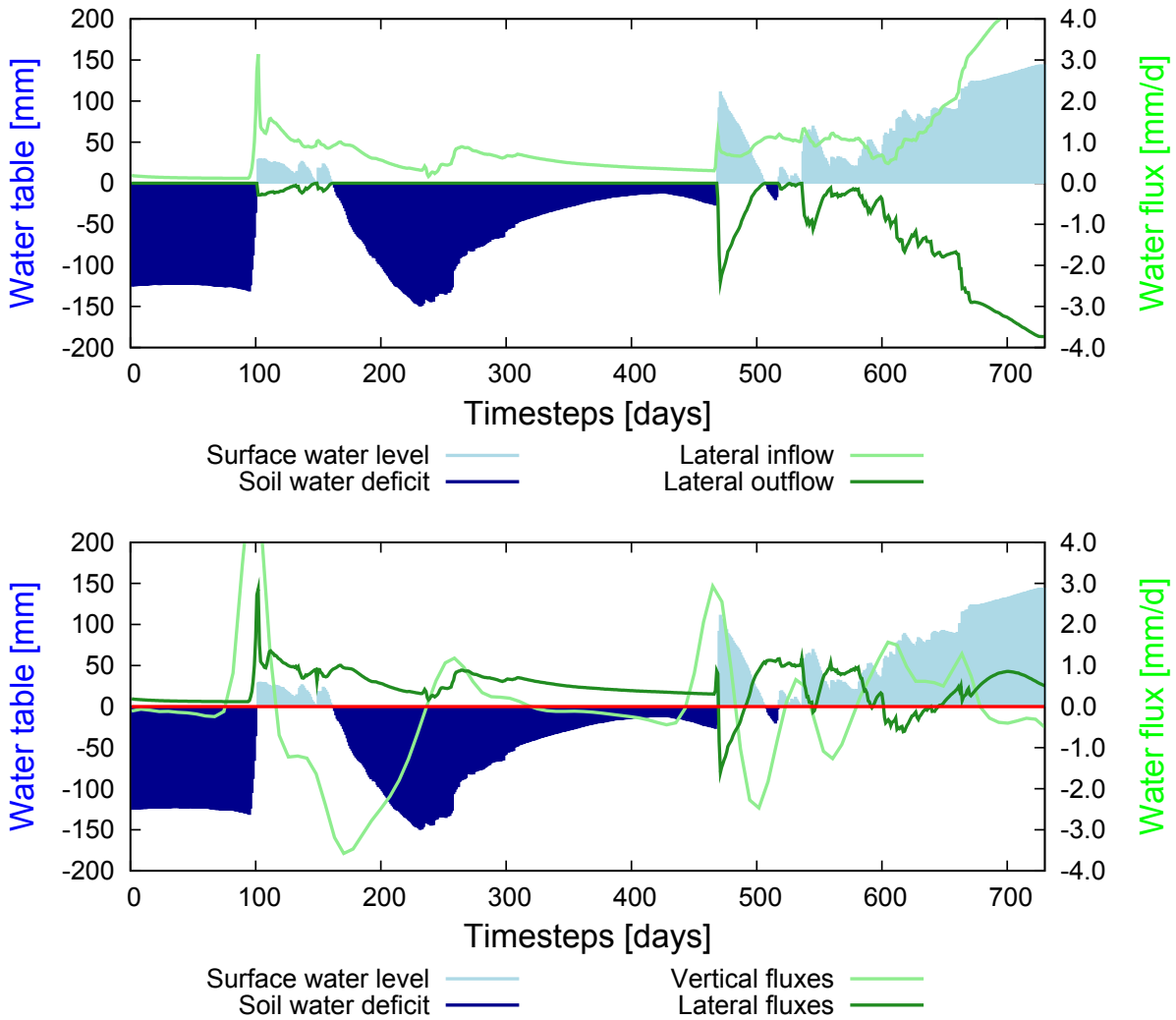
Figure 2.9.: Two years time series of water level variations (blue) and other water fluxes (green) for a single example grid cell. The top panel displays only lateral water flows. The bottom panel shows the balances of vertical as well as lateral water fluxes (green). The red line indicates the closure error (right axis) for the overall grid cell water balance.

2.3. Wetland dynamics

The topographical profile of a certain wetland as well as its water balance state (see Sect. 2.2) are the two most important features for the simulation of its extent dynamics. They are highly correlated, as the topography determines the shape of the water storage and especially the extent of the wetland-atmosphere interface. The water balance, on the other hand, determines how much water is available to be stored in topographical depressions. Thus, the knowledge of a valid relation between the surface area of wetlands and their water volume is crucial for the success of this study. This area-volume relation is determined by the geometry of the wetland.

2.3.1. Wetland geometry

Data about size, depth and volume of wetlands are usually available only on regional and local scale. However, global topographical datasets exist which might be used to derive the necessary information. Hayashi and Van Der Kamp (2000), Wetzel (2001) and Brooks and Hayashi (2002) show that water volume and area of wetlands as well as lakes depend on the geometry of the ground. They also state how this relation can be estimated using simple formulas. Hayashi and Van Der Kamp (2000) and Brooks and Hayashi (2002) have in common that both use a dimensionless shape parameter p to describe the basin profile of wetlands. Surface area A and water volume V are calculated as:

$$A = \frac{A_{max}}{\left(d/d_{max}\right)^{2/p}} \tag{2.27}$$

$$V = \frac{A_{max} \cdot d_{max}}{1 + 2/p} \left(d/d_{max}\right)^{1+2/p}, \tag{2.28}$$

where d is the water depth of the wetland. A_{max}, V_{max} and d_{max} are the respective parameters for the surface topography of the whole basin.

The formula presented by Wetzel (2001) is valid especially for lakes. Given that the shape of a lake can be approximated with a elliptic sinusoid (Neumann, 1959), the water volume is calculated as:

$$V = 4\left(1 - \frac{2}{\pi}\right) a \cdot b \cdot h_{max} \tag{2.29}$$

where a and b are the half-axes of the lake's surface ellipse and h_{max} is its depth.

In order to apply these formulas in a model A_{max}, d_{max}, p, and the product of the surface area half-axes a and b have to be extracted from a topographical dataset.

The basin approach

The most direct approach to derive geometry parameters from topography data is to identify depressions in the earth's surface, diagnose their extent, and then estimate their geometrical properties. In the next step, these parameters must be scaled to the model

resolution. Following that the shape parameter p can be calculated by transforming formula 2.28 to solve for p

$$p = \frac{2}{\frac{A_{max} \cdot d_{max}}{V_{max}} - 1} \tag{2.30}$$

it enables the estimation of surface extent A for basins with $V < V_{max}$.

Based on this considerations a computer program was developed to identify topographical depressions. These depressions would be potential wetland areas and therefore capture the biggest possible extent of all lakes and wetland worldwide. For this analysis the global *ETOPO2v2* elevation dataset (National Geophysical Data Center, 2006) was used. It has a horizontal resolution of $2'$ and a vertical resolution of 1 m.

Figure 2.10 displays the calculated basin fraction for every land surface grid cell at a resolution of 0.5°. Most grid cells have basin fractions below 0.4, but some basins spread over more than one grid cell. Most prominent are the Caspian Sea Basin, the Lake Eyre Basin (Australia), the Lake Chad Basin (Africa), the Pannonian Basin (Europa) and the Tarim Basin (Asia) which are successfully identified. However, a comparison of the basin
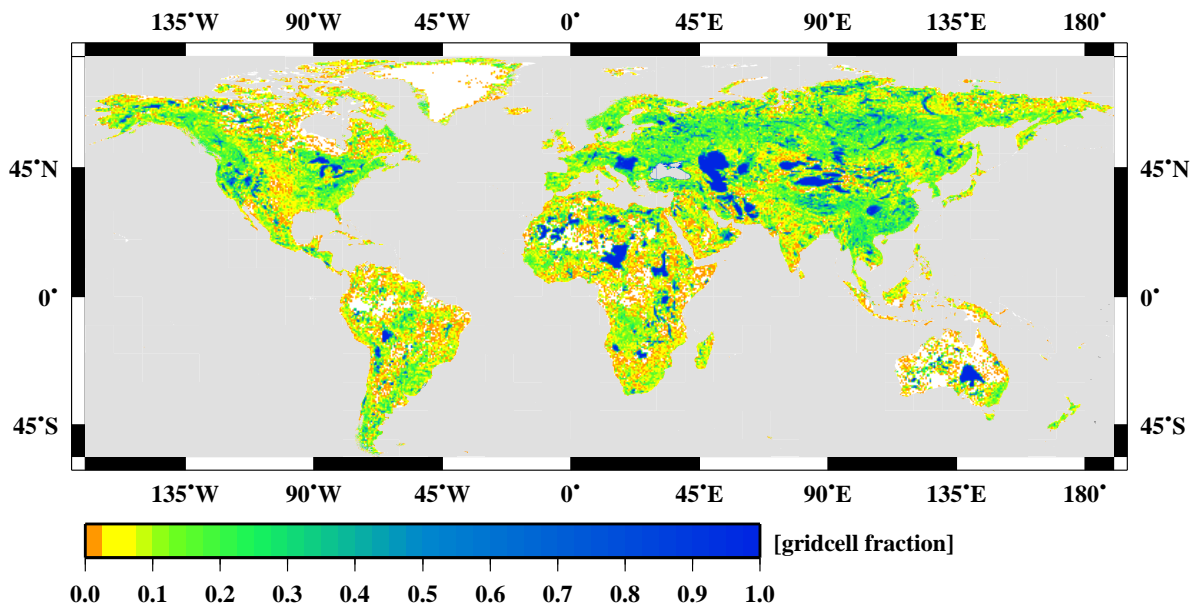

Figure 2.10.: Calculated basin fraction for grid cells on 0.5° horizontal resolution. The fractions are based on the ETOPO2v2 topographical dataset (National Geophysical Data Center, 2006).

fractions to the GLWD (Lehner and Döll, 2004) revealed a systematical disagreement. While big structures like the Great Lakes in North America were captured well, small lakes and wetlands could not be identified. This result implies, that the ratio of the horizontal resolution to the depression size might set a restriction to the identifiable basins. Even more important is the vertical resolution of the data. Most wetlands are just too small to decrease the average height of a grid cell strong enough to show up in an elevation dataset.

Additionally a comparison between identified lakes and observations was conducted (see Table 2.3). Even though the calculated basin size is close to observations, the observed lake water volumes match only occasionally with the topography derived ones. No regularities were obvious in these biases. However, it was found that most basins are very flat. This leads to a strong sensitivity of area and volume to depth. Thus the influence of uncertainty in the topographical dataset is significantly enhanced.

Lake	Volume [%]	Lake	Volume [%]
Superior	91.2	Malawi	2.2
Victoria	11.0	Great Slave	6.8
Huron	112.6	Erie	95.3
Michigan	80.1	Winnipeg	2.9
Tanganyika	3.3	Ontario	97.0
Baikal	2.1	Nicaragua	42.6
Great Bear	4.4		

Table 2.3.: Lake volumes calculated with the basin approach given as percentage of observed lake volumes (International Lake Environment Committee Foundation, 1999). The world's 13 largest lakes are shown.

From this study it can be concluded that the method itself is a valid approach to gain geometric information about topographical depressions. However, the resolution of the ETOPO2v2 dataset is too coarse for the simulation of wetlands on 0.5° scale. Therefore, the basin approach is not applicable to generate the necessary boundary data for the simulation of dynamical wetlands. These findings are in accordance with a study of Coe (1998) on coarser resolution.

The slope approach

The failure of the physical based basin approach (see Sect. 2.3.1) clearly demonstrates the limitations in the direct use of topographical data. Therefore, the slope approach does not aim anymore on the computation of maximum potential wetland areas and volumes, as the basin approach did. Instead, it aims to achieve an equilibrium state between surface water volume and the respective surface water area in dependence on the topographical conditions in every grid cell. The basic reasoning behind this is that some parts of the water balance are influenced stronger than others by either surface area or water volume. For example, the amount of water gain through precipitation is directly proportional to the extent of a wetland. In contrast, the lateral outflow depend via water depth on the water volume. Thus it can be expected that there are certain surface water area to surface water volume ratios for which wetlands are stable. At the same time other ratios exist which would result in desiccation or unlimited growing.

Again, topographical data is used for this approach. The elevation itself gives no information whether or not a grid cell is suited for wetland formation, but slope is a valuable indicator for this. Since wetlands are usually observed on very flat areas, it can

be assumed that flat terrains promote wetland formation while steep terrains suppress it. Thus, slope comes into account to provide a scaling factor for the surface area – water volume relation, which represents the topographical conditions in the respective grid cells. The following paragraph demonstrates the detailed deduction of the slope approach: Changes in the grid cell's wetland water volume V_{wetl} affect the area A_{wetl} of the respective wetland:

$$\frac{\Delta A_{wetl}}{A_{wetl}} \approx \frac{\Delta V_{wetl}}{V_{wetl}} \cdot C \tag{2.31}$$

where C is a scaling parameter accounting for the influence of geometry on the area-volume relation. Since the geometrical properties of a wetland are not known (see section 2.3.1), it is not possible to achieve an exact solution for this problem. However, it is possible to use slope as a proxy for detailed geometrical information. Figure 2.11 illustrates that, when changing the surface water volume of two wetlands by the same relative amount, the resulting relative area change is dependent on the actual slope. Here, the addition of a certain amount of water results in an increased relative extent change and a decreased relative water table depth change for flat wetlands compared to steep wetlands. C can be substituted with the slope under two presumptions. First, that
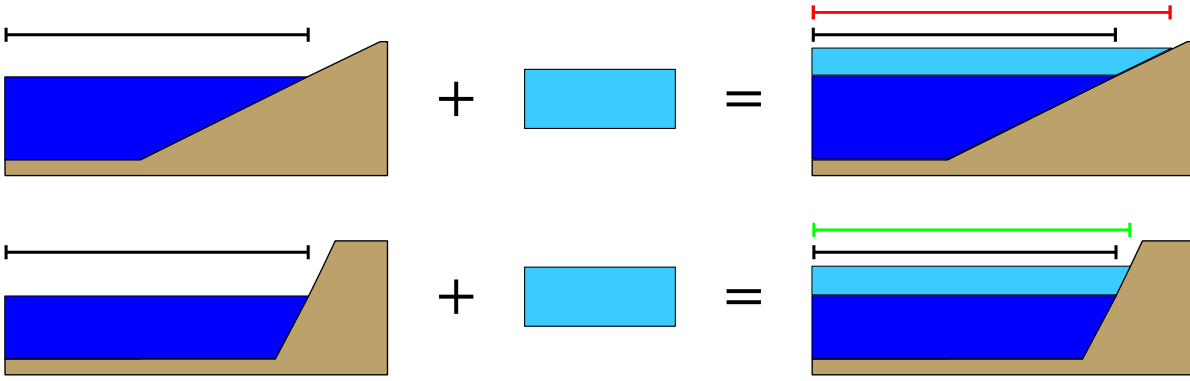

Figure 2.11.: Influence of slope on area-volume relation reduced to a two dimensional problem. Vertical profiles through two wetlands are shown. On the left side both have the same water volume (dark-blue) and surface area (black lines), but different slopes. Increasing them by the same amount of water (light-blue) leads to a 20% area increase (red line) for the flatter slope wetland (upper right panel), but only to a 5% area increase (green line) for the steeper slope wetland (lower right panel).

wetland occur preferably on flat terrain, and second that increasing slope within grid cells suppresses their formation. These presumptions are valid for the DWES. Equation 2.31 is then altered to

$$\frac{\Delta A_{wetl}}{A_{wetl}} = \frac{\Delta V_{wetl}}{V_{wetl}} \cdot \frac{1}{1 + s_f \cdot S_{sl}} \tag{2.32}$$

with s_f being the slope of a certain area fraction f and S_{sl} being the slope sensitivity. The slope sensitivity S_{sl} controls how strong the influence of slope on the area change is. It is defined as being constant for all grid cells and time steps. Since S_{sl} is not a physical measurable parameter but a scaling factor, it is necessary to optimize it (see Sect. 2.4.2).

2. Development of the dynamical extent scheme for wetlands

First tests using this approach revealed satisfying results. Thus the slope approach was developed further and finally implemented into the MPI-HM (see Sect. 2.3.3).

2.3.2. Analytical approximation of subgrid slope distribution

The slope information for the land surface were derived from the two global elevation datasets *GTOPO30* (Gesch et al., 1999) and *NOAA GLOBE* (Hastings et al., 1999) at $30''$ resolution. The slope of a single $30''$ grid cell i is calculated using the elevations h of the highest and lowest neighboring grid cell with distance Δx between them:

$$slope_i = \frac{\left|\frac{h_{max}-h_i}{\Delta x_{max}}\right| + \left|\frac{h_i-h_{min}}{\Delta x_{min}}\right|}{2} \tag{2.33}$$

The calculated slope values can be used to test the relation between wetlands and slope (see Fig. 2.12). Four global lake and wetland distribution datasets were converted to $0.5°$, and their wetland fractions were plotted against the 95th percentile of wetland covered slope values within the respective grid cells. These datasets are the GLWD (Lehner and Döll, 2004), the LSP2 (Hagemann, 2002; Hagemann et al., 1999), the MATT (Matthews and Fung, 1987) and the SIND (Prigent et al., 2001, 2007). This analysis reveals that
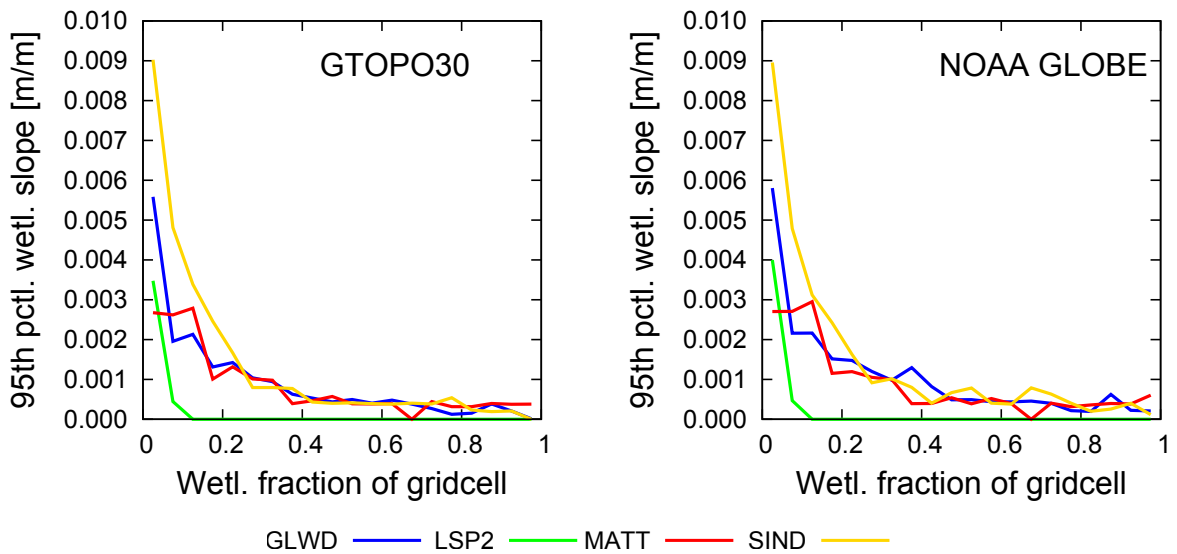

Figure 2.12.: 95th percentile of wetland covered slope at $0.5°$ horizontal resolution for four different wetland observation datasets and two slope datasets for the global land surface. The slope distributions are based on *GTOPO30* (left) and *NOAA GLOBE* (right).

neither the wetland observation datasets nor the slope datasets cause distinctive variations in the correlation of wetland fractions and slope. Large wetland fractions occur only in very flat grid cells below a slope of 0.001 $^m/_m$. In contrast, small wetland fractions, covering less than 10% of the grid cell area, are found on slopes up to 0.01 $^m/_m$. There is a clear anti-proportional relation between subgrid slope and wetland fraction. The LSP2

reacts somewhat more sensitive to slope than the other wetland observations but still in the same manner. Therefore, sub grid slope seems to be an adequate parameter to constrain wetland area.

At the given resolution of 0.5° for the model grid cells and 30″ for the elevation datasets, every model grid cell contains up to 3600 slope values. Using such detailed information would increase the computational cost of the model enormously. However, it is possible to ignore the spatial subgrid distribution of slope within the model grid cells and use the cumulative subgrid slope frequency instead. Figure 2.13 gives an impression of this subgrid slope frequency for two example grid cells. Thus, the information about the position of certain slope values within the model grid cells is lost, but their area fraction is still known. Further decrease of computational costs is gained by fitting an analytical function to the observed slope distribution instead of using the slope values directly. This slope distribution function is based on a power law function used by Hagemann
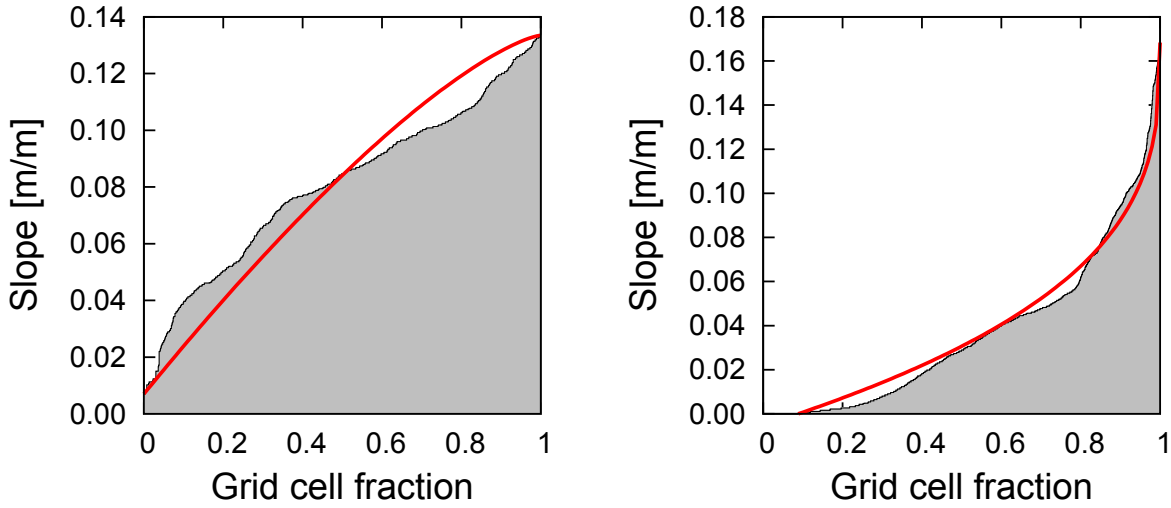

Figure 2.13.: Cumulative frequency distribution of internal slope based on GTOPO30 for two 0.5° sized grid cells with $b < 1$ and $s_{min} > 0$ (left) and $b > 1$ and $s_{zero} > 0$ (right). The gray areas indicate the calculated slope values, the red lines the analytical approximation.

and Dümenil Gates (2003) for the statistical distribution of soil water capacities within grid cells. Analogous to their formula the slope s as a function of area fraction f can be expressed as:

$$s(f) = \left(1 - (1 - f)^{\frac{1}{b}}\right) \cdot s_{max}, \tag{2.34}$$

where b is the shape parameter of the power law and s_{max} is the maximum slope within the model grid cell.

The examples in figure 2.13 show that the slope distribution does not always starts with zero. Instead, very frequently grid cells are found with a minimum slope larger then zero (Fig. 2.13, left) or a certain grid cell fraction with zero slope (Fig. 2.13, right). Especially for small wetland fractions it is important to simulated the slope as precisely

as possible (see Sect. 2.2.2). Thus, two more parameters are needed to constrain the slope distribution curve. These are the grid cells minimum slope s_{min} and the zero slope fraction s_{zero}. The slope distribution formula is then altered to:

$$s(f) = \left(1 - \left(1 - f + \frac{-s_{zero}}{1 - s_{zero}} f + \frac{s_{zero}}{1 - s_{zero}}\right)^{\frac{1}{b}}\right) \cdot (s_{max} - s_{min}) + s_{min} \qquad (2.35)$$

All of these four parameters are specific for every grid cell. While s_{max}, s_{min}, and s_{zero} can be easily extracted from the subgrid slope distribution, b is determined by fitting equation 2.35 to the slope distribution using the nonlinear least-squares Marquardt-Levenberg algorithm as it is implemented in the plotting software *gnuplot* (Williams and Kelley, 2004).

After b is fixed, it is possible to substitute s_{zero} by modifying s_{min}. If $s_{zero} > 0$, then s_{min} is zero. In this case the function crosses the abscissa at s_{zero} and hits the ordinate at a negative slope value. By using this intersection point as a modified s_{minmod} and replacing $(s_{max} - s_{minmod}) = s_{range}$, formula 2.35 becomes

$$s(f) = \left(1 - (1 - f)^{\frac{1}{b}}\right) \cdot s_{range} + s_{minmod}. \qquad (2.36)$$

This simplification allows for the calculation of slope with only three parameters. A negative s_{minmod} indicates area fractions with zero slope, while positive s_{minmod} indicates grid cells that do not contain zero slope areas.

The spatial distribution of these parameters is displayed in figure 2.14. A shape parameter around 1 indicates an even distribution of slope within that grid cell. Values below and above 1 identify grid cells with slope distribution shifted in the direction of maximum or minimum grid cell slope. As shown in figure 2.14 (top left), the slope distribution is biased towards low slopes for the greater part of the land surface. The asymptotic standard error (see Fig. 2.14, top right) is mostly confined below 1%, indicating an overall good fit of the analytical slope approximation to the cumulative slope frequency. No systematic bias of the error can be observed. The minimum and maximum grid cell slope distributions correlate very well with the orography of the land surface.

2.3.3. Implementation of wetland dynamics

Once every model time step, the actual extent of wetlands is calculated using the slope approach (see Sect. 2.3.1). This computation proceeds in four steps for every model grid cell:

1. Calculation of surface water volume change and preliminary water depth based on the water balance (see Sect. 2.2).
2. Computation of the maximum slope covered by the wetland fraction (see Sect. 2.3.2).
3. Evaluation of the wetland extent change based on maximum slope and surface water change.
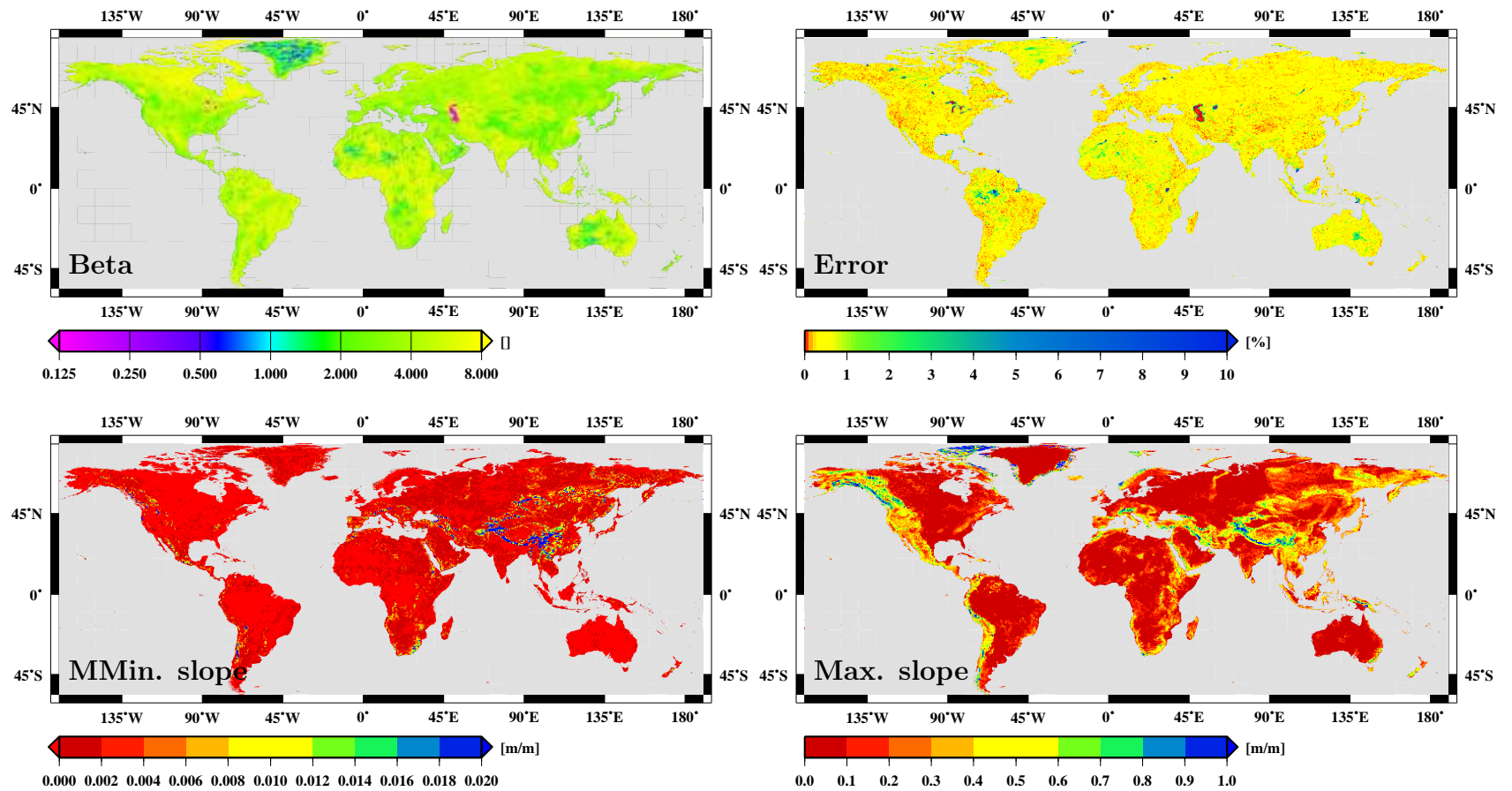
Figure 2.14.: Spatial distribution of slope parameters based on GTOPO30. The panels show the shape parameter β (top left), its asymptotic standard error (top right), the modified internal minimum slope (bottom left) and the maximum internal slope (bottom right).

4. Correction of the preliminary water depth based on the new wetland extent.

However, one problem is the formation and desiccation of wetlands, because their area fractions become zero. The land surface and wetland water balances are calculated separately and independent of their actual grid cell fractions. In contrast, the wetland dynamics and the lateral water balance use water volume as base unit. When datafields are exchanged between both water balances, the area fraction must not be equal to zero in order to allow for an unit conversion between water depth and water volume. Therefore, it is necessary to assume a non-zero minimum wetland fraction for every land surface grid cell. Here, a value of $1 \cdot 10^{-10}$ was chosen, as it proved to be numerically stable but still is smaller than the simulation uncertainty.

Figure 2.15 shows the effect of the subgrid slope approach. For the first testcase, the change in the maximal wetland covered grid cell slope was prescribed using a tanh function. Thus, a wetland was simulated which resides on a steep surface between timesteps $0 - 20$ and on a flat surface between timestep $30 - 50$. In the steep wetland
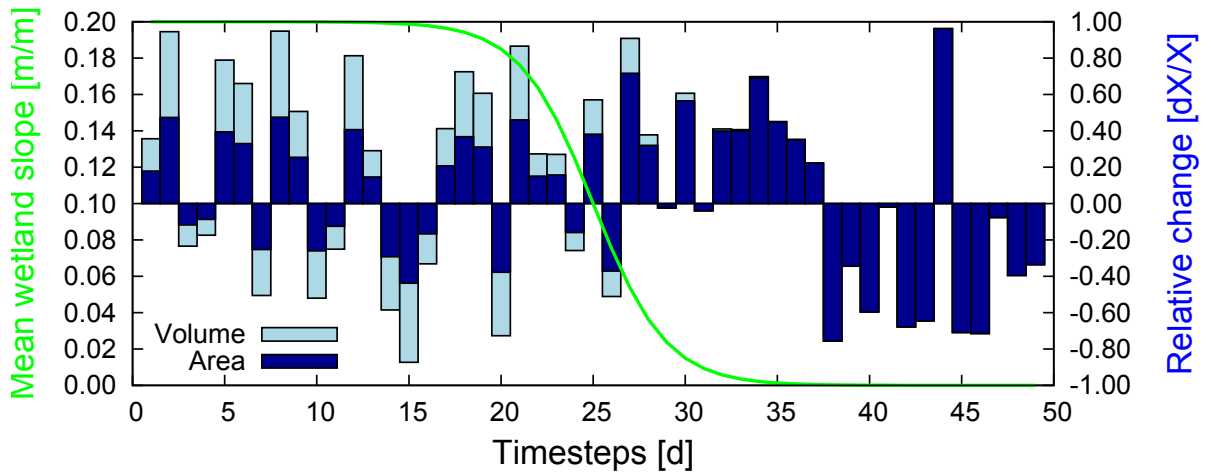

Figure 2.15.: Application of the slope approach for a single grid cell test case using a prescribed water balance and wetland slope coverage (green). The plot shows a time series of the responses of relative area change to surface water volume change (blue).

phase the response of relative area change to volume change is weak. This shows that in a high slope environment variations in the volume of surface water are transferred into water table variations rather than surface area variations. During the transition phase, the relative area change response increases and reaches its maximum under low slope conditions. There, the surface water spreads and floods the surroundings instead of increasing the water table.

A more realistic test case is presented in figure 2.16. Again, an artificial water balance was used as an external forcing. However, this time the slope was not prescribed anymore but responded freely to the water balance. The upper panel of figure 2.16 shows a similar behavior for the free test case as for the slope constraint one: high slope environments cause a weaker response of relative area change to volume change compared to low slope environments. Additionally, the response of water depth to slope was investigated (see
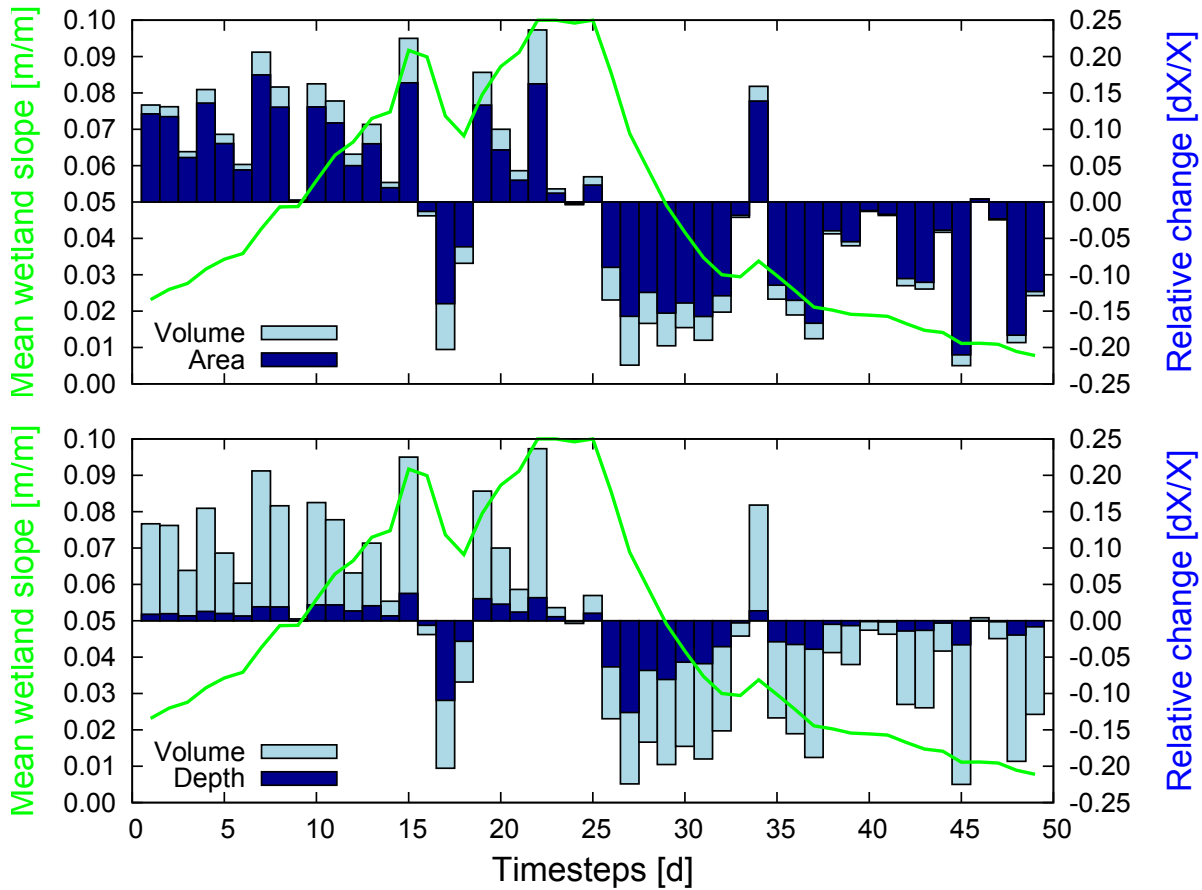
Figure 2.16.: Application of the slope approach for a single grid cell test case using a prescribed water balance. Both panels display a time series of slope change (green) and the responses of relative area change (dark-blue, top) as well as relative water depth change (dark-blue, bottom) to surface water volume change (blue).

Fig. 2.16, bottom). Oppositely to the relative area change, the relative water table depth change responds strongest to volume changes during high slope conditions and weaker during low slope conditions. This behavior again reflects the contrasting sensitivities of water table changes and surface area changes in dependence of slope conditions. These results are in agreement with the expected influence of slope on wetlands (see Sect. 2.3.1).

2.4. Optimization of scale dependent parameters

The scientific description of nature is usually realized using physical differential equations. However, in numerical models those equations cannot be applied in every case. Some of them are not analytically solvable, others are only valid at certain scales in space and time or require special physical properties which are not easily or not at all measurable. For this reason differential equations are often substituted with parametrized or empirical formulations. These formulations build on parameters whose values are chosen in such way as to produce a result in best possible agreement with the analytical solution. Furthermore, they should ensure a stable solution of the physical process. Usually parametrized or empirical equations allow for faster computations of the results, which is important especially for models of high complexity. However, their disadvantage is the restriction of their validity to a certain parameter range only.

In the MPI-HM, empirical formulations are applied for parts of the water balance calculations and the wetland extent dynamics. Subroutines which compute processes of the land surface water balance are transferred mostly without changes from the SL scheme and HD model into the MPI-HM. These are already parametrized. However, several new routines were developed to simulate the wetland processes which require new parameters. The following section describes the procedures to obtain optimal parameters for the wetland related processes.

All simulation results presented in this section were generated using 2m temperature, precipitation and PET provided by the WATCH project (see Sect. 3.1) as forcing data for the MPI-HM. The MPI-HM makes use of restart fields to ensure that every water storage is initialized properly. However, the new introduced fields of wetland water depth and extent could not be initialized before the parameter optimization is finished. Figure 2.17 indicates that the first 5 years of the simulations show a spin-up behavior. Therefore this first 5 years were neglected during the optimization.

2.4.1. Optimization of the static part

Some parameters are not directly involved in the wetland extent dynamics. Instead they control processes related to their water balance. In order to optimize these parameters the MPI-HM can be applied in an alternative mode which is called the static wetland mode. Here, global observations of wetland extent (see Sect. 1.3) are used as a boundary condition and replace the dynamical extent computation. Thereby, the simulation of wetland dynamics is confined to the hydrology above the soil layer and variations in its extent are not allowed. The soil moisture below wetlands is kept constantly at saturation. There are some advantages and disadvantages of this approach. On the one hand this mode violates the soil water balance by keeping it artificially constant. As it is still necessary to satisfy the water balance, wetland are temporarily excluded from the calculation in case their surface water storage drops to zero. On the other hand the static wetland mode allows for better comparability of its results with observations.
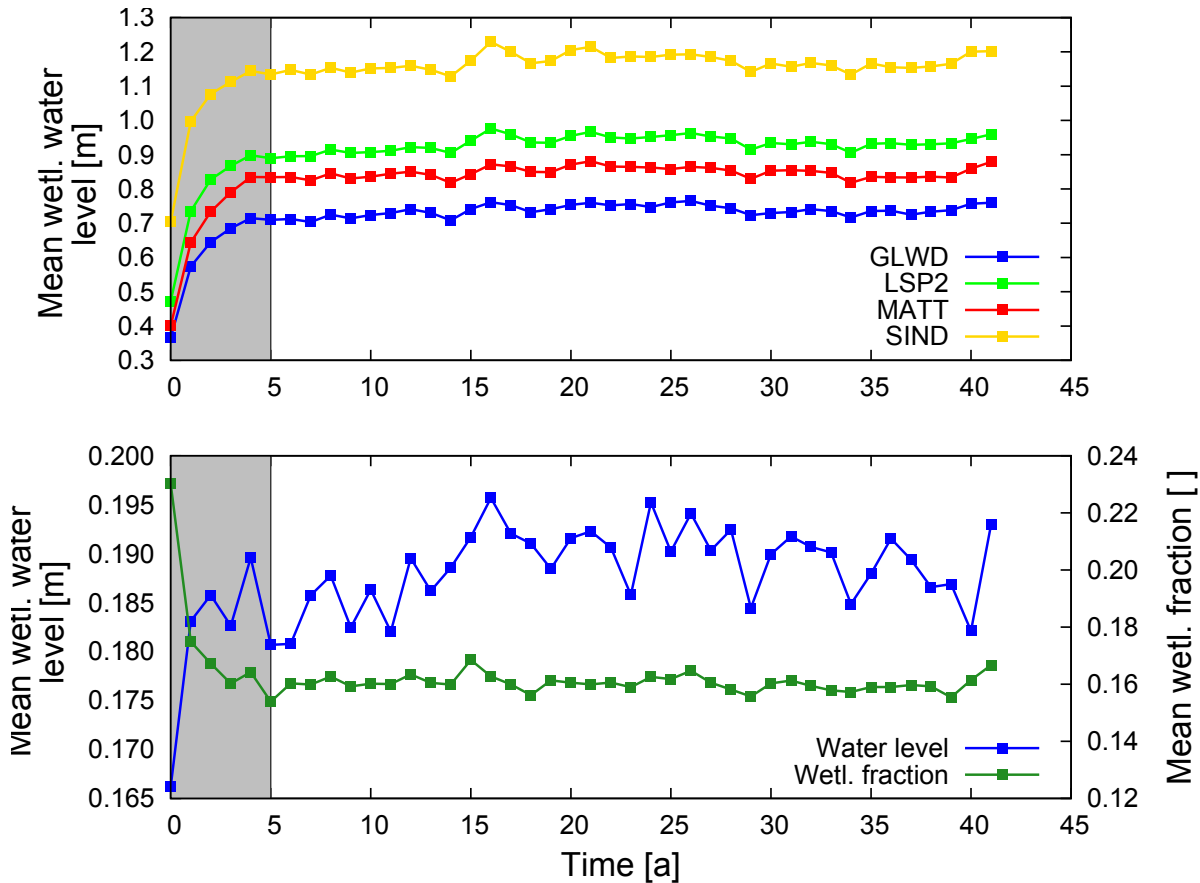
Figure 2.17.: Water storage variations for a 40 years period for different simulations. The gray areas mark the spin-up time. The upper panel displays the water table variations produced by the static wetland mode model with different wetland fraction boundary conditions. The bottom panel displays water level and wetland fraction variations produced by the dynamical wetland mode model.

Drainage parametrization

Observed hydraulic conductivities in soils range from 10^{-5} to 10^{-8} m/s (Dyck and Peschke, 1995) depending on whether their main component is sand, silt or clay. Usually wetlands evolve on soils with low hydraulic conductivity (Ingram, 1978). Recent measurements in the undisturbed part of an Israeli wetland produced values in the range of $3.47 \cdot 10^{-7}$ to $6.94 \cdot 10^{-8}$ m/s (Litaor et al., 2008) and thus concentrate on the lower end of conductivity range.

Soil hydraulic conductivity is strongly affected by soil type and texture, which makes the derivation of one global model parameter difficult. Additionally, they are influenced by the resolution of the model. Dümenil and Todini (1992) derived a parameter range between 10^{-7} and 10^{-9} m/s for the soil hydraulic conductivity in their drainage scheme. This clearly shows that the measured observations cannot be directly transferred into large scale models.

For this reason a conceptual approach was chosen to parametrize drainage for wetlands. It aims on calculating an estimate about how much water is available for drainage in wetland areas in the model. It is derived as follows:
For long time scales, changes in the storages of the land surface are very small compared to the sum of the water fluxes. Thus, the storages can be neglected and the vertical wetland water balance is simplified to

$$0 = P - PET - RO \tag{2.37}$$

where P is total precipitation and RO is total runoff. Equation 2.37 can be rearranged to solve for runoff. In wetland dominated grid cells drainage is expected to be the main component of total runoff since surface runoff is usually very low. Thus, the amount of water available for total runoff gives an approximation for drainage. Figure 2.18 (top) shows the distribution water flux available for drainage. There is a distinctive difference between tropical zones with up to $2 \cdot 10^{-7}$ m/s and the high latitudes with less than $1 \cdot 10^{-8}$ m/s available flux. Figure 2.18 (bottom) compares the water availability statistics for the whole land surface and several wetland observations. The box plots demonstrate a low sensitivity of the result to the different observations mask constrains. Since the drainage available water flux in most grid cells range between 10^{-8} to 10^{-9} m/s, this interval is used to confine wetland drainage in the MPI-HM.

Inflow scheme and discharge coefficient

The optimal choice of the wetland inflow parametrization and the optimization of the discharge coefficient k_{wetl} pose additional difficulties as there are no observations available to compare the results against (see Sect. 2.2.2). Therefore an indirect procedure is applied to optimize the parameters:
Being a global hydrological model, river discharge is one of the most important output variables of the MPI-HM. Figure 2.19 shows in two examples that the river discharge is in fact very sensitive to parameter perturbation. Thus, an iterative optimization procedure can be used which varies all parameter values systematically and evaluates the resulting river discharge in respect to observations. Finally, the parameter sets will be chosen that yields the smallest difference between simulated and observed river discharge. The optimization procedure applies a cost function to evaluate the agreement of simulated and observed river discharge. The best agreement is achieved when the cost function converges against zero. The cost function for a simulation S and the observation O is calculated as

$$\gamma(S) = \left(\frac{|P_S - P_O|}{6} + 1 \right) \cdot \left(\frac{|\text{VAR}_S - \text{VAR}_O|}{\text{VAR}_S + \text{VAR}_O} + 1 \right) \tag{2.38}$$

where P is the peak flow month of the river discharge curve and VAR is the river discharge variance. As the variance is used as a measure of seasonal variations in river discharge, both the variance and the peak time difference indicate the performance of the MPI-HM in respect to lateral water flow dynamics and water storage treatment. Another feature of the river discharge, the difference in absolute water amount, is deliberately omitted
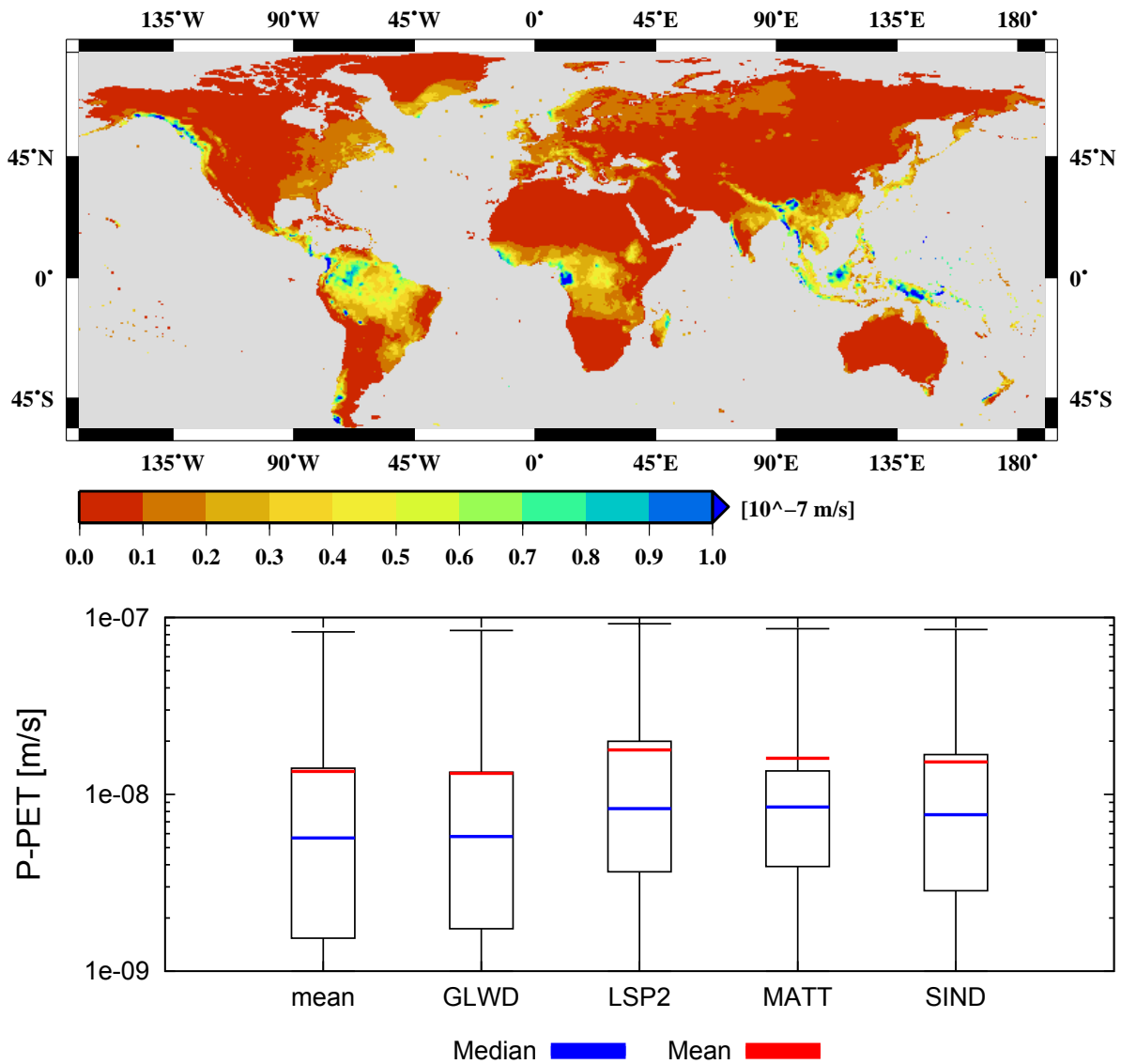
Figure 2.18.: Water flux available for drainage based on mean WFD precipitation and PET for the period 1958-1999. The top panel shows the spatial distribution of water flux available for drainage. The P - PET difference for most areas is below 10^{-8}. The bottom panel shows box plots of drainage available water flux for the whole land surface and restricted to wetland masks. The boxes display the 25th and 75th percentile and the whiskers display the 1st and 99th percentile. The 1st percentile for all masks is zero.
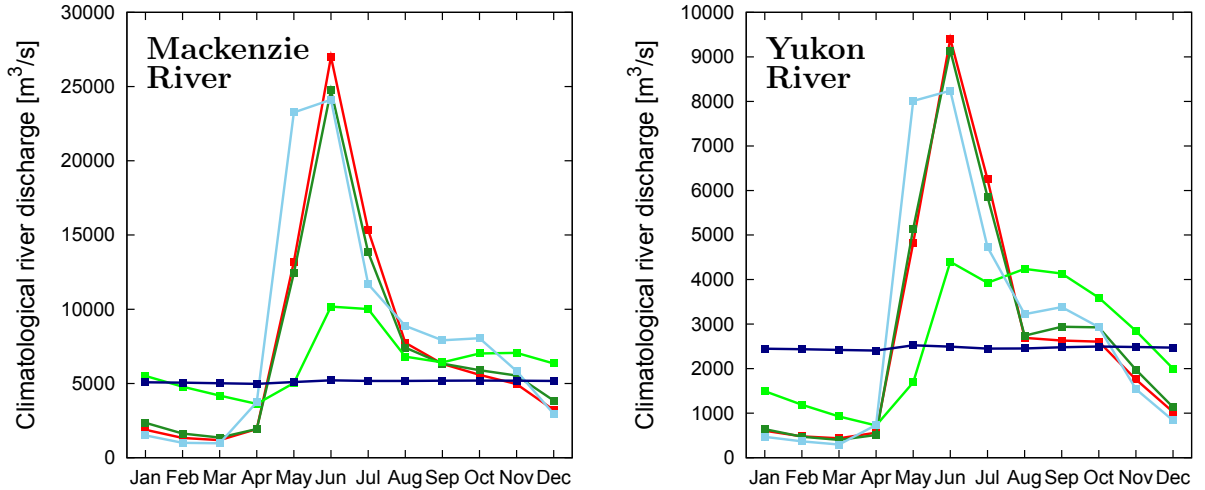
Figure 2.19.: Climatological river discharge simulated by the MPI-HM for two river catchments. While the green curves are generated using different inflow schemes compared to a baseline simulation (red), the blue curves indicate the application of different discharge coefficients k_{wetl}.

from the cost function equation as it is judged to be caused by precipitation input biases rather than by the model itself. It is possible to assign weighting factors to the members of a cost function. For this study the cost function is designed such that none of the factors can become zero and both, peak difference and variance difference, are scaled to their maximum possible value. Thus both members are weighted equally. The shape of this cost function is shown in figure 2.20.

Theoretically it would be possible to apply the optimization on grid cell scale and derive optimal parameters for every model grid cell. However, river discharge datasets do not exists on grid cell scales. Instead, station measurements act as integrals over whole river catchments. The most obvious next step would be to conduct the optimization on catchment scale, but there a major pitfall is waiting: The MPI-HM does not yet simulate river discharge perfectly in grid cells without wetland fractions. There are more missing processes in the model like the consideration of dams and reservoirs, groundwater interactions and others. Instead of focusing on wetland processes only, an optimization on catchment scale would inevitably try to compensate for such shortcomings, too. While this still leads to reasonable simulations under stable climate conditions, it would most likely not deliver robust results under different climate states.

Therefore, one has to fall back to the computation of globally homogeneous values that produce optimized results for the majority of wetland affected catchments while having as less as possible influence on the remaining catchments. Certainly globally uniform values do not reflect the strong diversity of wetlands and lakes but they avoid making false-positive corrections and thus ensure the parametrization of a certain process instead of being a mere model calibration.

The static parameter optimization was conducted using the newest global river discharge
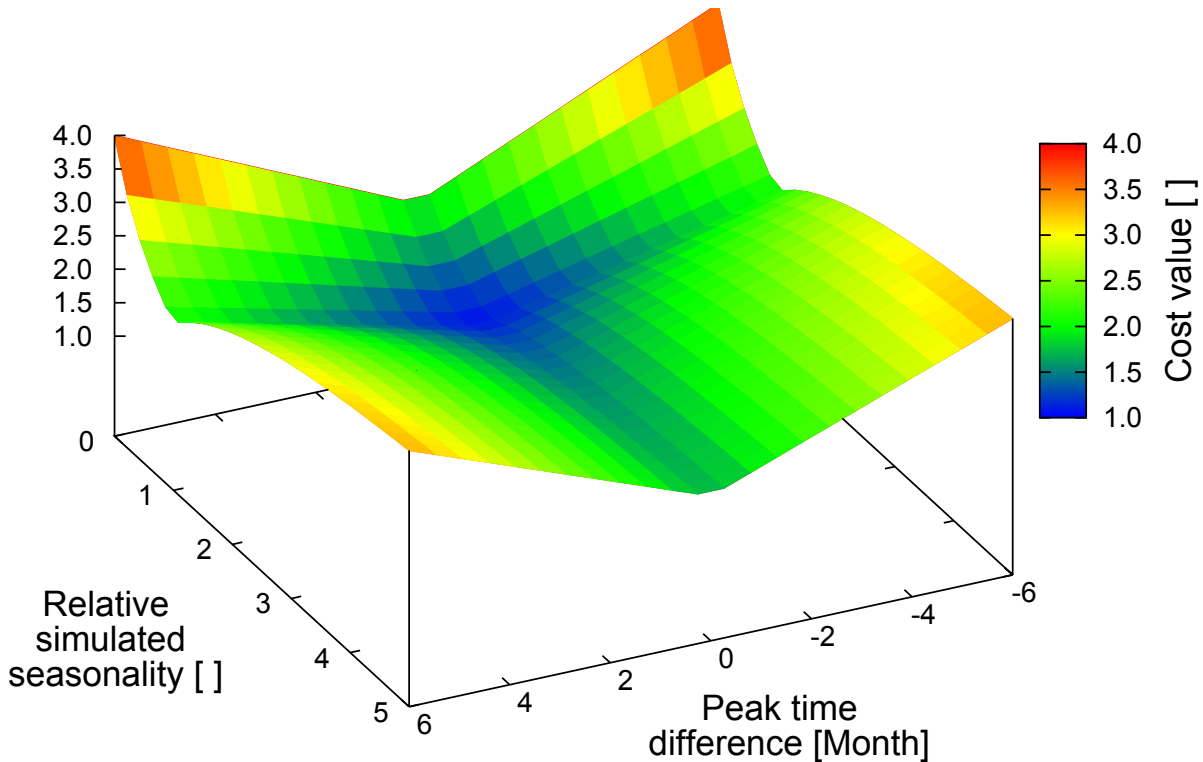
Figure 2.20.: Shape of the cost function within the parameter space. The lowest values can be found for peak time differences of zero and a relative discharge simulation seasonality of one indicating an equal variance of simulated and observed discharge. When the relation between simulated and observed variances changes, the impact of peak time differences on the cost value increases.

observations, the Global River Data Center (GRDC) dataset (Global Runoff Data Centre, 2011), as reference. These data include long term monthly means for 3579 river gauging stations, from which a subset was chosen. This selection is necessary to provide the cost function with catchments that can be simulated adequately by the MPI-HM in order to avoid correcting for model errors. Thus, the following considerations determine the catchment sampling:

1. A subset of the catchments was extracted that contains at least 40 model grid cell as the MPI-HM is expected to work best at large scales (Hagemann, 2010, pers. comm.).

2. This subset was restricted to catchments whose area is in agreement with the simulated catchment area within ±10%.

An overview about the location of the selected river catchments is shown in figure 2.21.

An additional problem arises because the inflow scheme parametrization and k_{wetl} parameter influence each other. Therefore, they cannot be optimized one after the other but at the same time only. In order to minimize the number of required simulations, the first combinations of parameters are distributed equally over a reasonable parameter
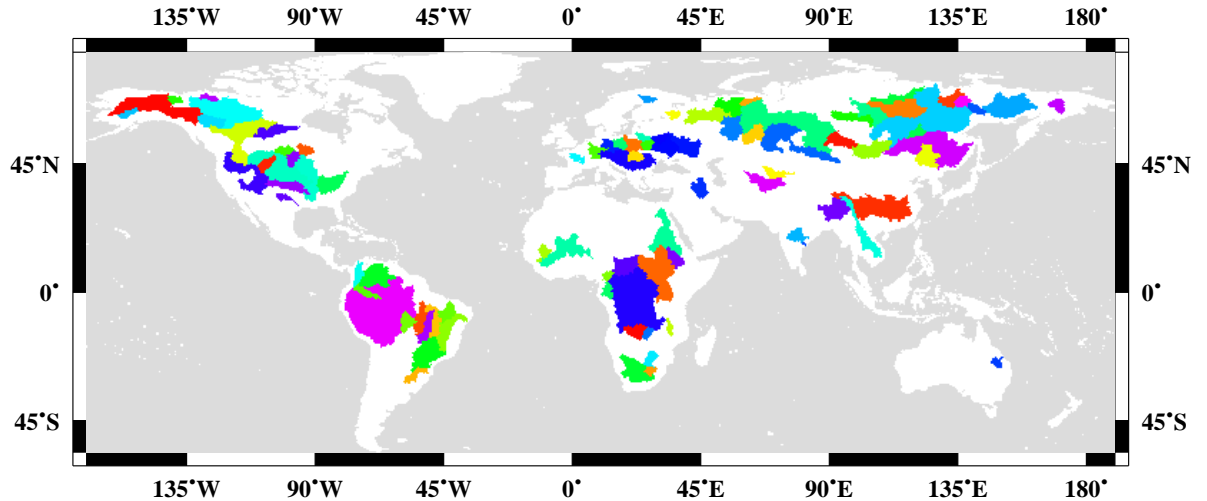
Figure 2.21.: Selection of the 96 river catchments used in the static parameter optimization. All catchments comprise more than 40 model grid cells and have less than 10% area difference between observed and simulated catchment size.

space. Later on, parameter space domains with good optimization results are sampled on finer resolutions.

The optimization itself is conducted in the following way. First, four series of simulations are conducted using systematically varied combinations of inflow scheme parametrization and k_{wetl} parameters for the GLWD, LSP2, MATT and SIND based boundary data, respectively. Using all available global wetland observations increases the robustness of the final parameter set. Of course, it has to be taken into account that the wetland fraction for most catchments varies between the different datasets. Figure 2.22 displays the frequency distribution of these fractions. The left panel points out that the wetland fraction distributions differ between the observation datasets. Their maximum frequency occurs at fractions between 0.02 to 0.06. The most common appearance of small fractions are found in the MATT and SIND dataset. However, in this analysis it is not yet taken into account whether wetlands occur at the boundaries of the catchments where they have almost no influence on the catchment integrated discharge, or close to the outlet which would impact the river discharge strongly. For this reason an effective wetland fraction was defined. Here, an additional weighting is applied to every grid cell depending on the number of upstream grid cells that discharge into it. This weighting reflects the intensity of wetland influence in the respective catchment, leading to an altered fraction frequency distribution shown in figure 2.22 (right). The distributions are shifted to higher fractions, indicating that several catchments include wetland grid cells close to the river channel. The distributions also show a wide but single peak at fractions between 0.03 and 0.5 for GLWD and LSP2 whereas MATT and SIND show two peaks. These are located at very low fractions around zero as well as between 0.03 and 0.06. The effective wetland fractions for all selected catchments are listed in table A.1.

For each simulation series the cost values for the different river catchments are averaged
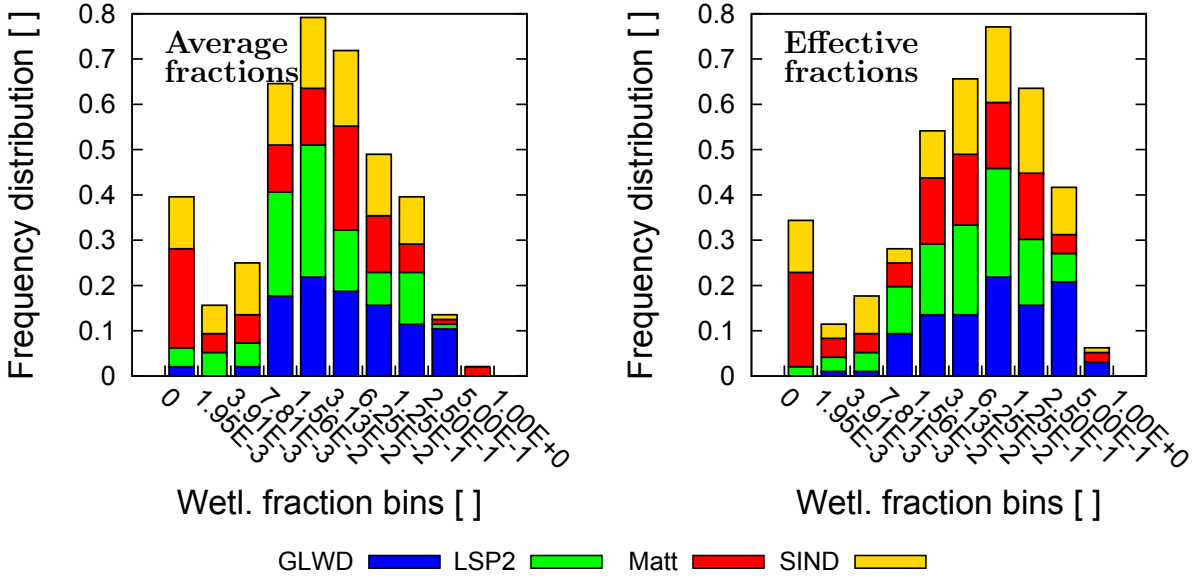
Figure 2.22.: Frequency distribution of mean wetland fractions of the selected river catchments.

depending on their effective wetland fraction. Thus, the cost value of a catchment with a large wetland fraction has a stronger influence on the average cost value compared to catchments with less wetland fraction. Figure 2.23 shows which points of the parameter space were sampled during the first round of optimization as well as the performance of the simulation under different wetland observations constrains. The four series of cost function results reveal similar patterns and cost values. The best results are generally obtained for a k_{wetl} between 1 to 10 $m^{1/3}s^{-1}$ using the exponential inflow. The worst cost values cluster at very low k_{wetl} in combination with exponential inflow schemes with exponents ≤ 1. Although the correlation between the cost values of the four simulation series seems to be good, there are differences in the absolute values. Most probably these differences are caused by the diverse wetland distribution in the observation data sets. Therefore the cost value series are averaged using a weighting based on the overall wetland content of the respective observations. The resulting mean values are displayed in figure 2.24.

At the coarse sampling resolution the lowest cost values are produced with a $k_{wetl} = 1.0 \ m^{1/3}s^{-1}$ in combination with the exponential inflow scheme using an exponent of two as well as the discharge inflow scheme at percentiles of 95 and 99 (see Fig. 2.24, left). Additionally a low cost value is found for $k_{wetl} = 0.1 \ m^{1/3}s^{-1}$ without any lateral inflow. However, test simulations revealed, that the none inflow and the discharge scheme shut down the wetland dynamics in the dynamical extent mode. Both inflow schemes are independent of the actual wetland extent. Hence, a major part of the feedback loop between wetland extent and water balance is disabled, which prevents the wetlands from obtaining an equilibrium state. For this reasons, both schemes are neglected from the further optimization. Thus, the combination of $k_{wetl} = 1.0 \ m^{1/3}s^{-1}$ and the exponential
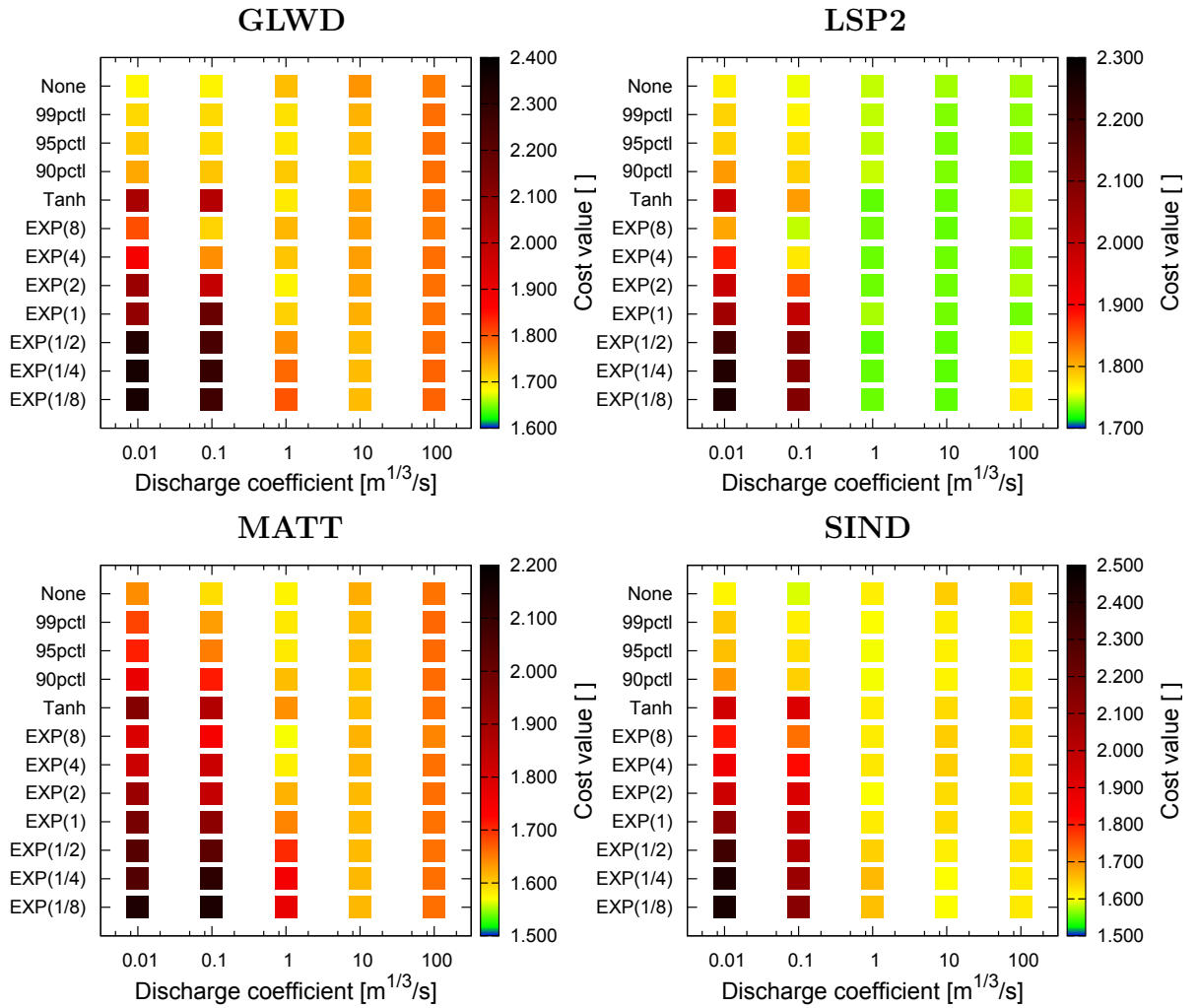
Figure 2.23.: Cost function values for systematically varied parameter combinations for four wetland fraction observation data sets.

inflow scheme with exponent 2 remains as the lowest value being 1.67. At this point the weighted standard deviation is 0.05 indicating a robust result based on all four wetland observations. Also the tanh inflow scheme will be considered in the further optimization, as its cost value is only slightly higher but more robust.

Two more refinement steps were conducted around this points with simulations within a much more confined range of k_{wetl} together with a limited choice of inflow schemes. The medium sampling resolution (see Fig 2.24, middle) reveals one additional cost value minima for $k_{wetl} = 2.0\ m^{1/3}s^{-1}$ and an inflow scheme exponent $1.\overline{3}$. There the cost value decreases to 1.66 while the standard deviation increases to 0.06. Therefore, this new minima does not show a considerable improvement to the already known minima. Additionally, it is expected that in the close vicinity of the know minima the cost value will further decrease at a stable standard deviation. Thus, the next optimization refinement concentrates around $k_{wetl} = 1.0\ m^{1/3}s^{-1}$ with inflow exponent 2. As the tanh inflow
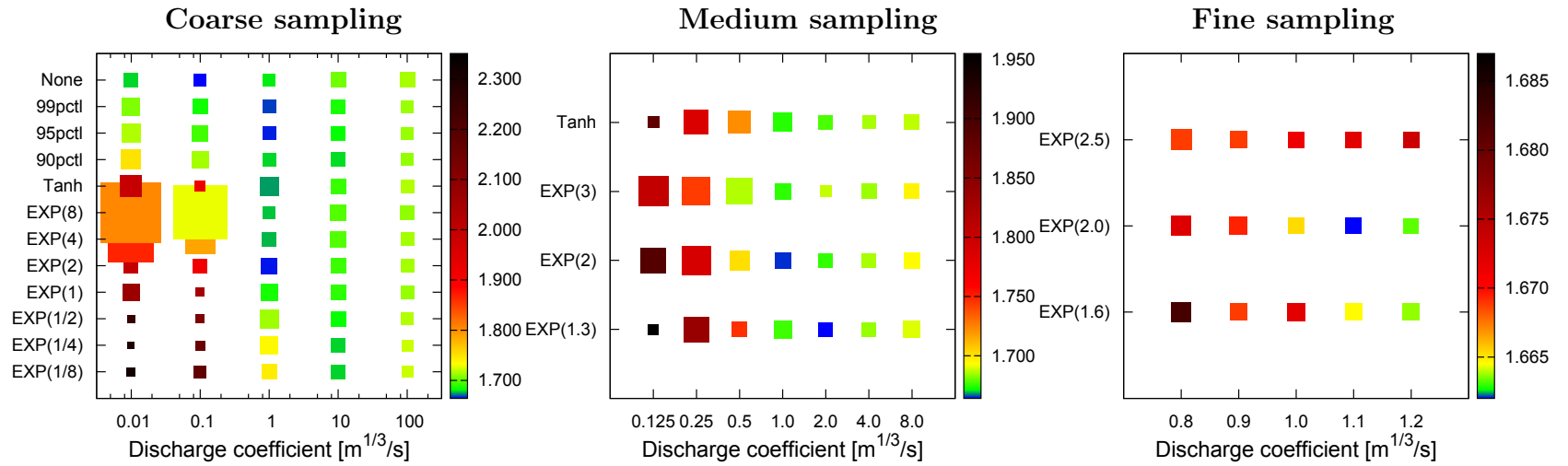
Figure 2.24.: Weighted averages of the cost function values obtained by four simulation series using different wetland fraction observations as boundaries. A square's size indicates the reciprocal weighted standard deviation. Therefore large squares indicate a good agreement between the cost function results. Some extremely robust but bad performing points were confined to a maximum square size to avoid them covering other points. The three plots show a different sampling of the parameter space.

scheme series is no longer part of the lowest cost values, it is not consider anymore during further optimization.

The fine sampling resolution (see Fig 2.24, right) locates the optimal parameter combination at $k_{wetl} = 1.1 \ m^{1/3}s^{-1}$ with an inflow scheme exponent 2.0. There the cost value is minimized at 1.66 while showing a small standard variation of 0.05. If this value is inserted back into the cost function, a rough estimated for the average discharge performance can be obtained. It reveals that the simulated river discharge curves have an averages peak dislocation of 1.7 month and disagree about 58% between simulated and observed seasonality. However, as there a some catchments with are simulated very bad due to missing processes in the model, most catchments perform much better than the average.

Although the optimization was not able to find a parameter combination that improves the discharge simulation for all investigated catchments, a combination was found that robustly minimizes the averaged disagreement between simulated and observed discharge for all wetland observations. Consequently, this parameter set is judged to be optimal and will be used in all following simulations.

2.4.2. Optimization of the dynamical part

Following the static parameter optimization, the optimization of the slope sensitivity is carried out. The slope sensitivity determines how intensive the subgrid slope affects the surface area – water volume ratio in the MPI-HM (see Sect. 2.3.1). For this reason the whole dynamical behavior of wetlands reacts very sensitive to perturbations in this parameter, which is also reflected in the variation of simulated river discharge (see Fig. 2.25). As the slope sensitivity is part of the wetland dynamics, the dynamical mode of the MPI-HM has to be used in order to optimize it.
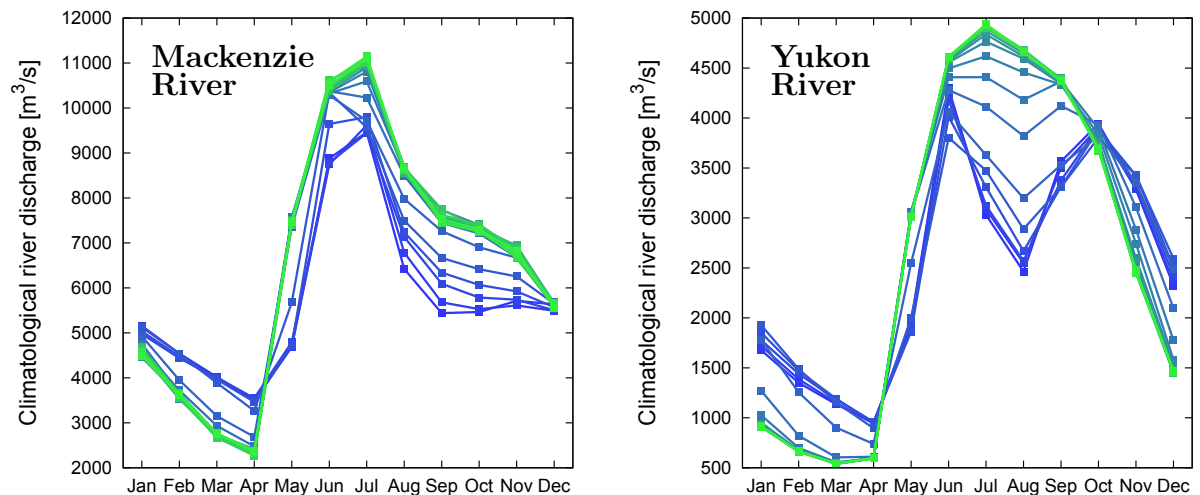

Figure 2.25.: Climatological river discharge simulated by the MPI-HM for two river catchments. The green to blue curve indicate simulations with increasing slope sensitivity.

Again, the river discharge will be employed to evaluate the performance of different slope sensitivity values. In contrast to the static parameter optimization, it is not necessary anymore to compare against observed river discharge. Instead, river discharge fields of the optimized static simulations can be used. That is because the river discharge fields are generated by the same model with identical input and forcing data. Thus, all differences between statically and dynamically simulated discharge are now caused solely by the various wetland distributions. In this way perturbing effects like missing processes and input data biases are bypassed which affected the static parameter optimization. In place of a feature specific cost function (see Sect. 2.4.1) it is now possible to use an error function. Here, the normalized root mean squared error (NRMSE) was chosen, since it verifies the overall agreement between the statically and dynamically simulated river discharge. The NRMSE is calculated as:

$$NRMSE = \frac{\sqrt{\sum_{i=1}^{n} \frac{\left(RD_{stat,i} - RD_{dyn,i}\right)^2}{n}}}{RD_{max} - RD_{min}} \ , \text{ with } n = 12 \tag{2.39}$$

RD indicates the river discharge. The subscript *dyn* refers to discharge simulated by the dynamical scheme and *stat* refers to the discharge simulated by the static scheme. RD_{stat} is computed as the mean river discharge of the four optimized static simulations using the different wetland datasets as boundary conditions. It is weighted by the effective wetland fractions of the respective simulations. As RD_{stat} is strongly influenced by the different wetland observation, its standard deviation σ_{stat} is expected to reflect the uncertainty in the real wetland observations. Therefore, any RD_{dyn} within the range of σ_{stat} should result from a simulated wetland distribution within the uncertainty of observation. RD_{stat} and σ_{stat} are displayed in figure 2.26 for two example river catchments.

A series of simulations with systematically varied slope sensitivity was conducted to detect its optimal value. The resulting NRMSE values are shown in figure 2.27. While high slope sensitivities increase the NRMSE significantly, their influence levels off at slope sensitivity values below 1. This indicates that the introduction of slope sensitivity provides no added value to the river discharge simulation. In conclusion of the dynamical optimization, the slope sensitivity parameter is set to one and thus will have no impact on further simulations.
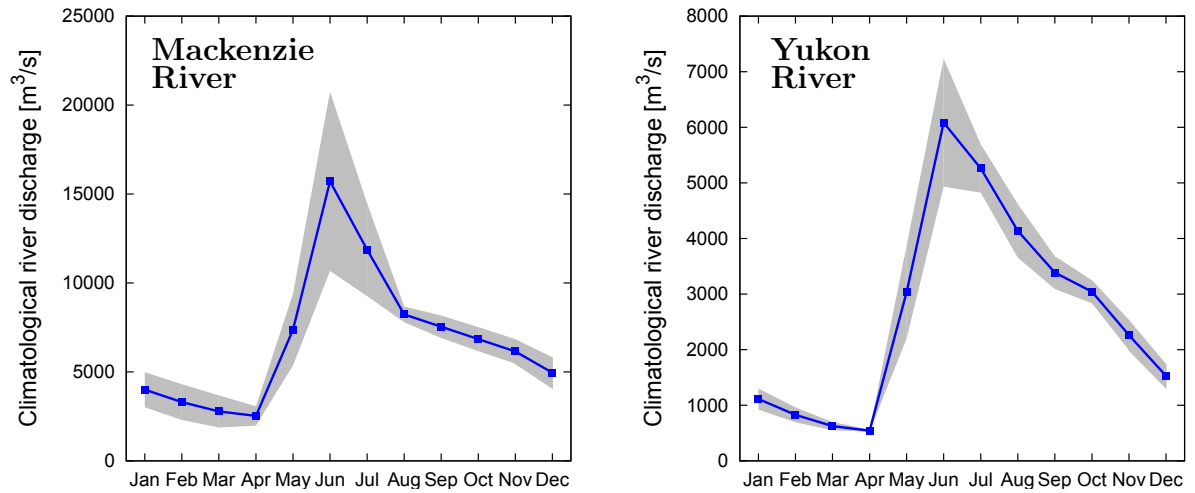
Figure 2.26.: Climatological river discharge simulated by the optimized MPI-HM in static mode. The blue curves display the mean discharge of the four optimized static simulations weighted by their respective wetland fractions. The gray shaded area indicate their standard deviation. It reflects the transformation of wetland observations uncertainty in river discharge uncertainty.
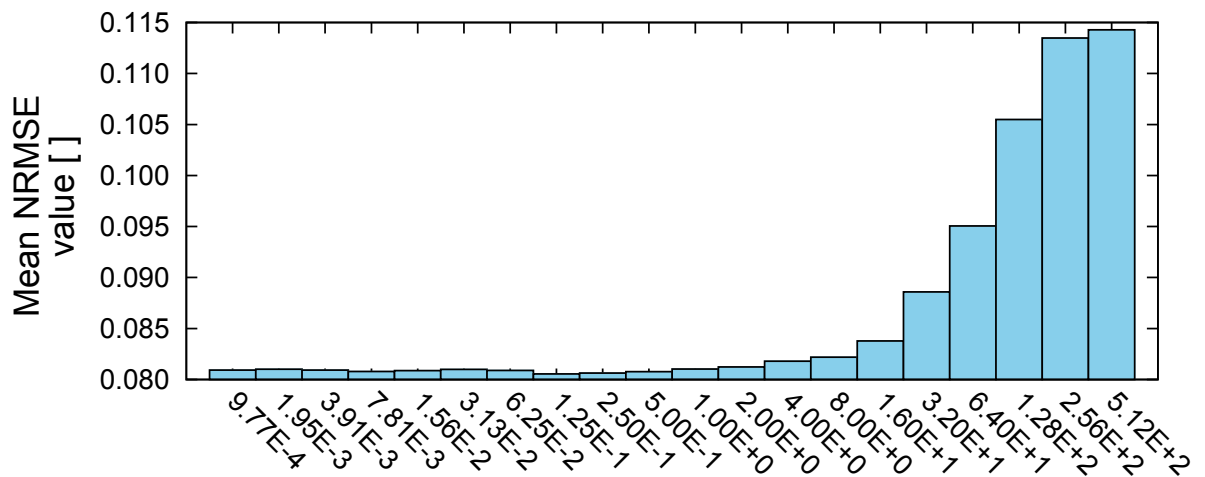
Figure 2.27.: NRMSE values of dynamical mode simulations using systematically varied slope sensitivity values.

2.5. Structure of the DWES module

In this section information are provided about the technical implementation of the DWES. Here, details about the different subroutines used for wetland dynamics in the MPI-HM are given and their interconnection is explained. Figure 2.28 shows an overview of these subroutines.

The MPI-HM is divided into an initialization phase, a simulation loop which is repeated for every time step, and a final phase. The following description of these phases focus only on routines related to wetland processes.

In the initial phase the model imports all boundary data, sets switches, and conducts calculations whose results stay constant during the whole simulation. The phase starts with the MPI-HM main routine `SLMAIN` reading restart data for the wetland soil water content, the wetland volume, and the wetland fraction. Next, it calls the subroutine `WELAINIT`. There, some switches determining the treatment of wetland soil are set. Boundary data are read for wetland drainage and subgrid slope. Additionally, some calculations are conducted regarding zero slope fractions (see Sect. 2.3.2), land surface fractions, and wetland fractions. When the HD model part is called in the first time step, initialization routines are run, too. `HDMAIN` calls the subroutine `WETLINIT` which sets the inflow scheme and discharge coefficient, calculates river flow velocity and computes the offset of the mean slope function (see Sect. 2.2.2).

During the simulation loop the actual water balance calculation takes place over all time steps. Every time step starts with the import of the respective forcing data. When the land surface water balance is solved, the subroutine `WELABALANCE` is called which focuses on the wetland water balance. First, vertical water fluxes are obtained partially from forcing data as well as from internal calculations by the subroutines `EVAPACT` and `DRAINAGE` (see Sect. 2.2.1). These routines originally belong to the land surface water balance. They are used again in the wetland water balance to calculate ET and drainage based on the actual wetland soil moisture content. Second, the lateral water flux is computed by the HD model part of the model, which is represented by the subroutine `HDMAIN`. The routine `HDMAIN` gets the actual wetland volume field from `WELABALANCE` and updates its internal wetland storage with it. It gives this information to the river routing subroutine `HDMODEL`. There, the river flow storage and the wetland flow storage are calculated together. For numerical stability this is done within a loop splitting the time step in separate sub time steps. Within every sub time step the subroutine `WELAIN` divides the grid cell inflow between the river and the wetland flow storage. Additionally, `WELAIN` calculates the actual water retention time for wetlands dependent on the mean wetland covered slope and the its water table depth (see Sect. 2.2.2). The flow cascade itself is computed by `KASGLOB`. When the river routing is finished, the updated wetland volume is given back, first to `HDMAIN` and then to `WELABALANCE`. The difference between the new and the old wetland volume yields the lateral water flux. Now all necessary water fluxes are gathered in `WELABALANCE` and the complete water balance is solved as described in section 2.2. Finally, `WELABALANCE` calls `UPDATEWELA`. This routine uses the relative change in wetland volume to compute the new wetland extent. Back in the main routine `SLMAIN` an internal check of the water balance fluxes is conducted. The water
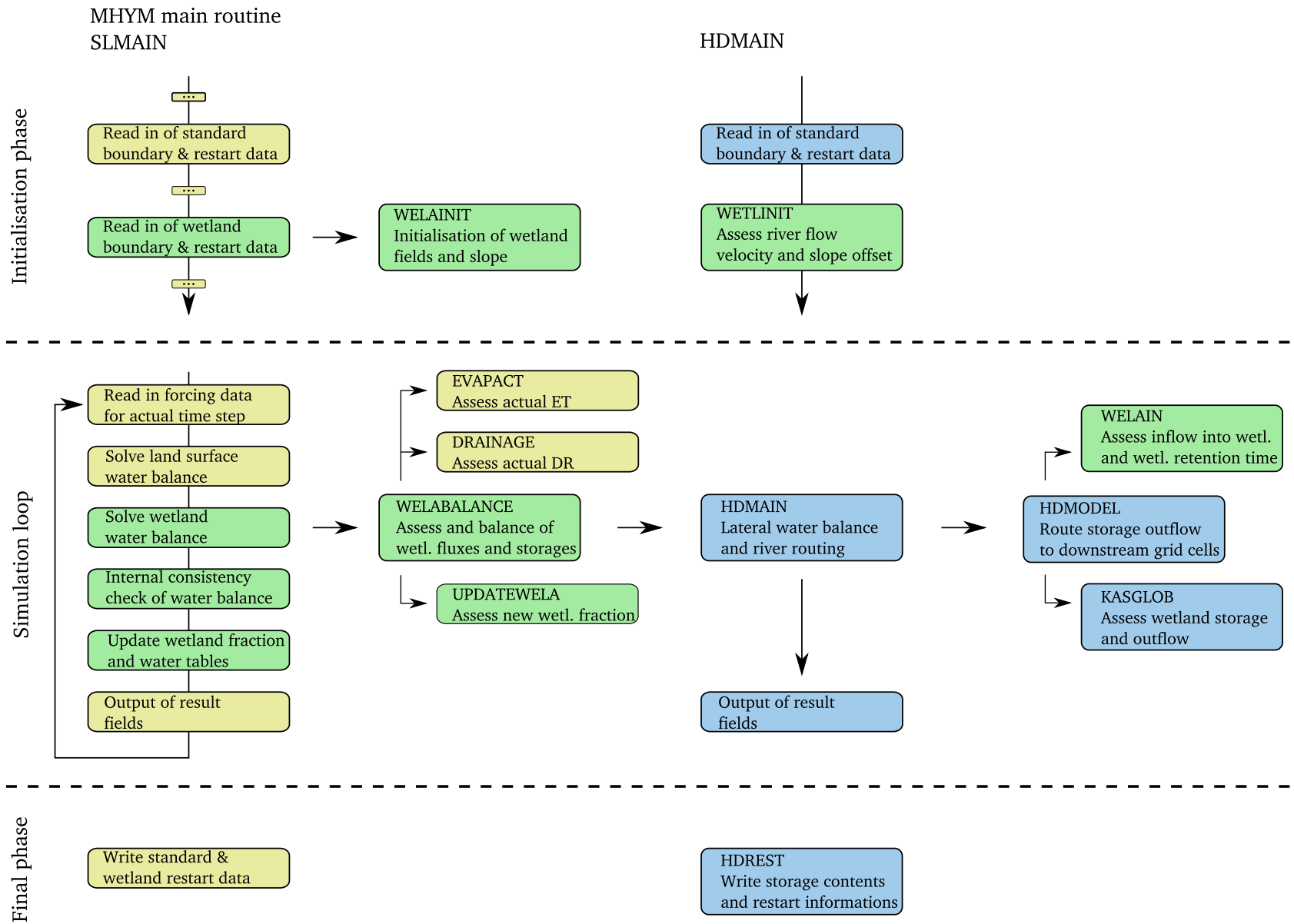
Figure 2.28.: Overview about the structure of the MPI-HM. Processes and subroutines colored in yellow belong to the former SL scheme, blue colors to the HD model, and green colors indicate new routines which enable the dynamic wetland simulation.

table is updated based on the new volume and extent fields. While all simulation results except river discharge are written by `SLMAIN` at the end of every time step, the river discharge field is outputted already by `HDMAIN`.

The final phase starts when the simulation has passed all time steps. Then restart data are written by `SLMAIN` that contains information about the wetland volume, extent and the soil moisture content below them.

3. Validation of the dynamical wetland extent scheme

The validation investigates the MPI-HM ability to simulate wetland processes in comparison to observations. It includes an analysis of the differences between model results and measurements. Thus, the validation gives details about regions where the model performs well and hints at missing or incorrectly parametrized processes. However, it is important to keep in mind that the validation results are only valid within a certain parameter range. The fact that a model might work well under recent climate conditions is no prove of its ability to project or hindcast successfully under different climate conditions.

While the model is able to archive every variable at model time step, the observations usually constrain the validation in terms of availability as well as resolution in time and space. The simulated wetland extent and distribution are the main output of the DWES and are focused on during the validation, but additional variables are taken into account, too. These are the wetland seasonal extent, their water level variations and river discharge at catchment outlets. The latter has only limited applicability as it was already used for the optimization of global model parameters (see Sect. 2.4). Nonetheless, it is an useful indicator for the overall model performance.

The validation is conducted for different spatial scales. Its focus was on global distribution and large scale features. Those wetlands cover large fractions of countries or even continents. For some analyses, the local scale is considered, too. In the present study, the local scale refers to single wetlands comprising just a small number of grid cells.

3.1. Climate forcing and boundary data

The model simulations were conducted on a horizontal resolution of 0.5° with a time step of one day. The simulation period comprises 42 years from 1958 to 1999. However, only the period between 1963 and 1999 was analyzed because the first 5 years show a spin up behavior in the newly introduced wetland fields (see Fig. 2.17). Other fields were already initialized by former model integrations. These fields are the land surface soil moisture, snow cover depth and the water volumes of the overland flow, base flow and river flow storages.

The validation as well as the optimization simulations (see Sect. 2.4) used the same forcing data and boundary conditions. The climate forcing data were generated in the framework of the WATCH project (`www.eu-watch.org`) for the period 1958-2001 and are documented in Weedon et al. (2010, 2011). The WATCH forcing data (WFD) comprise a wide range of meteorological forcing variables, including 2m temperature, rainfall and

snowfall. The data are available at 0.5° resolution and subdaily timesteps. They are restricted to the land-sea mask defined by the Climatic Research Unit (CRU) (New et al., 1999, 2000) which, hence, was applied to the MPI-HM as well. The WFD is based on ERA40 reanalysis data (Uppala et al., 2005). An extensive postprocessing was conducted in which the data were bilinearly interpolated from the original Gaussian 1.125° to 0.5° resolution and an elevation correction took place for most variables. Furthermore, rainfall and snowfall were subject to a wet day, bias and undercatch correction. Detailed information about the WFD generation can be found in Weedon et al. (2010, 2011). As additional product PET was generated based on the formula for reference crop evaporation after Penman-Montheith (Weedon et al., 2011).

Additional to the climate forcing data, there are a number of boundary fields which describe properties of the land surface. Most of them belong to the Land Surface Parameter Dataset 2 (LSP2) (Hagemann, 2002; Hagemann et al., 1999) and are based on satellite observations. These fields include monthly vegetation fraction, soil field capacity, plant available water holding capacity and grid cell glacier fraction. Furthermore, detailed topographical information are needed for the wetland dynamics. They are derived from the GTOPO30 dataset (Gesch et al., 1999) as described in section 2.3.2. Global distribution of lakes and wetlands can optionally be used for the static version of the MPI-HM and are either based on LSP2 or on other land cover data sets (see Sect. 1.3). Finally, grid cell fractions of permafrost areas have to be provided for the MPI-HM.

3.2. Validation of simulated wetlands

3.2.1. Extent and distribution

The scope of the first analysis is the assessment of the global distributions of the simulated wetlands. Figure 3.1 (top) displays a time series of their mean fraction for the land surface. During the simulation period the mean value oscillates around 0.060 with a yearly standard deviation of 0.003. The standard deviation reflects the simulated wetland seasonality. It shows that not only the mean value is relatively constant throughout the simulation period but also the sum of intra-annual variations remain stable. The observations prescribe a lower limit of 0.036 (MATT) and an upper limit of 0.078 (GLWD) for wetland coverage. Thus, the mean wetland fraction lies well within the range of observations during the whole simulation period.

More information can be gained by analyzing the earth's hemispheres separately. Figure 3.1 (bottom) displays the wetland fraction statistics for the northern and southern hemisphere, respectively. A good agreement with observational data can be seen for the northern hemisphere. The mean wetland fraction of 0.047 lies within the lower half of the observational range. In contrast, the southern hemisphere's mean wetland fraction is overestimated compared to observations. Having a mean fraction of 0.092, the simulation is well above the upper limit of 0.069 that is given by observations (GLWD). Both hemispheres show an increased standard deviation compared to the global plot. This is due to the seasonal variations which are almost balanced in the global statistics.

Time series of the global land surface wetland fraction

Northern hemisphere
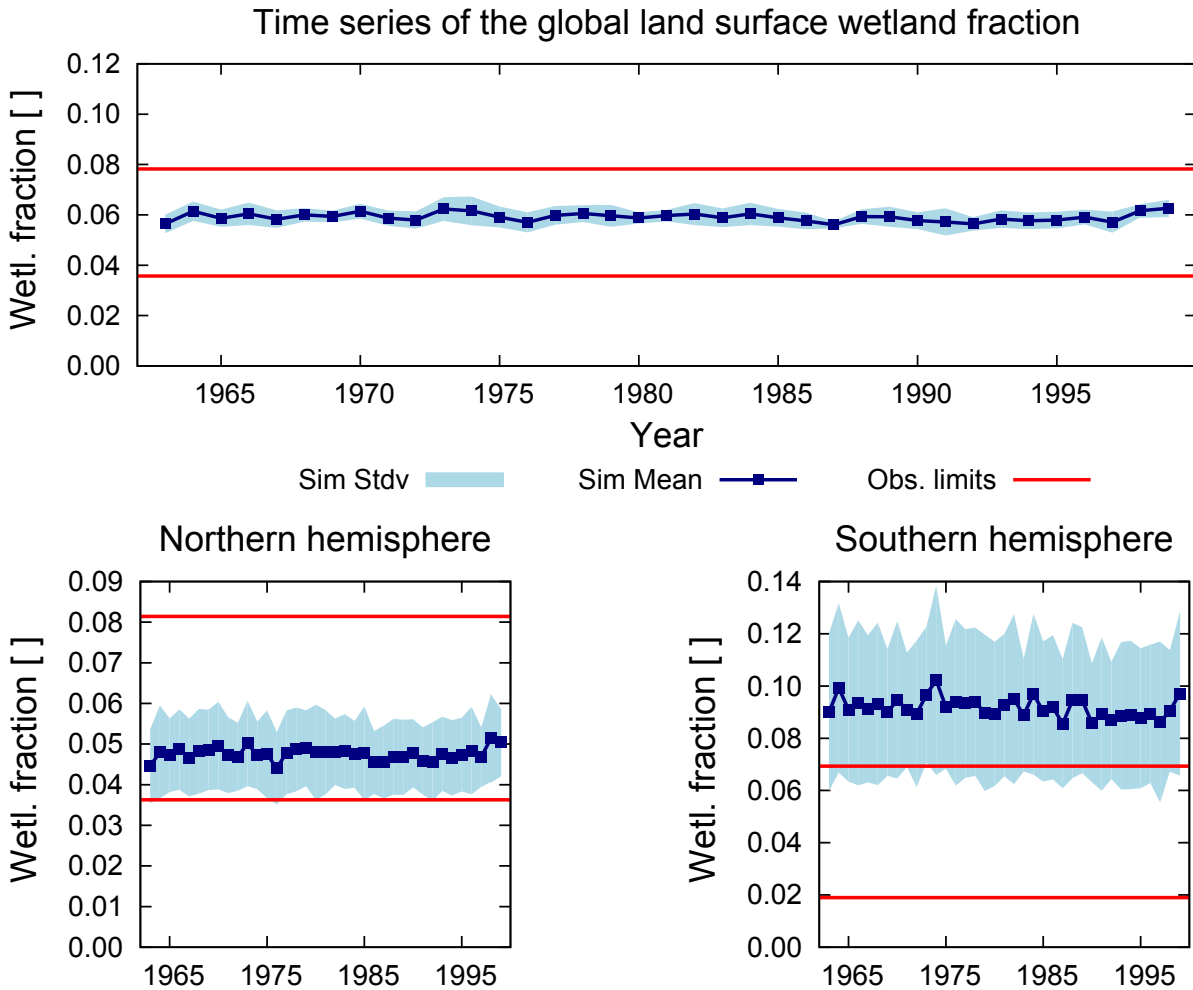
Southern hemisphere

Figure 3.1.: Time series of yearly mean values of the simulated wetland fraction and its standard deviation (blue colors) in comparison with the observational range (red).

In the next step the spatial distribution of wetlands has to be evaluated. Figure 3.2 shows global maps of wetland fraction. Figure 3.2 (top left) displays the ensemble mean of GLWD, LSP2, MATT and SIND. In the observational data the wetlands cluster on certain regions. The most prominent wetlands are found in the high northern latitudes of North America and Europe as well as Western and Eastern Siberia. Here, the largest wetlands maintain grid cell fractions around 0.8. Other wetland clusters are observed in southeastern Asia and – to a smaller extent – around the equator in Africa and South America. While the observation datasets agree on these large scale structures, there is a strong uncertainty in the absolute wetland fractions. This is emphasized by the standard deviation of the observation ensemble (see Fig. 3.2, top right). The effect is strongest in the focus regions, where standard deviations up to 0.5 occur.

In the simulation results these observed focus regions are clearly visible as shown in figure 3.2 (bottom left). The best agreement is achieved for Northern America. There, not only the distribution of wetland containing grid cells, but also their absolute fraction appears

to be well matched. The wetland clusters on the Eurasian continent are underestimated. The distribution similarity between simulation and observation seems to decrease from west to east. In contrast, the southern tropical wetland fractions are overestimated. Whereas wetlands are confined close to rivers in observations, they are more extensively distributed in the simulation.

Beside this visual validation, the agreement between observed and simulated wetlands can be more thoroughly investigated by means of a correlation analysis. This analysis is independent of the absolute wetland fractions, but it measures their spatial distribution only. Basically the correlation checks whether the relation of the wetland fraction in the grid cell of one dataset to the same grid cell in another dataset is the same as the respective relations for all other grid cell pairs. The correlation coefficient r is then calculated as:

$$r = \frac{\sum_{i=1}^{n} \left((x_i - \overline{x}) \cdot (y_i - \overline{y}) \right)}{\sqrt{\sum_{i=1}^{n} (x_i - \overline{x})^2 \cdot \sum_{i=1}^{n} (y_i - \overline{y})^2}} \tag{3.1}$$

with x and y as the wetland fractions of two different datasets and n as the population size. As grid cells in different latitudes differ in spatial extent, it is necessary to apply an area weighting for the correlation values of every latitude. The weighting factor is calculated as the fraction of the land surface area in the respective latitude to the global land surface area. Afterwards, the mean correlation value over the whole region of interest can be computed.

Figure 3.3 shows two examples for correlating wetland fractions at single latitudes. In both cases most wetland are found in the small fractions. In the high correlation example the linear relation between observation and simulation is clearly visible. However, even in the medium correlation example the data distribution does not just spread, but it seems to contain two subsets of relations. This could be an indicator that different boundary conditions occur along this latitude which cause differing but well correlating wetland fractions. For example is could be possible that two different states of topographical slope preferably occur along this latitude. The sensitivity of wetland formation to slope was optimized using a selection of river catchments only (see Fig. 2.21) and, thus, might not be valid for all regions. For the flat grid cells in this latitude the wetland area fraction may be systematically overestimated compared to observations leading to the upper branch of correlation values in figure 3.3 (top right panel), and vice versa for steep grid cells. During further development of the DWES, such analyses could help to fine-tune it on a local scale.

Figure 3.3 also shows the weighted and non weighted zonal means of correlation coefficients. The influence of area weighting reflects the non-uniform distribution of continents on the two hemispheres. The majority of latitudes show non weighted correlations between between 0.25 to 0.75. In consideration of the large amount of data, the correlation between the wetland observation ensemble mean and the simulated mean is satisfactory. Additionally to the correlation coefficient, the significance of the correlation is calculated using a t-test. The t-value t is given as

$$t = r \cdot \sqrt{\frac{n-2}{1-r^2}} \ . \tag{3.2}$$
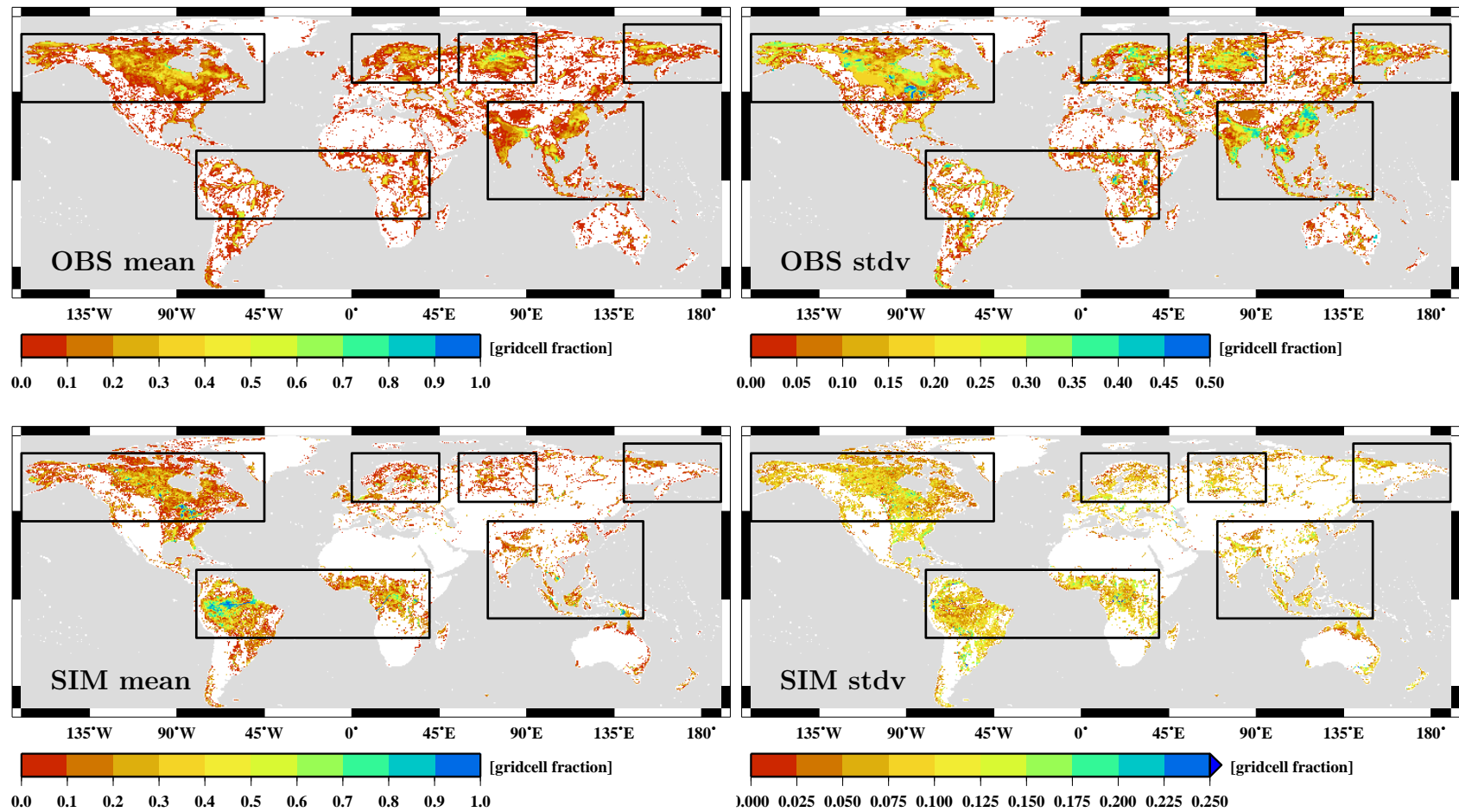
Figure 3.2.: Global wetland distribution for the observation ensemble (OBS) and simulation (SIM) during present climate conditions at 0.5° resolution. Black boxes mark areas of high interest. The top panels show the mean value (left) and the standard deviation (right) of the observation ensemble. The bottom panels show the mean simulated wetland fraction (left) and the standard deviation (right) of its yearly means.
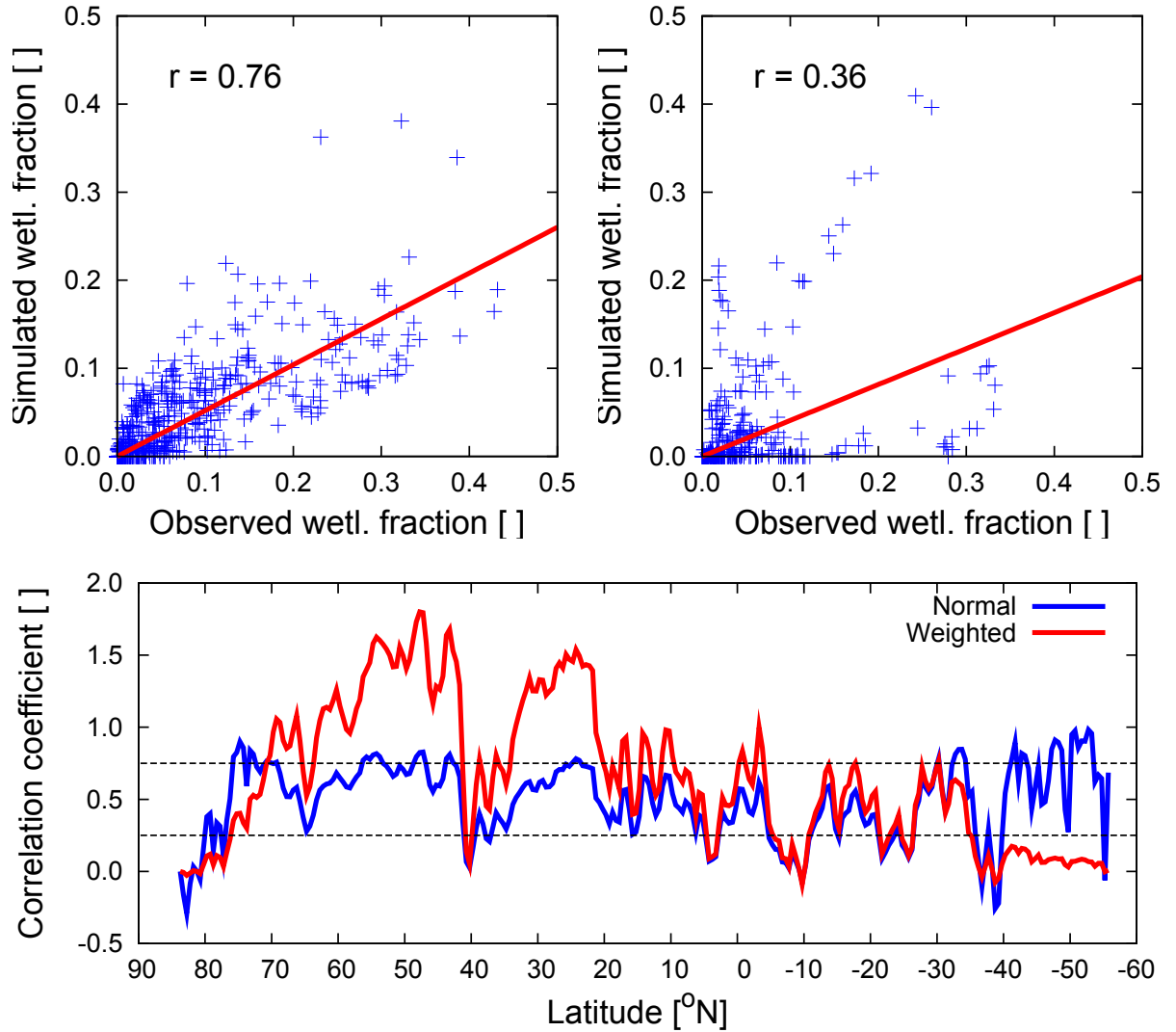
Figure 3.3.: Correlation between the observation ensemble mean wetland fraction and the simulated mean wetland fraction. The upper panels show two examples of wetland fraction relations at 69.25°N (left) with a high correlation and at 34.25°N (right) with a medium correlation. The lower panel displays the zonal mean of the correlation coefficient. In contrast to the normal correlation coefficient, the area weighted coefficient is not restricted to 1 anymore.

The significance of t is then evaluated using an incomplete beta function as described in Press et al. (1992). Based on this function, the probability of correlation significance can be derived.

One disadvantage of this point to point correlation is noticeable regarding the model validation. In case a wetland is observed in one grid cell $x_{i,j}$ and it is simulated by the model in the grid cell $y_{i,j+1}$, the correlation analysis would deny any correlation. However, in terms of model uncertainty an offset of one grid cell would be fully acceptable. For this reason, the correlation analysis is preceded by replacing the wetland fraction of every grid cell with the mean fraction over itself and its eight neighboring cells. This averaging is done for all datasets.

The analysis comprises correlation computations between all observation datasets, their ensemble mean, a random dataset and the simulation mean. The random dataset was included to provide control values to verify that all other data fields are significantly superior to randomly distributed wetlands. The correlation coefficients are displayed in figure 3.4 for the global land surface as well as separately for different continents.

Analyzing the global scale, the correlation coefficient r between the simulated and observed wetlands fraction ($\bar{r} = 0.38$) is in the same range as r between the different observations. There, it is varying between 0.11 (MATT-LSP2) and 0.47 (MATT-GLWD). As expected, the correlation between the observation ensemble mean and the single observations is high (around 0.68), but also its correlation to the simulation is increased to 0.50. In contrast, all datasets are strongly different from the random field which correlates with $\bar{r} = -6.7 \cdot 10^{-3}$ with the other datasets. Therefore, the correlation between the wetland observations and the simulation is not coincidentally caused by the huge population size of the datasets, but it is a prove of model performance.

Figure 3.4 also shows the correlation matrices for different continents. The best results are obtained for North America. Here, the simulation correlates with the ensemble mean even better ($r = 0.71$) than most observations do ($\bar{r} = 0.65$). Among the other continents, good correlations are revealed for Europe ($r = 0.46$) and Asia ($r = 0.55$), too. For South America, Africa and Australia these correlations are poor with r of 0.34, 0.26 and 0.07, respectively. However, it has to be noted that most correlations between the observations themselves are equally poor for these continents, except Australia. So far, this analysis shows that the agreement between wetland observations and simulation depends on the region and therefore on the climatic or topographical conditions. As the correlation between observations among each other is in the same range as the correlation between simulation and observations, the simulated wetland distribution is found to be in the uncertainty range of global observations.

The significance probability for all correlations is shown in figure B.1. The significance generally exceeds a value of 99.9% for almost all datasets. Exceptions are mostly the random field correlations and the correlation between simulation and GLWD as well as simulation and MATT for Australia. There the correlation significance drops to 46% and 93% indicating none and low significance, respectively.

Finally, the simulated wetland extent can be investigated on river catchment scale. Figure 3.5 displays global maps including all investigated catchments. The colors indicate the differences for the average as well as for the effective wetland fraction (see Sect.
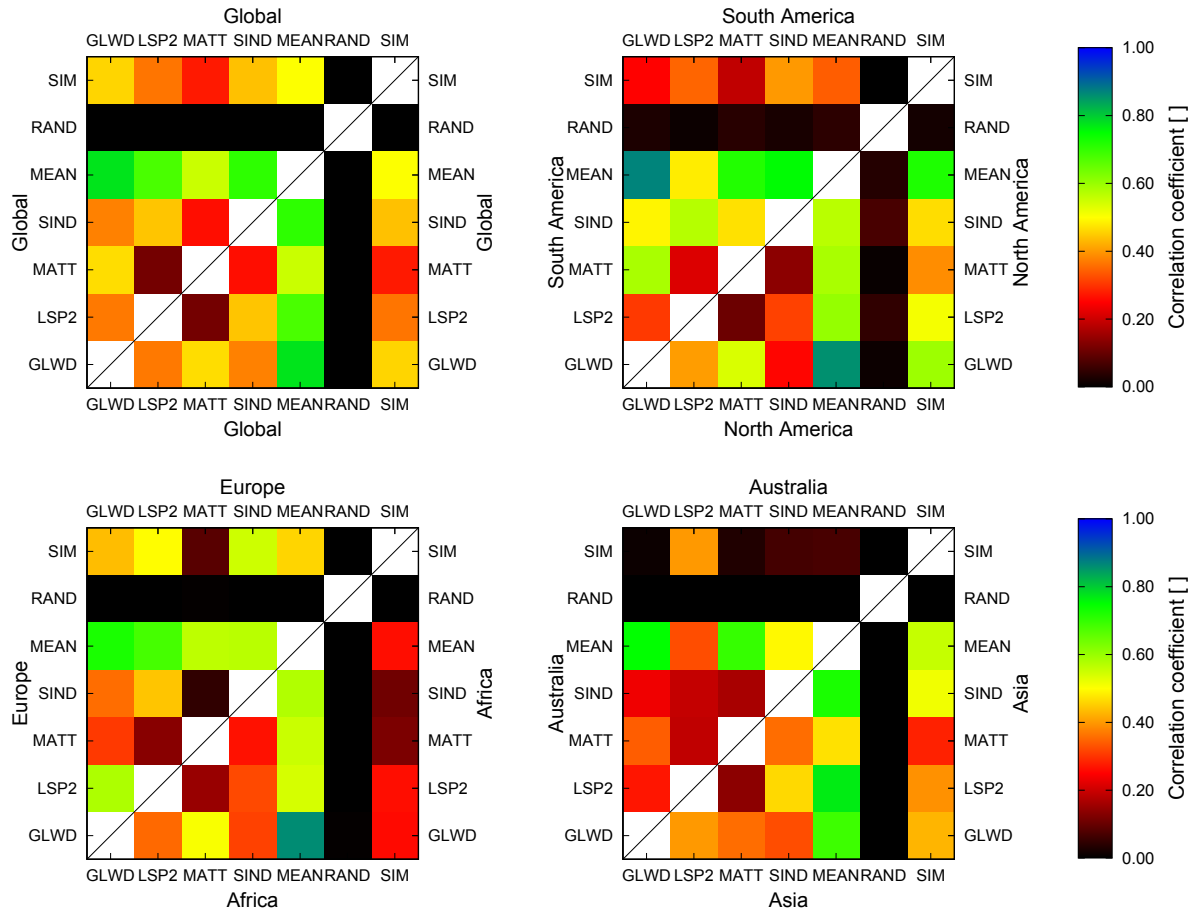
Figure 3.4.: Matrices showing the correlation between wetland observations (GLWD, LSP2, MATT, SIND), their ensemble mean (MEAN), a random mask (RAND) and the simulated wetland distribution (SIM). Except for the global correlation, all panels show two continents divided by a black line.

2.4.1) between simulation and observation. The absolute difference in the averaged wetland fraction is low. For most catchments the mean wetland fraction agrees with the observational mean within ±0.05. However, the Eurasian continent is simulated with slightly too less wetlands around -0.15, while there is an overestimation in central South America and Africa of about 0.3. There is no systematic bias recognizable that is connected directly to the model rather than to the precipitation. Generally, the tropical regions seems to be prone to overestimations. The differences become more pronounced when looking at the effective wetland fraction. This indicates that the overall amount of wetland fraction per catchment is simulated well, but the distribution of wetlands within the catchments differ from the observational mean. This is especially true for catchments which are already simulated too wet in the average fraction. There, not only the amount of wetlands is overestimated, but also they are located too close to the rivers.
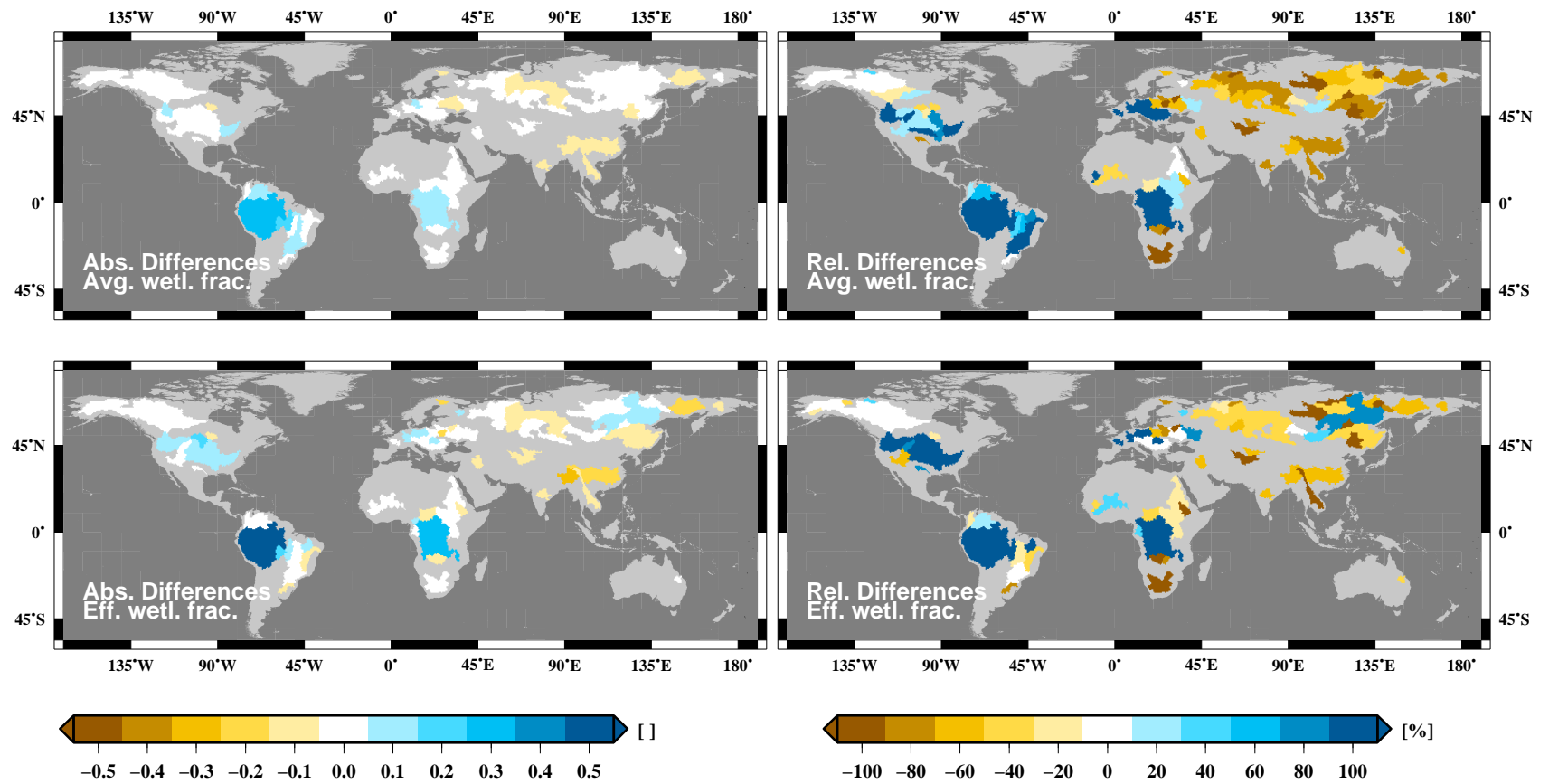
Figure 3.5.: Difference of mean simulated wetland fraction and observation ensemble mean wetland fraction on catchment scale. The upper panels display the average wetland fractions, and the lower panels display the effective wetland fractions. While the left side shows the absolute differences, the right side shows the differences relative to the observed wetland fraction.

Additional to the absolute wetland fraction difference, the difference relative to the mean observed wetland fraction is investigated. For most catchments the average wetland fraction is very small which leads to large relative differences between simulation and observation. The relative differences vary in a wide range with an average mismatch of 74%. The separation into a dry Asian and a wet South American continent remains the same, but now also North America and Europe are simulated too wet. These results do not change strongly when looking at the effective wetland fraction. Only locally some catchments change from over- to underestimation, indicating that while too much wetlands are simulated there, they are located too far away from the respective river path. This behavior is found for the eastern part of South America and upper Nile catchment. Also the opposite can occur as seen in Niger and Lena catchments. In some cases, like central USA and southeastern Europe, the wet bias is decreased or even removed.

3.2.2. Seasonality

Next to the mean wetland distribution and fractions, the wetland seasonality is one of the major products the MPI-HM generates. However, the validation possibilities for this feature are limited as the observation data availability is very scarce.

First, the seasonal variations are analyzed on the global scale (see Fig. 3.6). In this case, the mean wetland fraction is 0.059. Throughout the year the wetland fraction changes only by ± 0.002, because the signals of the northern and southern hemispheres almost balance each other. The standard deviation of this climatology is about 0.003. This indicates a robust wetland simulation during the simulation period. Considering the available global wetland observations, only the SIND includes monthly fractions of wetland extent instead of maximum or mean extent only. Its mean wetland fraction is 0.024 with a seasonal variation of ± 0.013. As the SIND comprises only 8 years, its standard deviation of 0.011 is high compared to the simulation. While the simulation is well within the range of static wetland observations, distinct differences are found between the simulation and the SIND. While having less overall wetland fraction, the SIND seasonal signal is much stronger. Additionally, both signals are out of phase. However, the SIND is derived from satellite data (see Sect. 1.3), and is restricted in its ability to observe wetlands below snow cover and dense vegetation. Papa et al. (2010) conducted a correction for the influence of vegetation and used snow cover data to mask out the respective grid cells. While it is not possible to adopt the vegetation correction for the simulated wetland distribution, the same snow mask can be applied to the simulation results. As shown in figure 3.6 (top), the agreement between simulation and SIND increases significantly. While the simulated wetland mean fraction is still overestimated $(\overline{f_{wetl}} = 4.5 \cdot 10^{-2})$, the seasonal signal is increased to $\pm 1.0 \cdot 10^{-2}$ and agrees now for the peak season. In summary, the global seasonality oscillates within the range of the wetland observations. Its amplitude can be confirmed by the SIND after correcting for snow cover.

A similar conclusion is valid for the northern hemisphere's wetland extent. Figure 3.6 (bottom left) reveals the simulated wetland fraction to be mostly within the range of observations. Its mean fraction is $4.8 \cdot 10^{-2}$ with a seasonal amplitude of $\pm 1.3 \cdot 10^{-2}$. In

Climatology of the global land surface wetland fraction

Northern hemisphere
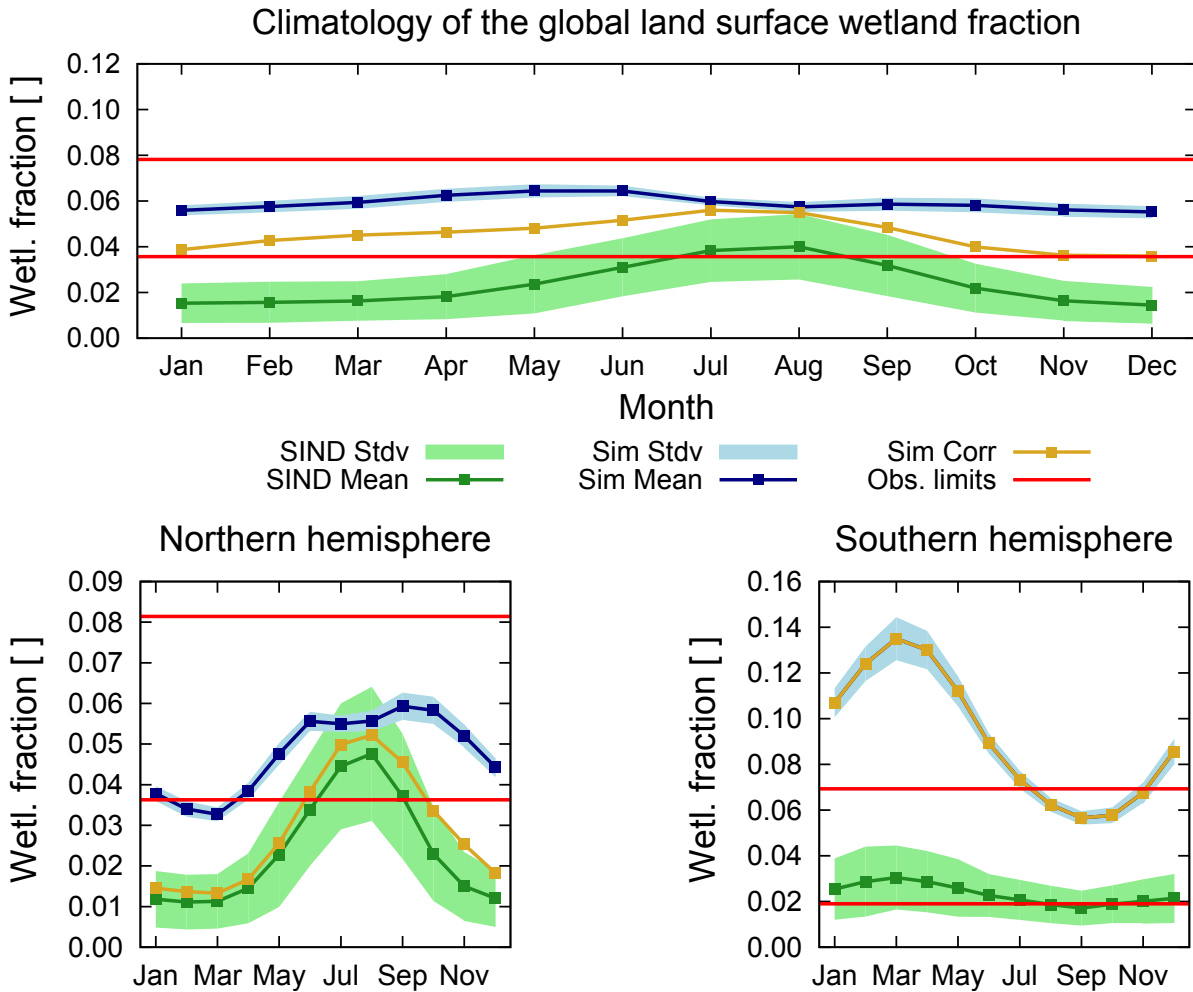
Southern hemisphere

Figure 3.6.: Climatology of the simulated wetland fraction and its standard deviation (blue colors) in comparison with the SIND (green colors) and the observational range (red). The golden curve is based on simulated wetland fraction climatology, but excludes the snow covered areas of the SIND.

contrast to the SIND, two peaks can be seen. The first peak marks the end of the snow melt which results in increased wetland fractions. The second peak is caused by the rainy season in the tropical region north of the equator. At this time the standard deviation of wetland fraction is slightly increased indicating a higher variability in tropical rainfall compared to the high latitude snow melt. In contrast, the SIND analysis produces only one peak. The SIND mean fraction is decreased to $2.3 \cdot 10^{-2}$ with an amplified seasonal cycle of $\pm 1.8 \cdot 10^{-2}$. However, when applying the snow mask, the agreement between both curve increases substantially. During most of the year the simulated wetland fraction is within the standard deviation of the SIND on the northern hemisphere.

The southern hemisphere analysis (see Fig. 3.6, bottom right)shows a strongly overestimated simulated wetland fraction compared to the SIND as well as the other observations for the larger part of the year. While the phase of the seasonal cycle matches, the absolute

fraction is $9.2 \cdot 10^{-2}$ and thus about 3 times higher than the mean fraction of the SIND. Similarly, the simulated seasonal amplitude of $\pm 4.0 \cdot 10^{-2}$ exceeds the SIND one by a factor of five. Here, the snow mask correction has no influence.

These first analyses indicate that the seasonal dynamics are represented well by the model. While on the northern hemisphere even the absolute wetland fractions agree almost perfectly with the observations, it is strongly overestimated on the southern hemisphere.

Next, the spatial features of the simulated seasonal wetland cycle are investigated. Figure 3.7 displays the deviation of every season from the annual mean wetland fraction. There are two major seasonal events noticeable on these maps. One event is the northern snowmelt. During DJF most wetland fractions north of 50°N are decreased, because wetlands are frozen or stagnate due to missing rainfall. In MAM snowmelt starts at the southern border of this region, which is indicated by increasing wetland fractions, and expands to the north during JJA. In SON the wetland fractions still exceed their annual mean, but they are already starting to decrease again.

The other event is the migration of the Inter-Tropical Convergence Zone (ITCZ) throughout the seasons and the associated rainfall. During DJF and MAM an extensive decrease of wetland fraction is visible north of the equator while the wetland fraction increases south of it. These features change place during JJA and SON and, thus, follow very well the rainy and dry seasons in the tropics. As the rainfall is strongest about one month after the sun has reached its zenith position, a time lag can be observed in the reaction of wetland extent. This seems realistic as the wetlands are not feed by rainfall only but also are supplied by rivers. Thus, the time lag can be explained by the lateral transport time within the simulated river network.

Finally, the local scale correlation is analyzed between the climatologies of the simulated wetland fraction and the fractions observed by SIND. This analysis is conducted for the wetland fraction time series of every model grid cell using equation 3.1. The correlation coefficient r gives an evaluation whether the simulated and observed seasonal cycles are proportional to each other. However, it does not account for absolute fractions.

Similar to the analysis described in section 3.2.1, mean f_{wetl} values over the nearest neighbors are computed for every grid cell in a first step. Furthermore, the snow mask of the SIND is applied to the simulated field. As the correlation is based on only 12 values for every grid cell, the probability of its significance has to be investigated, too. This is done using equation 3.2.

Figure 3.8 displays global maps of r and its significance probability. In the upper panel green and blue colors indicate a positive correlation between simulated and observed seasonality while yellow and red colors indicate no or even a negative correlation, respectively. A good correlation is evident for most wetland areas. Especially the northern parts of America, Europe and Asia as well as the Indian subcontinent show very high correlations between 0.6 and 1.0. In between those regions, some areas with no or even negative correlations are visible. Very prominent examples are wide parts of Europe as well as the southern parts of South America, Africa and Australia. However, considering the spatial significance probability distribution of the correlation (see Fig. 3.8), most of the none or negative correlating grid cells are below 0.9 and therefore not significant.
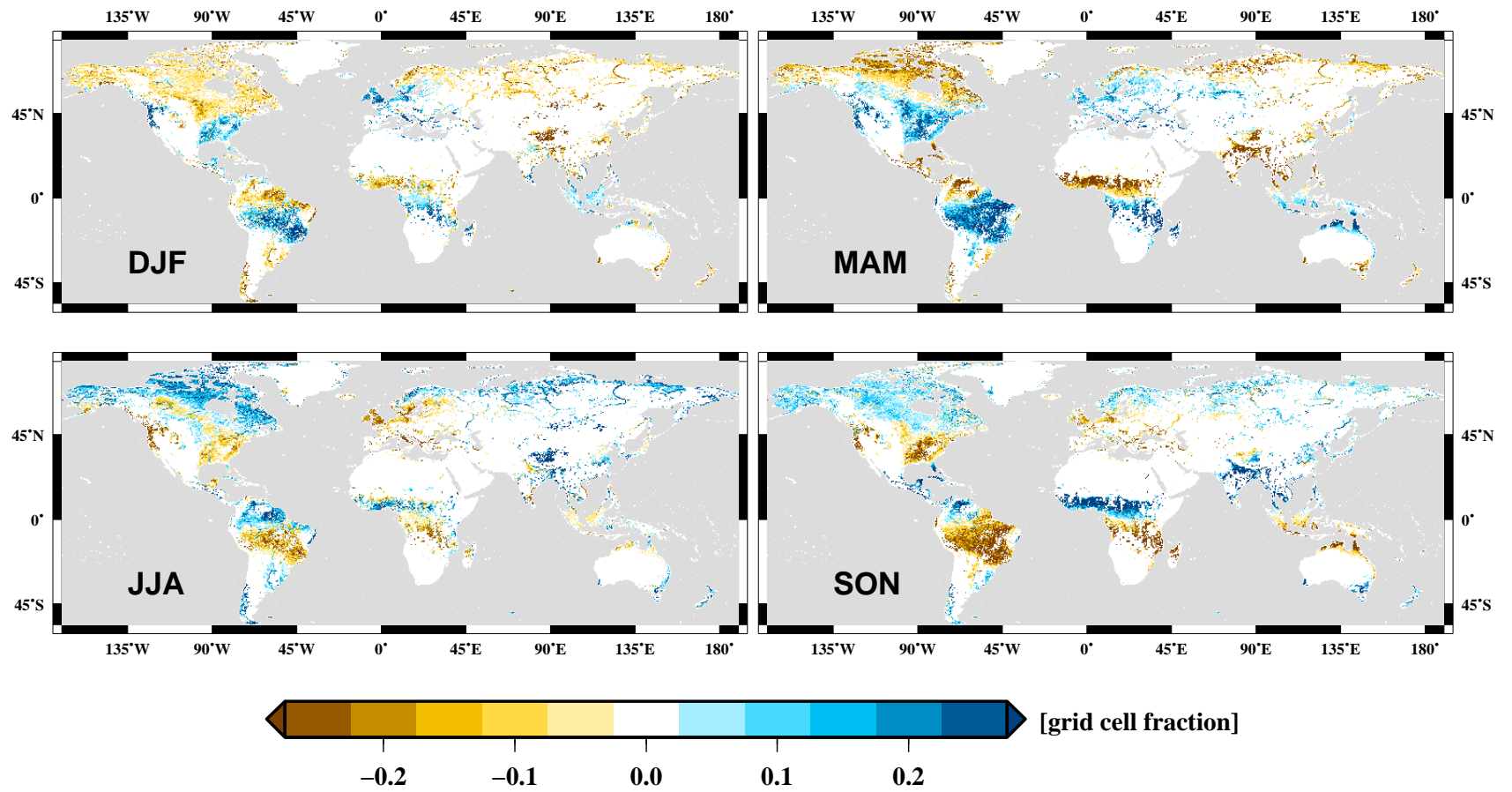
Figure 3.7.: Seasonal deviation of simulated wetland extent from its annual mean.
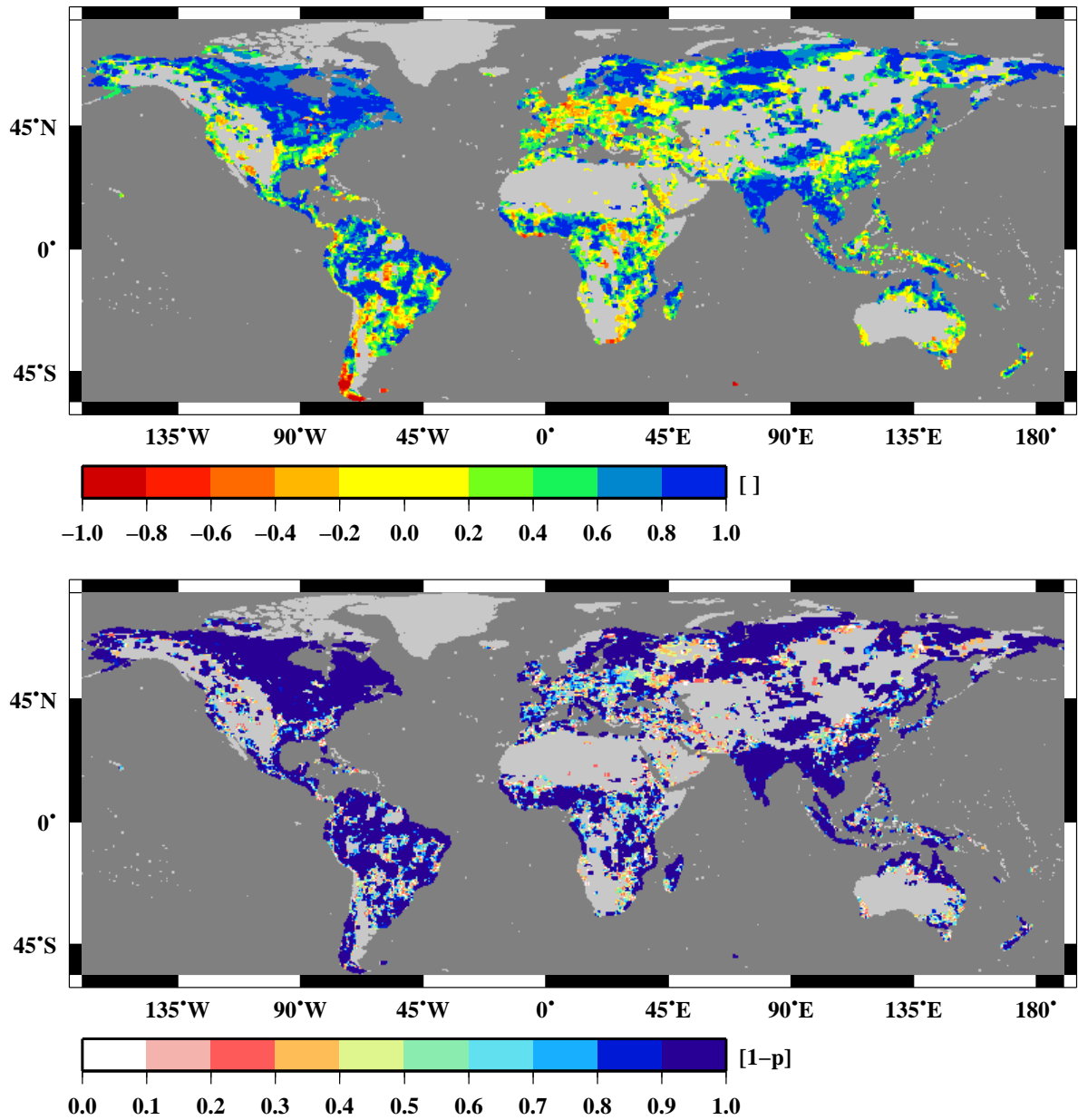
Figure 3.8.: Correlation coefficient (top) and its significance probability (bottom) obtained from the correlation analysis between simulated wetland fractions and SIND wetland fractions. Only the dark blue grid cells are considered to express a significant correlation.

Figure 3.9 displays the seasonal correlation without these insignificant regions. The
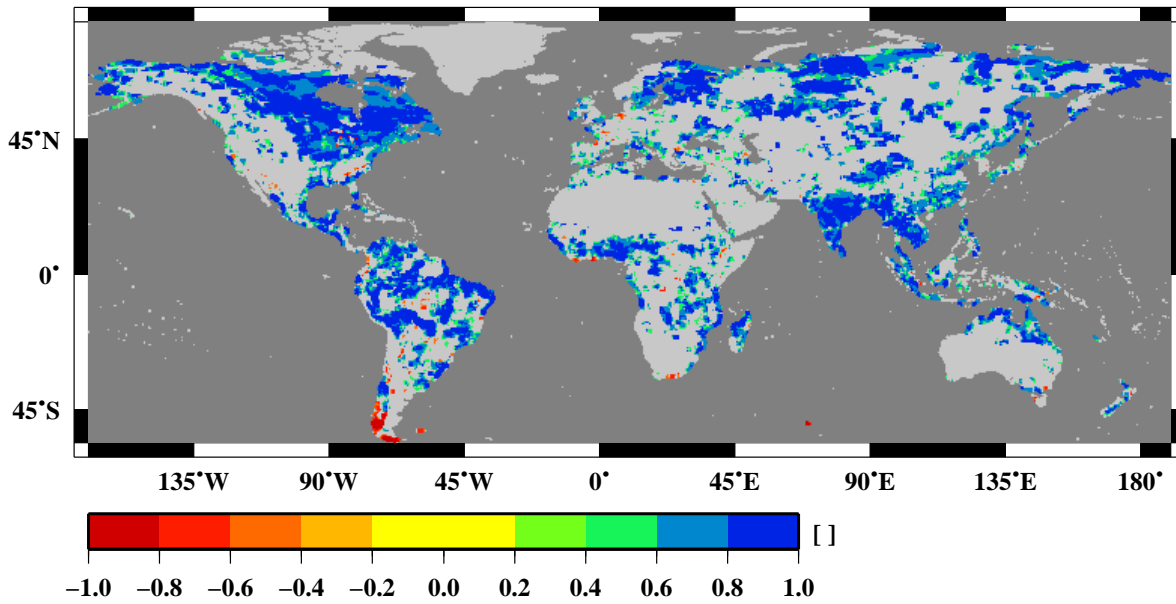

Figure 3.9.: Seasonality correlation coefficient between simulation and observation (SIND) restricted to grid cells with $\geq 90\%$ significance probability.

majority of the residual, significant grid cells indicate a very good seasonality correlation with an average coefficient $\bar{r} = 0.75$. Only the southern tip of the South American continent remains with a negative correlation.

The evaluation of this analysis has to consider that the application of the seasonal snow mask enforces a good correlation for the high northern latitudes. In order to estimate the effect of this modification, this analysis is repeated without using the snow mask. The respective correlation maps are shown in B.2. As expected, more non or negative correlating areas remain visible. Nonetheless, the majority of the northern land surface still indicates a good seasonal correlation. The average correlation coefficient for all wetlands is $\bar{r} = 0.64$.

3.3. Validation against station data

3.3.1. Water table depth

Up to date, there is no global observation dataset available that contains gridded information about the mean water depth of wetlands. Thus, a global validation of this variable is not yet possible. Alternatively, local data exist which can be used to get a first impression on this subject. These data are usually sampled at single stations and do not represent the average surface water table of a grid cell sized area. Especially in areas with a pronounced orography multiple catchments may exist within the size of one

model grid cell. Those small catchments are not necessarily connected to each other and can experience different climate conditions due to their elevation as well as upwind and downwind effects. In this case, the separate water tables are independent of each other, and the observation of just one catchment's water table gives no indication about the virtual average water table for the whole grid cell sized area. In conclusion, no direct comparison is possible between station data and model simulated grid cell averages.
However, very large structures like lakes or extensive wetlands have relatively homogeneous surface conditions. The closer their extent converges against the extent of the half degree grid cells, the stronger these grid cells should be dominated by the respective wetlands. Thus, there is an increased likelihood that large wetlands reflect the major part of the water balance for the grid cell they are located in. Still, a single station does not indicate the absolute average water table position as the geometric properties of the wetland are not known. However, its temporal variations might be well captured.
Additionally, the sampling frequency and the length of the observational time series play an important role as they affect the robustness of long term means of water table depth. While daily or five daily sampling intervals are most probable sufficient to compute monthly statistics, just one sample per season is most likely not representative for the water table depth variations throughout the year.
For these reasons, this analysis focuses on observation data of water table depth of large wetlands with a high sampling rate for a long time period. Again the validation is based on a correlation analysis employing the equations 3.1 and 3.2.

The analysis uses station data for the Lakes Ilmen, Syamozero and Udomlya which were kindly provided by Sergey Zhuravlev of the Russian State Hydrological Institute at Saint-Petersburg University and are partly published by the Russian State Hydrological Institute (1970). The lakes are located in western Russia. They are chosen such that their surface extent covers a range of two magnitudes. The largest one is lake Ilmen. Its water level data comprise the time period from 1886 till 1990 sampled at a five days interval. It has an surface area around 1000 km^2. Although the outflow of lake Ilmen is used by a hydropower plant, the lake's water level fluctuations are mostly natural due to its huge extent (Zhuravlev, 2011, pers. comm.).
A map of the Lake Ilmen area as well as wetland fractions and MPI-HM river flow directions are displayed in figure 3.10. The figure demonstrates that the extent of Lake Ilmen is simulated very well by the model. The lake is distributed over three model grid cells, and receives lateral inflow from the southern and western directions.
The simulated and observed time series overlap between 1963 and 1990. First, the observed and simulated time series are averaged to climatological mean values as displayed in figure 3.11. It is shown that the shape of the curve agree well. The first half of the year, until the maximum of the snowmelt peak, both curves show an identical behavior. After the snowmelt the water level decreases faster in the observation than in the simulation. The range of variation differs considerably by a factor of almost 10. The analysis is deepened by investigating the correlation between observed and simulated water level. This is done for the grid cell which is located at the center of the lake but also for its eight neighboring grid cells. The comparison of the center grid cell with its neighbors gives an indication whether the lake's water level variations are representative for the
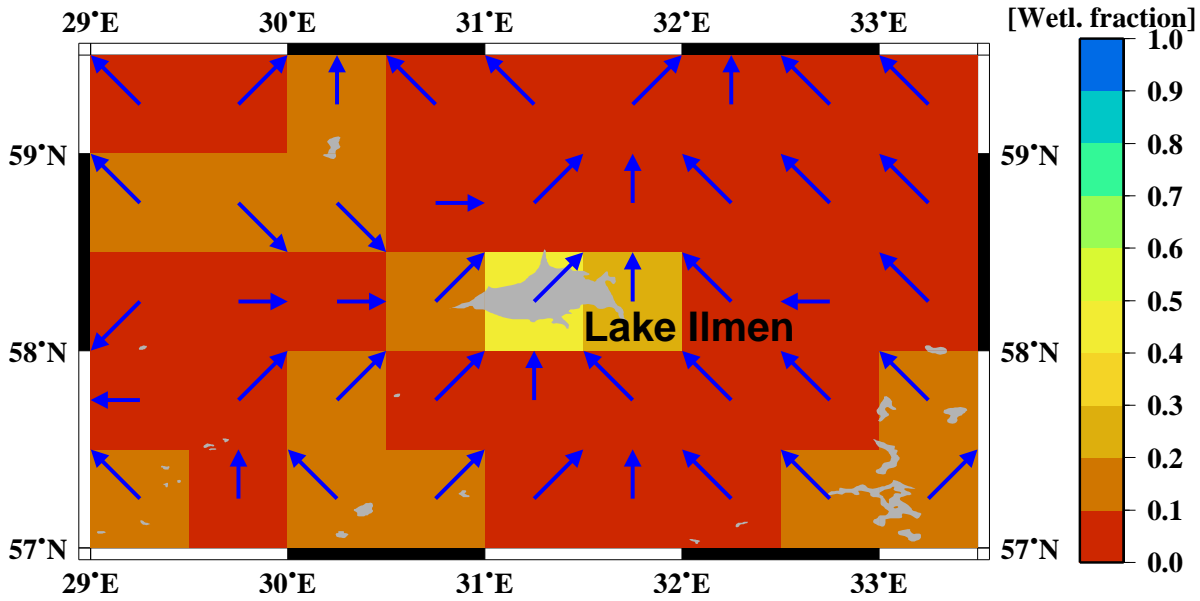
Figure 3.10.: This map displays the simulated wetland fraction in the Lake Ilmen area and the river flow directions (blue) within the MPI-HM. The gray structures indicate lake extent as included in the plotting software GMT (Wessel and Smith, 2010).
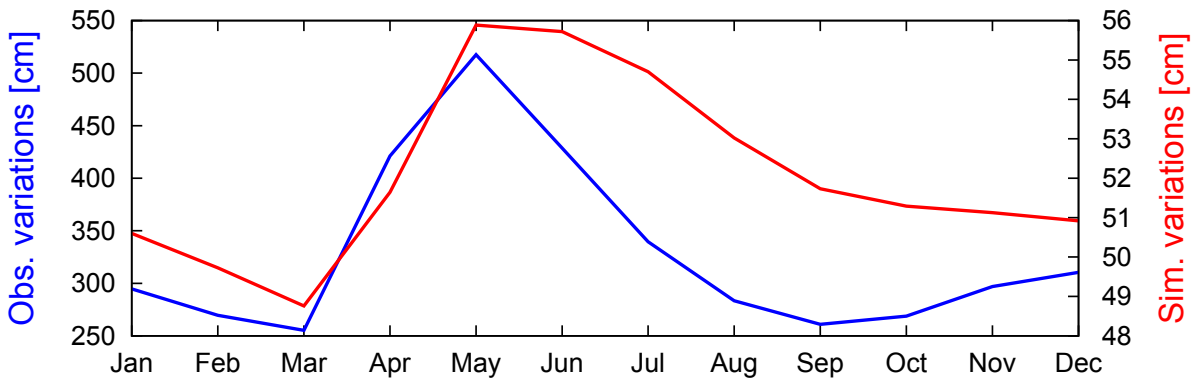
Figure 3.11.: Climatology of water level variations. The blue curve shows station data and the red one shows the simulated data. Note that both curve are scaled differently.

center grid cell only or even for a larger area. The results of the correlation are displayed in figure 3.12.

The grid cells which are partly covered by Lake Ilmen show a significant correlation of water level between simulation and observation. The correlation coefficient ranges between 0.76 up to 0.93. Thus, the model is able to explain between 58% and 86% of the observed climatological water level variations. The majority of the remaining neighboring grid cells show no significant correlation with the observation data. The reason for this is their small wetland fraction which only temporarily contains surface water. This result demonstrates the ability of the MPI-HM to simulate monthly water
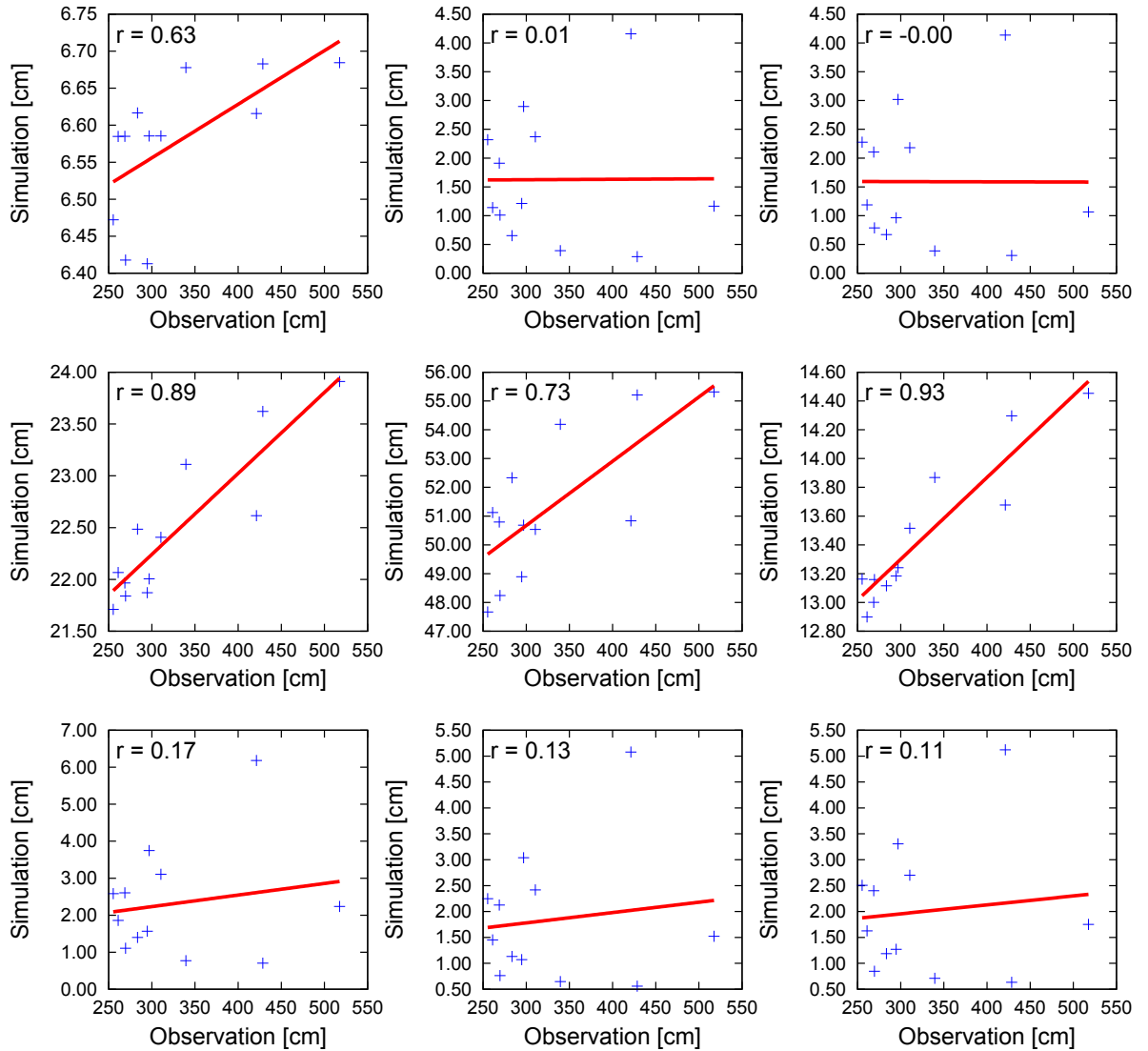
Figure 3.12.: Correlations between the climatological means of observed and simulated water table depth at lake Ilmen for the period 1963–1990. The center panel shows data for the model grid cell located at the position of the lake (31.25°E; 58.25°N). The other panels show simulation data from the neighboring grid cells with geographical north at the top. Only the results of the middle panels and the upper left panel are significant above 95%.

table depth variations in a satisfactory manner for this region.

However, the magnitude of variations is strongly underestimated by the MPI-HM. The simulated water table depth is an average value over the complete wetland fraction of a grid cell and not restricted to the lake fraction only. Thus, the simulated lake level variation might be dampened by smaller variations in flat wetlands of the same grid cell.

The same analyses were conducted for the lakes Syamozero and Udomlya. Both are smaller than lake Ilmen having a surface extent of 250 km^2 and 10 km^2, respectively. The sampling length period is from 1971–1999 for Lake Syamozero and from 1971–2005 for Lake Udomlya. The simulated wetland fractions around these lakes are displayed in B.3. Both lakes receive no lateral inflow from other grid cells in the MPI-HM. Lake Syamozero covers about one third of the grid cell in the center of the map and is also simulated with this fraction. In the east and southwest of the map the lakes Onego and Ladoga are shown. There the simulated wetland fractions are simulated in agreement with observations, too. In contrast, Lake Udomlya is too small to be seen in the observations at this resolution and accordingly the simulated wetland fraction in this grid cell is almost zero. Looking at the climatology of water level variations of the station data and the simulation in the respective grid cells (see Fig. 3.13), an agreement is seen for Lake Syamozero only. Again, the range of variations between water level observation and simulation varies strongly. However, the seasonality of the observed data matches well with the simulation in case of Lake Syamozero, though it is delayed by one month. Lake Udomlya is simulated with the right peak month but otherwise observations and simulation do not agree. The water level correlations are shown for both lakes in figure 3.14. For Lake Syamozero observations and simulations correlate significantly with a coefficient of 0.58 during the overlapping time. For Lake Udomlya the coefficient is decreased to 0.32 and is not significant anymore.

Additionally to the station observations, satellites can be employed to register variations in the water table of big lakes. Such data are available in the Global Reservoir and Lake Monitor (GRLM) database (GRLM, 2011). The GRLM contains lake level anomalies recorded in intervals of approximately 10 days. The database collects observations from several satellites. Depending on their availability, the database suffers from large gaps in the time series as well as overlapping data and offsets. The avoid such problems, only data collected by one satellite is used for this analysis. These time series include the years between 1992 until about 2002 for 79 lakes.

In a first step the agreement between the simulated wetland fractions and lake extent is checked for the positions of the lakes in the GRLM. In total 12 lakes are not simulated by the MPI-HM. On the one hand, this includes temporary or desiccating lakes like Lake Eyre in Australia, the Lake Aral in central Asia and Lake Chad in Africa. Here, the precipitation input is too low to maintain a lake in the MPI-HM. On the other hand, some of these 12 lakes are artificial reservoirs which are not accounted for by the model. A few lakes, like the Caspian Sea or Lake Kara Bogaz are masked out by the land sea mask of the model. However, most of the other lakes are not just identified by the model, but they are also simulated with a appropriate wetland fraction. Three examples are shown in figure 3.15. As not only lakes but also wetlands are simulated by the MPI-HM, the wetland fractions usually are larger than indicated by the lake mask. The best agreement
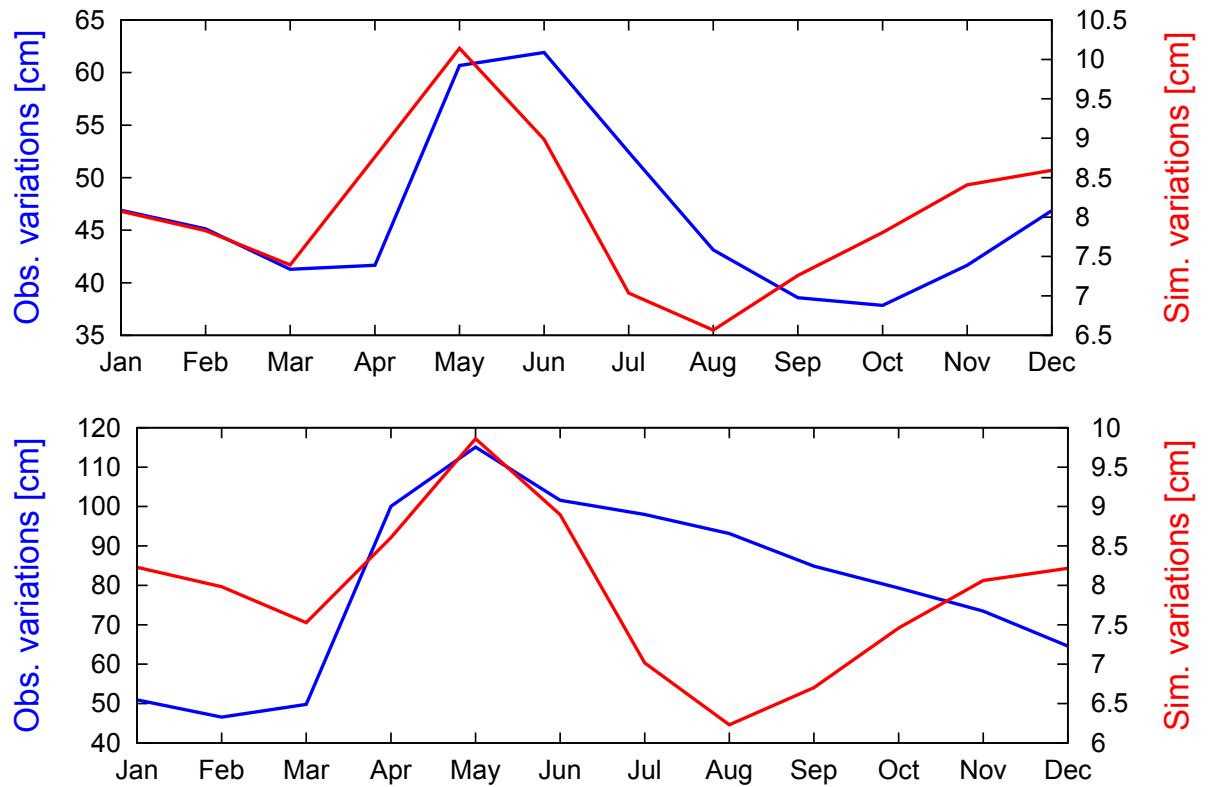
Figure 3.13.: Climatology of water level variations for the lakes Syamozero (top panel) and Udomlya (bottom panel). The blue curves show station data and the red ones show the simulated data. Note that both curve are scaled differently.
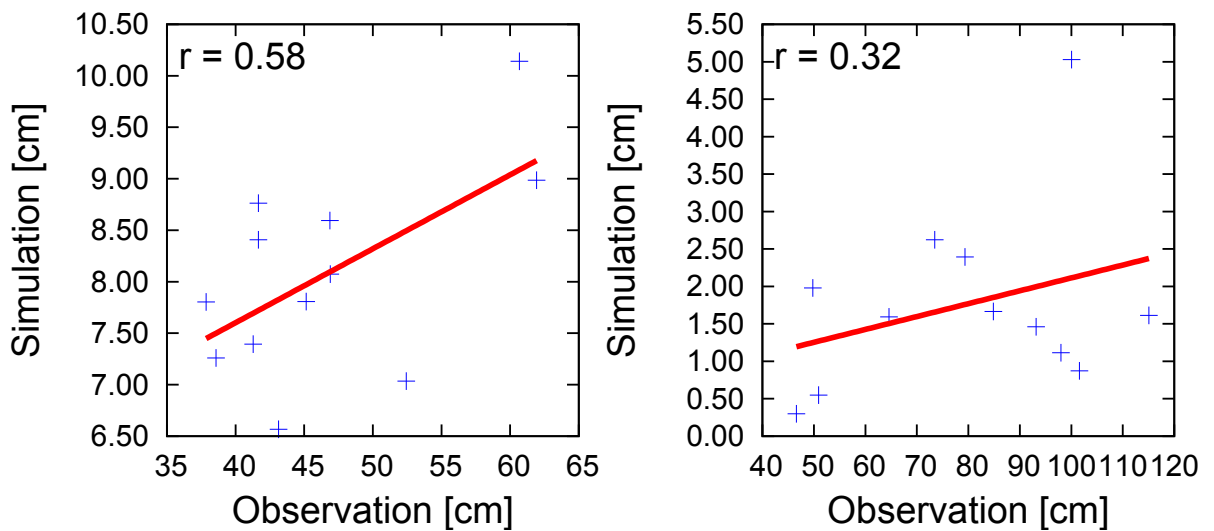
Figure 3.14.: Correlations between the climatological means of observed and simulated water table depth at the lakes Syamozero (left panel) and Udomlya (right panel). Only the Lake Syamozero correlation is significant above 95%.
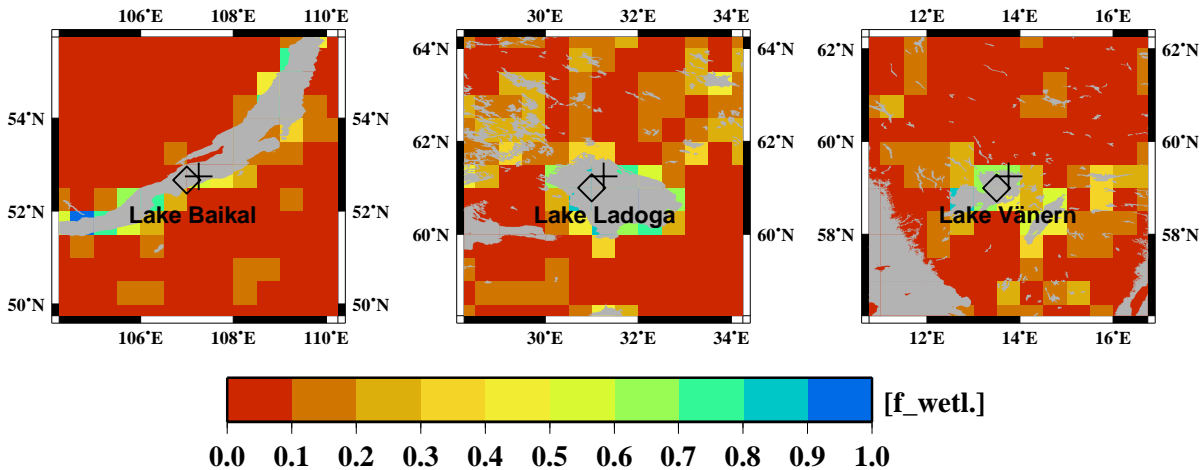
Figure 3.15.: Wetland fractions around the positions of the lakes Baikal (left), Ladoga (middle) and Vänern (right). The gray structures are the lake extent as included in the plotting software GMT (Wessel and Smith, 2010). The diamonds indicate the center positions of the lakes as seen by the satellite, and the crosses indicate the grid cells which are sampled for lake level variations.

with the lake mask is found for Lake Ladoga where even the small lakes are reflected in the model with an increased wetland fraction. However, in complicated topographical settings, like north of Lake Vänern, not all lakes can be reproduced by the MPI-HM. The validation proceeds by interpolating the satellite lake level observations to daily values which are averaged to a monthly climatology. Simulated climatological lake variations are taken from the grid cell close to the satellite position but still containing a wetland fraction greater than zero. A comparison between these revealed that the range of variation is underestimated by the MPI-HM for most lakes. Concerning the course of seasonal variations, 48 of the 67 simulated lakes agree very well with the GRLM data, as shown in figure 3.16 for Lake Vänern as an example. A subset of 17 lakes show a time lag of up to 2 month between simulation and observation (see Lake Erie in Fig. 3.16). For the remaining lakes the MPI-HM simulates lake level variations which have a lag time of more than 2 months or do not resemble the observations at all. An example for this is Lake Huron in North America (see Fig. 3.16) whose simulated peak level occurs three months too early with a too short peak width.

Next, the correlation of the monthly climatologies are calculated for the lake level variations. For 41 lakes a significant correlation is found with a correlation coefficient between 0.50 and 0.99 including three exceptions which have a negative correlation between -0.90 and -0.56. The remaining 26 lakes do not show a significant correlation between observed and simulated water level variations. The spatial distribution of these results is shown in figure 3.17. Several attempts are made to identify the reasons for the difference in simulation performance. First, it is investigated whether a dependency of correlation exists to the wetland fraction of the respective grid cells, their catchments size, their latitude or the combined standard deviations of the simulated and observed
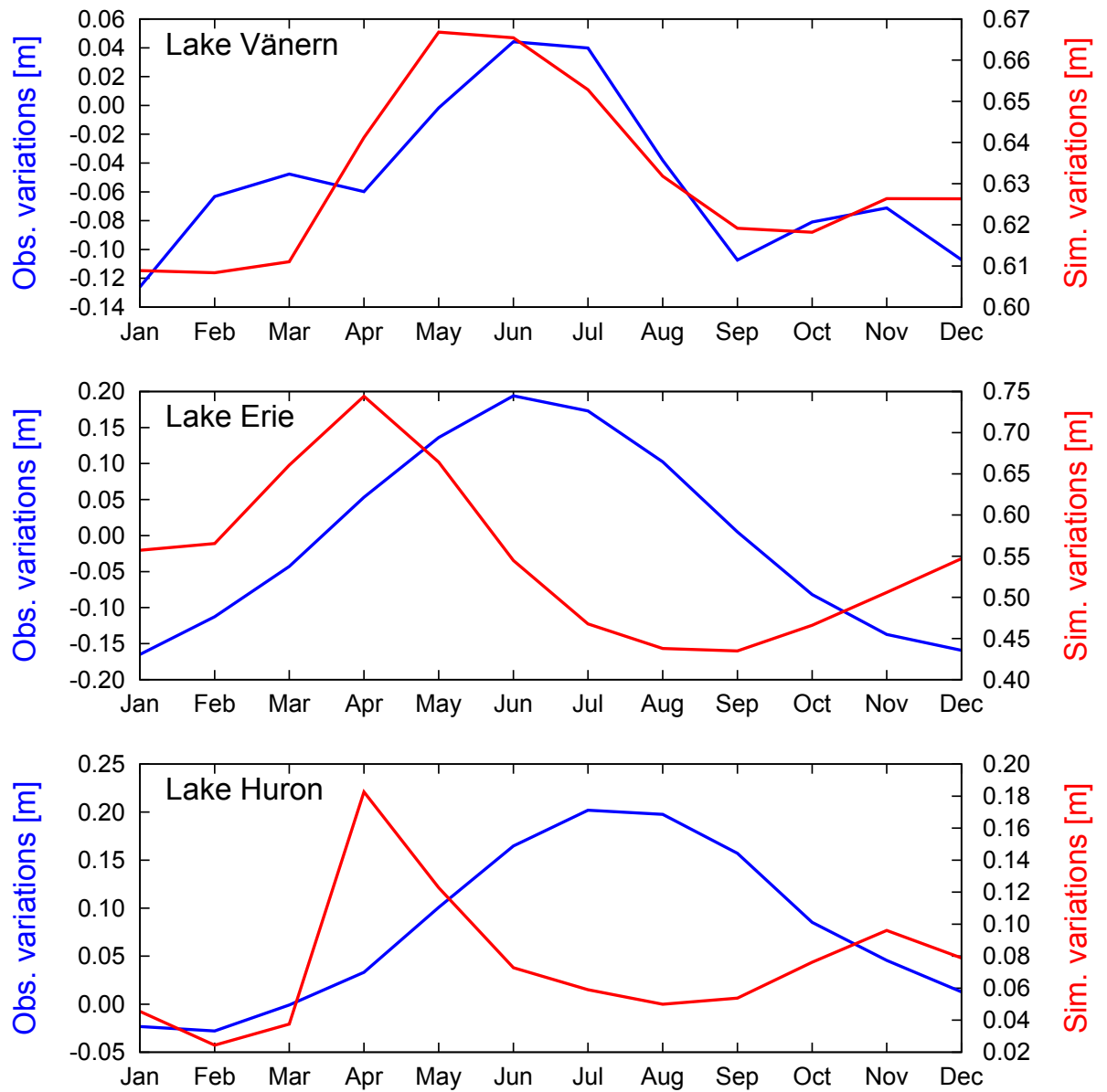
Figure 3.16.: Monthly climatology of lake level observation and simulation for Lake Vänern (top), Lake Erie (middle) and Lake Huron (bottom). The blue curve indicates observations, and the red curve indicates the simulation.
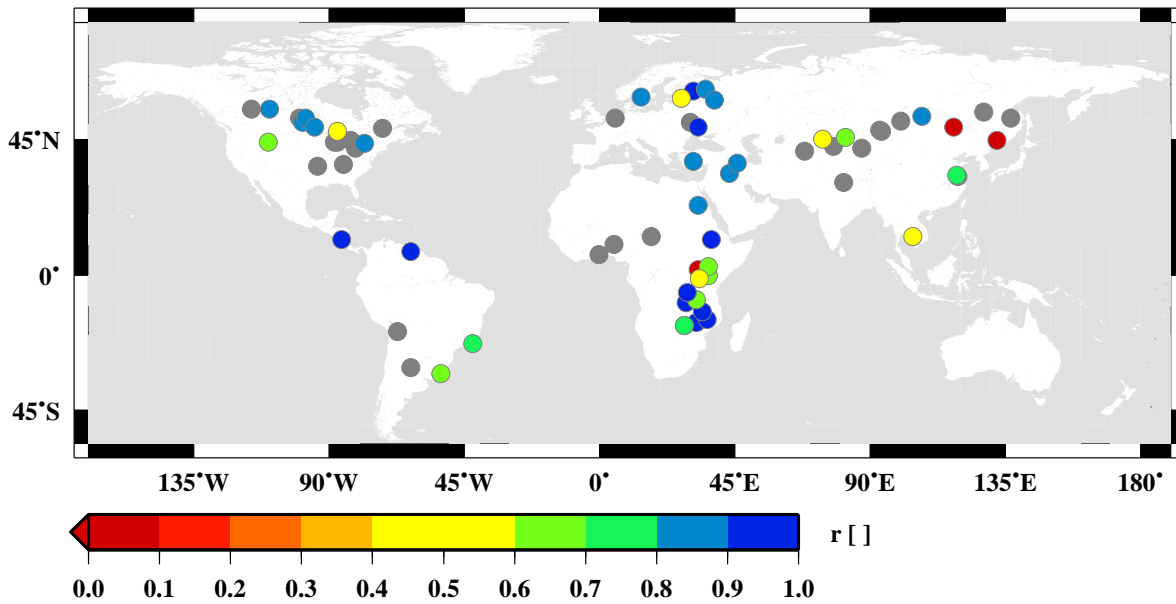
Figure 3.17.: Correlation coefficient of lake level variations between simulated values and observed GRLM data. Insignificant correlations with $< 90\%$ probability are drawn in gray. Note that some of the lakes suffer low or insignificant correlations due to a time lag between otherwise well agreeing lake level variation curves.

time series. The results are presented in figure B.4. None of these express distinctive differences in the distribution of significantly high correlating lakes and not significantly correlating lakes. Yet, significant correlations are visible in the whole range of the plots while the insignificant ones seem to concentrate on smaller values for wetland fraction and catchment size as well as higher latitudes. This behavior is confirmed when investigating the dependency of correlation on wetland water flux turnover. There, a small discrepancy is found between the different correlations, too. Figure 3.18 reveals a weak surplus of significant correlations at high water turnover rates while insignificant correlations concentrate at lower rates. However, in all cases the correlations overlap in the total range of the investigated variables and thus the dependency is not exclusive.

In conclusion of this section the MPI-HM's ability of simulating water level variations is demonstrated based on three observations time series at stations and 79 time series acquired by satellite surveys. While the correlation between observation and simulation is high for the majority of investigated lakes, the lake level variation range is strongly underestimated. Most probable the latter is due to the inconsistency when comparing data derived from the lakes only with grid cell averages which also include all other wetlands in this cell. Usually, small wetlands have less variation in their water level compared to large lakes. In case, all wetlands and small ponds could be taken into account when constructing the average water level of a grid cell sized area, this water table would vary less and become closer to the simulated values.

The validation reveals a slightly higher probability of good model performance for lakes
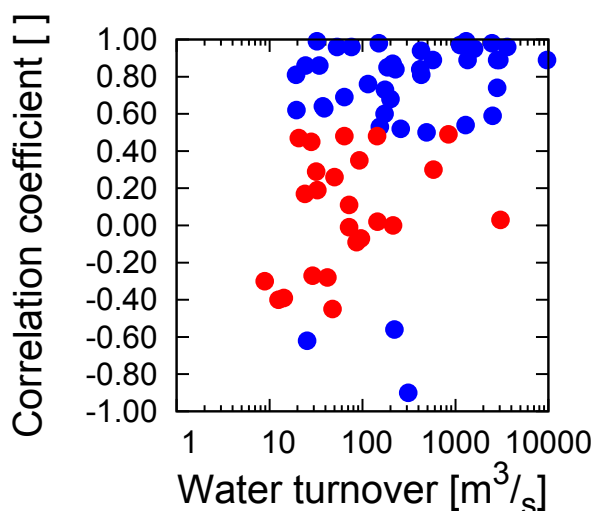
Figure 3.18.: Dependency of correlation coefficient and significance on the simulated wetland turnover in the model grid cell. The blue points indicate significant correlations while the red points indicate the insignificant correlations.

which cover a large grid cell fraction, have a large catchment or a large water flux turnover. However, also for a number of small lakes a good agreement is found between observed and simulated seasonality.

Finally, the location of the observed lakes is compared against the simulated wetland fraction on local scale. In most cases the lakes themselves as well as their surroundings are reflected well by the simulation results.

3.3.2. River discharge

River discharge observations were used to derive several parameters of the MPI-HM (see Sect. 2.4). These parameters were optimized such that the differences between simulated and observed discharge are minimized. For this reason, the use of river discharge for validation purposes is very limited. However, as the optimized parameters are globally constant instead of catchment specific, the validation is still useful to explore which regions are simulated well by the MPI-HM and why it fails in other regions in terms of river discharge.

A first overview is given by figure 3.19 for 96 river catchments. It displays the quality of river discharge simulations relative to the GRDC observations. This simulation quality is evaluated using the NRMSE and the cost function method, which are described in section 2.4. The two methods produce different results.

The NRMSE evaluation (see Eq. 2.39) shows that most river catchments are simulated well by the MPI-HM during the control simulation. The average monthly deviation between observed and simulated river discharge lies within 30% of its total range. The largest differences are found in Africa and Europe. Most likely they are caused by anthropogenic influences that are not considered in the model like irrigation, dams and other river regulations. Analyzing the differences in the NRMSE between the dynamical
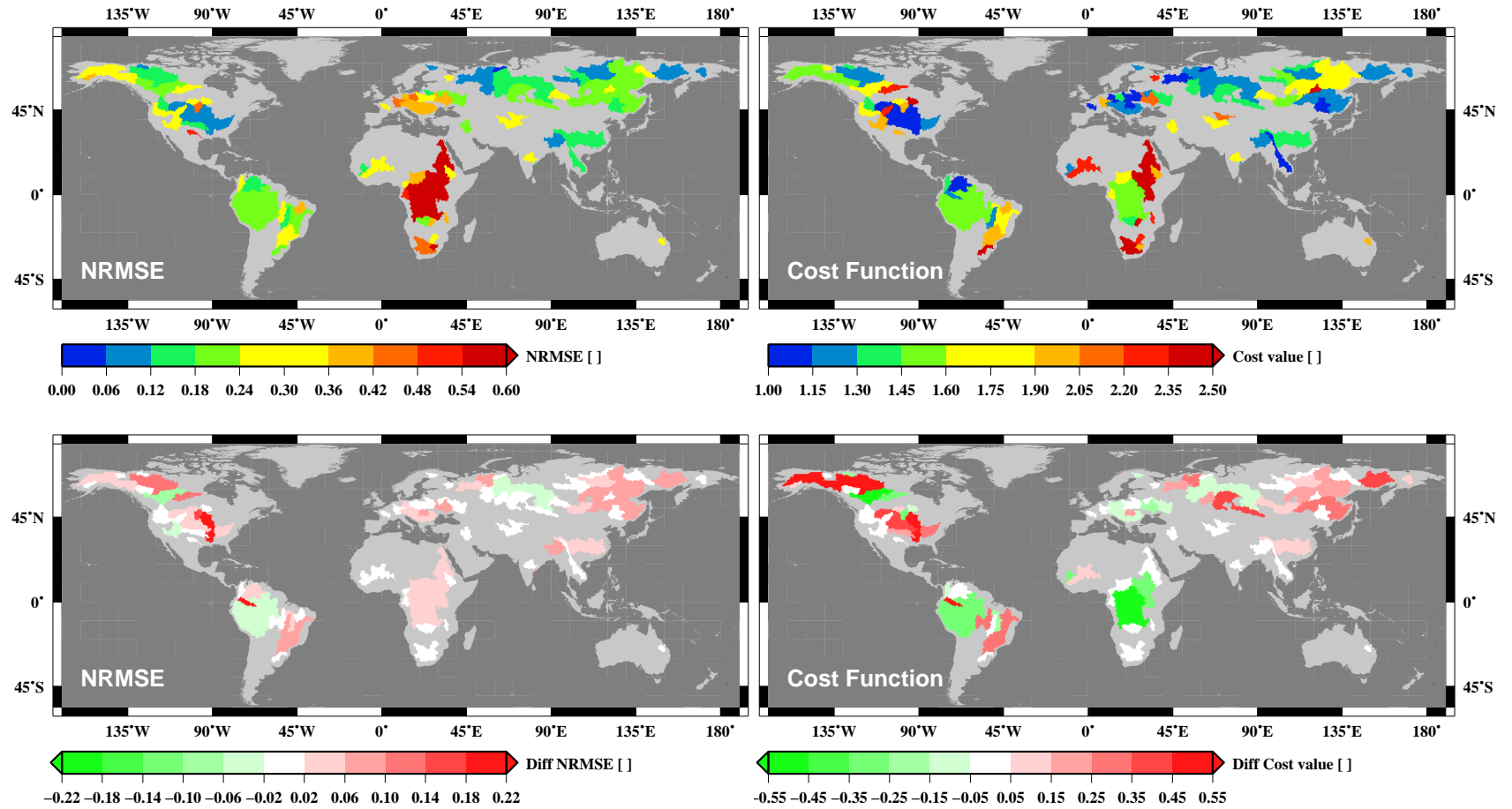
Figure 3.19.: Evaluation of river discharge simulations at river catchment scale. The upper figures give information about the quality of river discharge simulated by the control simulation in respect to observations. The lower figures display which catchment's river discharge is improved or degraded by the DWES compared to a control simulation. The two methods used for the evaluation are the NRMSE (left) and the cost function calculation (right). In all cases lower values indicate results which are in better agreement with observations.

wetland simulation and the control simulation, the influence of the new model processes is very low. Most catchment's river discharge curves differ within 2% compared to the control simulation. The others remain within 6% deviation. On average, the river discharge quality is slightly decreased. The strongest effects are visible for the Mississippi River in central North America and the Rio Japura in northwestern South America, whose river discharge simulation quality is decreased by 20%.

The evaluation based on the cost function method (see Eq. 2.38) produces a different result. The simulation quality does not seem to depend on the region anymore. Instead, the catchments with the largest cost values are distributed more equally over the land surface. With the exception of the Nile, they are confined to the smaller river catchments. The largest cost value is found for the Nile catchment with 3.99. This is comparable to a discharge peak difference of almost half a year and a relative seasonality difference of 97%. However, in most of the other catchments the simulated river discharge results in cost values below 1.27 which equal an averaged peak difference of 0.75 months and a relative seasonality difference of 13%. Looking at the differences between the dynamical wetland simulation and the control simulation, the influence of the DWES is more pronounce than seen for the NRMSE evaluation. The Amazon catchment as well as almost all catchments in Africa show a decreased cost value. However, also increased values are found for the northern hemisphere between 135°E and 120°W as well as in the central USA. The range of cost value changes lies between -0.69 (Slave River) and 0.99 (Rio Japura).

A better impression of the meaning of this evaluation can be obtained by considering the climatological river discharge curves of some rivers, directly. Figure 3.20 displays these for the catchment outlets of the rivers Amazon, Congo, Mackenzie and Nile. For the Amazon River both methods agree on an improvement of the DWES compared to the statical one and to the control simulation. The latter two ably simulate the discharge during the second half of the year. However, their peak flow is too high and occurs too early in the year. Using the DWES, the peak matches exactly and the river discharge is within the standard deviation of the observations for the greater part of the year. During the last five months the water stored in wetlands is released and causes a too high river discharge.

The simulated river discharge from the Congo catchment is overestimated for all three model versions. Thus, it can be suspected that the precipitation input is also overestimated for this region. The peak months are calculated well in all cases but the seasonality is is too strong in the control and static wetland simulations. For this reason the cost function method judges the dynamical wetland model as superior. The static wetland model is favored by the NRMSE method because the seasonality is slightly more pronounced to lower values which decreases the overall error.

The simulated discharge of the Mackenzie River catchments is evaluated to be worse for the DWES compared to the static one. Here, the static scheme is clearly superior as it simulates the peak month and seasonality better. In the DWES the influence of wetland is too strong which leads to a delayed peak and a decreased seasonality.

The Nile is an example for catchments which can not be simulated with the MPI-HM. All three simulations overestimate the amount and the seasonality of river discharge and
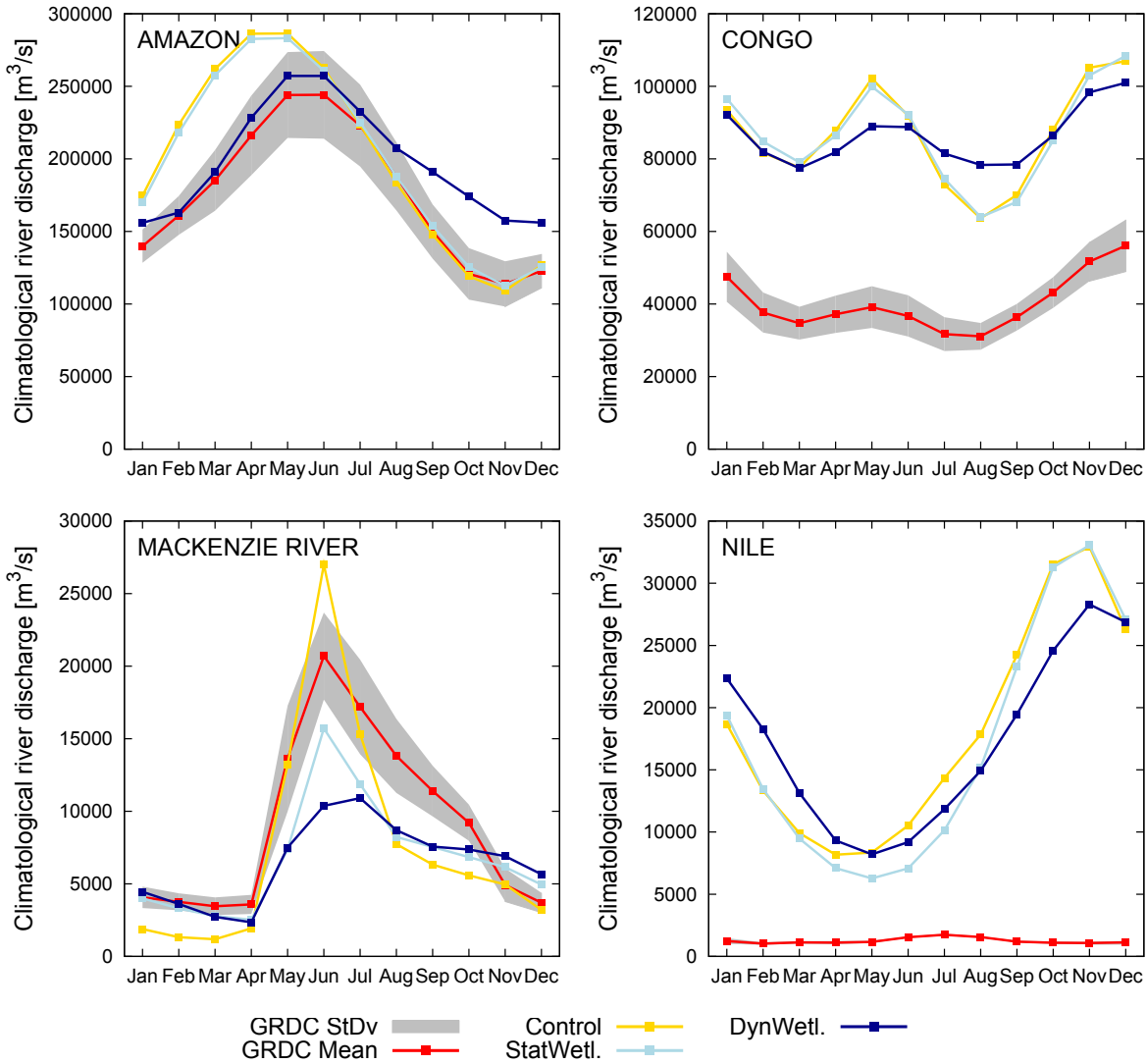
Figure 3.20.: Climatological river discharge curves for four river catchments. The observed river discharge is shown in red with its standard deviation in gray. The yellow, light-blue and dark-blue curves display the simulated river discharge of the control, static and dynamical wetland simulations, respectively.

produce the peak flow with a delay of four months. This could be due to several reasons. The most probable suspect is the Aswan Dam which stopped the yearly inundation of the downstream area and decreased the seasonality of the river discharge as well as its overall amount. As dams are not included in the MPI-HM, this missing feature is expected to have a strong influence in this region. Another process which is not yet accounted for by the MPI-HM is irrigation. In the Nile catchment water withdrawal for irrigation plays a important role. Water is diverted by numerous channels from the main stream of the Nile and transported to agricultural areas (Gohar and Ward, 2010). Additionally to this artificial alterations, the Nile crosses a huge swamp area, the Sudd, in the southern

Sudan. About half of the Nile's river discharge is expected to evaporate there (Sutcliffe and Parks, 1999). Although this swamp is simulated well by the DWES, it is possible that the simulated evaporation is too low for this region. Finally, precipitation input could be overestimated as it is already suspected for the Congo catchment.

3.4. Conclusion on model performance

The validation focused on the evaluation of wetland extent and distribution, on their seasonal variations, water level variations and on the river discharge. These were investigated from the global scale down to single grid cell output.

In summary, the validation reveals that the MPI-HM is able to simulate the distribution of wetlands on global and regional scale. The model successfully identifies the large scale wetland center regions, which are found in the global observation data. The simulated wetland fraction correlates with the observations within the same range as the observations correlate with each other. The best correlation is found for North America while the worst occurs for the Australian region.

The absolute amount of wetlands is simulated well on a global average. Generally, the northern hemisphere's wetland fraction lies within the observational range, but close to its lower limit. The southern hemisphere is strongly overestimated, especially for the Amazon and Congo catchments. This is confirmed by a detailed investigation of the average and effective wetland fractions on catchment scale. There, most northern catchments are slightly too dry while central South America and Africa are simulated too wet. Beside the difference between the hemispheres no systematic bias is evident.

The seasonal variations in wetland fraction show a realistic behavior, which reflects the northern hemisphere snowmelt as well as the movement of the Inter-Tropical Convergence Zone. Compared to a dataset of monthly wetland observation, the simulated seasonality shows are very good correlation for all grid cells with a significant signal. This results could be confirmed even on local scale for water level variations. Although the river discharge is significantly influenced by the wetland fractions in most investigated catchments, their averaged effect on the discharge simulation ability is small. About the same number of catchments are simulated with an improved river discharge signal as there are catchments simulated with decreased simulation quality. In most cases the quality decrease is confined to small catchments.

This study demonstrates that the DWES reliably simulates the extent, distribution and intra-annual variations of large scale wetlands for the larger part of the land surface under recent climate conditions. Its performance is best in mid to high northern latitudes. Although it is failing in some tropical catchments, there is no systematic bias obvious that points to failures in the DWES's simulated processes or parametrization rather then to biases in input data. Therefore, it is expected to be applicable also for simulations under different climate conditions.

4. Application of the dynamical wetland extent scheme

The MPI-HM has demonstrated its ability to simulate dynamical wetland extent in the validation chapter (see Sect. 3). If forced with reanalyzed climate data, it computes the extent and seasonality of wetlands in good agreement with observations for the larger part of the land surface. The fact that it works reliably under present day climate conditions is, however, no prove for its ability to simulate the wetland extent successfully in the past or project it into the future. Thus, in this chapter the MPI-HM is applied under different climate conditions to explore the validity range of its parameters and the DWES itself.

In the first experiment the MPI-HM is driven by Mid Holocene climate conditions. Although reconstructions of the Holocene climate are not as extensive as today's observations, it is possible to investigate whether or not the simulation results are in agreement with the state of the art paleoclimate research. Additionally, the sensitivity of the model against changes in the climate forcing variables can be estimated.

The second experiment exposes the MPI-HM to the future state of climate as projected by a state of the art climate model for different emission scenarios. Again a sensitivity study conducted for the results, and they are analyzed in terms of plausibility.

Up to now, there are only few studies focusing on the simulation of wetland extent under different climate conditions. For the Mid-Holocene these studies either use a very simple approach to estimate wetland extent (Kaplan, 2002; Kaplan et al., 2006) or are limited to regional simulations (Coe, 1997). Additionally, there is a study by De Noblet-Ducoudré et al. (2002) but the authors focus on earlier time periods.

Future wetland extent is simulated by Gedney and Cox (2003). Their findings are discussed in section 4.2.2.

4.1. Holocene simulations

4.1.1. Evidence from geological archives

Variations in the earth's climate are thought to be mainly driven by changes in the solar insolation. These insolation changes are caused by regular alterations in the earth's orbit around the sun. Milanković (1941) explored this connection and attributed the formation of the last ice ages to variations in the orbital parameters.

As direct measurements of climate variables did not exist before the development of human civilizations, proxy data are used to derive information about the climate

conditions on a regional and even global scale. Proxy data are based on still measureable conditions which are known to be influenced by temperature or precipitation. They are usually derived from pollen or tree ring analysis, lake sediment composition, isotope ratio of ^{16}O to ^{18}O in ice or sediment cores and many more (e.g. Häckel, 2008).

A good review about the state of the art in paleoclimatic research for the Holocene is given by Wanner et al. (2008) and some points are summarized in the following paragraph. Focusing on summer insolation, the authors stated that its maximum occurred around 11000 years before present (yBP). At this time parts of North America were still covered by extensive ice sheets which cooled the climate till 9000 yBP when the ice sheets became too small to affect climate on a large scale anymore. The maximum warming lasted till around 5000 yBP, before the effect of the decreasing northern summer insolation led to a global decrease in temperature, again. The warming period had a significant influence on the temperature contrast between continents and oceans and caused strong summer monsoons. This induced changes in the precipitation patterns.

Most interesting for the present study are reconstructions of the Holocene lake and wetland distribution to compare them against the simulation results. Wanner et al. (2008) compiled a map showing the state of lakes during the Mid Holocene (see Fig. 4.1). The
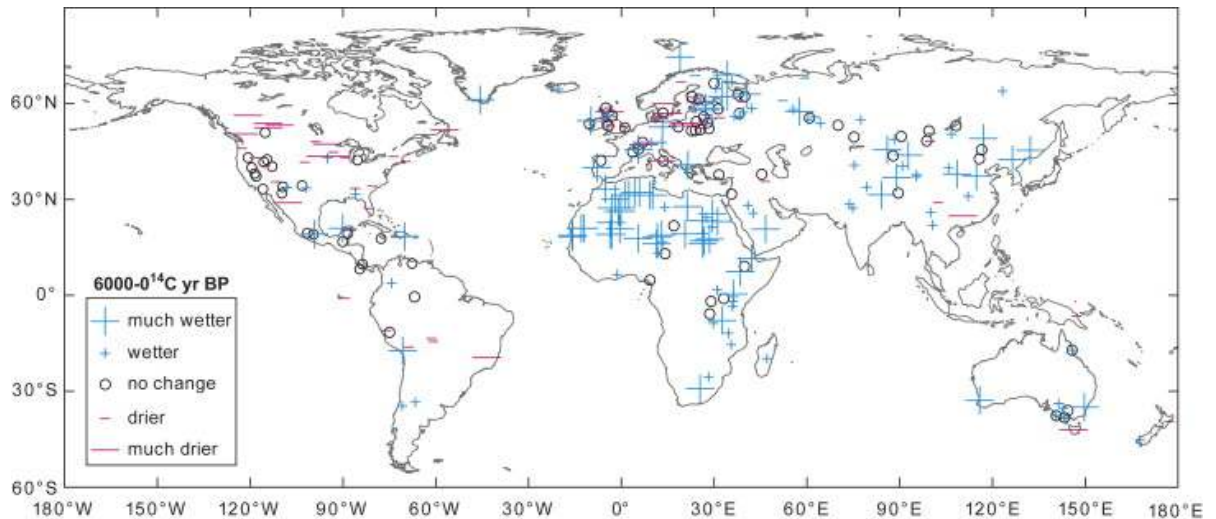
Figure 4.1.: Change in global lake levels at 6000 yBP compared to present-day (Wanner et al., 2008).

most obvious changes to today are much wetter conditions in the Sahara and southeastern Asia, while central North America and parts of Europe and South America appear to be drier. Liu et al. (2004) investigated this change using a coupled atmosphere-ocean model. They found a strengthening of the monsoon on the northern hemisphere which increased precipitation in the tropical regions. In contrast, the southern hemisphere monsoon became weaker, and, therefore, the precipitation in the respective regions was reduced. The altered monsoon patterns were caused by the changes in insolation as well as oceanic feedbacks. Due to a northwards shift of the ITCZ on the American continent, which was simulated by Harrison et al. (2003), the central part of South America became

drier. The authors argued that the enhanced convection in the monsoon area of central America lead to subsidence and therefore decreased precipitation in Northern America. These changes were reflected by the reconstructed lake level changes displayed in figure 4.1.

4.1.2. Holocene climate forcing for the MPI-HM

In order to test the MPI-HM under Holocene climate conditions, global fields of daily temperature, precipitation and PET are necessary as input for the MPI-HM for this period. As there is no global observation or reanalysis data available, temperature and precipitation must be extracted from climate model data. For this study, a climate model simulation was chosen which was generated in the framework of a study by Fischer and Jungclaus (2011). They conducted a transient model simulation for the last 6000 years – Mid Holocene to today – using the coupled earth system model ECHAM5/JSBACH/MPI-OM. Beside the orbital forcing, the authors did not include any other external forcing and set the greenhouse gas concentration to pre-industrial values for the whole simulation period.

In respect to surface temperature compared to today, they found an increase at middle and high latitudes and a decrease at low latitudes during the Mid Holocene due to the higher summer insolation. The negative temperature anomaly in the tropics was caused by an increase in cloud cover and latent heat flux. In an earlier study Fischer and Jungclaus (2010) stated that this, together with the increased vegetation cover, lead to an intensification of the hydrological cycle and caused more precipitation in these regions. Fischer and Jungclaus (2011) also compared their findings against temperature reconstructions for Europe. While the results agreed with reconstructions for some seasons and regions, they found the most important discrepancy for southern European summer temperatures where the model failed to represent the expected negative temperature anomaly. However, the model performed much better on the global scale as it showed a similar response of zonal temperature gradient to insolation forcing as it was seen in the reconstructions. This result demonstrated the ability of the ECHAM5/JSBACH/MPI-OM model to simulate Holocene climate.

From this model simulation 6 timeslices of 35 years each are extracted to generate the climate forcing data needed by the MPI-HM. They range over the time period from Mid Holocene (6000 yBP) to today. As the climate model does not archive fields of PET, it had to be calculated separately. This is done similarly to the study by Weedon et al. (2011) using the Penman-Montheith equation for reference crop evaporation as PET surrogate. All applied equations were summarized by Allen (2001). Here, the Penman-Montheith evaporation ET_{PM} is given as

$$ET_{PM} = \frac{\left(\frac{\Delta(R_n - G) + k_t \rho_a c_p \frac{e_s - e_a}{r_a}}{\Delta + \gamma \left(1 + \frac{r_s}{r_a}\right)} \right)}{\lambda} \tag{4.1}$$

where R_n is the net radiation at the surface, G is the soil heat flux, e_s is the saturation vapor pressure, e_a is the actual vapor pressure, ρ_a is the mean air density, c_p is the specific

heat of air, Δ is the slope of the saturation vapor pressure curve, γ is the psychrometric constant, r_s is the surface resistance, r_a is the aerodynamic resistance, λ is the latent head of vaporisation and k_t is a constant for unit conversion. The computation of ET_{PM} needs daily mean values of 6 variables from the climate model which are surface pressure, surface temperature, surface dew point temperature, 10 m wind speed, net surface shortwave radiation and net surface longwave radiation. These variables can be converted into those needed by equation 4.1 with the equations provided by Allen (2001). The calculation is conducted at the original 3.75° resolution of the climate model. The resulting PET field together with the temperature and precipitation data are remapped conservatively onto the 0.5° resolution of the MPI-HM.

Figure 4.2 displays the anomaly between the Mid Holocene climate forcing to today. The temperature and precipitation anomalies show the patterns which are explained by Fischer and Jungclaus (2010, 2011). The PET is increased globally except in the tropics. There, the decreased surface temperatures and the increased cloud cover constrain it to lower values than today. The difference between precipitation and PET gives the minimum amount of water that is available at the surface for runoff or storage recharge. Compared to today, during the Mid Holocene a pronounced water surplus is seen around the equator for Africa and also for India. Almost all other regions experience a water deficit, which is strongest in South America and central USA.

In the optimal case the MPI-HM boundary conditions of every time slice should be adapted to Holocene conditions, too. Obviously, this includes the vegetation cover, permafrost fractions and glacier masks but also soil characteristics and river routing directions. While proxy data exists for some of these variables, they are too sparse to convert them into robust, gridded boundary files for the MPI-HM. Therefore, the same boundary conditions that were already used for the validation are applied again for the Holocene simulation. It is expected that this inconsistency affect the simulation results and maybe decrease the agreement between the simulated wetland extent and reconstructions of lake extent. Nonetheless, the influence of different climate forcing data on the DWES is visible in the results, and thus the sensitivity of the MPI-HM to climate change can be estimated.

4.1.3. Simulation analysis

Altogether this sensitivity study comprises 14 simulations by the MPI-HM. The first model integration is carried out from 36 yBP to 0 yBP to provide a baseline simulation for present-day climate. The next six model runs are scenario simulations. They start at every full millennium before today and last for 35 years. All time slices are conducted twice, first with the MPI-HM including the DWES and then again without considering wetlands at all. This second set of simulations serves as a control simulation series and are used to explore the impact of the DWES on river discharge and ET. Thus, it can be estimated whether there is a significant effect of the dynamical wetland simulation on the hydrological cycle.
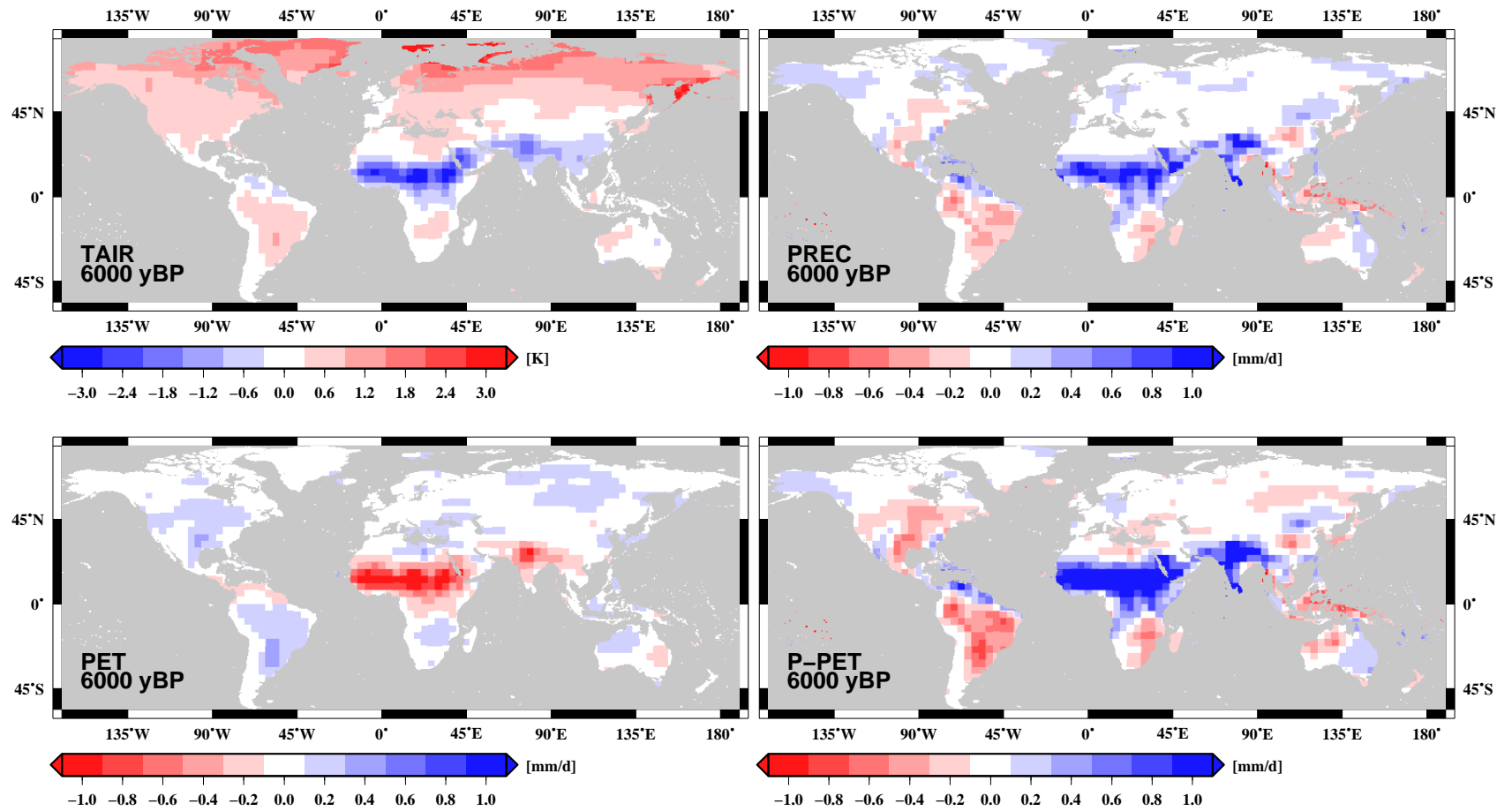
Figure 4.2.: Anomalies in the mean climate forcing for Mid Holocene compared to today. The panels display the anomalies for the 2m surface temperature (top left), total precipitation (top right), the externally calculated PET (bottom left) and the balance of precipitation and PET (bottom right) remapped to 0.5° resolution. The temperature and precipitation data were extracted from a simulation conducted by Fischer and Jungclaus (2011).

Analysis of time slices

Every simulation is initialized with the same restart files. In all cases the wetland fraction and surface water storage is set to zero, thus forcing the model to include a spin-up period. In the results the evolution of these fields is checked to ensure that the spin-up time is omitted from the simulation analysis. Agreeing with former investigations (see Fig. 2.17), the storages and the wetland fraction are found to stabilize within the first five years of the simulation as shown in figure 4.3 for the Mid-Holocene and the baseline time slices. The storage contents and wetland fraction of the remaining time slices are shown
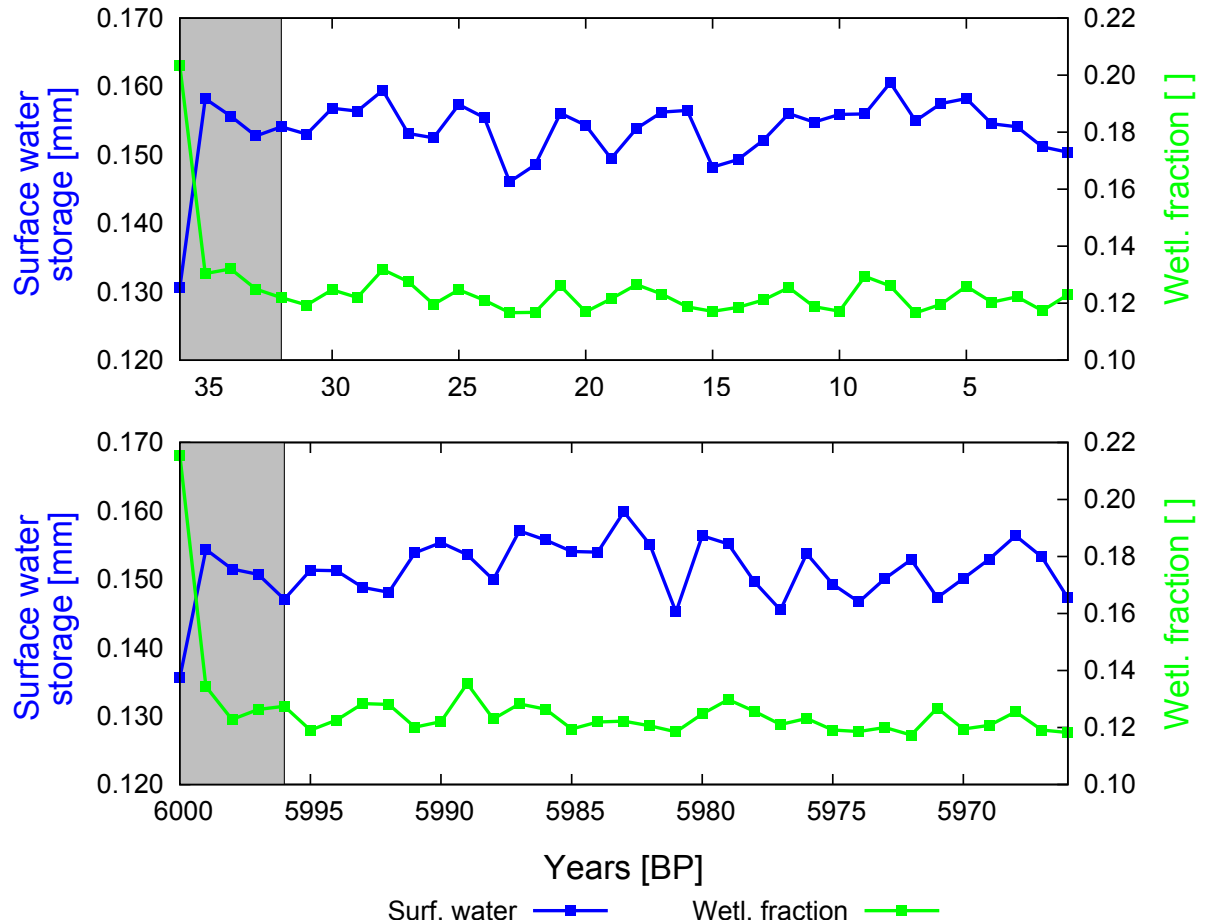
Figure 4.3.: Evolution of the annual mean land surface water storage and wetland fraction for timeslices at 0 (top) and 6000 yBP (bottom). The gray areas indicate years which are omitted from the analysis because of their spin-up behavior.

in figure B.5. The strongest effects are visible for the wetland fraction and the surface water storage. All other storages are already initialized by former MPI-HM simulations and adapt much faster to the altered climate forcing.

First, it is investigated whether the simulated wetlands change gradually between Mid Holocene and present-day or develop a more complex behavior. Figure 4.4 displays the mean land surface anomalies of wetland distribution, wetland soil moisture and surface

water for every timeslice. At 6000 yBP all variables have higher values compared to
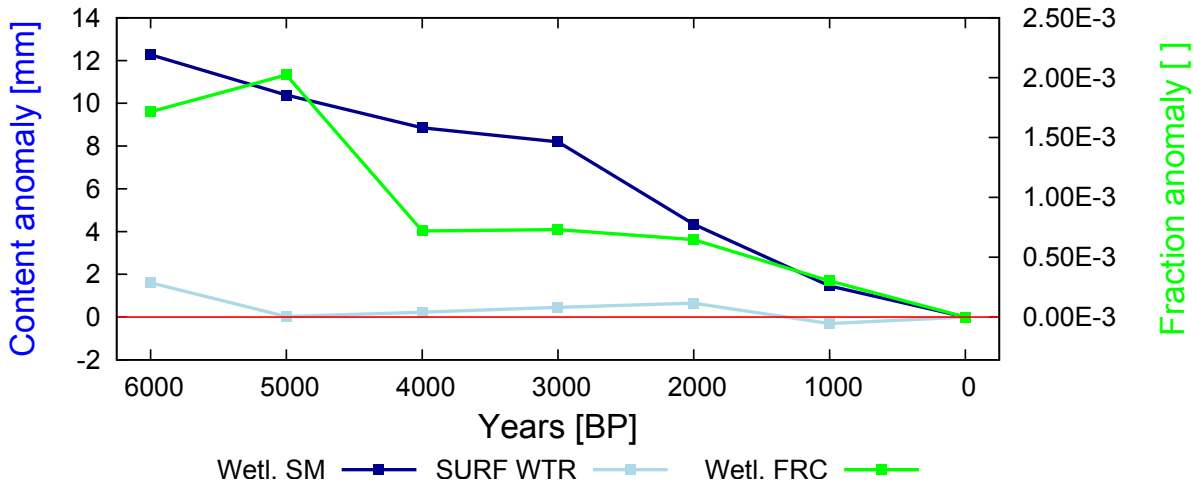
Figure 4.4.: Mean land surface anomalies of wetland soil moisture (Wetl. SM), surface water level (SURF WTR) and wetland fraction (Wetl. FRC) for all simulated time slices.

today. With a mean decrease of 12 mm until present-day the wetland soil moisture reacts strongest to the changed climate conditions. The surface water curve has a similar shape but only drops by about 2 mm. In contrast, the wetland fraction anomaly increases slightly until 5000 yBP, and then is reduced by half at 4000 yBP. It stabilizes there for 2000 years and finally drops to zero. The overall average anomaly in wetland fraction is 0.002. Both, wetland soil moisture and extent, remain comparatively stable between the initial and the final value decrease.

The shape of the curves indicates that the wetland dynamics do not just scale the wetlands extent to the mean state of the climate. Instead, they react very specific to regional conditions. The stabilization phase between 4000 yBP and 3000 yBP can be explained by an analysis of the separate hemispheres (see Fig. B.6). Indeed, the northern hemisphere shows an almost linear decrease for all anomalies. For the southern hemisphere, however, the wetland variables during Mid-Holocene are at much lower values than today. They increase strongly, showing a peak around 2000 yBP and then converge against their present state. This increase counteracts the linear northern hemisphere's wetland decrease in the global average. Although the anomalies on both hemisphere are of a similar magnitude, the southern hemisphere's wetland increase leads only to a global stabilization as the southern land area is much less than the northern one. The reason for the more complex changes on the southern hemisphere is the different timing of the wetland fraction change in South America, South Africa and Australia.

Global wetland distribution during Mid-Holocene

The next part of the analysis focuses on the spatial distribution of the simulated differences between the Mid Holocene and present-day model results. It focuses on the soil moisture and surface water of wetlands as well as on their overall grid cell fraction. Figure 4.5

displays the anomalies for these variables averaged over the last 30 years of both time slices. Before the results are discussed is should be noted that for some fields the original resolution of the climate forcing is still visible in the MPI-HM output. Here, the boundary condition necessary for the calculation of the respective fields are almost spatial homogeneous and, thus, do not introduce many fine scale processes. Among others, this is true for soil moisture and ET. In contrast, some fields like the surface water depth or the wetland fraction rely much stronger on fine scale information and result in a thoroughly downscaled field. This indicates that the MPI-HM does not utilize its high resolution for every process. This might be due to the formulation of the respective processes themselves or caused by the unavailability of appropriate boundary data.

The wetland soil moisture and surface water anomalies (see Fig. 4.5) reflect the P-PET anomaly in the climate forcing data (see Fig. 4.2) very well for most regions. The central parts of North and South America as well as southeastern Africa and western Australia become much drier while eastern Australia, the Tropics north of the equator and the Eurasian mid latitudes become wetter. On average, the wetland soilmoisture increases by 18.2 mm in wet areas and decreases by -5.9 mm in dry areas compared to today. The surface water depth shows an averaged increase of 6.4 mm and a decrease of -4.8 mm in the respective regions. In contrast to these two fields, the anomaly of wetland fractions does not directly match with the climate forcing data. Its overall response is very weak with an average increase of only 0.006 and a decrease of -0.005 in wet and dry areas, respectively. As the increase is strongest around the Sahel region and the decrease concentrates on the American continents, the large scale patterns agree with the anomalies in the climate forcing data. In order to verify the validity of these results, the significance of the anomaly is investigated using the Student's t-test as described in Press et al. (1992). Here, the t-value t is calculated for every grid cell GB of two time slices i and j as

$$t = \frac{\overline{GB_i} - \overline{GB_j}}{s_D}, \text{ with} \tag{4.2}$$

$$s_D = \sqrt{\frac{\sum_{i=1}^{N_i}\left(GB_i - \overline{GB_i}\right) + \sum_{j=1}^{N_j}\left(GB_j - \overline{GB_j}\right)}{N_i + N_j - 2}\left(\frac{1}{N_i} + \frac{1}{N_j}\right)} \tag{4.3}$$

where s_D is the standard error of the difference of the means of every grid cell and N is the population size. In this case, N equals the number of time steps in the respective time slices. It is found that the simulated anomalies of wetland soil moisture, surface water level and wetland extent are highly significant in almost every grid cell.

However, in some areas the wetland fraction change appears to contradict the surface water level anomaly. In Scandinavia, for example, the surface water level decreases while the actual wetland fraction is increased. The opposite is true for parts of Brazil. These examples demonstrate the influence of input variability on the equilibrium approach that is the basis for the DWES (see Sect. 2.3.1). Instead of using a fixed relation between surface water level and wetland extent, the DWES relies on finding an equilibrium state between the incoming and outgoing water fluxes in the grid cell. The first approach would inevitably result in an oscillation between large and deep wetlands as well as
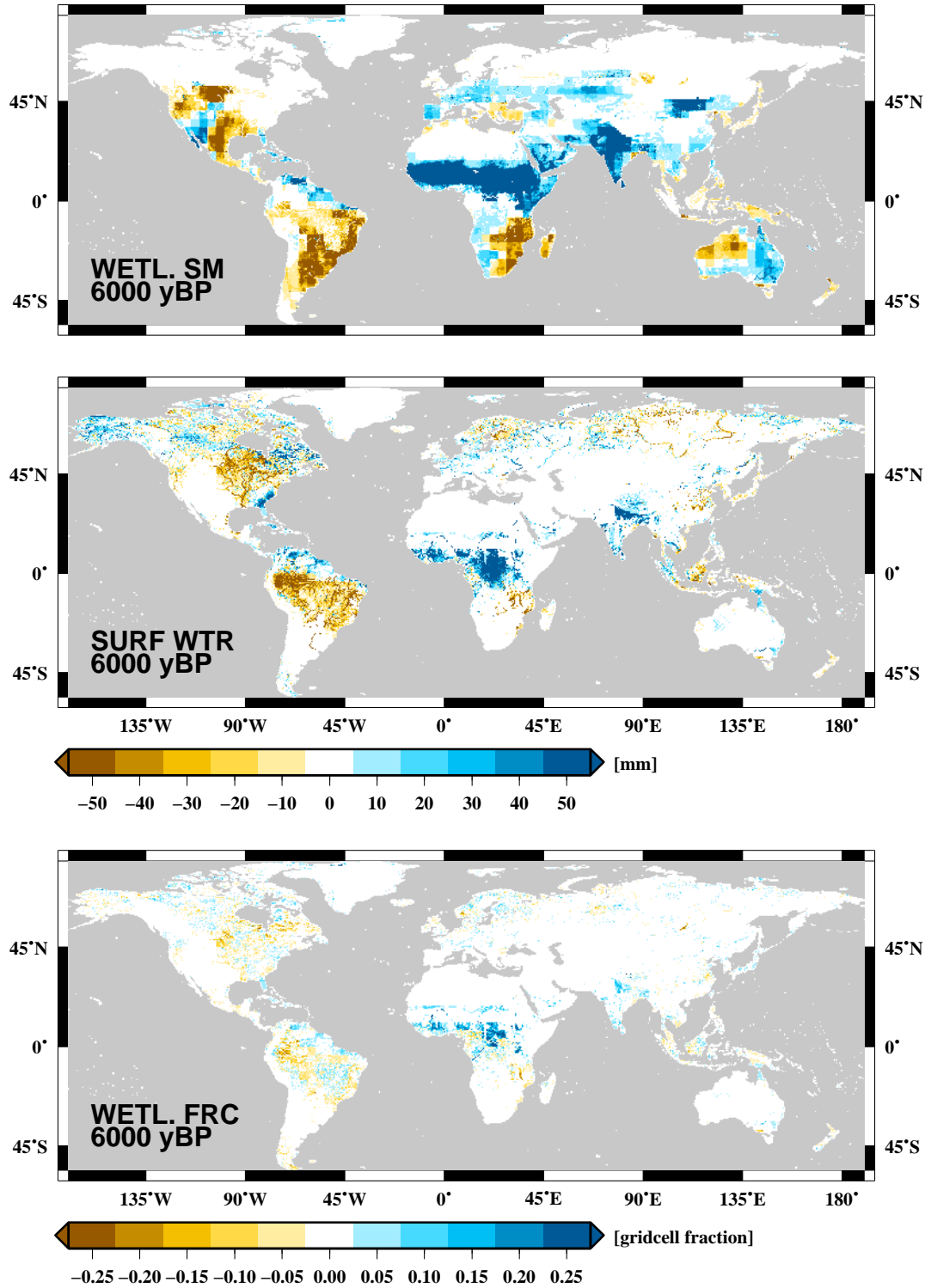
Figure 4.5.: Simulated anomalies for mean Mid Holocene compared to today. The panels display the soil moisture below wetlands (top), their surface water level (middle) and the wetland fraction (bottom).

4. Application of the dynamical wetland extent scheme

small and shallow wetlands in phase with the variability of climate forcing. In contrast, the latter approach reacts differently to variability. An increase in variability leads to flooding events rather than to long term sustainable wetlands. This results in a shallow inundation which spreads fast but is not stable. Instead, the surface water soon drains into the soil or evaporates. In contrast, decreased water input variability allows for stable wetlands which are in equilibrium between water inflow and outflow. Figure 4.6 illustrates that in Brazil and Scandinavia the inflow variability switches from one state into the other between Mid-Holocene and today. In Brazil during the Mid Holocene the
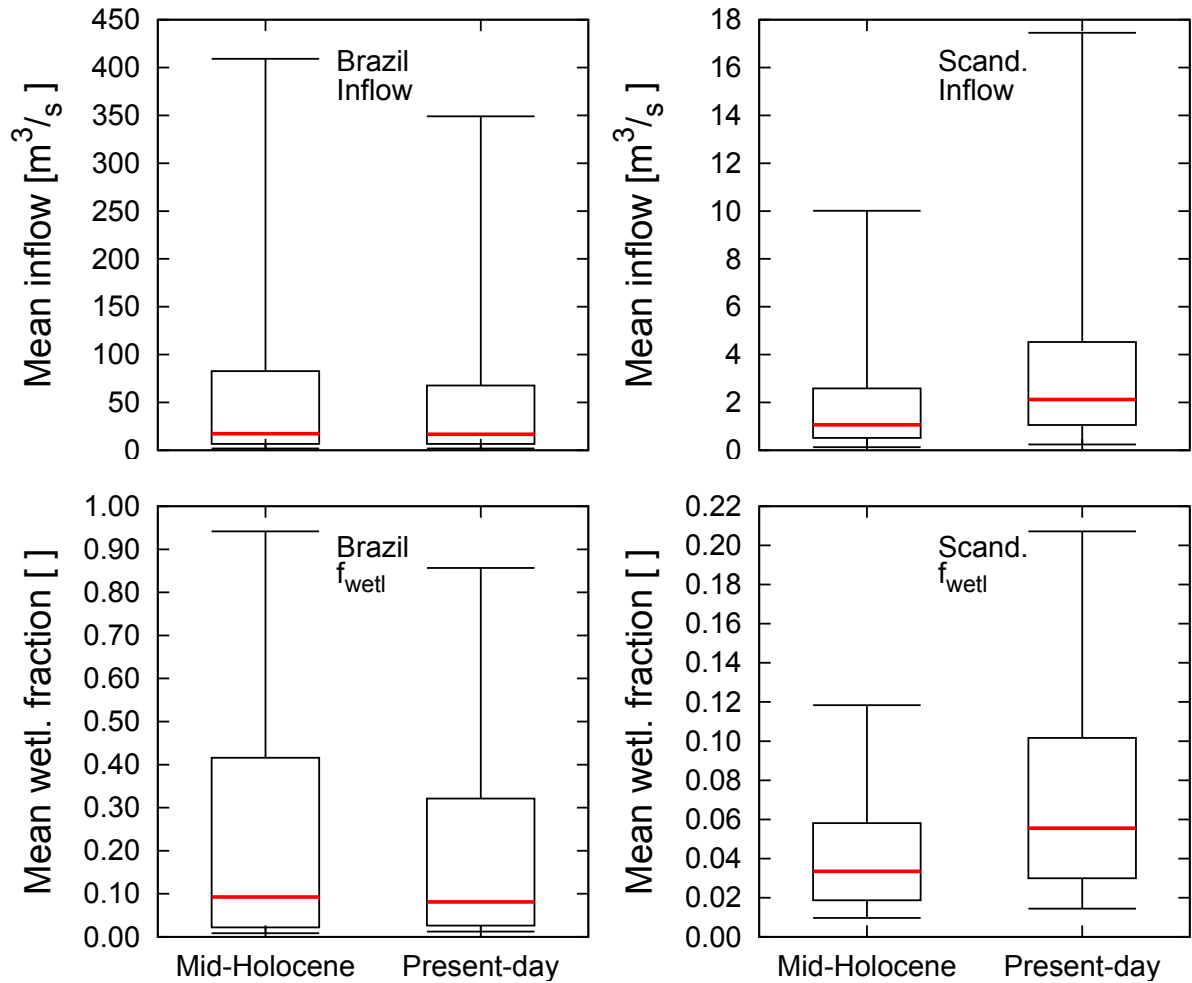
Figure 4.6.: Boxplots of grid cell inflow and wetland fractions for Brazil and Scandinavia. The red line indicates the median of the daily values, the box indicates the 25th and 75th percentile, and the whiskers indicate the 5th and 95th percentile.

simulated wetlands appear to be shifted towards an episodic, inundation like character while they change into more stable wetlands today. In Scandinavia the change goes into the opposite direction.

The possibilities to validate the simulation results are very limited. On a global scale

it is possible to compare the water level anomalies between Mid-Holocene and today to the map of Wanner et al. (2008) (see Fig. 4.1). Here, the general patterns in both agree well. The Mid-Holocene's lower lake levels in the centers of North and South America as well as China are visible in the model results. Also the simulated higher levels in Central America, the Sahel and India are confirmed by the reconstruction. In detail, however, some difference are seen for the African continent. The simulated lake level increase in Africa is shifted about 20 degrees to the South. Additionally, a lake level decrease can be seen around Mozambique. Furthermore, in Central Asia the simulation mostly lacks the reconstructed lake level increase.

These differences can be largely explained by the climate forcing data. In Africa, already the precipitation field of the climate model does not spread as extensively into the Sahara as suggested by the reconstruction. Here, also the drier conditions in southeastern Africa are visible which are reflected by a simulated soil moisture decrease in the MPI-HM. Further discrepancies are introduced by the calculated PET field as the Penman-Montheith equation assumes very specific surface conditions. In agreement with Weedon et al. (2011), PET is calculated for the reference case of well-watered, 12 cm high grass. As this land surface parametrization is not met everywhere, the real PET deviate from the calculated value. This simplification might be the cause for the simulated decrease in water levels, for instance, in northern Siberia.

While the simulated wetland soil moisture anomaly reacts very sensitive to the precipitation input, the response of the surface water field is comparatively weak in Northern Africa. Looking at the absolute ratio of soil moisture saturation (see Fig. B.7), it becomes obvious that in spite of the soil moisture increase the soil north of 10°N is not saturated. Therefore, no water is stored on the surface to form wetlands. In more detail this can be seen for the example of the West Nubian Lake basin in northwestern Sudan. Based on satellite surveys and fieldwork, Pachur and Rottinger (1997) stated that a large lake with about 15000 km^2 surface area covered this basin from the Early- to the Mid-Holocene. As figure 4.7 displays, a soil moisture increase is indeed simulated in this area. However, there is too less water for the formation of wetlands. The small wetland fraction which is found in the model indicates more likely episodic flood events rather than small but stable wetlands.

There are two possible explanations for the MPI-HM's inability to simulate wetlands in North Africa. On the one hand, the soil characteristics of this region might be incorrectly parametrized. In this region, the soil storage is very small resulting in high relative soil moisture values even for minor precipitation event. As the drainage and ET calculations are scaled with relative soil moisture, the small soil storage promotes a fast transition of its water content into these fluxes. Thus, the soil is not saturated long enough to enable the formation of wetlands in the model. Furthermore, the MPI-HM uses a simple bucket scheme as realization of the soil storage. Introducing a scheme with several layers would distribute the moisture throughout the soil profile instead of filling it up from the bottom and, thus, could promote the formation of wetlands. On the other hand, the calculated PET could be the cause for the low soil moisture. Li and Morrill (2010) proposed that the raised lake levels were due to increased precipitation and decreased evaporation caused by lower insolation and increased cloud cover and humidity. While the climate model
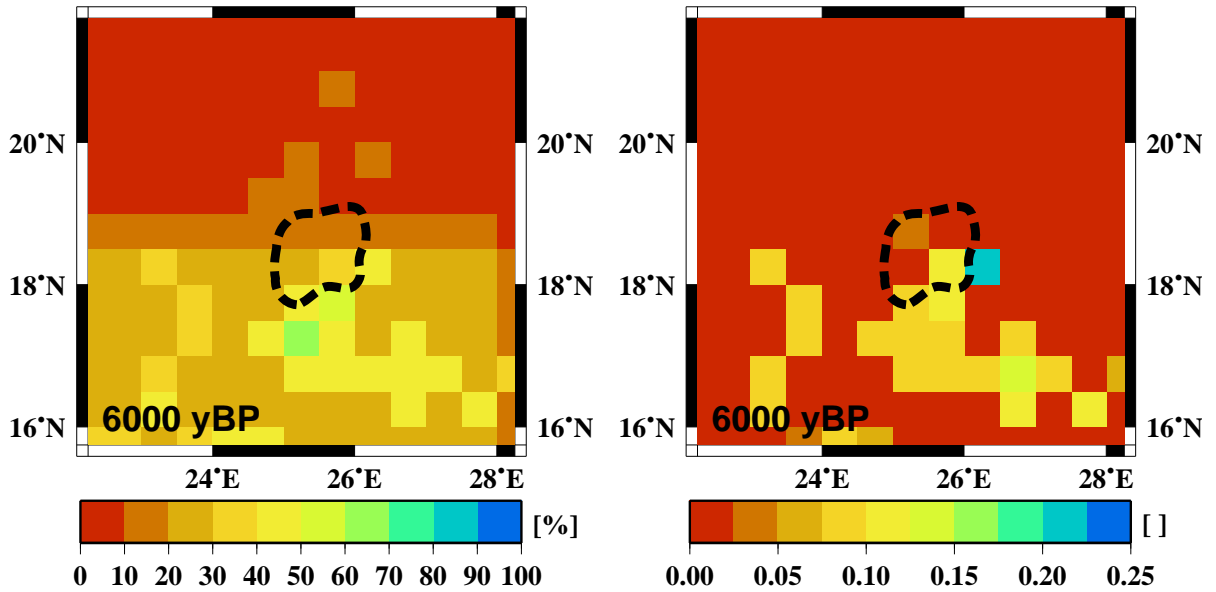
Figure 4.7.: Relative wetland soil moisture (left) and wetland fraction (right) at the estimated position of the West Nubian Lake (black dashed outline, Pachur and Rottinger, 1997) during Mid-Holocene.

considers these factors in the range valid for wet soil, the cloud cover and air humidity would increase much stronger in case the climate model would know about wetlands (Coe and Bonan, 1997). Then a feedback might occur which would reduce the evaporation and might allow for the development of stable lakes in this region. In order to verify this hypothesis it would be necessary to implement the DWES into the climate model.

Additionally to the inherent wetland variables, the change in river discharge is analyzed. Figure 4.8 demonstrates that the river discharge reflects most of the overall moisture changes which are indicated by the lake level reconstructions. One exception is South Africa, where a river discharge decrease is simulated for the Mid-Holocene while the reconstructions indicates a lake level rise.

For all catchments, the simulated river discharge change reflects the input data anomaly. On average more water is available for the river discharge. The strongest effects are seen for northern Africa with a maximum of about 600% increase for the Blue Nile during the Mid-Holocene time slice. The most intense decrease is found for the centers of North and South America. Here, the river discharge is reduced by almost one third.

As this result demonstrates, the river discharge change is strongly dominated by the climate input. It remains unclear to what extent the simulated wetlands might play a role for the river discharge anomaly. This question are discussed later during this chapter.

Regional analysis of lake level changes

While the lake level reconstructions are sparse on a global scale, some studies generated detailed reconstructions about local climatic changes during the Holocene. In this section
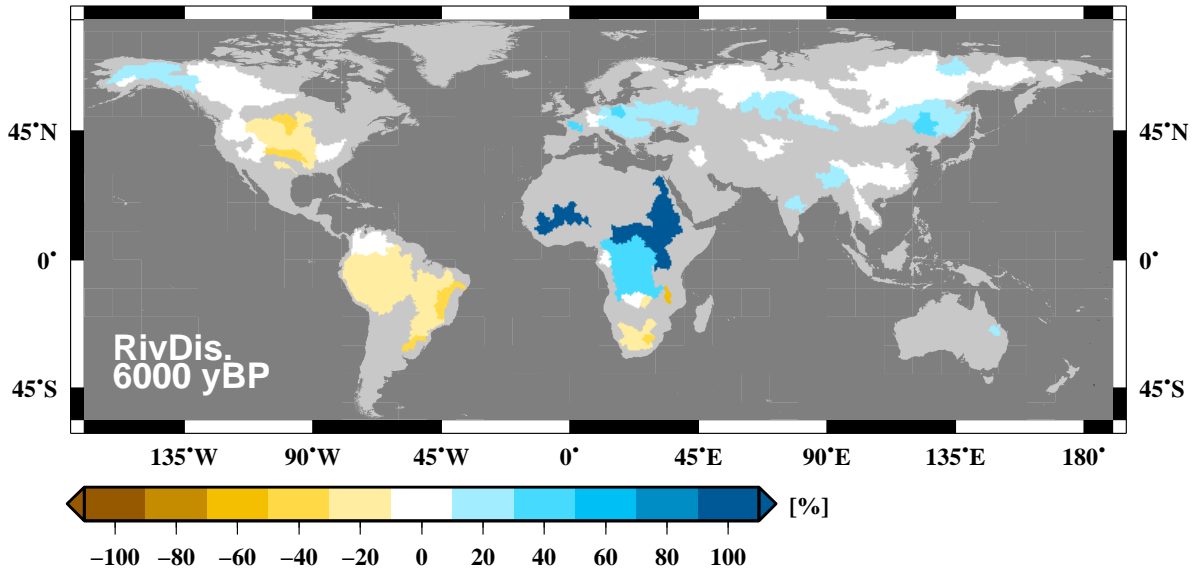
Figure 4.8.: Relative change of mean river discharge at catchment scale for the Mid-Holocene compared to today.

some of the local lake level reconstructions are compared against the simulation results. The comparison of averaged grid cell data against local point data is very problematic. For present climate condition is has been shown in section 3.3.1 that for some lakes a good correlation is visible between observation and simulation. However, the range of variation is usually underestimated.

First, the area around the Grenadier Pond at western shore of Lake Ontario (North America) is investigated. The simulated water level (see Fig. 4.9) shows a steady increase throughout the whole simulation period. Two periods are visible with elevated rise from 3000 yBP to 2000 yBP as well as from 1000 yBP to today. Based on pollen and makrofossil analysis, McCarthy and McAndrews (1988) confirm the overall rise. They reconstructed two events with strong increase at 3000 yBP and 2000 yBP. The latter of these was also reported by Finkelstein et al. (2005) for another wetland at Lake Ontario and is visible in the simulation data, too. Additionally, they found hints for a more recent lake level rise which coincides with the second simulated rise.

Another reconstruction is available for the Braamhoek wetland in southeastern Africa. Here, the simulated surface water level is very low. The lake level is increasing towards today with two peaks at 3000 yBP and 1000 yBP. A study by Norström et al. (2009) revealed relatively dry conditions within the wetland till 4000 yBP, shifting to wetter conditions after 1500 yBP. However, they reported a very low sampling resolution for this time period. The model agrees on the general trend with drier conditions in the middle Holocene and increasing water level towards present-day. However, it shows a relatively smooth transition instead of a shift in the data. The 1000 yBP peak could be interpreted as indicator of increasing moisture but it hardly exceeds the variance of the time series.

High resolved lake level data for the period 10000 yBP until 1000 yBP were reconstructed for Lake Cerin in eastern France by Magny et al. (2011). They found centennial fluctuation of shallow levels until 4000 yBP. Following a small increase, the water level stabilized between 3000 yBP and 1000 yBP. From this it had to increase again to reach the present-day lake level. The simulated water level agrees with these findings until 3000 yBP. However, instead of stabilizing and finally rising again, the level decreases. Contrary to the reconstruction, the MPI-HM calculates a lower lake water table for present-day than for the Mid-Holocene at the Lake Cerin grid cell.

Finally, the Tso Kar basin in the northwestern Himalayas is investigated. Here, the MPI-HM simulates a continually decreasing water table with two stabilization phases between 4000 yBP and 3000 yBP as well as 2000 yBP and 1000 yBP. A study by Wünnemann et al. (2010) confirms the decreasing trend. For the Mid- and Late-Holocene they reported very shallow fluctuations with two minor lake level recoveries at similar intervals as the stabilization phases calculated by the MPI-HM.

The comparison of these four sites shows a good correlation for Grenadier Pond and the Tso Kar basin. The Braamhoek wetland water level variations are at least simulated with the correct trend. However, Lake Cerin's water table is not captured by the model. For several reasons, the four examples do not allow to draw a valid conclusion about the hindcast performance of the MPI-HM on local scale. First, the water level variations are not solely caused by climatic forcing. Sometimes, tectonic processes can be of major importance, e.g. isostatic rebound in case of the Grenadier Pond or earthquakes at the Tso Kar basin which significantly alter the landscape and riverflow. Furthermore, most reconstructions show strong fluctuations of the lake levels on scales of centuries. Neither are the 30 years time slices long enough to smooth the fluctuations, nor is the number of simulation sufficient to capture these. Nonetheless, the comparison indicates that the MPI-HM might be able to reproduce the trends in the lake level development between Mid-Holocene to today. More time slices are necessary to verify the robustness of this assumption.

Impact of dynamical wetlands on climate simulations

Finally, it is investigated how strong the DWES affects the model results in comparison to a simulation without considering wetlands. Thus, the analysis' focus shifts from investigating the effect of climate change on the state of wetlands to an estimate of how strongly wetlands might feedback to climate. This research question requires a control simulation series which does not calculate any wetland interactions and considers the wetland fraction as normal land cover. Instead of excess water remaining on the surface over saturated soil in the DWES, this surplus is simply added to the surface runoff for the control simulation. The following analysis focuses on the effect of the wetland implementation on evaporation and river discharge as these two variables would act as feedback paths in a fully coupled climate system.

Figure 4.10 displays the simulated differences between the dynamical wetland simulation and control simulation for the Mid-Holocene. The application of the DWES generates an increased grid cell ET for most grid cell areas compared to the control simulation. As
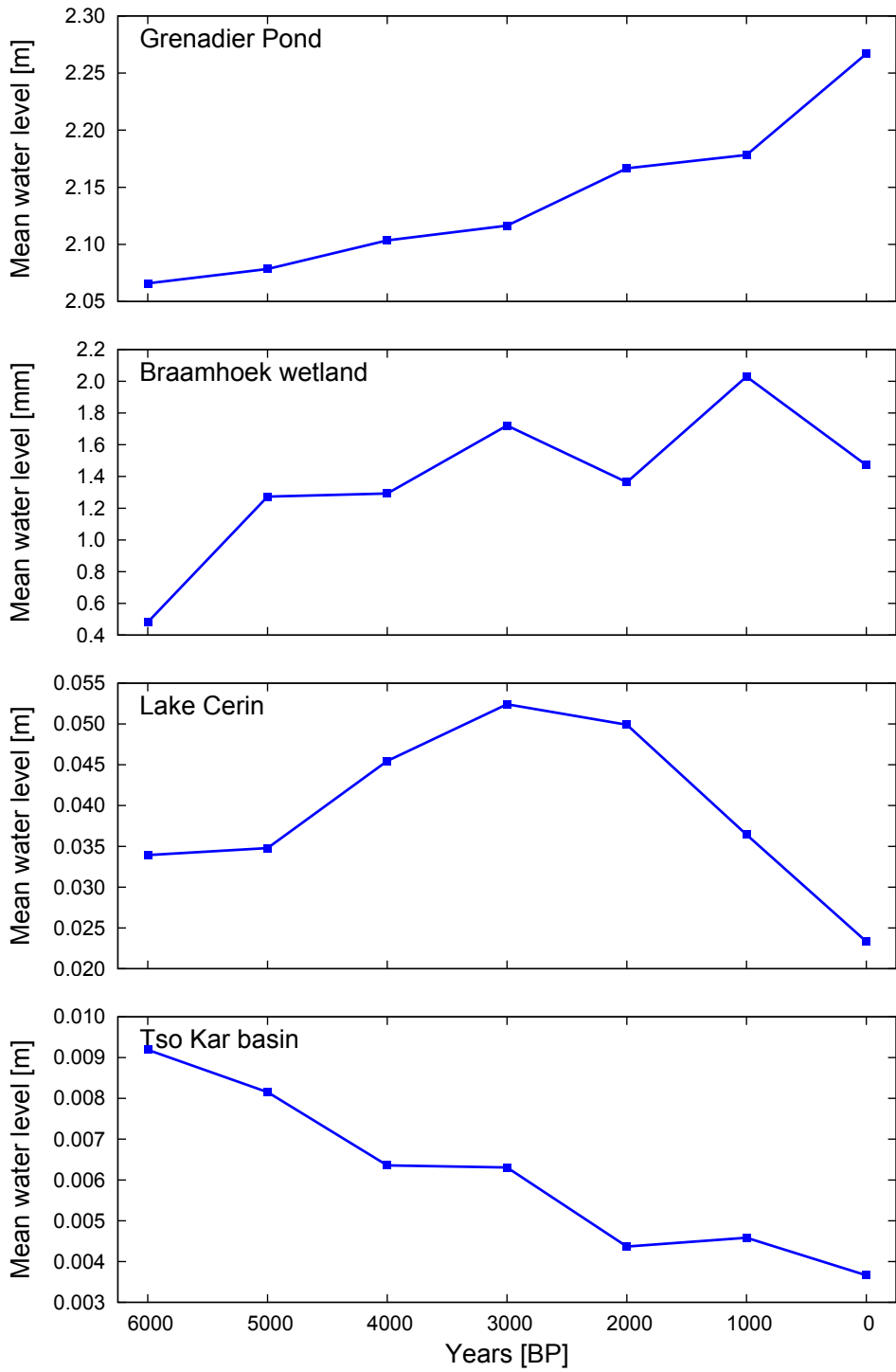
Figure 4.9.: Simulated mean surface water levels for the Holocene time slices at different locations.
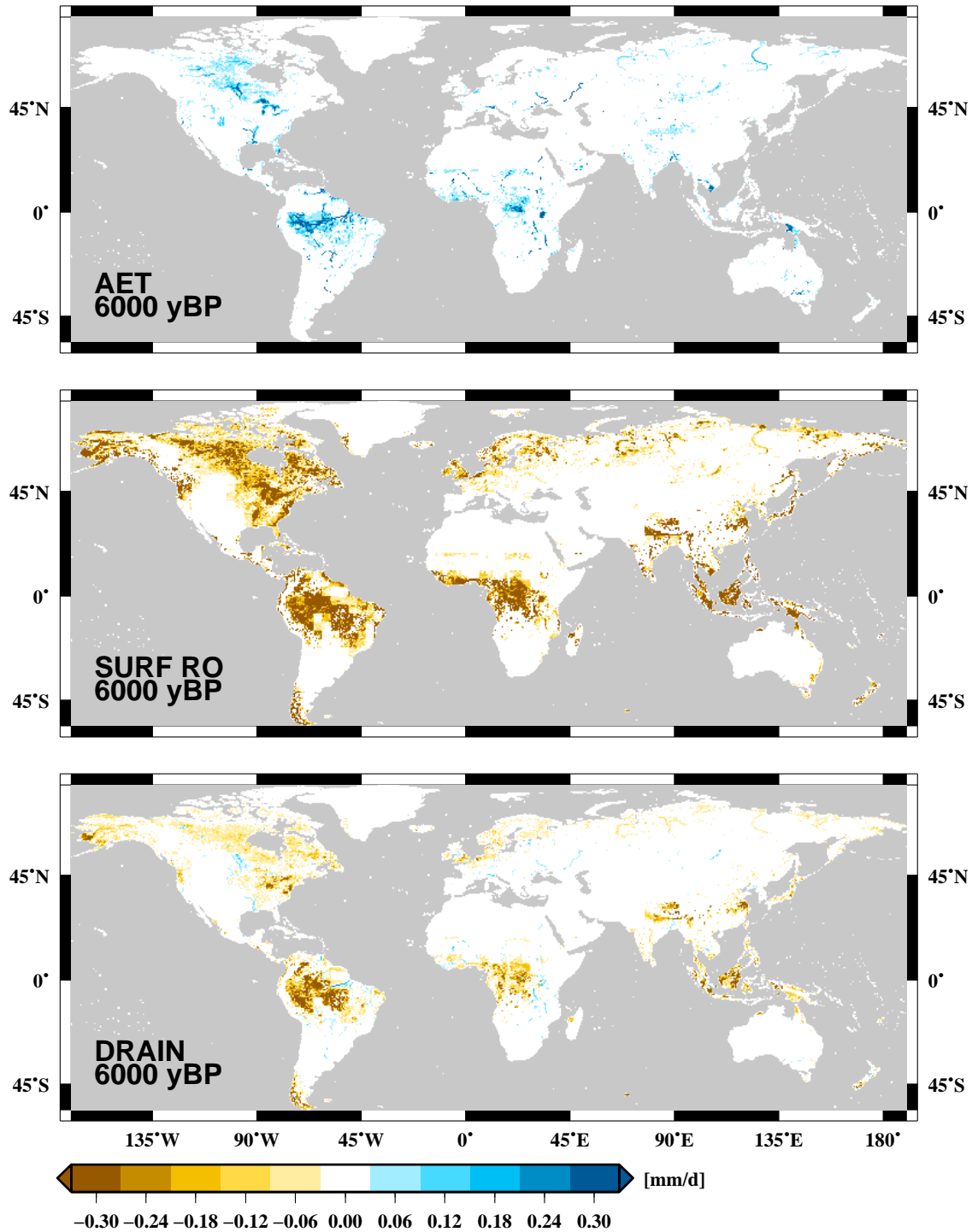
Figure 4.10.: Simulated difference between 30 year means of the dynamical wetland simulation and the control simulation without any wetlands during Mid-Holocene. The panels show the average grid cell ET (top), the surface runoff (middle) and the drainage (bottom).

water is stored on the land surface in wetlands, it is longer available for ET instead of being lost to surface runoff. On average, this increase adds up to 0.03 $^{mm}/_d$ with local maxima about 0.5 $^{mm}/_d$ in the Amazon catchment. Comparing these values to the total ET change between the Mid-Holocene and the present-day time slice, the DWES accounts for 1.6 % of the average simulated ET increase during the Mid-Holocene. Subsequently, the surface runoff is reduced in all grid cells which contain wetlands. Especially in the high northern latitudes and the tropics, the reduction appears to exceed the additional ET. In such regions the soil is saturated for both simulation types and, thus, the ET shows less or no increase. However, the surface water now takes the pathway via the wetlands into the river network and is not visible in the surface runoff output anymore. Therefore, the apparently too strong reduction is a rather technical artifact and does not influence the overall simulation results. In other areas like the Amazon outlet, ET is increased without the respective reduction in surface runoff. Here, water from the river storages enters the wetland storage and is subject to ET, again.

Additionally, changes are visible in the drainage field, too. In most regions the drainage is decreased for the same reason as they are found for the surface runoff. Locally, however, the drainage is increased by the dynamical wetlands. Here, additional water is transported into the area by river flow leading to the formation of wetlands which provide additional water to drainage and ET. In the control simulation this process is not possible because water that once entered the river flow storage is removed the vertical water balance.

Also the river discharge is affected by the DWES as the scheme interacts with ET, surface runoff and drainage as well as directly with the river flow storage. The relative differences in river discharge between both simulations are presented in figure 4.17 for the major catchments. In agreement with the increased ET, most catchments show a distinct decrease in average river flow. On average, this decrease amounts to 4.5 % of the dynamically simulated discharge, but is in the range of about 50 % of the simulated river discharge change between present-day and Mid-Holocene. A small number of basin experience an increased of about 6.6 % on average of the Mid-Holocene discharge which amounts to about 60 % of the climate change induced river discharge alteration. As all wetland processes result in increased ET and, thus, are strengthening the water recycling, it is not trivial to explain why a few catchments experience an increased river discharge. However, a thorough analysis reveals that the river discharge increase is an unexpected side effect of the different water storages. In the control MPI-HM simulation without DWES all river flow input travels from the earth surface via the overland or baseflow storage into the river flow storage. However, the DWES introduces the wetland storage which also discharges into the river flow and allows to bypass the overland and baseflow storages. While both, the overland and baseflow storage, have fixed water retention times, this time varies for the wetland storage depending on its water level and size. For deep and large wetlands, their retention time may be lower than the respective times of the other storages and, thus, results in a more efficient transport of water into the river storage. In case of a steady state simulation this effect would be compensated, but in a transient simulation with irregular inflow it leads to an increased river discharge. Although unexpected, this model behavior is realistic and was already presented in a
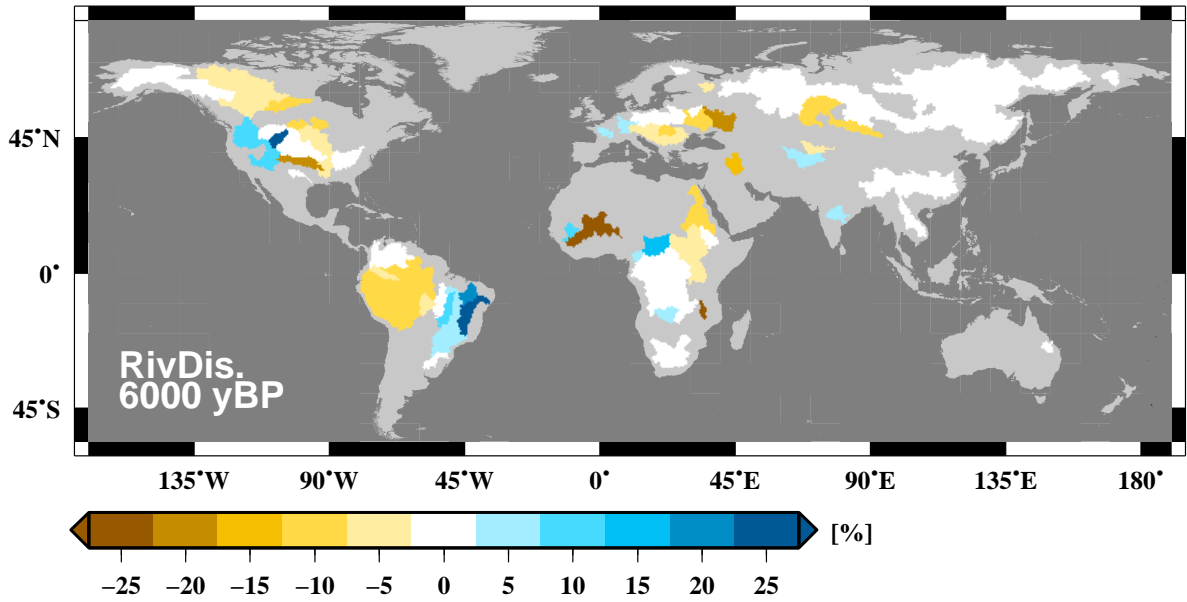
Figure 4.11.: Mean relative river discharge difference between the DWES and the control simulation during Mid-Holocene.

review about hydrological functions of wetlands by Bullock and Acreman (2003).
Figure 4.12 shows two examples of climatological river discharge curve for the dynamical simulation and the control simulation. Here, the Churchill River represents a catchment with decreased river discharge. The peak flow is found to be delayed in the dynamical simulation as it is usually expected for the influence of wetlands. Compared to the present-day simulation the delay is slightly increased indicating the larger wetland extent. In contrast, the Sao Francisco shows an increased river discharge. Still, wetlands cause a peak delay compared to the control simulation. As wetlands are smaller during Mid-Holocene, the river discharge is simulated to be less than for present-day.
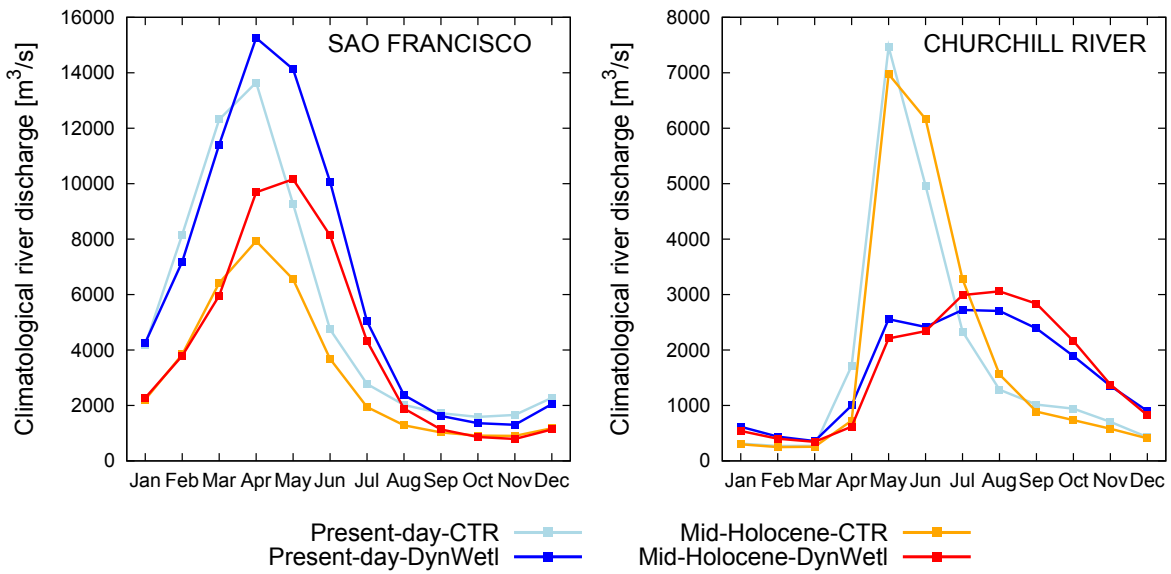
Figure 4.12.: Climatological river discharge curves for two river catchments. The panels display the simulated present-day and Mid-Holocene river discharge for the DWES and the control.

4.2. Future projections

4.2.1. Climate change scenario forcing for the MPI-HM

Similar to the Holocene simulation the projection simulation is forced by climate model output of the earth system model ECHAM5/MPI-OM. These simulations were conducted in the framework of the ENSEMBLES project (`http://www.ensembles-eu.org/`). One part of these runs are baseline simulations which apply observed greenhouse gas concentrations until the year 2000. The other part are emission scenarios simulations. They are initialized from the baseline run in the year 2000 and are forced with different greenhouse gas emission scenarios until 2100 which are defined by IPCC (2000).

A part of the ENSEMBLES ECHAM5/MPI-OM simulations are employed again by the WATCH project (`http://www.eu-watch.org/`). As the climate model data were to be used by hydrological models, a bias correction was developed by Piani et al. (2010) which aimed to shift the probability distribution of simulated temperature and precipitation towards the probability distribution of the WFD. This method was applied by Hagemann et al. (2011) to investigate the impact of this correction on projected changes in the simulated hydrological cycle. In their study, the bias correction was employed for the third member of the ECHAM/MPI-OM simulation ensemble for the baseline simulation and the scenario simulations A2 and B1. In order to profit from the bias corrections, the already corrected model simulations are used as climate forcing for the projection of future wetland extent.

Besides surface temperature and precipitation, PET is needed as an input for the MPI-HM. Similar to the Holocene simulation, PET is calculate using equation 4.1 at the native model resolution of about 1.875°. Afterwards, the PET field is interpolated to 0.5° resolution. As there are no global observations of PET, there is no possibility to apply the bias correction to the calculated PET. Thus, the PET is not consistent to the bias corrected surface temperature. However, this inconsistency is judged minor compared to applying the Thornthwaite equations which would otherwise be the default in the MPI-HM (see Sect. 2.1.1).

The A2 emission scenario is based on the assumption of continuously increasing population and regional oriented economic development (IPCC, 2000) and considered as high emission case. In contrast, the B1 emission scenario assumes a ecologically friendly world with a stabilizing population and a strong global cooperation (IPCC, 2000). This scenario describes a low emission case. Figure 4.13 displays the anomalies between the mean of the last 30 years of the scenario and baseline simulations. Both scenarios respond with the same patterns to the different emission concentrations. Generally, the difference between B1 and A2 has the opposite sign of the A2 anomaly but a smaller absolute value. This indicates that both scenarios react in the same way, but the B1 scenario responds weaker to the emission concentration. The climate model simulates a strong warming of the land surface of 4.3 K (2.9 K) on average for the A2 (B1) scenario. The strongest effects are seen in the high northern latitudes with maximum anomalies of 11.6 K (9.1 K). Globally the precipitation is slightly increasing. The high northern latitudes and the larger parts of the tropics experience a precipitation increase up to 7.5 $^{mm/d}$ (4.3 $^{mm/d}$)

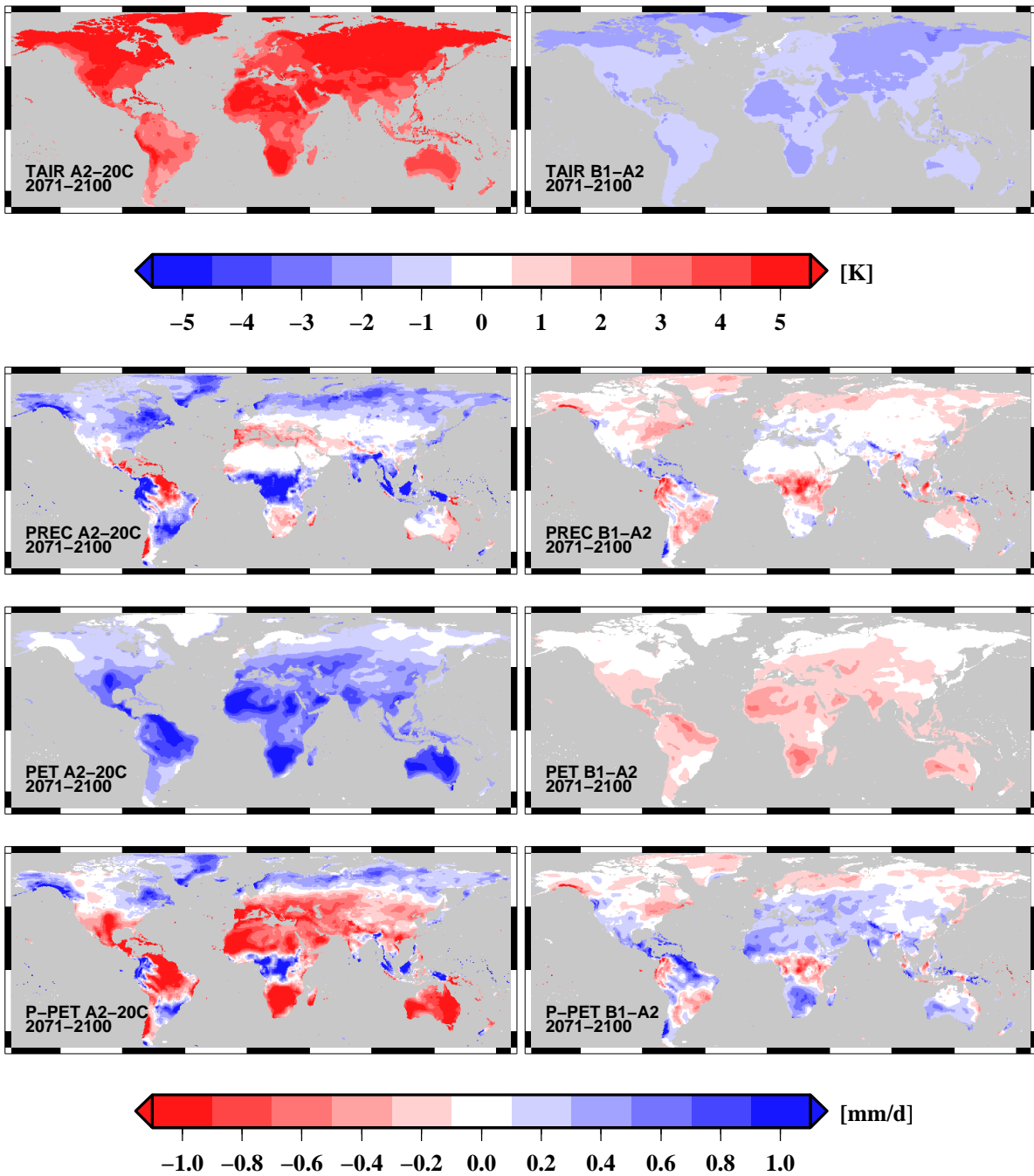Figure 4.13.: Climate forcing anomalies for wetland projections at 0.5° horizontal resolution. The left panels display the mean difference between the A2 emission scenario (Roeckner, 2007b) for the period 2071-2100 and the 20th century baseline simulation (Roeckner, 2007a) for the period 1971-2000. The right panels display the mean difference between the B1 (Roeckner, 2007c) and A2 emission scenario for the period 2071-2100.

for A2 (B1). A precipitation decrease is found for the Mediterranean region, the Amazon catchment, South Africa and Australia with values of -3.7 $^{mm}/_d$ (-3.0 $^{mm}/_d$). PET show an overall increase of 0.49 $^{mm}/_d$ (0.32 $^{mm}/_d$) on average, focusing on Central America, the western Sahara and South Africa as well as Australia. Thus, the balance of precipitation and PET is strongly negative for most regions. While the high northern latitudes and some parts of the tropics have about 0.41 $^{mm}/_d$ (0.31 $^{mm}/_d$) more water available on the surface, the remaining areas suffer a decrease of -0.63 $^{mm}/_d$ (-0.42 $^{mm}/_d$). The simulated anomalies for temperature and precipitation are in agreement with the IPCC (2007b).

4.2.2. Simulation analysis

Six simulations are conducted for the projection analysis. The first set of three simulations uses the DWES. It comprises a baseline simulation from 1961-2000 with observed greenhouse gas emissions and two scenario simulations for the B1 and A2 scenario from 2001 until 2100. Both scenario simulations are initialized with the restart information from the last time step of the baseline experiment including the wetland fractions, surface water depth and wetland soil moisture. Similar to the Holocene study (see Sect. 4.1), a second simulation series is conducted which neglects wetlands in all three simulations.

Global analysis

First, the analysis focuses on the global response of wetlands to the different emission scenarios. Figure 4.14 displays the land surface mean values of wetland soil moisture, surface water depth and wetland extent for both scenarios. All three variables express a very strong variability enforcing the calculation of running means over a 31 years period to visualize their long term trends. In all cases, the two emission scenario simulations agree in the sign of the change. The wetland soil moisture decreases globally by about 10 mm. During the first decades of the scenario simulations the soil moisture even increases for the A2 scenario while in the B1 the decline already starts. Around 2050 the A2 scenario catches up with the B1 and finally drops below the B1. Apparently contradictory, the surface water depth and global wetland fraction increase steadily. This indicates that the soil moisture loss is mostly occurring in regions which were already too dry to sustain wetlands during the baseline run. In those regions a further decrease of soil moisture does not lead to a decrease on surface water or wetland fractions. The surface water rise takes place in two steps. The first phase stabilizes around 2010 with a mean increase of 1.5 to 2.5 mm over the whole land surface. 2040 the second phase starts adding another 2.5 mm water depth in the B1 case and 4.5 mm in the A2 case, respectively. The surface water fraction increases uniformly for both scenarios until 2060. Thereafter, the B1 simulation slows it increase while A2 proceeds. Finally, the wetland fraction grows about 0.0015 for B1 and 0.0021 for A2.

Next, the global distribution of wetland change is investigated comparing its mean 2071-2100 period value of the scenarios to the mean 1971-2000 period value of the baseline simulation. The resulting fields are presented in figure 4.15. As the overall changes between the A2 and B1 results are hardly distinguishable, the B1 simulation results are
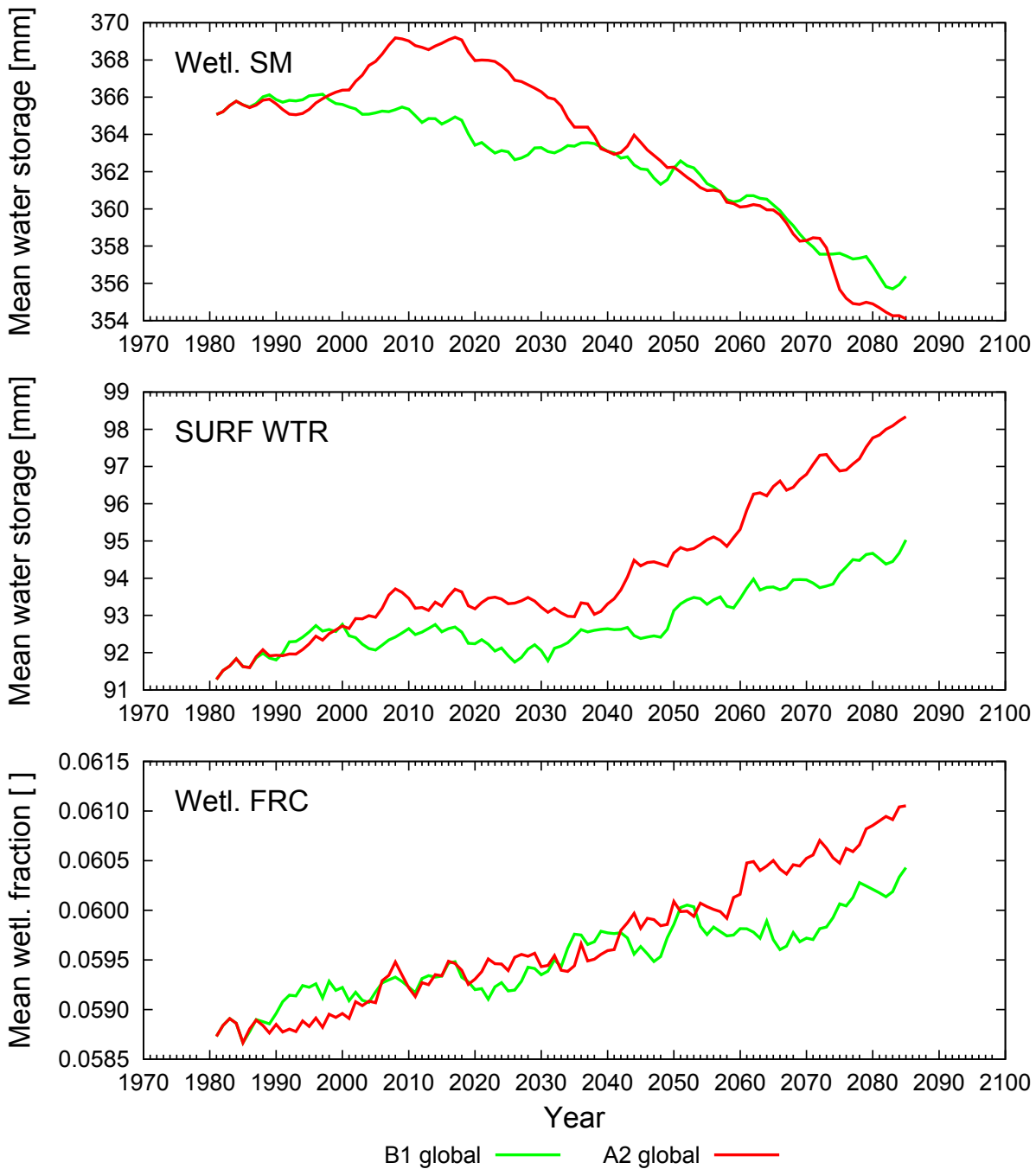
Figure 4.14.: 31 years running mean for the B1 (green) and A2 (red) simulation results including the baseline period. The panels show the wetland soil moisture (top), the surface water level (middle) and the wetland land surface fraction (bottom). Note that the running mean calculation causes both time series to deviate from each other even before the baseline period ends.
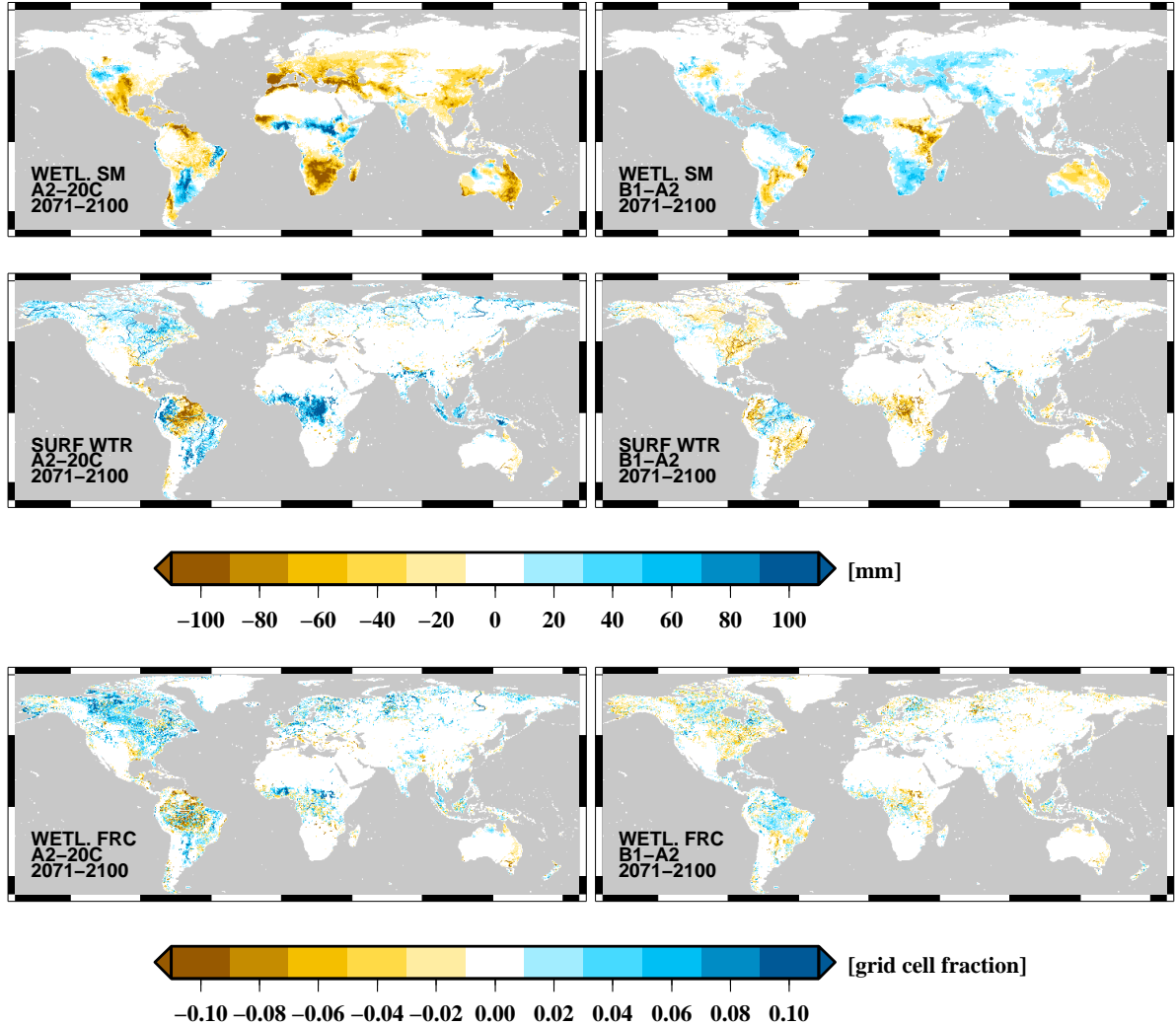
Figure 4.15.: Mean simulation results for the period 2071-2100. The left side displays the anomaly for the A2 simulation compared to the baseline period 1971-2000. The right side displays the anomaly between the B1 and A2 simulations. The panels show the wetland soil moisture (top), the surface water depth (middle) and the wetland grid cell fraction (bottom).

displayed as differences to the A2 simulation results for the following plots. Focusing first on the A2 results, the overall wetland soil moisture decreases by about 12 mm with local extremes of 360 mm. Like South Africa, the Mediterranean and southeastern Asia, most of these desiccating area are indeed no major wetland focus regions and, thus, the drying does not affect the general wetland distribution strongly. Solely the South American center, eastern Australia and the central USA respond with a distinct decrease in surface water and wetland fraction to this development. A much stronger signal is seen for all northern latitudes above 45 °N as well as central Africa, southeastern South America and Indonesia. Here, the soil storage for the wetland fractions is already saturated in the baseline run, thus, promoting an averaged surface water increase of 10 mm and a wetland fraction growing of 0.007. In contrast, the simulated desiccation affects the wetlands only by a surface water depth and extent decrease of 3.2 mm and 0.0035, respectively.

The difference between the B1 and A2 scenario results indicate that the B1 simulation is responding in the same way as the A2 although in a weaker intensity. In the B1 simulation both, the simulated wetland soil moisture decrease and the surface water increase, are reduced by 5 mm compared to the A2 simulation. Also, the wetland extent grows less in the B1 simulation by a value of 0.0038.

Comparing the precipitation - PET difference of the climate forcing to the wetland soil moisture and surface water changes, it is obvious that the climate input is the main contributor to the simulated changes in the water storages. However, some regions are visible where wetlands grow although the climate forcing indicates a negative surface water balance. Examples for this are the center of Europe, parts of the South American east coast, northern Canada and the eastern USA as well as northern Australia. More rarely the opposite takes place such as in parts of Alaska and southern Brazil. Those regions clearly demonstrate that the lateral water transport plays an important role in the formation as well as drainage of wetlands. This conclusion is illustrated by Figure 4.16 displaying the ratio of the vertical water fluxes in wetlands in relation to the overall water balance for the A2 simulation. Especially in wetland areas, the ratio of the vertical water balance is decreased and allows the lateral water flow to balance the precipitation - evaporation induced water deficits or surpluses.

The climate change simulations also yield altered river discharge fields. Figure 4.17 displays the relative change for the A2 simulation results as well as the B1 - A2 difference in relative change. Also the river discharge field is dominated by the climate forcing. In the high northern latitudes and the African center river discharge increases by 25% on average with some river catchments almost doubling their river flow. The opposite effect is seen for a band from middle Europe to China, South America and South Africa. On average the flow reduction is only about 4% but locally river discharge is reduced almost by half as seen for the Euphrates catchment.

In contrast to the wetlands which react mostly locally to the water balance change, the river discharge equals an integral over a large area. Thus, some rivers experience an increased flow in spite of large part of their catchments being drier than in the baseline simulation. An example for this is the Nile. Its simulated discharge is increased by about 60% because of the precipitation increase in central Africa. Similar effects are visible for the Amazon whose flow decreases only by 6% while most of its catchment
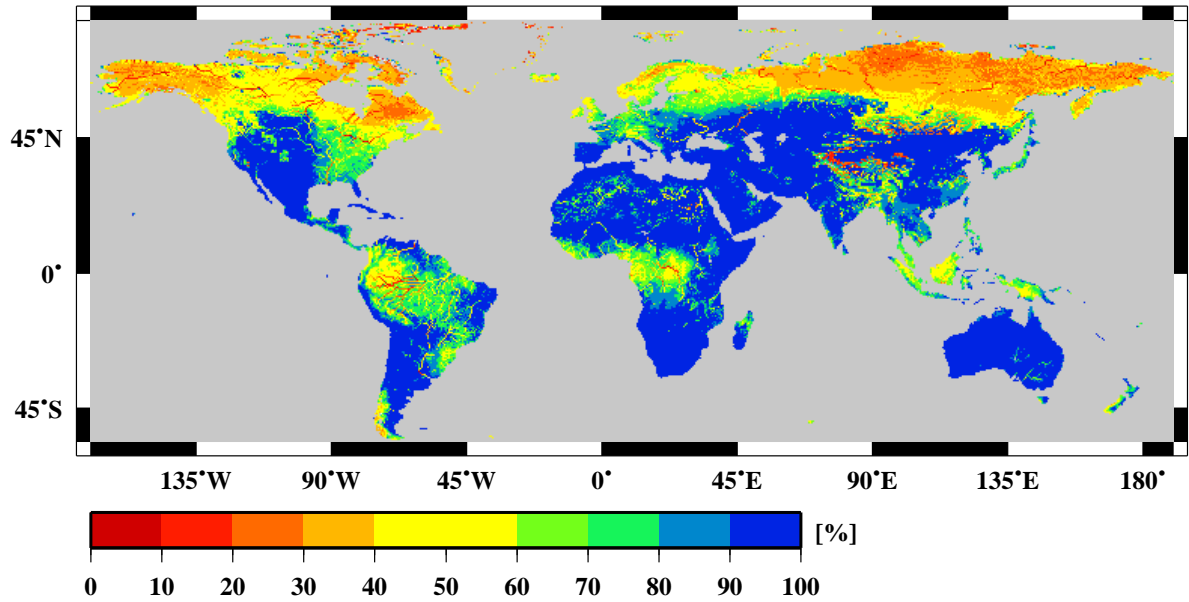
Figure 4.16.: Mean share of the vertical water balance flux in relation to the overall water balance for the period 2071-2100 of the A2 simulation. Red regions are dominated by the lateral water transport while blue area are dominate by vertical water fluxes.

suffers an annual precipitation decrease of about 1 $^{mm}/_d$. To some extent, this loss is balanced by the increased precipitation over Peru and Columbia. These examples show how local desiccation is counteracted by water transport in rivers and, thus, underline the importance of the lateral water balance for climate impact studies.

Influence of wetlands on projected climate change

The influence of wetlands on the simulated ET and river discharge confirms the respective analyses in the Holocene study. The comparison of simulations with and without DWES revealed an increased ET of about 0.02 $^{mm}/_d$ with local maxima around 0.4 $^{mm}/_d$ (see Fig. B.8) for the A2 simulation. Compared to the simulated change between projection and baseline period, the contribution of the DWES adds up to 0.4 % on average and up to 1 % locally. The absolute value is slightly less for the B1 simulation but the relative wetland contribution to the overall ET increase rises to 0.55 % and 1.3 %, respectively. Similar to the Holocene simulation, the ET increase correlates with a decrease in surface runoff and drainage. Additionally, the few areas of increased drainage occur at the same positions as seen in the Holocene study. This indicates that the drainage increase due to lateral water transport from wet into dry regions is a robust feature of the DWES.
Similar patterns as for the Holocene simulation are also found for the relative river discharge change between simulations using the DWES and neglecting it (see Fig. B.9). Here, the majority of catchments suffer from the increased ET and transport less water while the others show no response or even an increase in river flow.

Figure 4.17.: Mean simulated river discharge for the period 2071-2100. The top panel displays the relative difference between the A2 simulation and the baseline period 1971-2000. The bottom panel displays the difference between the relative B1 and A2 anomalies.

Plausibility analysis

Naturally it is not possible to validate the results of a climate projection. However, the plausibility of its results can be evaluated in a qualitative way.

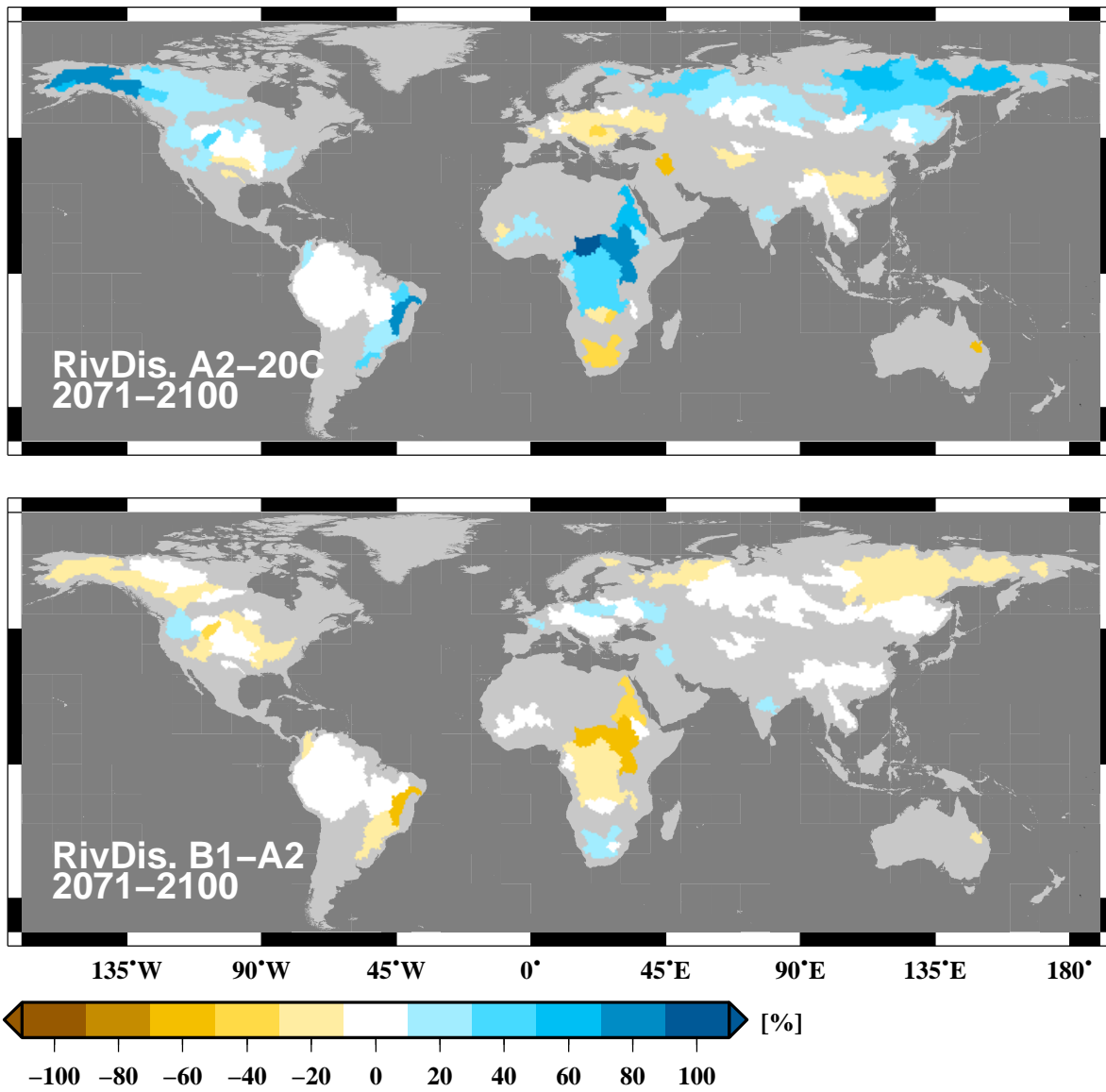As presented for the climate forcing data (see Fig. 4.13), the projected difference between precipitation and PET leads to wetter conditions in the high northern latitudes, southeastern South America, central Africa and Indonesia. In all other regions the surface water availability is decreased. The distribution of wetter and drier areas is reflected well by the simulation of the wetland soil moisture, water depth and wetland distribution. In those regions which disagree with this statement, it is found that the lateral water transport brings additional moisture in otherwise dry regions. These patterns are similar for the A2 and B1 emission scenario simulations. As the influence of the B1 scenario on climate forcing is less than for the A2, wetland react stronger in the A2 case. Given the strong reflection of the climate forcing by the simulations, the MPI-HM is judged to generate plausible results.

Additionally, another study exists which focuses on global wetland simulation. This study by Gedney and Cox (2003) used the *TOPMODEL* approach (see Sect. 1.4) to model wetland extent dynamically and to project their distribution for the next century. The authors implemented their wetland scheme into the land surface scheme MOSES of the Hadley center climate model HadAM3.

However, when comparing both studies, it has to be noted first that there are several discrepancies between the applied models. First of all, they use forcing from different climate models, which are expected to have a major impact on the simulated wetland distribution. Next to the different horizontal resolution and the difference in the wetland modeling approach, the MPI-HM is a pure hydrological model whereas MOSES is a land surface scheme with an implemented energy balance. The latter was coupled to a general circulation model and thus able to deliver feedbacks to the atmosphere. The parameters of the DWES are derived indirectly using river discharge while Gedney and Cox (2003) calibrated their wetland scheme to match the observed present-day wetland distribution as best as possible. Thus, the simulation results are not comparable in terms of their simulated present-day wetland distributions. Nonetheless, it is worth knowing whether – in spite of these numerous differences – both simulations qualitatively agree in the projected changes for some regions. For those regions the simulation of wetlands change is a more robust signal than for the remaining regions.

Figure 4.18 displays simulated wetland change for the MPI-HM simulation and the Gedney and Cox (2003) study. Focusing on large scale features, both simulations agree on a wetland increase in Southeastern South America, Central Africa and most of Europe as well as on a decrease in Central South America. This agreement indicates that the processes which determine the wetland extent are capture well by both models.

For the high northern latitudes, both models react differently. The MPI-HM shows mostly increased wetland fractions whereas MOSES additionally identifies regions with wetland extent decrease in Alaska, Eastern Canada and Western Siberia. Here, wetland extent seems to be influenced by very complex processes such as permafrost interactions or are very sensitive to the energy balance. In conclusion, the simulated wetland change
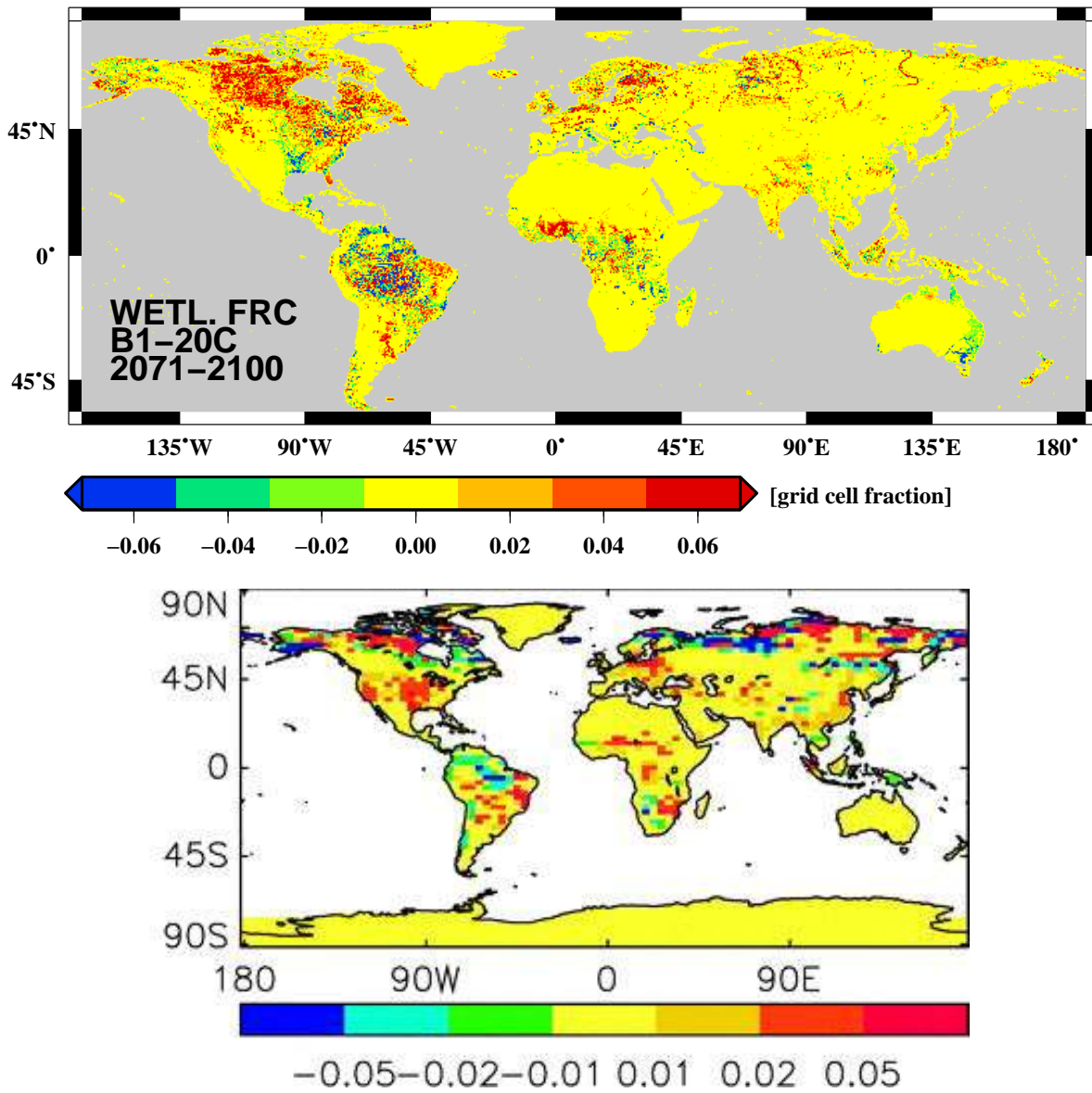
Figure 4.18.: Projected change in wetland fraction for the B1 scenario at 0.5° resolution using the MPI-HM (top) and for a double CO_2 simulation at a grid box size of 2.5° latitude and 3.75° longitude using the landsurface scheme MOSES (bottom, Gedney and Cox, 2003).

signal is subject to a higher uncertainty in the high northern latitudes than in the tropical regions.

4.3. Conclusion on the model's sensitivity to different climate conditions

At the end of the validation analysis (see Sect. 3) it was speculated that the MPI-HM would be qualified to project the wetland distribution under changed climate conditions. The recent experiments are conducted using climate forcing data from a transient Mid-Holocene to present-day simulation as well as from climate change projections based on different emission scenarios. These simulation allow for conclusion about the model's sensitivity to changed orbital parameters and greenhouse gas emissions.

The Holocene simulation results are validated against reconstructed lake level changes and agree with wetter and drier conditions for most regions. Even on local scale some surface water changes match with the trends in reconstructed data. However, much more lakes have to be investigated to conclude whether the local scale agreements are a robust feature or just coincidence. The projections for future wetland distributions cannot be validated, but they are found to respond plausibly to the climate forcing. Mostly, they reflect the changes in the precipitation patterns. Some regions show a modified response which can be attributed to the influence of lateral water transport.

However, these results also hint on deficits in the model's climate forcing data or process representation. For Mid-Holocene, the MPI-HM does not simulate the moisture increase in Northern Africa as strongly as it can be expected by the reconstructions. Most probable, this is due to the climate forcing data whose precipitation increase is also limited to the southern part of the Sahel. It is also possible that the missing feedbacks between the MPI-HM and the climate model are causing parts of this shortcoming. Implementing the DWES into a coupled climate model, the increased ET would cool the surface and increase air humidity. Thus, the ET would decrease which allows more water to remain on the surface and form wetlands. Some of the differences between the projected wetland distribution between the MPI-HM and the MOSES land surface scheme (Gedney and Cox, 2003) could also be explained by missing feedbacks. As the ET feedback enhances the formation of wetlands in wet regions as well as their desiccation in dry regions, it may be the reason for the overall lesser response of the MPI-HM. Additionally, the lack of appropriate boundary data for an altered land surface might affect the simulation results. Next to changes in the vegetation cover, the permafrost distribution has a significant influence on the formation of wetlands in high northern latitude. Here, an interactive permafrost scheme (e.g. Blome and Hagemann, 2011) could improve the simulated distribution.

The amount of simulations conducted for the validation and the application chapter of this thesis allows to investigate whether a climate change sensitivity can be derived for the global wetland distribution. Figure 4.19 displays the mean land surface wetland fraction and surface water depth for all simulations in respect to the different climate forcing

fields. The figure clearly demonstrates a strong difference between the simulations. The
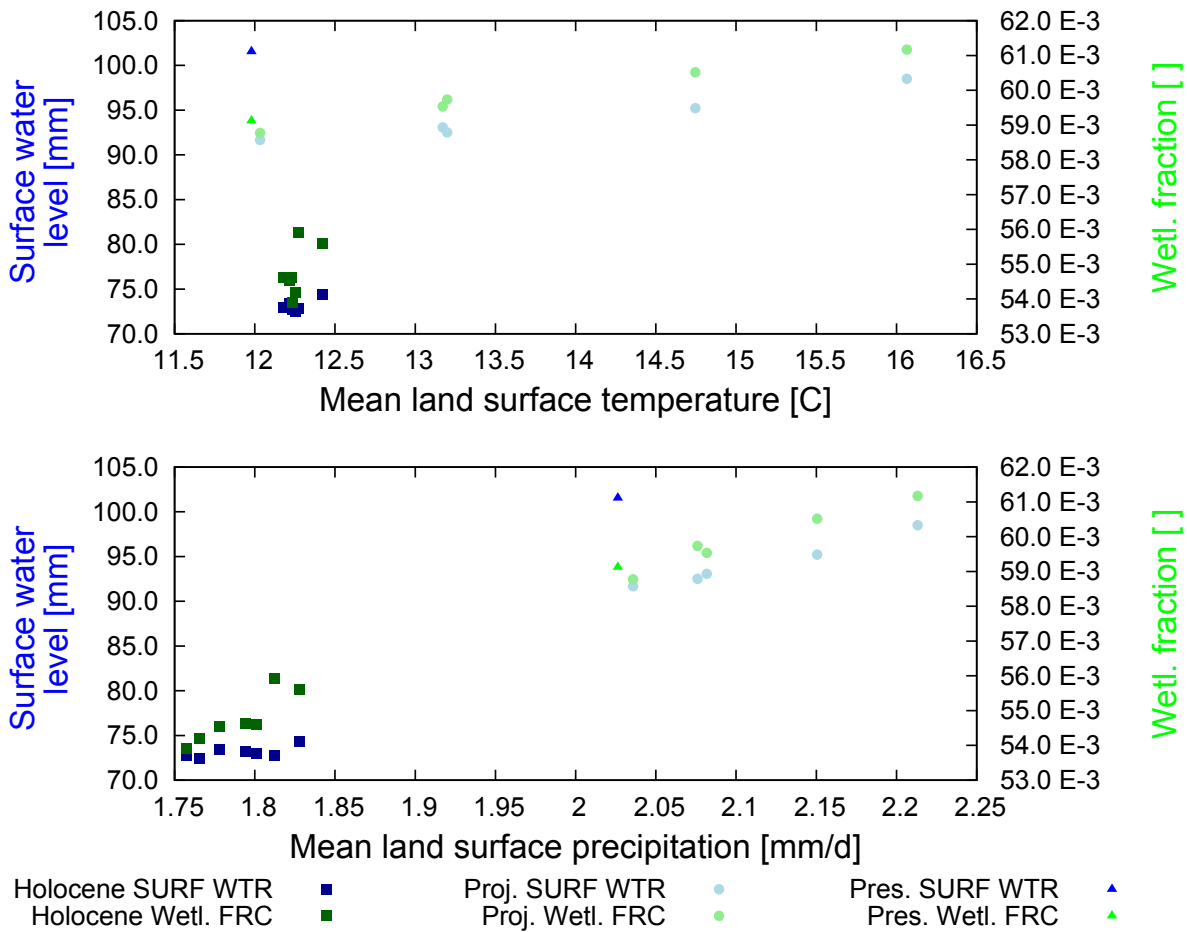
Figure 4.19.: Sensitivity of simulated surface water and wetland fraction on climate forcing for all dynamical wetland simulations.

upper panel shows the wetland sensitivity to temperature. While the future projections indicate a almost linear dependence of wetland fraction on temperature, the Holocene simulations do not support this finding. Furthermore, it becomes visible that both climate change simulations are very different from each other. During the last 6000 years, the temperature change was insolation driven. Locally, temperatures were very different from today causing different circulation and precipitation patterns. However, the average temperature over the whole land surface is relatively stable for all Holocene time slices. In contrast, the projected future climate change leads to a global increase in temperature covering a range of 4 K. In both cases wetland varied in a similar range. Thus, temperature change may be connected to wetland change but not in a linear manner.

In contrast, all simulations agree on an almost linear correlation between mean land surface precipitation and wetland fraction. The simulated wetland fraction increase is about 0.016 per 1 $^{mm}/_d$ of precipitation increase. Of course, it is not known how this trend may change outside of the mean precipitation range of 1.75 to 2.25 $^{mm}/_d$. A similar

trend can be seen for the wetland water depth. Here, the validation simulation deviates from the mean trend indicating a considerable uncertainty of this trend.

In summary, it is found that the DWES delivers plausible results within the investigated range of climate forcing. The agreement with observations and reconstructions is best for large scale features. The model's ability to simulate the local scale wetlands is limited for some regions, such as the high northern latitudes, because of unaccounted permafrost dynamics. This is a task for further model development in the future.

5. Concluding remarks

5.1. Summary of the PhD research

The objective of this PhD research was the development of the dynamical wetland extent scheme (DWES). This work was motivated by the necessity to provide boundary data for the biogeochemical modeling of wetland methane emissions for present-day climate as well as for different climate conditions. Furthermore, the scheme should calculate the full wetland water cycle and, thus, compute water flux feedbacks from wetlands to the atmosphere. Based on the newly developed subgrid slope approach, the DWES was able to transfer changes in the wetland water balances into variations of its surface extent. Therefore, not only the water table but the whole wetland might now react dynamically to changes in the earth's climate.

The scheme was embedded into the Max Planck Institute – Hydrology Model (MPI-HM) and then validated against present-day observations of global wetland distribution, wetland seasonality and water level variations. It was shown that the simulated wetland distribution as well as their seasonal variations agreed well with the range of observations. However, the wetland extent was overestimated for the southern hemisphere. Additionally, water level variations were investigated for single grid cells. Their simulated seasonality showed a high correlation to satellite observations but the overall range of water level fluctuations is underestimated.

Its application under projected Mid-Holocene and future climate conditions revealed a plausible response of the wetland's distribution and their water depth to changes in precipitation patterns. For most regions, a precipitation increase led to more extensive wetlands and vice versa. This reaction was modified by processes like lateral water transport. Thus, in some areas wetland extent increased in spite of less precipitation because water was transported into this region by rivers. Both experiments were compared against control simulations which did not consider any wetland interactions. Thus, the intensity of potential feedbacks between wetland and atmosphere was investigated. Here, the wetland generated evapotranspiration (ET) was found to add up to 0.4 $^{mm}/_d$ to the annual ET response to the changed climate conditions.

This PhD study was guided by a number of research questions. While these are answered to some extent within the different chapters, they will be explicitly discussed in the following paragraphs:

1. The first question inquired the possibility to simulate wetland dynamics with a simple approach. The DWES is simple insofar that it neither increased the computational costs of the MPI-HM distinctively nor did it require any boundary

5. Concluding remarks

data that is not readily available at global scale and for different time periods. In spite of these prerequisites, the scheme successfully simulated the large scale wetland distribution of the northern hemisphere and even some single wetland structures. It largely captures the seasonal dynamics of wetland extent and water table. However, tropical wetlands were overestimated which might be connected to the applied ET calculation rather than to the DWES itself.

Furthermore, the DWES had a strong influence on the simulated river discharge and mostly led to a decrease in the overall amount of river flow. In agreement with the expectations (see Sect. 1.2), the river peak flow was delayed.

2. Second, it was asked whether or not the DWES can be applied for different climate conditions. This question was answered in section 4 where the DWES has been used to simulate the wetland distribution under Mid-Holocene and present-day climate conditions. For both projections the DWES responded in a plausible way to changes in the precipitation patterns. In general, it agreed with reconstructed lake level changes for the Mid-Holocene, but it did not succeed in capturing the full reconstructed extent of the North African moisture increase. However, this insufficiency could be mainly attributed to the climate forcing data as well as the missing feedbacks to the atmosphere. Otherwise, none of the simulation results gave any indication that the DWES's parameters might be invalid for these different climate conditions.

3. The third question deals with the projected wetland change for future climate conditions. The DWES responded to both emission scenarios' climate forcings with increased wetland fractions and water tables in the high northern latitudes. Decreasing water tables were found in the Mediterranean region, the Amazon catchment and Eastern Australia. The changes in wetland fraction also influenced the simulated open water evaporation. North of 60°, the response of open water evaporation was relatively weak due to the low surface temperatures. However, in the tropical regions the open water evaporation increased by up to $0.5^{mm}/d$.

   Both emission scenarios resulted in very similar wetland alterations for the 2021-2050 time slice. Towards the end of the century, the differences between both scenarios grow. This was the case, e.g., for the Eastern US and Eastern Africa where the A2 scenario projected more extensive and deeper wetlands than today while the B1 scenario stated the opposite.

4. The last question asked about the added value of the new DWES for climate science. While the DWES is more simple than most models, it stands out among other approaches by its global applicability and its independence from regional limited boundary data. Furthermore, the DWES was not calibrated against observed wetland extent (see Gedney and Cox, 2003; Kaplan, 2002; Kaplan et al., 2006). Instead, it used river discharge observations to optimize wetland specific parameters and, still, simulated a reasonable wetland distribution. Finally, the DWES was not designed as a one dimensional model that only regards the water fluxes of single grid cells separately. Instead, it combined fluxes from a land surface scheme with

116

the ones from the river routing model. By these means, not only the water flows within the respective grid cells were accounted for but also river discharge from upstream grid cells was considered in the water balance calculation. Consequently, the new DWES advances the understanding of hydrological interactions between wetlands and climate.

5.2. Outlook

The validation and application of the DWES raised some new research questions as well as indicated some shortcomings of the scheme itself and of the MPI-HM. Thus, new ideas were developed about possible improvements of the shortcomings and about model enhancements to broaden its range of applications. An outlook on these ideas is condensed into a few bullet points:

- Above all, it is encouraged to implement the DWES into the land surface scheme of a coupled climate system model (e.g. ECHAM6/JSBACH). Here, it would be able to profit from a complete energy balance and, thus, a consistent open water evaporation would be available for the DWES. In return, the DWES could provide feedbacks to the atmosphere. This setup might even improve the simulation of wetter conditions in Northern Africa during the Mid-Holocene.

- From the results of this PhD study only speculations about the impact of wetland emissions on climate are possible. Here, it would be expected that the raised water tables in the high northern latitudes would promote anaerobic carbon decomposition in this region. Thus, the amount of methane production would increase. It is difficult to estimate the net effect of the altered greenhouse gas release on climate. On the one hand, methane is a more efficient greenhouse gas than CO_2. On the other hand, decomposition proceeds much slower in anaerobic conditions than in aerobic ones (St-Hilaire et al., 2010). However, the additional temperature increase supports an enhanced carbon respiration even under anoxic conditions (St-Hilaire et al., 2010). Therefore, an enhanced greenhouse gas release from the projected wetland change is rated as more probable.
  In order to test this speculations, the results of the DWES simulations should be fed into a biogeochemical model for wetland methane emissions to estimate the impact of wetland alterations on greenhouse gas emissions.

- The extent dynamics calculation of the DWES was limited to wetlands with surface water. Areas with water tables below the soil surface, were allocated with a stable wetland extent depending on the slope conditions within the grid cell. However, several wetland types are only episodically flooded or do not possess surface water at all. Those were usually underestimated by the DWES. This issue could be improved by including a simple peat growth model. This peat layer would protect the wetland water from evaporation and drainage, and would grow as function of the water table. Computing the wetland water table in relation to the peat surface

5. Concluding remarks

would also provide an improved input for biogeochemical wetland models. Alternatively to the previous proposal, the wetland dynamics itself could be upgraded to account for non-flooded wetlands. Similar to the *TOPMODEL* approach (Beven and Kirkby, 1979) or to the improved arno scheme (Dümenil and Todini, 1992; Hagemann and Dümenil Gates, 2003), the subgrid slope approach might be applicable to modify the sub grid soil moisture distribution. Wetland area can then be allocated with the grid cell fraction which is exceeding a certain soil moisture threshold.

- Wetlands are found to be strongly influenced by permafrost (e.g. Robinson and Moore, 2000). While for today's climate static boundary masks of permafrost are sufficient to indicate its distribution, the permafrost distribution will change for different climate conditions (Etzelmüller et al., 2011; Hipp et al., 2011). The effects of permafrost change can be quite divers and may lead to increasing wetlands over melting permafrost which delivers water as well as to decreasing wetlands over melted permafrost which is not able to constrain drainage anymore (Smith et al., 2005). Thus, for long term projections of past or future wetland distribution it would be preferable to combine the DWES with a dynamical permafrost scheme.

- It is recommended to improve the MPI-HM in several ways in order to defend its status as a state of the art global hydrology model. Nowadays, high resolved river routing networks are available (e.g. Lehner et al., 2006) which should replace the 0.5° river direction data. Additionally, it is necessary to include artificial river catchment alterations such as dams and irrigation. Thus, not only the simulated river discharge may become more realistic but also the comparability to river discharge observations would be improved.

Acknowledgments

During the four years of my PhD research I was supported by many people. First, I like to thank my principal advisor Stefan Hagemann who provided this interesting and challenging research topic. He was always available to discuss new ideas about my research and reviewed the first draft of this thesis. Furthermore, I like to thank my advisory panel members Martin Claußen and Victor Brovkin for supervising my research progress and keeping me on track. The founding for this work was provided by the European Union (FP6) funded Integrated Project called WATCH (contract number 036946).

A special thanks goes to the whole THY workgroup. During countless group meetings, test talks and coffee breaks they did not only provide valuable input for my work, but they were there to discuss non-scientific matters, too. Andreas Hänsler was a frequent and reliable reviewer of my research abstracts, Jan Härter adviced me about the fine art of statistical analysis and Tanja Blome was a great helper for finding solutions for tricky problems.

For this thesis, several scientists supported me with data of their own. Here, I want to thank Nils Fischer from MPI who did the Holocene simulations with ECHAM5, Sergey Zhuravlev from the Russian State Hydrological Institute at Saint-Petersburg University for the lake level station time series, and Catherine Prigent from the CNRS Observatoire de Paris for the satellite based wetland dataset. Additionally, I thank Lars Kutzbach from the University Hamburg for providing me with contacts to soil scientists.

Many thanks go to Antje Weitz and Conny Kampmann from the IMPRS office who look after us PhD students. They are a great support in organizing the PhD time and stand up for us whenever their help is needed.

Finally and most of all, I want to thank my family. My wife Christina was a great help and motivation during my PhD time. She never complained about my working weekends, provided me with heaps of LaTeXtricks and made sure I did not starve in the final writing phase. I warmly thank my parents for supporting me during my studies and my PhD research. Not only did they encouraged me to find my way but also helped me going it. My cousin Bernhard I thank very much for spending his rare free time to review some chapters of this thesis.

Bibliography

Allen, R. G. (2001). REF-ET: Reference Evapotranspiration Calculation Software for FAO and ASCE Standardized Equations. Version 2.0. University of Idaho (cit. on pp. 85, 86).

Barling, R.D., I.D. Moore, and R.B. Grayson (1994). A quasi-dynamic wetness index for characterizing the spatial distribution of zones of surface saturation and soil water content. *Water Resour. Res.* 30(4), pp. 1029–1044. DOI: 10.1029/93WR03346 (cit. on p. 11).

Bauer, H., E. Heise, J. Pfaendtner, V. Renner, and P. Schmidt (1983). Entwicklung und Erprobung eines ökonomischen Erdbodenmodells zur Vorhersage von Oberflächen-parametern im Rahmen eines Klimamodells. Tech. rep. Final report for contract CLI-001-80-D (B). Offenbach, Germany: DWD (cit. on p. 15).

Bavina, L.G. (1970). Water balance of swamps and its compution. In: *Symposium on World Water Balance.* 2 UNESCO Studies and reports in hydrology. Paris, pp. 461–466 (cit. on p. 12).

Beven, K.J. and M.J. Kirkby (1979). A physically based, variable contributing area model of basin hydrology. *Hydrol. Sci. Bull. Sci. Hydrol.* 24(1), pp. 43–69 (cit. on pp. 11, 118).

Blome, T. and S. Hagemann (2011). Simulations of Siberian climate using REMO with changed soil parameterizations: Influence of permafrost-relevant processes. In: *Geophys. Res. Abstr.* 13 EGU General Assembly (cit. on p. 112).

Bohn, T., D. Lettenmaier, K. Sathulur, L. Bowling, E. Podest, and K. McDonald (2007). Methane emissions from western Siberian wetlands: heterogeneity and sensitivity to climate change. *Environ. Res. Lett.* 2(4). DOI: 10.1088/1748-9326/2/4/045015 (cit. on pp. 3, 4, 11).

Bonan, G.B. (1995). Sensitivity of a GCM simulation to inclusion of inland water surfaces. *J. Climate* 8(11), pp. 2691–2704 (cit. on p. 3).

Bowling, L. and D. P. Lettenmaier (2010). Modeling the Effects of Lakes and Wetlands on the Water Balance of Arctic Environments. *J. Hydrometeorol.* 11(2), pp. 276–295. DOI: 10.1175/2009JHM1084.1 (cit. on pp. 4, 11).

Brooks, R. T. and M. Hayashi (2002). Depth-area-volume and hydroperiod relationships of ephemeral (vernal) forest pools in southern New England. *Wetlands* 22(2), pp. 247–255 (cit. on p. 28).

Bullock, A. and M. Acreman (2003). The role of wetlands in the hydrological cycle. *Hydrol. Earth Syst. Sci.* 7(3), pp. 358–389 (cit. on pp. 3, 7, 8, 100).

Coe, M.T. (1997). Simulating continental surface waters: An application to holocene Northern Africa. *J. Climate* 10(7), pp. 1680–1689 (cit. on p. 83).

Bibliography

Coe, M.T. (1998). A linked global model of terrestrial hydrologic processes: simulation of modern rivers, lakes, and wetlands. *J. Geophys. Res. D Atmos.* 103(D8), pp. 8885–8899. DOI: 10.1029/98JD00347 (cit. on pp. 11, 30).

Coe, M.T. and G.B. Bonan (1997). Feedbacks between climate and surface water in northern Africa during the middle Holocene. *J. Geophys. Res. D Atmos.* 102(10), pp. 11087–11101. DOI: 10.1029/97JD00343 (cit. on pp. 3, 94).

Comer, N.T., P.M. Lafleur, N.T. Roulet, M.G. Letts, M. Skarupa, and D. Verseghy (2000). A test of the Canadian Land Surface Scheme (CLASS) for a variety of wetland types. *Atmos. Ocean* 38(1), pp. 161–179 (cit. on p. 12).

Cowardin, L.M. and F.C. Golet (1995). US Fish and Wildlife Service 1979 wetland classification: A review. *Vegetatio* 118(1-2), pp. 139–152. DOI: 10.1007/BF00045196 (cit. on p. 5).

De Noblet-Ducoudré, N., E. Poutou, J. Chappellaz, M. Coe, and G. Krinner (2002). Indirect relationship between surface water budget and wetland extent. *Geophys. Res. Lett.* 29(4), pp. 5–1 –5–4. DOI: 10.1029/2001GL013929 (cit. on p. 83).

Dümenil, L. and E. Todini (1992). A rainfall-runoff scheme for use in the Hamburg climate model. In: *Advances in theoretical hydrology - a tribute to James Dooge.* Ed. by J.P. Kane. 1 European Geophysical Society Series of Hydrological Sciences. Amsterdam: Elsevier Science, pp. 129–157 (cit. on pp. 15, 39, 118).

Dyck, S. and G. Peschke (1995). Grundlagen der Hydrologie. 3rd ed. Berlin: Verlag für Bauwesen, p. 536 (cit. on p. 39).

Etzelmüller, B., T.V. Schuler, K. Isaksen, H.H. Christiansen, H. Farbrot, and R. Benestad (2011). Modeling the temperature evolution of Svalbard permafrost during the 20th and 21st century. *Cryosphere* 5(1), pp. 67–79. DOI: 10.5194/tc-5-67-2011 (cit. on p. 118).

Federer, C.A., C. Vörösmarty, and B. Fekete (1996). Intercomparison of methods for calculating potential evaporation in regional and global water balance models. *Water Resour. Res.* 32(7), pp. 2315–2321. DOI: 10.1029/96WR00801 (cit. on p. 15).

Finkelstein, S.A., M.C. Peros, and A.M. Davis (2005). Late Holocene paleoenvironmental change in a Great Lakes coastal wetland: Integrating pollen and diatom datasets. *J. Paleolimnol.* 33(1), pp. 1–12. DOI: 10.1007/s10933-004-0423-3 (cit. on p. 95).

Fischer, N. and J.H. Jungclaus (2010). Effects of orbital forcing on atmosphere and ocean heat transports in Holocene and Eemian climate simulations with a comprehensive Earth system model. *Clim. Past* 6(2), pp. 155–168 (cit. on pp. 85, 86).

– (2011). Evolution of the seasonal temperature cycle in a transient Holocene simulation: Orbital forcing and sea-ice. *Clim. Past Discuss.* 7(1), pp. 463–483. DOI: 10.5194/cpd-7-463-2011 (cit. on pp. 85–87).

Frey, K.E. and L.C. Smith (2007). How well do we know northern land cover? Comparison of four global vegetation and wetland products with a new ground-truth database for West Siberia. *Global Biogeochem. Cycles* 21(1). DOI: 10.1029/2006GB002706 (cit. on pp. 3, 9, 11).

Friborg, T., H. Soegaard, T.R. Christensen, C.R. Lloyd, and N.S. Panikov (2003). Siberian wetlands: Where a sink is a source. *Geophys. Res. Lett.* 30(21), pp. CLM 5–1 –CLM 5–4. DOI: 10.1029/2003GL017797 (cit. on p. 3).

Gamble, D.L. and W.J. Mitsch (2009). Hydroperiods of created and natural vernal pools in central Ohio: A comparison of depth and duration of inundation. *Wetlands Ecol. Manage.* 17(4), pp. 385–395. DOI: 10.1007/s11273-008-9115-5 (cit. on p. 5).

Gedney, N. and P.M. Cox (2003). The sensitivity of global climate model simulations to the representation of soil moisture heterogeneity. *J. Hydrometeorol.* 4(6), pp. 1265–1275 (cit. on pp. 12, 83, 110–112, 116).

Gesch, D.B., K.L. Verdin, and S.K. Greenlee (1999). New land surface digital elevation model covers the earth. *Eos Trans. AGU* 80(6), pp. 69–70. DOI: 10.1029/99E0000050 (cit. on pp. 32, 56).

Global Runoff Data Centre (2011). Long-Term Mean Monthly Discharges and Annual Characteristics of GRDC Station. Tech. rep. Koblenz, Germany: Global Runoff Data Centre, Federal Institute of Hydrology (BfG). URL: http://www.bafg.de/cln_007/nn_298422/GRDC/EN/02__Services/02__DataProducts/LongTermMonthly Means/longtermmonthly__node.html?__nnn=true (cit. on p. 43).

Gohar, A.A. and F.A. Ward (2010). Gains from expanded irrigation water trading in Egypt: An integrated basin approach. *Ecol. Econ.* 69(12), pp. 2535–2548. DOI: 10.1016/j.ecolecon.2010.07.030 (cit. on p. 81).

Gorham, E. (1991). Northern peatlands: role in the carbon cycle and probable responses to climatic warming. *Ecol. Appl.* 1(2), pp. 182–195. DOI: 10.2307/1941811 (cit. on p. 3).

Graham, L.P., S. Hagemann, S. Jaun, and M. Beniston (2007). On interpreting hydrological change from regional climate models. *Clim. Change* 81(SUPPL. 1), pp. 97–122. DOI: 10.1007/s10584-006-9217-0 (cit. on p. 16).

GRLM (2011). USDA/FAS/OGA and NASA Global Agriculture Monitoring (GLAM) Project. Lake and reservoir surface height variations from the USDA's Global Reservoir and Lake (GRLM) web site. Altimetric lake level time-series variations from the Topex/Poseidon, Jason-1, Jason-2/OSTM, and Geosat Follow-On (GFO) missions. URL: http://www.pecad.fas.usda.gov/cropexplorer/global_reservoir/ (cit. on p. 73).

Häckel, H. (2008). Meteorologie. 6. and corr. Ed. Stuttgart: Ulmer, p. 447 (cit. on p. 84).

Hagemann, S. (2002). An improved land surface parameter dataset for global and regional climate models. MPI-Report (336). Hamburg, Germany: Max Planck Institute for Meteorology (cit. on pp. 8, 32, 56).

Hagemann, S. and L. Dümenil (1998a). A parametrization of the lateral waterflow for the global scale. *Clim. Dyn.* 14(1), pp. 17–31. DOI: 10.1007/s003820050205 (cit. on pp. 14, 16).

– (1998b). Documentation for the Hydrological Discharge Model. MPI-Report (17). Hamburg, Germany: Max Planck Institute for Meteorology (cit. on pp. 20, 23).

– (1999). Application of a global discharge model to atmospheric model simulations in the BALTEX region. *Nord. Hydrol.* 30(3), pp. 209–230 (cit. on pp. 14, 16).

Hagemann, S. and L. Dümenil Gates (2001). Validation of the hydrological cycle ECMWF and NCEP reanalyses using the MPI hydrological discharge model. *J. Geophys. Res. D Atmos.* 106(2), pp. 1503–1510. DOI: 10.1029/2000JD900568 (cit. on pp. 14, 16).

Hagemann, S. and L. Dümenil Gates (2003). Improving a subgrid runoff parameterization scheme for climate models by the use of high resolution data derived from satellite observations. *Clim. Dyn.* 21(3-4), pp. 349–359. DOI: 10.1007/s00382-003-0349-x (cit. on pp. 14, 15, 33, 118).

Hagemann, S., M. Botzet, L. Dümenil, and B. Machenhauer (1999). Derivation of global GCM boundary conditions from 1 km land use satellite data. MPI-Report (289). Hamburg, Germany: Max Planck Institute for Meteorology (cit. on pp. 8, 32, 56).

Hagemann, S., C. Chen, J.O. Haerter, J. Heinke, D. Gerten, and C. Piani (2011). Impact of a statistical bias correction on the projected hydrological changes obtained from three GCMs and two hydrology models. *J. Hydrometeorol.* 12(4), pp. 556–578. DOI: 10.1175/2011JHM1336.1 (cit. on p. 102).

Harrison, S. P., J. E. Kutzbach, Z. Liu, P.J. Bartlein, B. Otto-Bliesner, D. Muhs, I. C. Prentice, and R. S. Thompson (2003). Mid-Holocene climates of the Americas: A dynamical response to changed seasonality. *Clim. Dyn.* 20(7-8) (7), pp. 663–688. DOI: 10.1007/s00382-002-0300-6 (cit. on p. 84).

Hastings, D. A., P. K. Dunbar, G. M. Elphingstone, M. Bootz, H. Murakami, H. Maruyama, H. Masaharu, P. Holland, J. Payne, N. A. Bryant, T. L. Logan, J.-P. Muller, G. Schreier, and J. S. MacDonald (1999). The Global Land One-kilometer Base Elevation (GLOBE) Digital Elevation Model, Version 1.0. Tech. rep. Boulder, U.S.A: National Oceanic and Atmospheric Administration. URL: http://www.ngdc.noaa.gov/mgg/topo/globe.html (cit. on p. 32).

Hayashi, M. and G. Van Der Kamp (2000). Simple equations to represent the volume-area-depth relations of shallow wetlands in small topographic depressions. *J. Hydrol.* 237(1-2), pp. 74–85. DOI: 10.1016/S0022-1694(00)00300-0 (cit. on p. 28).

Hipp, T., B. Etzelmüller, H. Farbrot, and T.V. Schuler (2011). Modelling the temperature evolution of permafrost and seasonal frost in southern Norway during the 20th and 21st century. *Cryosphere Discuss.* 5(2), pp. 811–854. DOI: 10.5194/tcd-5-811-2011 (cit. on p. 118).

Holden, J. (2005). Peatland hydrology and carbon release: Why small-scale process matters. *Philos. Trans. R. Soc. A Math. Phys. Eng. Sci.* 363(1837), pp. 2891–2913. DOI: 10.1098/rsta.2005.1671 (cit. on p. 6).

Ingram, H.A.P. (1978). Soil Layers in Mires - Function and Terminology. *J. Soil Sci.* 29(2), pp. 224–227. DOI: 10.1111/j.1365-2389.1978.tb02053.x (cit. on p. 39).

International Lake Environment Committee Foundation (1999). World Lakes Database. retrieved 29.01.2008. URL: http://wldb.ilec.or.jp/ (cit. on p. 30).

IPCC (2000). Special Report on Emissions Scenarios. A Special Report of Working Group III of the intergovernmental Panel on Climate Change. Cambridge, UK and New York, USA: Cambridge University Press (cit. on p. 102).

– (2007a). Climate Change 2007: Synthesis Report. Contribution of Working Groups I, II and III to the Fourth Assessment Report of the Intergovernmental Panel on Climate Change. Ed. by Core Writing Team, R.K Pachauri, and A. Reisinger. Geneva, Switzerland (cit. on p. 3).

– (2007b). Contribution of Working Group I to the Fourth Assessment Report of the Intergovernmental Panel on Climate Change. Ed. by S. Solomon, D. Qin, M. Manning,

Z. Chen, M. Marquis, K.B. Averyt, M. Tignor, and H.L. Miller. Cambridge, UK and New York, USA: Cambridge University Press (cit. on pp. 3, 104).

Jirka, G. H. (2007). Einführung in die Hydromechanik. 3rd ed. Karlsruhe: Universitätsverlag Karlsruhe, p. 246 (cit. on pp. 24, 25).

Kaplan, J.O. (2002). Wetlands at the Last Glacial Maximum: Distribution and methane emissions. *Geophys. Res. Lett.* 29(6), pp. 3–1. DOI: `10.1029/2001GL013366` (cit. on pp. 12, 83, 116).

Kaplan, J.O., G. Folberth, and D.A. Hauglustaine (2006). Role of methane and biogenic volatile organic compound sources in the late glacial and Holocene fluctuations of atmospheric methane concentrations. *Global Biogeochem. Cycles* 20(2), pp. 3–1 –3–4. DOI: `10.1029/2005GB002590` (cit. on pp. 12, 83, 116).

Lai, D.Y.F. (2009). Methane Dynamics in Northern Peatlands: A Review. *Pedosphere* 19(4), pp. 409–421. DOI: `10.1016/S1002-0160(09)00003-4` (cit. on pp. 6, 7).

Lehner, B. and P. Döll (2004). Development and validation of a global database of lakes, reservoirs and wetlands. *J. Hydrol.* 296(1-4), pp. 1–22. DOI: `10.1016/j.jhydrol.2004.03.028` (cit. on pp. 9, 29, 32).

Lehner, B., K. Verdin, and A. Jarvis (2006). HydroSHEDS Technical Documentation. Tech. rep. Washington, DC: World Wildlife Fund US. URL: `http://hydrosheds.cr.usgs.gov` (cit. on p. 118).

Li, Y. and C. Morrill (2010). Multiple factors causing Holocene lake-level change in monsoonal and arid central Asia as identified by model experiments. *Clim. Dyn.* 35(6), pp. 1115–1128. DOI: `10.1007/s00382-010-0861-8` (cit. on p. 93).

Litaor, M.I., G. Eshel, R. Sade, A. Rimmer, and M. Shenker (2008). Hydrogeological characterization of an altered wetland. *J. Hydrol.* 349(3-4), pp. 333–349. DOI: `10.1016/j.jhydrol.2007.11.007` (cit. on p. 39).

Liu, Z, S.P. Harrison, J. Kutzbach, and B. Otto-Bliesner (2004). Global monsoons in the mid-Holocene and oceanic feedback. *Clim. Dyn.* 22(2-3), pp. 157–182. DOI: `10.1007/s00382-003-0372-y` (cit. on p. 84).

Magny, M., G. Bossuet, P. Ruffaldi, A. Leroux, and J. Mouthon (2011). Orbital imprint on Holocene palaeohydrological variations in west-central Europe as reflected by lake-level changes at Cerin (Jura Mountains, eastern France). *J. Quat. Sci.* 26(2), pp. 171–177. DOI: `10.1002/jqs.1436` (cit. on p. 96).

Matthews, E. and I. Fung (1987). Methane emission from natural wetlands: Global distribution, area, and environmental characteristics of sources. *Global Biogeochem. Cycles* 1(1), pp. 61–86. DOI: `10.1029/GB001i001p00061` (cit. on pp. 8, 32).

McCarthy, F.M.G. and J.H. McAndrews (1988). Water levels in Lake Ontario 4230-2000 years B.P.: evidence from Grenadier Pond, Toronto, Canada. *J. Paleolimnol.* 1(2), pp. 99–113. DOI: `10.1007/BF00196067` (cit. on p. 95).

Megonigal, J.P., W.H. Patrick Jr, and S.P. Faulkner (1993). Wetland identification in seasonally flooded forest soils: soil morphology and redox dynamics. *Soil Sci. Soc. Am. J.* 57(1), pp. 140–149. DOI: `10.2136/sssaj1993.03615995005700010027x` (cit. on p. 8).

Merot, Ph., H. Squividant, P. Aurousseau, M. Hefting, T. Burt, V. Maitre, M. Kruk, A. Butturini, C. Thenail, and V. Viaud (2003). Testing a climato-topographic index

for predicting wetlands distribution along an European climate gradient. *Ecol. Model.* 163(1-2), pp. 51–71. DOI: 10.1016/S0304-3800(02)00387-3 (cit. on p. 11).

Milanković, M. (1941). Kanon der Erdbestrahlung und seine Anwendung auf das Eiszeitenproblem. *Special Publication, R. Serb. Acad. Belgrade* 132 p. 633 (cit. on p. 83).

Mishra, V., K.A. Cherkauer, and L.C. Bowling (2010). Parameterization of lakes and wetlands for energy and water balance studies in the great lakes region. *J. Hydrometeorol.* 11(5), pp. 1057–1082. DOI: 10.1175/2010JHM1207.1 (cit. on p. 3).

Mitra, S., R. Wassmann, and P.L.G. Vlek (2005). An appraisal of global wetland area and its organic carbon stock. *Curr. Sci.* 88(1), pp. 25–35 (cit. on p. 7).

Mitsch, W. J. and J. G. Gosselink (1993). Wetlands. 2nd ed. New York: Van Nostrand Reinhold, p. 722 (cit. on pp. 5, 6).

National Geophysical Data Center (2006). ETOPO2v2 Global Gridded 2-minute Database. Tech. rep. National Oceanic and Atmospheric Administration, U.S. Dept. of Commerce. URL: http://www.ngdc.noaa.gov/mgg/global/etopo2.html (cit. on p. 29).

Neumann, J. (1959). Maximum depth and average depth of lakes. *J. Fish. Res. Board Can.* 16(6), pp. 923–927 (cit. on p. 28).

New, M., M. Hulme, and P. Jones (1999). Representing twentieth-century space-time climate variability. Part I: Development of a 1961-90 mean monthly terrestrial climatology. *J. Climate* 12(2-3), pp. 829–856 (cit. on p. 56).

– (2000). Representing twentieth-century space-time climate variability. Part II: Development of 1901-96 monthly grids of terrestrial surface climate. *J. Climate* 13(13), pp. 2217–2238 (cit. on p. 56).

Niemuth, N.D., B. Wangler, and R.E. Reynolds (2010). Spatial and Temporal Variation in Wet Area of Wetlands in the Prairie Pothole Region of North Dakota and South Dakota. *Wetlands*, pp. 1–12. DOI: 10.1007/s13157-010-0111-1 (cit. on p. 5).

Norström, E., L. Scott, T.C. Partridge, and K. Risberg J.and Holmgren (2009). Reconstruction of environmental and climate changes at Braamhoek wetland, eastern escarpment South Africa, during the last 16,000 years with emphasis on the Pleistocene-Holocene transition. *Palaeogeogr. Palaeoclimatol. Palaeoecol.* 271(3-4), pp. 240–258. DOI: 10.1016/j.palaeo.2008.10.018 (cit. on p. 95).

O'Connor, F.M., O. Boucher, N. Gedney, C.D. Jones, G.A. Folberth, R. Coppell, P. Friedlingstein, W.J. Collins, J. Chappellaz, J. Ridley, and C.E. Johnson (2010). Possible role of wetlands, permafrost, and methane hydrates in the methane cycle under future climate change: A review. *Rev. Geophys.* 48(4). DOI: 10.1029/2010RG000326 (cit. on p. 3).

O'Loughlin, E.M. (1986). Prediction of Surface Saturation Zones in Natural Catchments by Topographic Analysis. *Water Resour. Res.* 22(5), pp. 794–804. DOI: 10.1029/WR022i005p00794 (cit. on p. 11).

Pachur, H.-J. and F. Rottinger (1997). Evidence for a large extended paleolake in the eastern Sahara as revealed by spaceborne radar lab images. *Remote Sens. Environ.* 61(3), pp. 437–440. DOI: 10.1016/S0034-4257(96)00210-6 (cit. on pp. 93, 94).

Papa, F., C. Prigent, F. Aires, C. Jimenez, W.B. Rossow, and E. Matthews (2010). Interannual variability of surface water extent at the global scale, 1993-2004. *J. Geophys. Res. D Atmos.* 115(12). DOI: 10.1029/2009JD012674 (cit. on pp. 9, 64).

Petrescu, A.M.R., L.P.H. Van Beek, J. Van Huissteden, C. Prigent, T. Sachs, C.A.R. Corradi, F.J.W. Parmentier, and A.J. Dolman (2010). Modeling regional to global CH4 emissions of boreal and arctic wetlands. *Global Biogeochem. Cycles* 24(4). DOI: `10.1029/2009GB003610` (cit. on p. 12).

Piani, C., G.P. Weedon, M. Best, S.M. Gomes, P. Viterbo, S. Hagemann, and J.O. Haerter (2010). Statistical bias correction of global simulated daily precipitation and temperature for the application of hydrological models. *J. Hydrol.* 395(3-4), pp. 199–215. DOI: `10.1016/j.jhydrol.2010.10.024` (cit. on p. 102).

Press, William H., Brian P. Flannery, Saul A. Teukolsky, and William T. Vetterling (1992). Numerical Recipes in FORTRAN. The Art of Scientific Computing. 2nd ed. Cambridge: Cambridge University Press (cit. on pp. 61, 90).

Prigent, C., E. Matthews, F. Aires, and W.B. Rossow (2001). Remote sensing of global wetland dynamics with multiple satellite data sets. *Geophys. Res. Lett.* 28(24), pp. 4631–4634. DOI: `10.1029/2001GL013263` (cit. on pp. 9, 32).

Prigent, C., F. Papa, F. Aires, W.B. Rossow, and E. Matthews (2007). Global inundation dynamics inferred from multiple satellite observations, 1993-2000. *J. Geophys. Res. D Atmos.* 112(12). DOI: `10.1029/2006JD007847` (cit. on pp. 9, 32).

Ramsar, ed. (2007). What are wetlands? Ramsar Information Paper (1). URL: `http://www.ramsar.org/pdf/about/info2007-01-e.pdf` (cit. on p. 5).

Reichhardt, T. (1995). Academy under fire on 'wetlands' definition. *Nature* 375(6528), p. 171 (cit. on p. 5).

Riefner Jr, R.E. and S. Boyd (2007). New records of wetland and riparian plants in southern California, with recommendations and additions to the national list of plant species that occur in wetlands. *J. Bot. Res. Inst. Tex.* 1(1), pp. 719–740 (cit. on p. 8).

Robinson, S.D. and T.R. Moore (2000). The influence of permafrost and fire upon carbon accumulation in high boreal peatlands, Northwest Territories, Canada. *Arctic Antarct. Alp. Res.* 32(2), pp. 155–166. DOI: `10.2307/1552447` (cit. on p. 118).

Roeckner, E. (2007a). ENSEMBLES ECHAM5-MPI-OM 20C3M run3, daily values. World Data Center for Climate. CERA-DB "ENSEMBLES_MPEH5_20C3M_3_D". URL: `http://cera-www.dkrz.de/WDCC/ui/Entry.jsp?acronym=ENSEMBLES_MPEH5_20C3M_3_D` (cit. on p. 103).

– (2007b). ENSEMBLES ECHAM5-MPI-OM SRESA2 run3, daily values. World Data Center for Climate. CERA-DB "ENSEMBLES_MPEH5_SRA2_3_D". URL: `http://cera-www.dkrz.de/WDCC/ui/Entry.jsp?acronym=ENSEMBLES_MPEH5_SRA2_3_D` (cit. on p. 103).

– (2007c). ENSEMBLES ECHAM5-MPI-OM SRESB1 run3, daily values. World Data Center for Climate. CERA-DB "ENSEMBLES_MPEH5_SRB1_3_D". URL: `http://cera-www.dkrz.de/WDCC/ui/Entry.jsp?acronym=ENSEMBLES_MPEH5_SRB1_3_D` (cit. on p. 103).

Schedlbauer, J.L., S.F. Oberbauer, G. Starr, and K.L. Jimenez (2010). Seasonal differences in the CO2 exchange of a short-hydroperiod Florida Everglades marsh. *Agric. For. Meteorol.* 150(7-8), pp. 994–1006. DOI: `10.1016/j.agrformet.2010.03.005` (cit. on p. 5).

Bibliography

Singh, V.P. (1988). Hydrological Systems: Rainfall-Runoff Modeling. Ed. by C. Fellows. 1 Englewood Cliffs, New Jersey: Prentice Hall, p. 480 (cit. on p. 16).

Smith, L.C., Y. Sheng, G.M. MacDonald, and L.D. Hinzman (2005). Atmospheric Science: Disappearing Arctic lakes. *Science* 308(5727), p. 1429. DOI: `10.1126/science.1108142` (cit. on p. 118).

Soil Conservation Service (1991). Hydric soils of the United States. Tech. rep. Washington, DC: US Department of Agriculture Miscellaneous. Publication. 1491, in cooperation with the National Technical Committee for Hydric Soils (cit. on pp. 6, 8).

St-Hilaire, F., J. Wu, N.T. Roulet, S. Frolking, P.M. Lafleur, E.R. Humphreys, and V. Arora (2010). McGill wetland model: Evaluation of a peatland carbon simulator developed for global assessments. *Biogeosciences* 7(11), pp. 3517–3530. DOI: `10.5194/bg-7-3517-2010` (cit. on pp. 3, 117).

State Hydrological Institute (1970). Resources of Surface Water of the USSR. In: *Hydrological Year Book*. Ed. by Y. A. Elshin. 1 Gidrometeoizdat, Leningrad, Russia (cit. on p. 70).

Stern, D.A., R. Khanbilvardi, J.C. Alair, and W. Richardson (2001). Description of flow through a natural wetland using dye tracer tests. *Ecol. Eng.* 18(2), pp. 173–184. DOI: `10.1016/S0925-8574(01)00076-3` (cit. on p. 23).

Sutcliffe, J. V. and Y. P. Parks (1999). The hydrology of the Nile. Ed. by H. Salz and Z. W. Kundzewicz. IAHS special publication (5). Wallingford, UK: International Association of Hydrological Sciences, p. 179 (cit. on p. 82).

Tamea, S., R. Muneepeerakul, F. Laio, L. Ridolfi, and I. Rodriguez-Iturbe (2010). Stochastic description of water table fluctuations in wetlands. *Geophys. Res. Lett.* 37(6), p. 5. DOI: `10.1029/2009GL041633` (cit. on p. 12).

Thornthwaite, C. W. (1948). An Approach toward a Rational Classification of Climate. *Geogr. Rev.* 38(1), pp. 55–94 (cit. on p. 15).

Thornthwaite, C. W. and J. R. Mather (1955). The water balance. *Pubbl. Climatol.* 8(1), pp. 1–104 (cit. on p. 15).

Tiner, R.W. (2006). Lists of potential hydrophytes for the United States: A regional review and their use in wetland identification. *Wetlands* 26(2), pp. 624–634 (cit. on p. 8).

Uppala, S.M., P.W. Kållberg, A.J. Simmons, U. Andrae, V. da Costa Bechtold, M. Fiorino, J.K. Gibson, J. Haseler, A. Hernandez, G.A. Kelly, X. Li, K. Onogi, S. Saarinen, N. Sokka, R.P. Allan, E. Andersson, K. Arpe, M.A. Balmaseda, A.C.M. Beljaars, L. van de Berg, J. Bidlot, N. Bormann, S. Caires, F. Chevallier, A. Dethof, M. Dragosavac, M. Fisher, M. Fuentes, S. Hagemann, E. Hólm, B.J. Hoskins, L. Isaksen, P.A.E.M. Janssen, R. Jenne, A.P. McNally, J.-F. Mahfouf, J.-J. Morcrette, N.A. Rayner, R.W. Saunders, P. Simon, A. Sterl, K.E. Trenberth, A. Untch, D. Vasiljevic, P. Viterbo, and J. Woollen (2005). The ERA-40 re-analysis. *Q. J. R. Meteorol. Soc.* 131(612), pp. 2961–3012. DOI: `10.1256/qj.04.176` (cit. on p. 56).

U.S. Geological Survey (2001). Global Land Cover Characteristics Data Base Version 2.0. online. URL: `http://edc2.usgs.gov/glcc/globdoc2_0.php` (cit. on p. 8).

Van Huissteden, J., A.M. R. Petrescu, D.M. D. Hendriks, and K.T. Rebel (2009). Sensitivity analysis of a wetland methane emission model based on temperate and arctic wetland sites. *Biogeosciences* 6(12), pp. 3035–3051 (cit. on p. 12).

Vörösmarty, C.J., C.A. Federer, and A.L. Schloss (1998). Potential evaporation functions compared on US watersheds: Possible implications for global-scale water balance and terrestrial ecosystem modeling. *J. Hydrol.* 207(3-4), pp. 147–169. DOI: `10.1016/S0022-1694(98)00109-7` (cit. on p. 15).

Wakeley, J.S. (1994). Identification of wetlands in the Southern Appalachian Region and the certification of wetland delineators. *Water Air Soil Pollut.* 77(3-4), pp. 217–226. DOI: `10.1007/BF00478420` (cit. on p. 8).

Walter, B.P., M. Heimann, and E. Matthews (2001). Modeling modern methane emissions from natural wetlands 1. Model description and results. *J. Geophys. Res. D Atmos.* 106(D24), pp. 34189–34206. DOI: `10.1029/2001JD900165` (cit. on p. 12).

Wania, R., L. Ross, and I.C. Prentice (2009). Integrating peatlands and permafrost into a dynamic global vegetation model: 1. Evaluation and sensitivity of physical land surface processes. *Global Biogeochem. Cycles* 23(3), p. 19. DOI: `10.1029/2008GB003412` (cit. on p. 12).

Wanner, H., J. Beer, J. Bütikofer, T.J. Crowley, U. Cubasch, J. Flückiger, H. Goosse, M. Grosjean, F. Joos, J.O. Kaplan, M. Küttel, S.A. Müller, I.C. Prentice, O. Solomina, T.F. Stocker, P. Tarasov, M. Wagner, and M. Widmann (2008). Mid- to Late Holocene climate change: an overview. *Quat. Sci. Rev.* 27(19-20), pp. 1791–1828. DOI: `10.1016/j.quascirev.2008.06.013` (cit. on pp. 84, 93).

Weedon, G. P., S. Gomes, P. Viterbo, H. Österle, J. C. Adam, N. Bellouin, O. Boucher, and M. Best (2010). The WATCH Forcing Data 1958-2001: A Meteorological Forcing Dataset for Land Surface- and Hydrological-Models. Technical Reports (22). WATCH (cit. on pp. 55, 56).

Weedon, G. P., S. Gomes, P. Viterbo, W. J. Shuttleworth, E. Blyth, H. Österle, J. C. Adam, N. Bellouin, O. Boucher, and M. Best (2011). Creation of the WATCH Forcing Data and its use to assess global and regional reference crop evaporation over land during the twentieth century. *J. Hydrometeorol.* submitted (cit. on pp. 55, 56, 85, 93).

Wessel, P. and W. H. F. Smith (2010). GMT v. 4.5.5. URL: `http://gmt.soest.hawaii.edu/` (cit. on pp. 71, 75, 137).

Wetzel, R. G. (2001). Limnology: Lake and River Ecosystems. 3rd ed. San Diego, London: Elsevier, p. 1006 (cit. on p. 28).

Williams, T. and C. Kelley (2004). Gnuplot. URL: `http://www.gnuplot.info/` (cit. on p. 34).

Wünnemann, B., D. Demske, P. Tarasov, B.S. Kotlia, C. Reinhardt, J. Bloemendal, B. Diekmann, K. Hartmann, J. Krois, F. Riedel, and N. Arya (2010). Hydrological evolution during the last 15 kyr in the Tso Kar lake basin (Ladakh, India), derived from geomorphological, sedimentological and palynological records. *Quat. Sci. Rev.* 29(9-10), pp. 1138–1155. DOI: `10.1016/j.quascirev.2010.02.017` (cit. on p. 96).

Yu, Z., D. Pollard, and L. Cheng (2006). On continental-scale hydrologic simulations with a coupled hydrologic model. *J. Hydrol.* 331(1-2), pp. 110–124. DOI: `10.1016/j.jhydrol.2006.05.021` (cit. on pp. 4, 12).

A. Tables

Catchment	Periode	Effective wetland fraction			
		GLWD	LSP2	MATT	SIND
Adycha	1937-1999	2.06E-002	1.89E-002	2.63E-002	3.12E-004
Amazon	1928-1998	2.82E-001	1.07E-001	5.40E-002	2.49E-001
Amu Darya	1931-1973	3.76E-002	2.06E-001	1.32E-002	4.97E-002
Amur	1963-1987	1.54E-001	9.33E-002	1.34E-001	1.04E-001
Anadyr	1958-1994	7.96E-002	8.64E-002	2.63E-001	1.01E-001
Anderson River	1969-2008	7.64E-002	4.57E-002	0.00E+000	1.43E-001
Araguaia	1974-1987	5.08E-001	7.24E-002	1.21E-001	2.38E-001
Arkansas River	1927-2007	7.77E-002	3.86E-002	4.30E-003	7.01E-002
Assiniboine River	1913-2007	2.53E-001	1.30E-002	5.29E-002	9.78E-002
Blue Nile	1900-1982	3.99E-002	1.84E-001	7.55E-003	1.72E-001
Brahmaputra	1969-1992	6.21E-001	4.79E-001	2.14E-003	6.45E-001
Brazos River	1903-2009	2.88E-002	1.52E-002	0.00E+000	5.56E-003
Chari	1933-1991	3.32E-001	2.80E-002	2.88E-001	1.70E-001
Churchill River	1971-2007	4.90E-001	1.63E-001	1.36E-001	3.16E-001
Colorado River	1934-2007	3.17E-002	1.42E-002	8.94E-006	2.82E-002
Columbia River	1878-2009	4.61E-002	9.44E-002	0.00E+000	2.63E-003
Congo	1903-1983	2.98E-001	7.43E-002	1.03E-001	1.34E-001
Danube River	1921-2002	1.15E-001	8.52E-002	2.43E-002	3.74E-002
Desna	1884-1985	1.96E-001	1.30E-003	1.53E-001	7.34E-002
Dnepr	1959-1988	1.91E-001	1.09E-001	1.13E-001	1.92E-001
Don	1881-1995	5.46E-002	6.68E-002	1.60E-002	2.81E-002
Elbe River	1874-2008	9.40E-003	9.56E-003	1.88E-001	2.61E-002
Euphrates	1923-1972	6.14E-002	5.73E-002	2.19E-002	2.88E-001
Fitzroy	1914-1973	2.26E-002	2.77E-003	7.97E-004	1.63E-003
Godavari	1901-1979	1.90E-002	1.88E-001	3.73E-003	3.36E-001
Indigirka	1944-1999	1.98E-002	2.55E-002	1.97E-002	4.77E-004
Irtysh	1891-1999	1.65E-001	6.56E-002	1.49E-001	4.73E-002
Kafue	1973-2005	1.94E-001	1.67E-002	2.37E-001	2.96E-002
Kama	1954-1973	1.41E-001	6.59E-002	3.55E-002	1.41E-001
Kansas River	1917-2009	2.67E-002	4.72E-002	0.00E+000	7.11E-003
Kemijoki	1911-2004	2.93E-002	3.82E-002	7.78E-001	2.92E-002
Kolyma	1978-2000	3.14E-001	3.25E-001	1.73E-001	1.85E-001

Continues on next page . . .

Catchment	Periode	GLWD	LSP2	MATT	SIND
Krishna	1901-1979	1.39E-002	1.57E-001	0.00E+000	2.89E-001
Kuskokwim River	1951-2008	3.25E-001	2.28E-003	6.04E-002	1.32E-003
Lena	1951-2002	1.48E-001	1.47E-001	1.38E-001	1.71E-001
Liard River	1942-2008	1.16E-001	8.67E-003	1.36E-002	1.37E-005
Limpopo	1955-1992	5.86E-003	1.15E-002	0.00E+000	2.40E-003
Loire	1863-1979	1.41E-002	2.93E-002	0.00E+000	4.34E-002
Mackenzie River	1972-2008	4.99E-001	1.31E-001	8.95E-002	9.13E-002
Magdalena	1971-1990	8.00E-002	8.76E-002	5.52E-002	2.04E-001
Mekong	1960-1970	8.69E-002	2.33E-001	1.42E-002	2.72E-001
Mississippi River	1928-1999	1.57E-001	2.93E-002	1.94E-002	1.98E-001
Missouri River	1897-2009	9.37E-002	3.70E-002	3.47E-004	3.48E-002
Nemunas	1812-2003	9.47E-003	6.15E-003	8.77E-002	9.40E-003
Niger	1952-2000	1.82E-001	3.90E-002	8.33E-002	1.02E-001
Nile	1973-1984	9.75E-002	1.02E-001	3.02E-002	7.44E-002
Nizhnaya Tunguska	1939-1995	7.98E-002	8.02E-002	2.26E-002	0.00E+000
Ob	1930-2003	3.19E-001	2.22E-001	4.35E-001	3.96E-001
Oder River	1920-2004	1.73E-002	2.18E-002	6.85E-004	3.07E-002
Ogooue	1930-1975	8.85E-002	4.68E-002	1.91E-002	3.92E-002
Ohio River	1928-2004	6.52E-002	1.12E-002	0.00E+000	8.56E-002
Olekma	1936-1999	1.24E-002	1.23E-002	1.79E-002	0.00E+000
Olenek	1952-1963	3.32E-002	4.00E-002	0.00E+000	4.26E-006
Orange	1935-2001	9.99E-003	3.41E-003	0.00E+000	2.34E-002
Orinoco	1923-1989	3.80E-001	5.97E-002	5.76E-002	3.08E-001
Parana	1901-1986	1.18E-001	9.75E-002	4.49E-002	1.36E-001
Peace River	1959-2007	4.59E-001	1.29E-002	5.07E-002	7.16E-003
Pechora	1916-2003	2.32E-001	9.71E-002	2.74E-001	8.57E-002
Podkamennaya Tunguska	1979-1999	1.99E-002	2.47E-002	1.57E-004	0.00E+000
Porcupine River	1987-2007	2.61E-001	2.90E-002	5.40E-002	3.77E-002
Prypyat	1965-2002	4.66E-002	6.56E-003	7.71E-001	8.08E-002
Red River of the North	1962-2007	3.05E-001	5.75E-002	2.61E-002	7.77E-002
Rhine River	1901-2007	1.25E-002	9.44E-003	1.47E-003	1.55E-001
Rio Japura	1973-1993	8.88E-002	3.24E-002	3.11E-003	3.47E-002
Rio Parnaiba	1982-1993	2.73E-001	6.30E-003	5.05E-002	5.91E-003
Rio Tapajos	1975-1994	1.48E-002	1.96E-002	2.41E-004	3.18E-003
Sanaga	1943-1980	1.60E-002	1.63E-002	2.40E-003	5.16E-003
Sao Francisco	1938-1999	3.95E-001	1.05E-001	1.98E-002	9.16E-002
Selenga	1936-1999	1.96E-001	1.99E-001	7.84E-003	1.55E-003
Senegal	1904-1989	2.55E-002	2.45E-002	1.19E-002	4.34E-002
Severnaya Dvina	1881-2003	8.93E-002	5.19E-002	1.28E-001	2.12E-002
Shire	1965-1984	3.52E-001	3.08E-001	3.58E-002	5.77E-002
Slave River	1921-2007	5.29E-001	9.45E-002	1.09E-001	5.36E-002

Catchment	Periode	GLWD	LSP2	MATT	SIND
Snake River	1912-2000	6.37E-002	6.48E-002	0.00E+000	6.41E-003
Songhua Jiang	1898-1987	6.26E-002	7.04E-002	7.09E-002	2.99E-001
Svir	1955-1988	2.23E-001	2.33E-001	8.32E-002	1.00E-001
Syr Darya	1930-1986	6.68E-002	2.98E-001	2.57E-002	6.21E-002
Tavda	1967-1995	6.30E-002	3.82E-002	1.64E-001	1.36E-001
Tisza	1921-1999	3.03E-003	5.65E-003	2.30E-002	6.59E-003
Tobol	1961-1996	1.20E-001	3.66E-002	1.60E-001	1.34E-001
Tocantins	1978-1999	4.02E-001	1.07E-001	8.31E-002	1.38E-001
Uruguay	1965-1994	5.75E-002	6.90E-002	8.88E-002	5.13E-002
Usa	1931-1998	3.10E-002	3.16E-002	9.81E-002	1.56E-002
Vaal	1909-2001	2.45E-002	3.58E-002	0.00E+000	4.44E-003
Victoria Nile	1948-1970	3.64E-001	3.00E-001	8.05E-002	8.99E-002
Vilyuy	1936-1998	6.22E-002	5.02E-002	6.20E-002	4.56E-002
Vistula Wisla	1900-1994	1.28E-002	2.00E-002	3.62E-002	1.04E-002
White Nile	1973-1982	2.03E-001	1.28E-001	1.06E-001	9.53E-002
Winnipeg River	1987-2007	4.98E-001	2.19E-001	1.51E-001	3.07E-001
Xingu	1971-1998	9.62E-002	7.23E-002	4.24E-002	4.74E-002
Yana	1972-2003	6.03E-002	4.20E-002	6.11E-002	1.84E-002
Yangtze River	1922-2004	2.28E-001	3.13E-001	5.62E-003	4.96E-001
Yellowstone River	1910-2008	3.55E-002	2.95E-002	0.00E+000	1.62E-005
Yenisey	1902-1999	5.78E-002	1.30E-001	7.04E-003	2.57E-002
Yukon River	1975-2008	4.14E-001	2.12E-002	1.54E-001	5.54E-002
Zambezi	1942-2006	2.04E-001	9.83E-006	1.80E-001	2.05E-001

Table A.1.: Selection of river catchments used for the static optimization. Shown are the names as stated by the GRDC, the data sampling periods and the effective wetland fraction for all wetland observation databases.
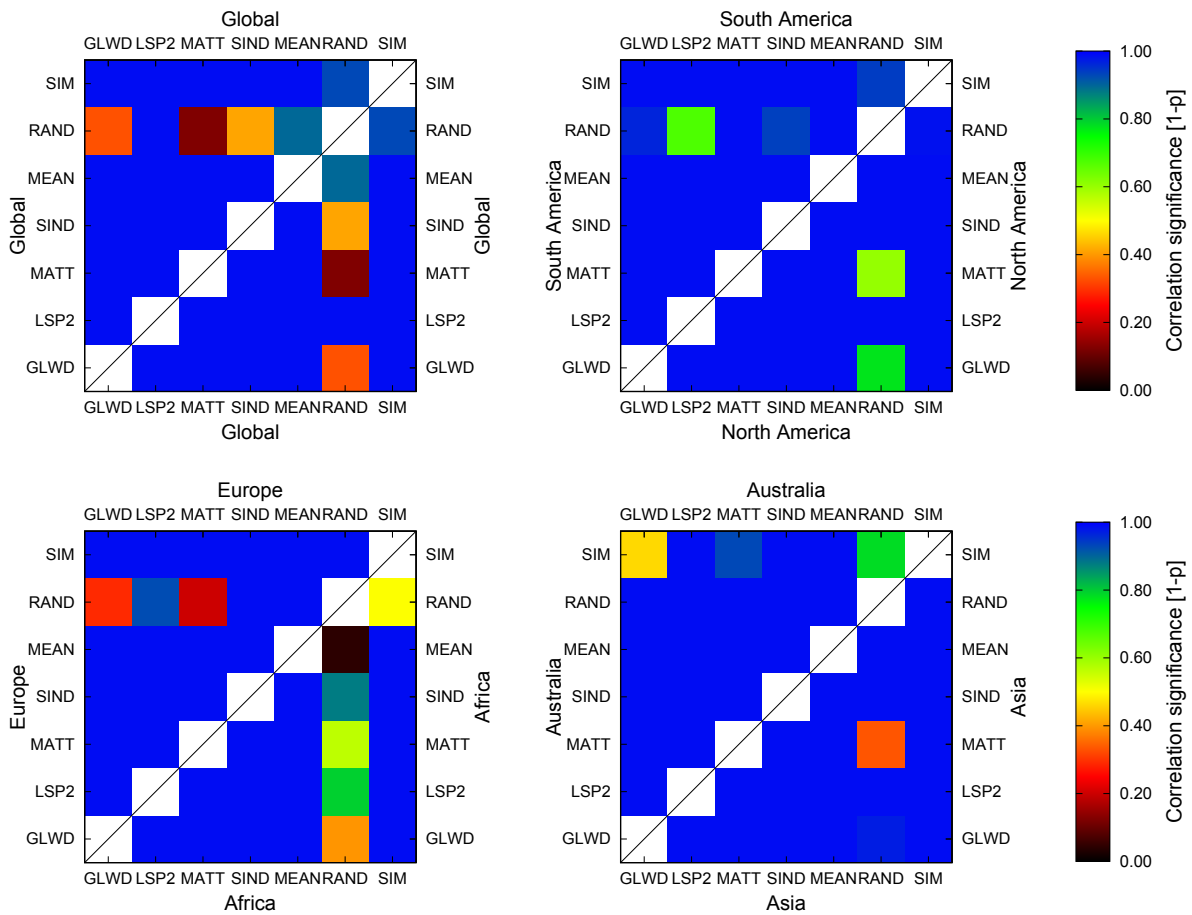
B. Figures

Figure B.1.: Matrices showing the correlation significance probability between wetland observations (GLWD, LSP2, MATT, SIND), their ensemble mean (MEAN), a random mask (RAND) and the simulated wetland distribution (SIM). Except for the global correlation, all panels show two continents divided by a black line.
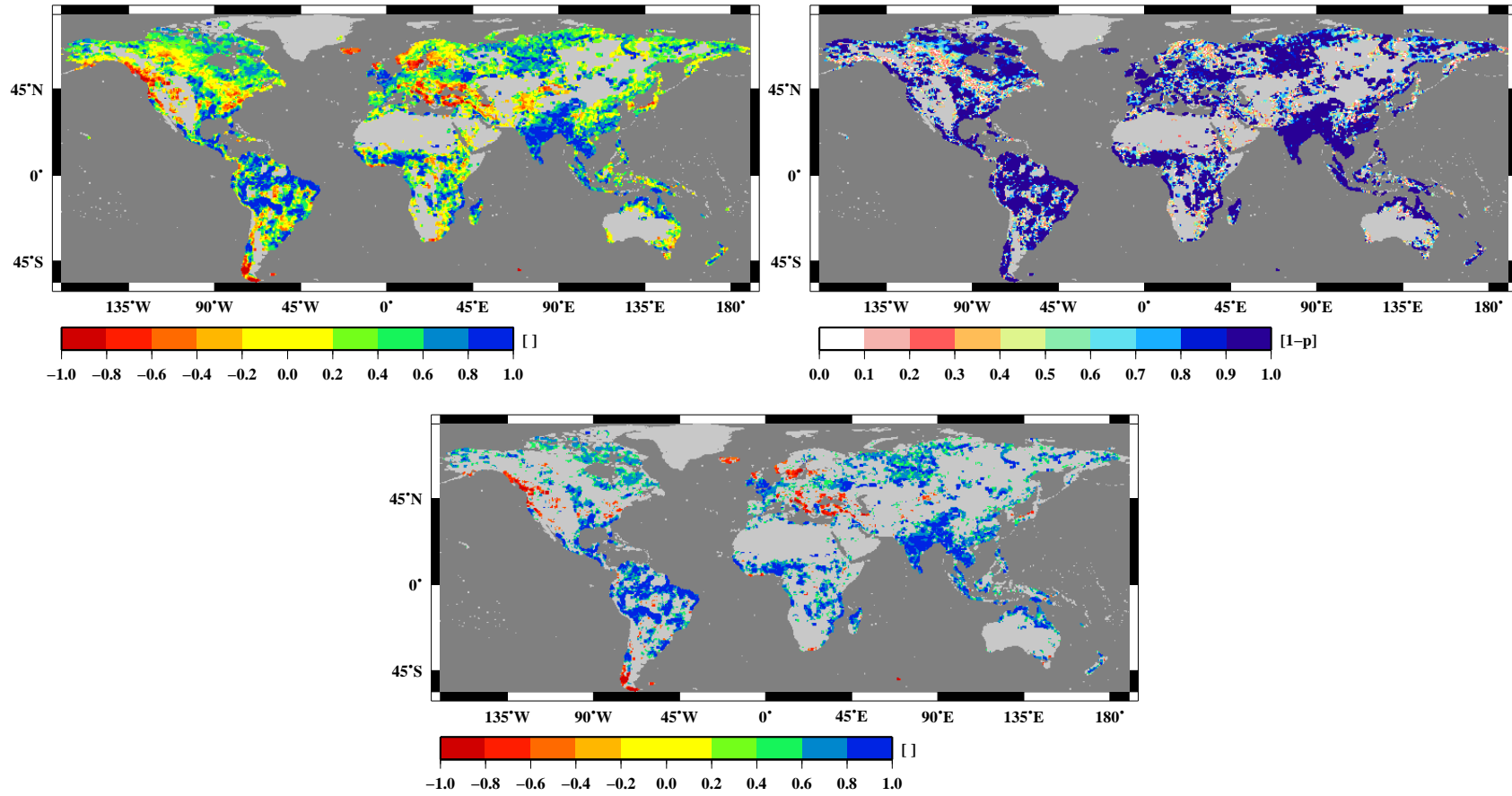
Figure B.2.: Correlation coefficient r (top left) and its significance probability (top right) obtained from the correlation analysis between simulated wetland fractions and SIND wetland fractions. Only the dark blue grid cells are considered to express a significant correlation. The bottom panel shows r restricted to grid cell which exceed the 90% significance level. In this correlation analysis the snow mask is not applied to the simulated wetland distribution.
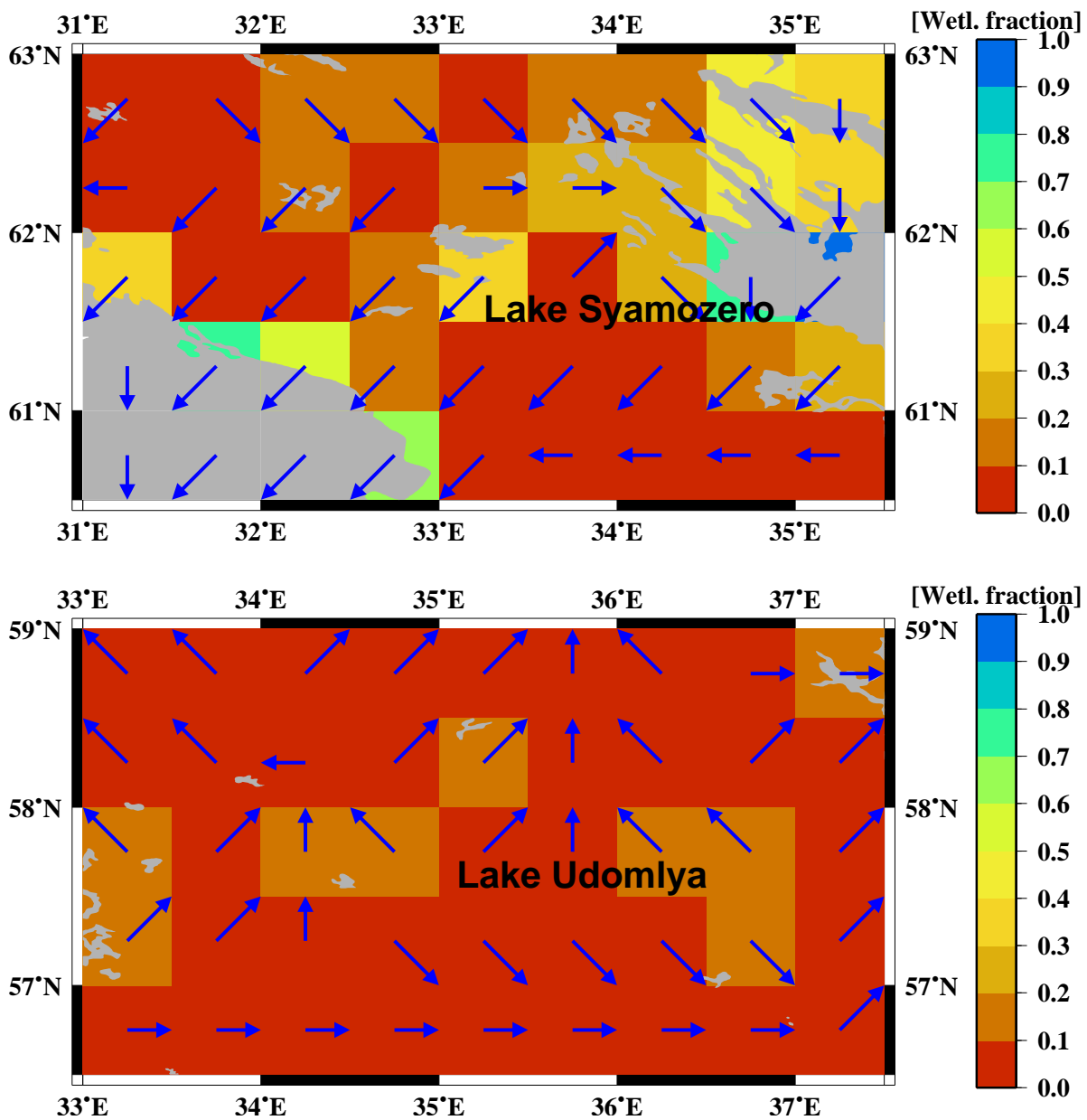
Figure B.3.: This maps display the simulated wetland fractions for Lake Syamozero (top panel) and Lake Udomlya (bottom panel) as well as river flow directions (blue) within the MPI-HM. The gray structures indicate lake extent as included in the plotting software GMT (Wessel and Smith, 2010).
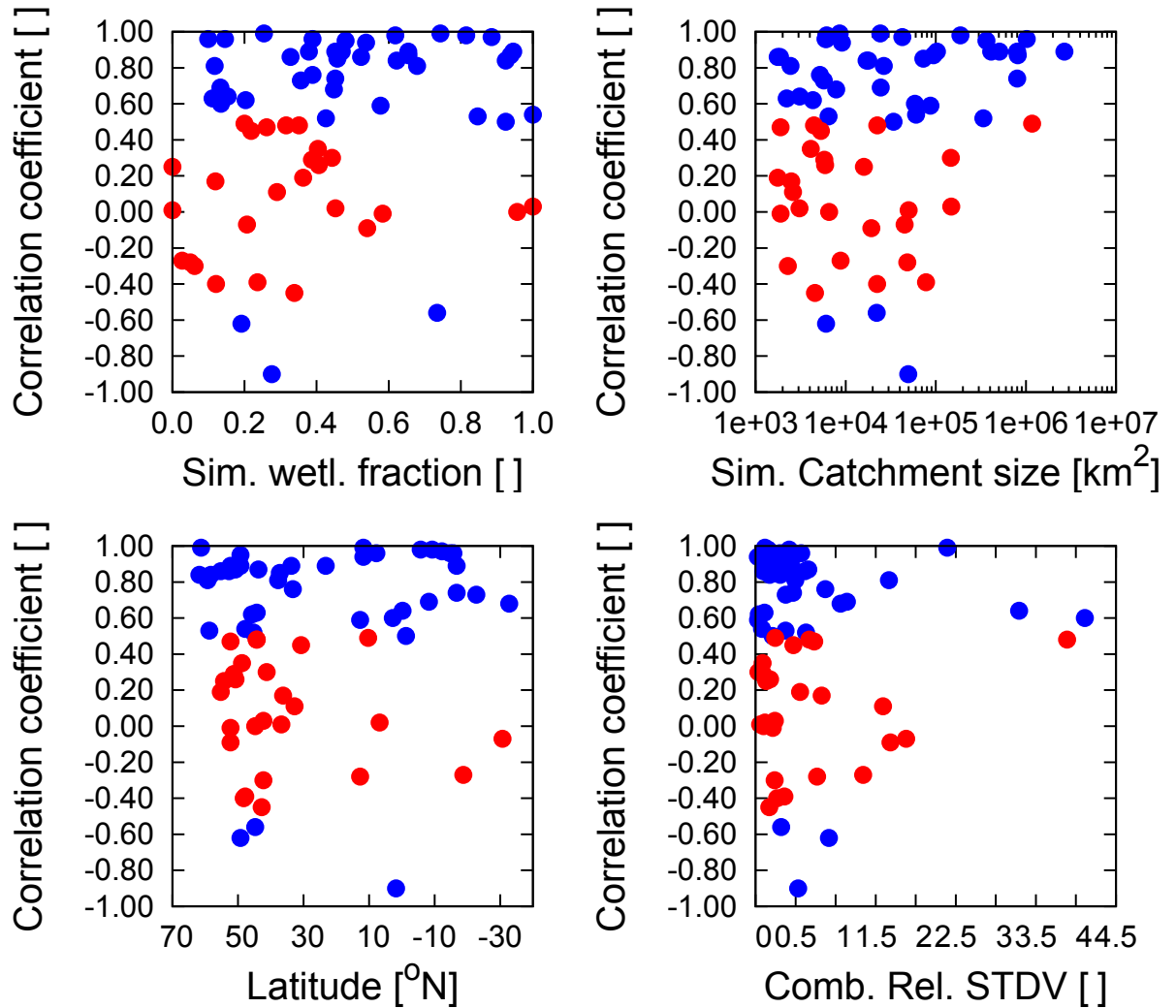
Figure B.4.: Dependency of correlation coefficient and significance on the simulated wetland fraction of the respective grid cell (top left) as well as their catchment size (top right), latitude (bottom left) and the combined standard deviation of observed and simulated lake level observations (bottom right). Blue points indicate significant correlation, and red points indicate insignificant correlations.
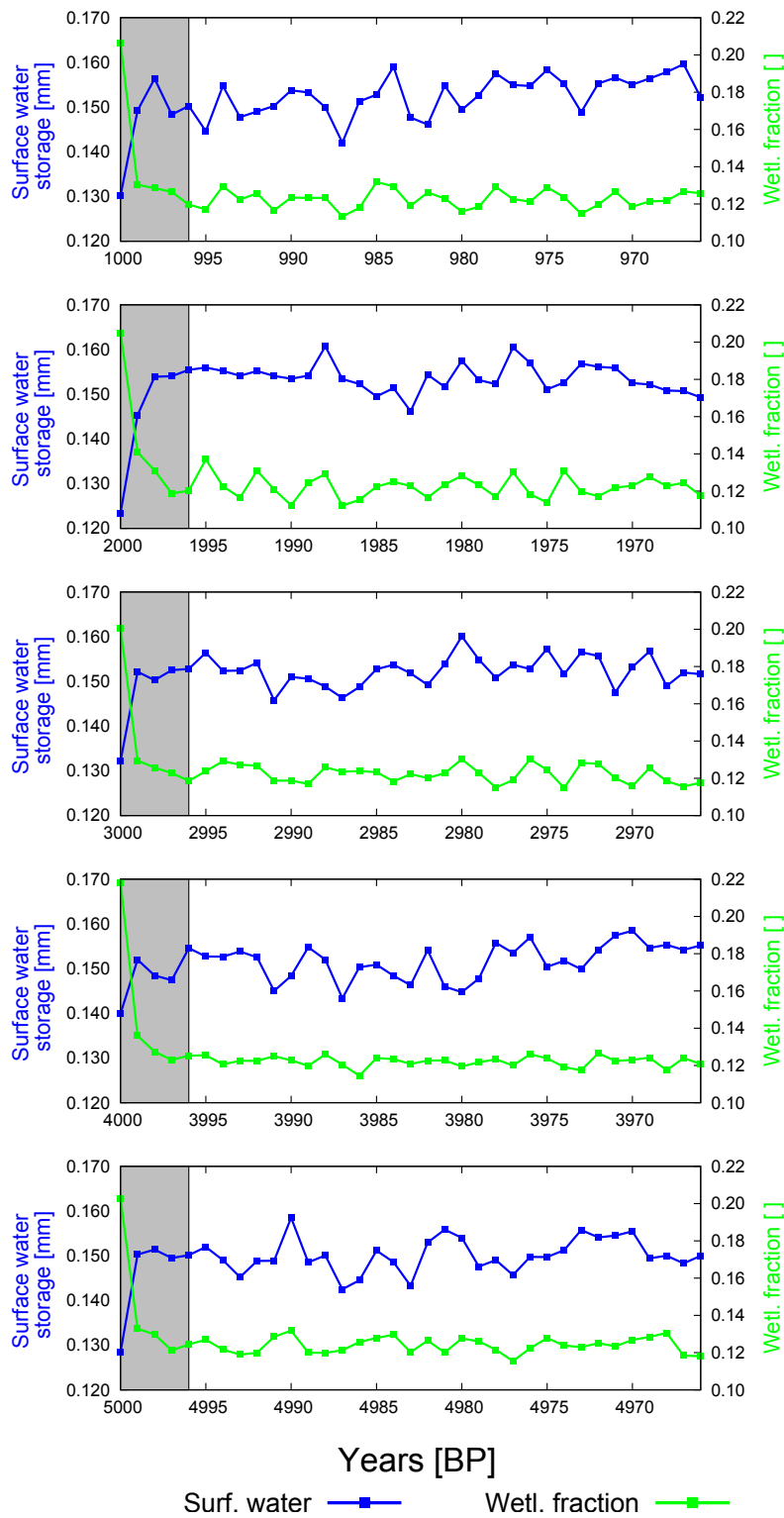
Figure B.5.: Evolution of the annual mean land surface water storage and wetland fraction for timeslices between 5000 and 1000 yBP. The gray areas indicate years which are omitted from the analysis because of their spin-up behavior.
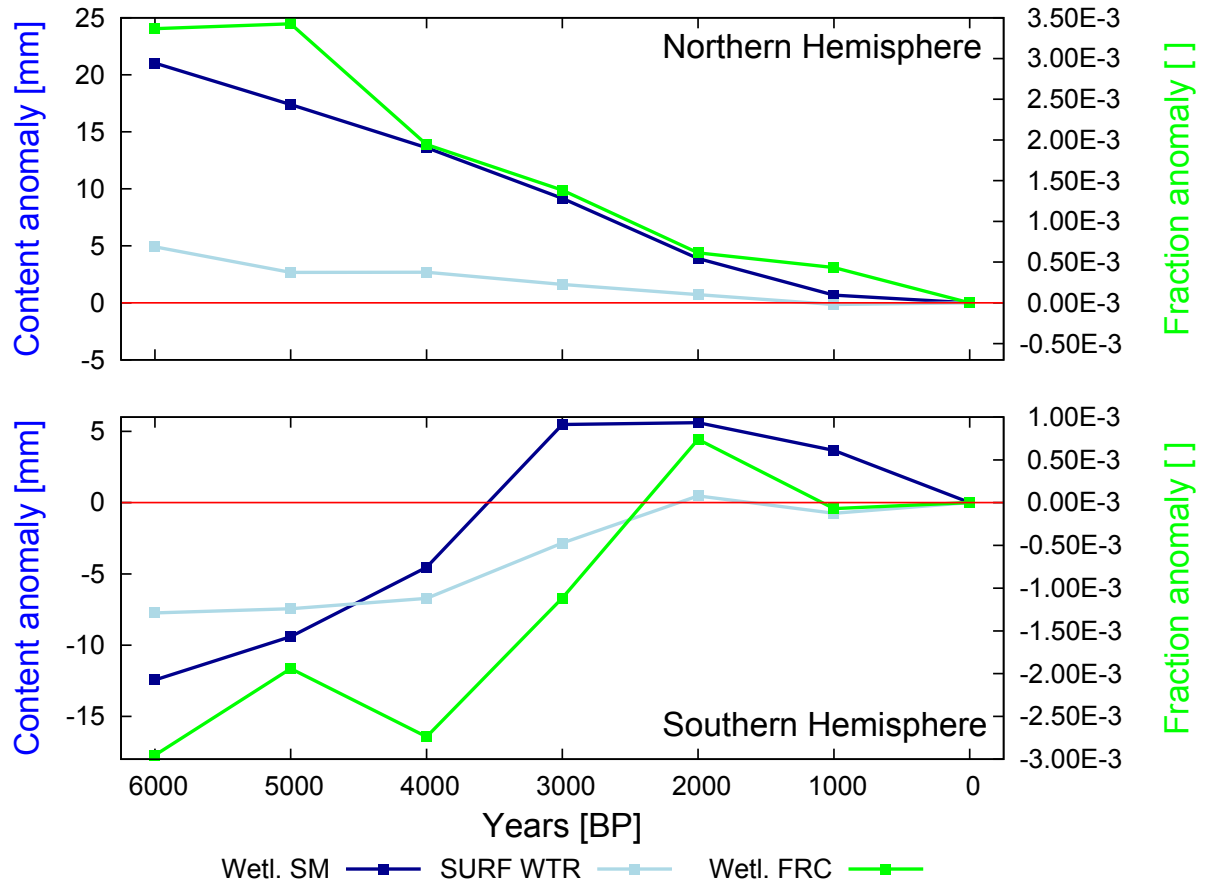
Figure B.6.: Mean land surface anomalies of wetland soil moisture (Wetl. SM), surface water level (SURF WTR) and wetland fraction (Wetl. FRC) for all simulated time slices. The upper panel shows the northern hemisphere, and the lower panel shows the southern hemisphere.
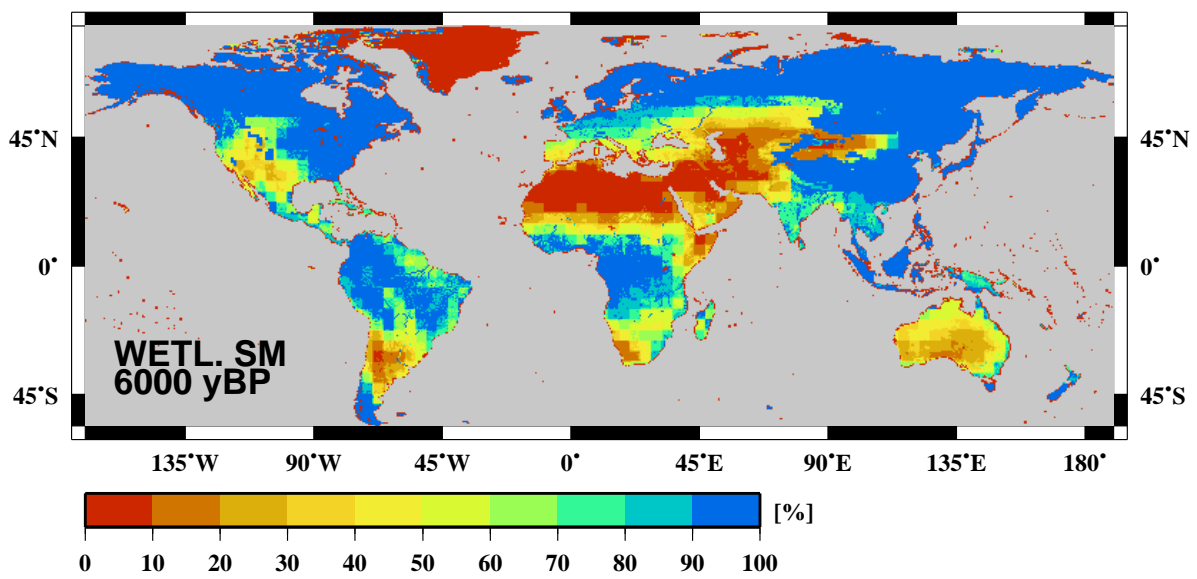
Figure B.7.: Relative soil moisture saturation for wetlands in the Mid Holocene simulation.
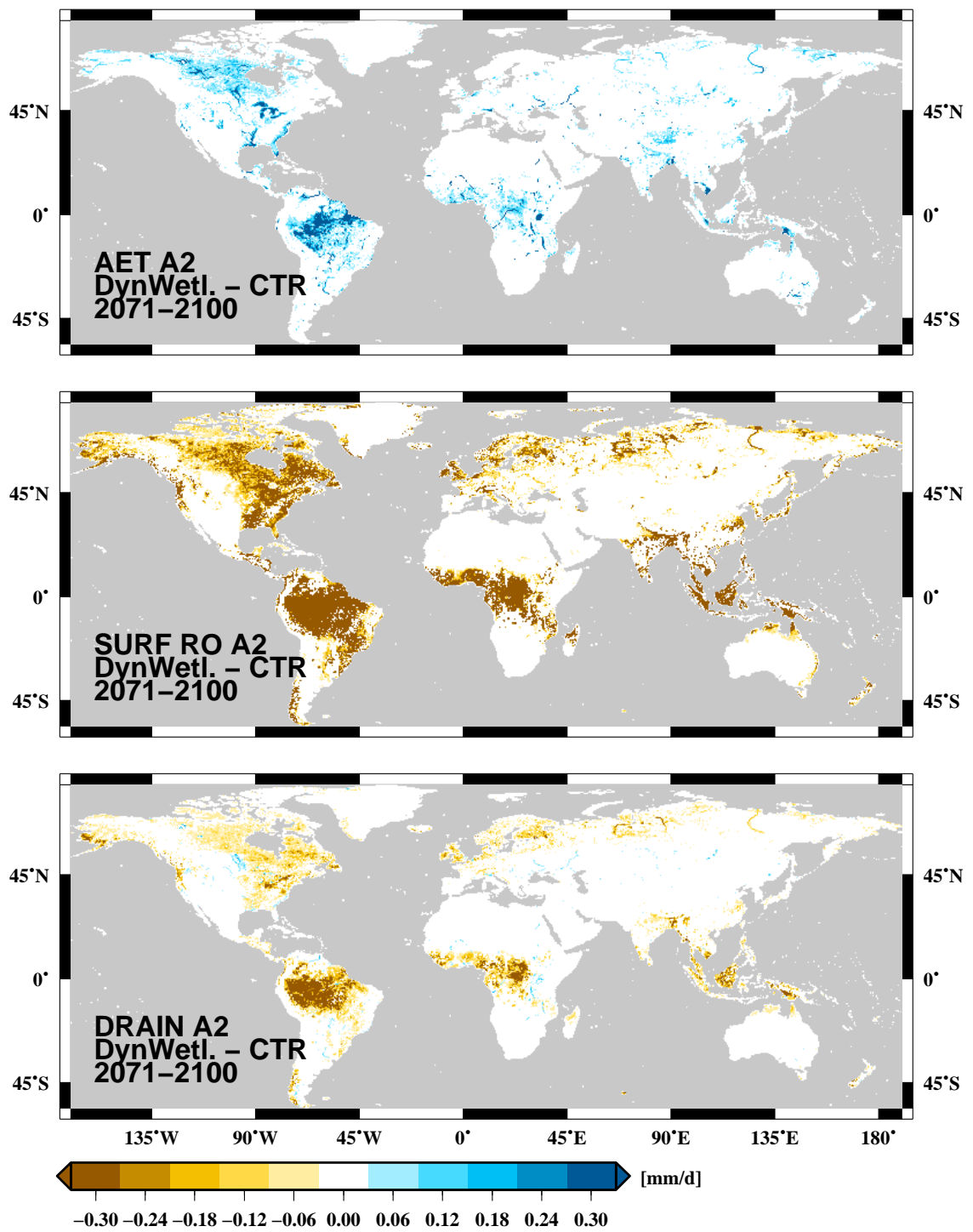
Figure B.8.: Mean simulated difference for the period 2071-2100 between the dynamical wetland A2 simulation and the respective control simulation. The panels show the average grid cell ET (top), the surface runoff (middle) and the drainage (bottom).
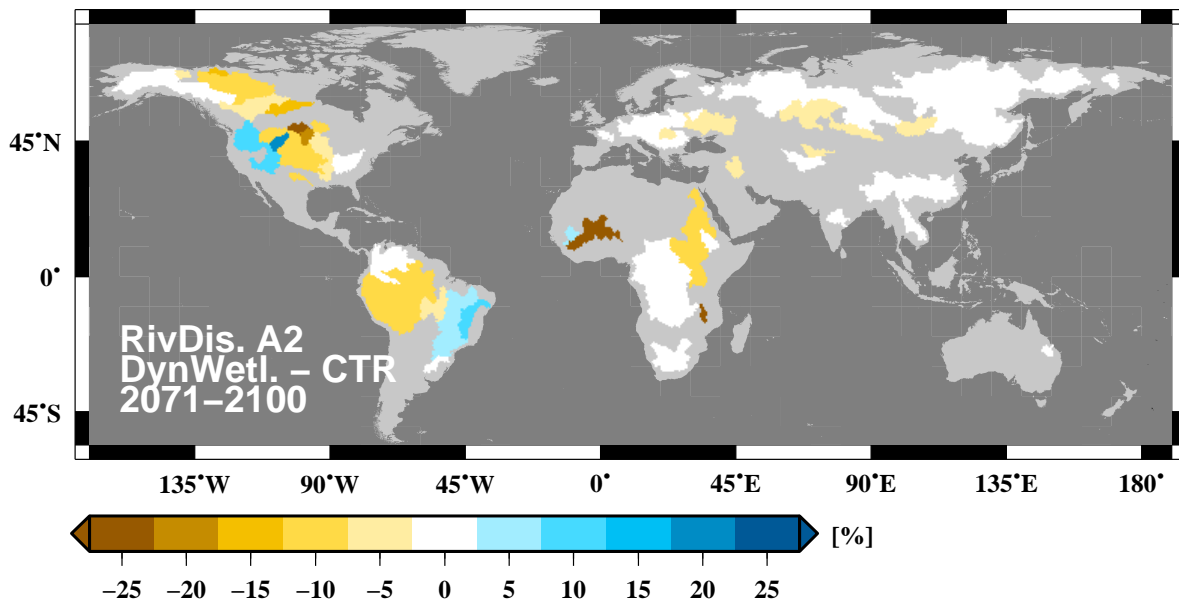
Figure B.9.: Mean relative river discharge difference between the dynamical wetland scheme and the control simulation for the A2 simulation.